UNIVERSITY OF OXFORD

DPHIL IN MATERIALS SCIENCE

Oxide Based Ceramic Matrix Composites For High Temperature Aerospace Sealing Applications

Author:
Talha J. PIRZADA

Supervisors:
Professor Thomas J. MARROW
Professor Marina GALANO

December 12th, 2021

A Thesis submitted for the Degree of

Doctor of Philosophy

Linacre College

جہانِ تازہ کی افکارِ تازہ سے ہے نمود
کہ سنگ و خشت سے ہوتے نہیں جہاں پیدا

New worlds are born out of ideas fresh and new
From bricks and stones a world was never built nor grown

- Iqbal

DEDICATION

First and foremost, I dedicate my thesis to my mother, Aasia Owais Pirzada, the most intellectually-curious woman I know, who made me fall in love with books, and who dreamt the dream that I am living today.

To my late grandmother, Mumtaz Jamal Shah, whose love for knowledge instilled in me a curiosity for learning.

To my father, Ahmed Owais Pirzada, who never lost faith in me, even when I hit rock bottom.

To my late grandfather, Justice Pir Karam Shah, who was my guiding star all along. Whenever I am lost, his words echo in my mind and I now understand what those words meant, "When the flame of knowledge burns out, human contemplation is incinerated by absurdity.".

ACKNOWLEGDEMENTS

کمالِ همنشیں در من اثر کرد
وگرنه من همان خاکم که هستم
سعدی

All attributes and knowledge that you see were taught to me by other people,
My own reality is merely that of an empty vessel
- Saadi

Family
I would like to acknowledge the man who believed in me when I was a failure, who motivated me, who told me what I was capable of when I was doubting myself. The man who was constantly there, every day, listening to my doubts for hours on end. Whispering in my ears that I was destined for greater things. He was the person who told me I was made for Oxbridge when I failed 8th grade. With a report card filled with U's, he would go to my teachers and tell them how intelligent I was. Thanks for believing in me, Baba. You taught me the importance of hard work, knowledge, character and most of all, giving. I have much to learn, and I know I am not even halfway there, but every time you look at me with pride in your eyes, it means the world to me. Love you, Baba!

I would like to thank all my family members including my brothers, Shahzad Ali Akbar, Ahmed Jamal Pirzada, Ahsan Jamal Pirzada and Sachal Jamal Pirzada, for their love and unwavering support. I would like to thank my sisters-in-law, Amna Arif and Amna Shah, for consistently supporting me throughout the process.

Thanks to Mian Tayyab Hassan, who has always been a grandfather-figure to me, and to Uncle Asif Bajwa who has consistently provided me with amazing advice. I would like to thank all my friends, especially Haseeb, Shayan, Haris, Saad, Imad, Maryam, Allayar, Sachal, Nida, Hina and Uzair for invariably uplifting my spirits.

To my Oxford family, Mohsin Javed, Sarah Salim, Dr Adeel Malik, Vikaran Khanna, Arslan, Taimoor, Fatima, Naeem, Hamayun Talat and Amal, for being my strength throughout my DPhil journey, for introducing me to my one and only love, poetry, and I can't thank you enough!

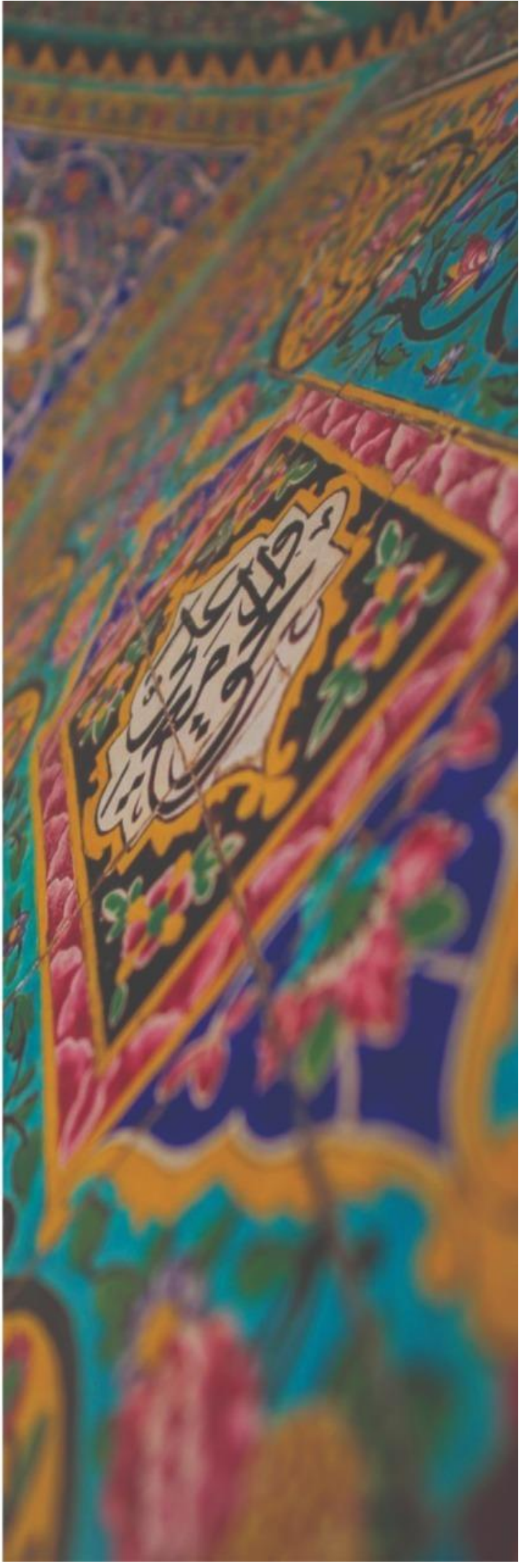

Cross
I would start by thanking Paul Blanchard, my Manager, my teacher, my friend, who supported me in every endeavour, no matter how crazy it sounded at first.

I would like to acknowledge my Industrial Supervisor and Technical Director, Edward Cross, who guided and supported me at every step of my DPhil journey. I would like to thank Richard Cross and Mark Bradley who provided me with technical, moral and financial support. Without their assistance, this would not have been possible.

To the met-lab crew, Lewys White and Aidan Bew, who have been exceptionally supportive, ensuring the Metallurgical Laboratory functioned smoothly when I was not around. Lewys, thank you for also proof-reading my dissertation. To Danny, Henry and Darren in the design office for their support and everyone at Cross, thank you for making this possible!

To Sue and Victor Butchers: thank you for being my family at Cross!

Mentors
On this journey, I came across two people who served as my mentors, who taught me wisdom and knowledge, who showered on me their love and affection and I am ever grateful. Professor Adeel Malik, who treated me like a younger brother, cared for me, fed me and taught me more about myself than I had known before. I would always be indebted to him, and I hope to keep learning from him.

Syed Babar Ali, to whom I was introduced during a leadership course at Oxford, and later had the marvellous opportunity to work-shadow under his guidance. During this, I realised what excellence, character, humility, knowledge, honesty, wisdom and leadership meant. I observed first-hand how he lived, impacted the world around him, helped build institutions, and how multi-skilled and versatile he is and most of all how effective he has been in making the world around him more beautiful.

If I imagine my three-and-a-half year journey without my two mentors, I believe I would still be a lantern searching for its light. One made me understand my purpose whilst the other showed me how to achieve it, for this I am forever grateful to both.

Oxford
I would like to acknowledge Professor James Marrow, who taught me with great patience, who provided me with technical supervision, mentored me, and supported me throughout the journey. I would also like to thank Professor Marina Galano for her supervision and support during my DPhil. I would like to thank Professor Richard Todd at Oxford, Professor Luc Vandeperre at Imperial and Dr. Dong Liu at Bristol for the technical guidance they provided and Jalal al Lami for not only helping me carry out high temperature creep testing but also proofreading my work.

To all my friends at Oxford, the list is too long to be written down, I love you and I thank you for making these 3.5 years of my life the best ones yet.

I would like to thank each and every member of my PhD group, and specifically Shruddha, Yang, Abdul, Phil, Robin, Thomas. It was an absolute pleasure working with you all.

I would like to thank Linacre College Principal, Nick Brown. and my Senior Tutor, Jane Hoverd, for their massive support and guidance. Linacre made me feel at home! Thanks to all its amazing members.

To the city itself, Oxford! I came here thinking I would learn so much about the world, and I finished knowing a bit more about myself.

Abstract

This thesis looks at the viability of using oxide based ceramic matrix composites for high temperature gas turbine sealing applications. Two material systems namely Nextel312/SiOC, Nextel 312 fibre with SiOC matrix, and Nextel720/Alumina, Nextel 720 fibre with alumina matrix, were studied in detail and modified in order to produce CMC variants that could perform adequately as seals materials.

Nextel 312/SiCO composites were optimised for sealing applications at service temperatures of up to 900°C, using repeated matrix impregnation and pyrolysis (polymer infiltration processing, PIP) at different temperatures. The microstructures were analysed using SEM, TEM, XRD and X-ray computed tomography in order to quantify the differences arising from the manufacturing process. The materials were tested mechanically to determine their strength, ductility, interfacial shear strength and fracture behaviour. The thermal stability of the composites was investigated using thermo-gravimetric analysis (TGA). The objective was to identify the PIP temperature that could provide the optimum combination of properties of high elastic flexural deflection, thermal stability, low interfacial shear stress for toughening and low mass loss up to the intended service temperature. Processing at 950°C or above gave a combination of high effective elastic modulus, good resistance to mechanical damage from tensile strain and good thermal stability. The temperature capability of this material system, as studied in literature and by carrying out experiments in this piece of work, suggests that this material system would not be able to perform adequately as a seal at temperatures ≥ 900°C for extended periods, hence it was not investigated further in this study.

After identifying the key gaps in literature, an investigation was carried out that looked at the deformation and fracture of a 0/90° Nextel 720 alumina/Mullite fibre with alumina matrix ceramic-

matrix composite material by *in situ* synchrotron X-ray computed micro-tomography at ambient temperature and at 1100°C. A three-point loading configuration was used and samples were loaded monotonically until final fracture. The flexural strength was found to be unaffected by temperature. 3D visualisation of the microstructure showed that fracture occurred by propagation of internal cracks at stresses close to the flexural strength. Shear fractures propagated across fibre bundles that were oriented perpendicular to the flexural stress at both room temperature and 1100°C. At 1100°C however, an additional failure mode of delamination was observed, in the form of needle shaped cracks in between fibre bundles parallel to x axis. This may arise from relaxation of thermal residual stresses or could be a function of the creep strains which could develop within the sample.

Once it was established that Nextel 720 with alumina matrix could perform adequately at the given temperature, 8 different variants, each with different fibre layup, weave pattern and processing temperature, were produced. Three-point bend tests were done at 1100°C, to quantify the effective flexural modulus along with the proportional limit stress, PLS, for each of the samples. The results suggested that out of all 8 samples, EF 20, which had a unidirectional fibre weave architecture, sintered at 1250°C, with an involute layup, had the most optimum mechanical properties.

Creep tests were carried out on beam specimens in three-point bend test configuration at 25MPa stress, at 1100°C. The results indicated that EF 20, due to its unidirectional weave configuration, developed lower primary and secondary creep strains, in comparison to EF 19 which had 50% fibre tows in the warp and the weft directions. The involute layup outperformed the 0/90° layup, due to higher shear strength between the layers. The samples sintered at 1250°C had similar creep performance to the samples sintered at 1200°C. Using the effective modulus values calculated for EF 19-1 and EF 20-1, piston rings with a gauge diameter of 140 mm were designed and subjected to a

constant deflection condition with a nominal stress of 25 MPa, at 1100°C. The EF 19 ring performed adequately, only losing 13% of their spring at 1100°C. When the fitted stress was beyond the PLS limit permanent microstructural deformation was observed in the sample, EF 20, which resulted in higher stress relaxation than normal. Hence future ring design must be done keeping in mind the PLS. The manufacturing process should be reviewed, such that the machining of the piston ring does not result in cutting through the fibre layers, lowering the number of defects and consequently resulting in a higher PLS. This work was successful in identifying and modifying an oxide based ceramic matrix composite system for use in gas turbine sealing applications at 1100°C.

Author's note

Over the period of the DPhil the author has published 4 papers, 2 as first author and two as collaborative work.

Publications

The research presented in **CHAPTER 4** of this thesis, was published in Composites Part A: Applied Science and Manufacturing **in November 2020**.

(https://www.sciencedirect.com/science/article/pii/S1359835X20304346)

The research presented in **CHAPTER 5** of this thesis has been published in "Journal of European Ceramic Society" **in July 2021.**

In situ observation of the deformation and fracture of an alumina-alumina ceramic-matrix composite at elevated temperature using x-ray computed tomography - ScienceDirect

The author of this thesis is the first author of both these papers.

Other Publications

"Structure and flexural properties of 3D needled carbon fiber reinforced carbon and silicon carbide (C/C-SiC) composites fabricated by gaseous and liquid silicon infiltration" Fan Wan **Talha J. Pirzada**, Rongjun, Liu Yanfei Wang, Gongjin Qi, Changrui Zhang, Thomas James Marrow Ceramics International 45 (2019) 17978–17986.

https://www.sciencedirect.com/science/article/pii/S0272884219315007?via%3Dihub

"Hydrothermal aging and structural damage of a jute/poly (lactic acid) (PLA) composite observed by X-ray tomography" Ning Jiang, Tao Yu, Yan Li, **Talha J. Pirzada**, Thomas James Marrow, Composites Science and Technology 173 (2019) 15-23.

https://www.sciencedirect.com/science/article/pii/S0266353818313733

Conference

The author presented the paper titled “In situ observation of elevated temperature deformation and fracture of an oxide (alumina-alumina) ceramic matrix composite” at the international “HTCMC Conference 2019” in Bordeaux.

Table of Contents

List of Figures

List of Tables

CHAPTER 1. INTRODUCTION

1.1 Introduction

Materials for high temperature gas seals in aerospace components, such as aero-engines and rockets, have received attention in recent years due to the need for reduced weight and higher operating temperatures for increased efficiency [1–3]. Advance sealing technologies such as brush seals and labyrinth seals can boost the overall efficiency of a gas turbine by 1-2% [4]. Superalloys are currently being used for sealing applications above 700°C. These include nickel and cobalt based alloys like Waspaloy, X750, Inconel 718 and Haynes 25 [5]. Oxide dispersion-strengthened alloys are also being used for sealing application as they provide thermal stability at temperatures around 1000°C [6]. Only one grade of oxide dispersion-strengthened alloys (ODS alloys), MA956, can achieve spring retention up to a temperature of 1000°C. Due to the constant increase in turbine entry temperature, materials which can perform adequately at temperatures in access of 1000°C are required [7].

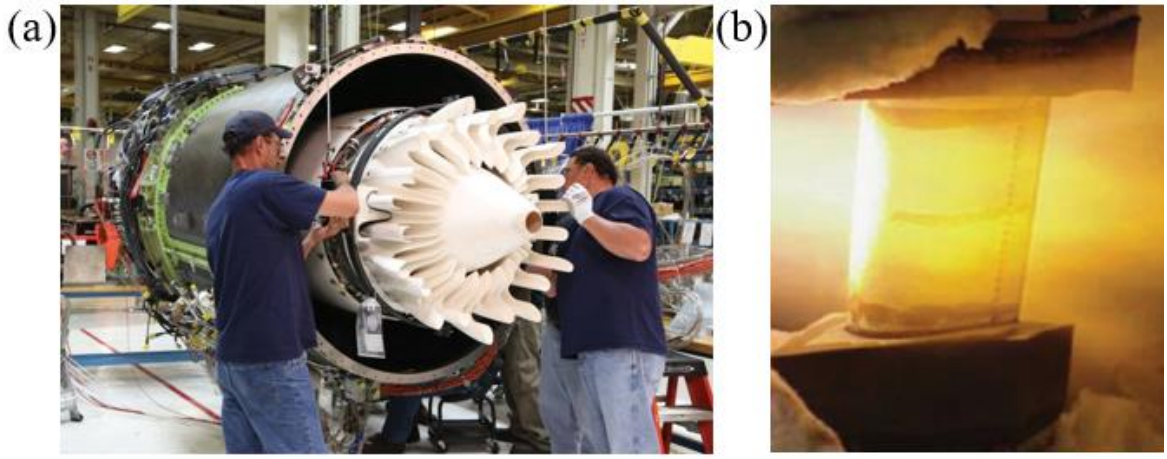

Figure 1: *Oxide-CMCs used in gas turbine applications (a) An exhaust diffuser nozzle and (b) a turbine stator vane made from CMCs* [8]

Ceramic matrix composites (CMCs) are currently being incorporated in gas turbines due to their improved fracture toughness while maintaining excellent mechanical and corrosion properties at temperatures in access of a 1000°C. In comparison to monolithic ceramics, CMCs offer good thermal shock resistance [1, 5]. They can also have high toughness by encouraging quasi-ductile deformation as toughening mechanisms, such as crack deflection, fibre pull-out, crack bridging and debonding; achieved through optimal control of the interface between fibre and matrix [6, 7]. Lower interfacial shear strength between the fibre and the matrix can maximise crack deflection and increase fracture resistance to provide flaw insensitivity and damage tolerant behaviour [1]. To design CMCs for critical high-temperature aerospace applications such as seals, the three main material components (i.e. the fibre, matrix and the interface) must be selected and controlled to obtain the required performance; to (a) maximise the range of elastic deformation in the component; (b) minimise stress relaxation at service temperature; and (c) have a fibre/matrix interface that is chemically stable at service temperatures [8, 9].

Due to their chemical stability oxide-based CMCs (Ox-CMCs) are used as structural materials in high temperature, ≥1000°C , oxidising environments including combustion gases [15]. Due to their thermal stability, continuous fibre Ox-CMCs have been used to make aircraft exhaust components *e.g.*, nozzle flaps [16,17], light weight helicopter exhaust ducts [9,16], sealing/casting shrouds and stationary vanes in gas turbines [17,18]. They have also been used to make exhaust diffusers and turbine blades as seen in **Figure 1** [8]. One such material, aluminosilicate fibre/mullite matrix composite has a porous matrix and exhibits damage tolerant behaviour up to 1200°C [14,19,20]. The infiltration-processed mullite matrix retains strength at 1200°C while providing oxidation stability [21,22].

Compared with SiC CMCs, Ox-CMCs offer a superior environmental stability and can be made into larger components at significantly lower cost, as processing does not involve repetitive re-infiltration or pyrolysation steps [17,23]. For example, alumina (Nextel 720) fibre-based CMCs have been proposed for novel revolutionary combustors [24] that will shorten the combustion length by up to 50%. Furthermore, compared to the aerospace alloys currently being used for gas turbine seals, Ox-CMCs can provide resistance to creep at temperatures 200-300ºC higher than current operating temperatures [17]. To the author's knowledge, Ox-CMCs have not been incorporated in sealing applications. The purpose of this project is to evaluate and enhance a range of Ox-CMCs to achieve high fracture toughness and minimise stress relaxation at temperatures around 900°C to 1100°C, for sealing applications, over extended periods [25–28].

Two different Ox-CMCs were investigated in this study namely:

- Nextel 312 system with SiCO matrix and boron nitride as the interface coating
- Nextel 720/fibre-based system with porous alumina matrix with no interface coating

This thesis carries out in-situ and ex-situ experiments at temperature to pinpoint how the failure mode changes at temperature. Using techniques such as Digital Volume Correlation, X-Ray tomography and flexural loading, the aim was to understand how the CMC fails, particularly whether it is creep or microstructure fracture that governs the failure mechanism at high temperature. Using microstructure modification techniques specified in the literature, the objective was then to maximise elastic deflection and minimise permanent strain development by modifying the material either by altering the processing parameters or looking at the fibre/fabric layup.

The thesis starts by defining the key properties required for any material that will be used for gas turbine sealing applications. A brief overview of ceramic matrix composites and its key constituents is presented along with the beneficial mechanical and thermal properties that these materials have to offer. Different mechanisms through which permanent strain in composite materials could occur have also been identified. Permanent strain in these materials is governed not only by the classic creep mechanisms like diffusion and dislocation creep, it is also a function of interfacial sliding and microstructural cracking within the material which would result in loss of stiffness giving rise to a higher strain at the same stress level.

Chapter 2 goes through the manufacturing procedure of the two material systems. It contains a detailed review on the Nextel 312 with SiCO matrix and BN interface and Nextel 720/Alumina Matrix, and the techniques used by researchers to study them. It summarises key studies carried out on these two materials. The literature covers certain strands mainly revolving around optimising processing parameters and mechanical testing. The key gaps identified in the literature were limited understanding of the failure mechanism, in-situ, at elevated temperatures. Limited work had been done on optimisation of material systems by either process parameter optimisation or by fabric layup techniques. Literature

on techniques that would be used extensively in this study have been looked at to understand the capabilities and limitations of each one.

Chapter 3 covers the parameters used to carry out each of the experiments, the results of which have been detailed in later chapters. It clearly specifies which experiment and data processing was carried out by the author and identifies the ones which were carried out by other individuals. Chapter 4 looks at optimising the processing parameters for manufacturing Nextel 312/SiCO CMCs for use in sealing applications at 900°C. Nextel312/SiOC offers a major cost advantage over other Ox-CMCs systems hence this system was fully optimised to see if it could perform at the operating temperatures of this study. It also carries out detailed testing to determine the mechanical and morphological properties of each of the four systems produced.

Chapter 5 looks at the deformation and fracture of a Nextel 720, Alumina/Mullite, fibre with alumina matrix CMC material using *in situ* synchrotron x-ray computed micro-tomography at ambient temperature and at 1100°C. It looks into how microstructural damage in the material system is different at RT in comparison to 1100°C.

Chapter 6 looks at understanding the effects of different combinations of weaves, layups and processing parameters on the mechanical properties of Nextel720/Alumina based composites, at 1100°C. Modulus and proportional limit stress (PLS) values for each sample were quantified at 1100°C, using a three-point bend test configuration. It studies the behaviour of different composite designs under constant stress at 1100°C. Beams of each layup type were loaded using a three-point bend configuration, at 1100°C, to quantify the creep rates. Using the modulus values calculated for the two shortlisted samples, piston rings, with a gauge diameter of 140 mm and 5x5 mm cross-section, were designed and tested at service conditions. The rings were put under constant displacement conditions, at 1100°C, in order to

compare their stress relaxation behaviour. *Ex situ* X-ray tomography was carried out on the beams and the sealing rings to analyse the damage development mechanisms in the sample microstructure after the creep tests and stress relaxation experiments.

Chapter 7 covers outlines the main conclusions of the study and talks about the future work that should be carried out beyond this thesis.

1.2 Aerospace seals

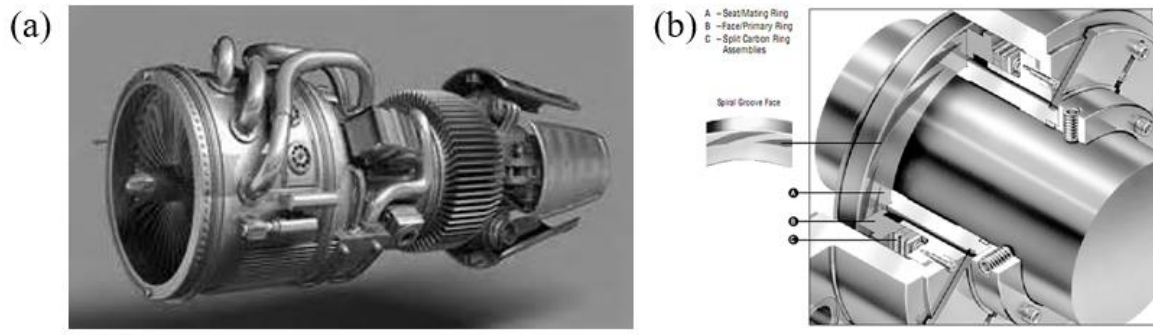

Figure 2: *(a) A gas turbine along with the (b) seals present on the rotating shaft* [29]

Gas turbines, **Figure 2**, are one of the most widely used power generating technologies in the world today [30]. This is due to their *high energy to weight ratio*, which makes them suitable for aero engine applications. Gas turbines are also used as land-based power-generating units due to their high efficiency, reaching up to 52% in combined cycle applications [30]. They can be switched on and off very quickly, and hence play a major role in balancing the intermittency, inherently present in the energy demand. Gas turbines, as the name suggest, are high-temperature high-pressure systems that function on the flow of air through the engine. Any leakage path present in a gas turbine would reduce the overall efficiency of the component [4]. Seals are critical components in turbomachinery due to their impact on the efficiency, especially on systems which function at high pressure and high velocity. Not only are

they an integral part of the rotor system, depending on their geometry and size they also affect the stiffness and engine damping. Due to the system being highly pressurised, approximately 20-30 times atmospheric pressure, even a small leakage could detrimentally affect the overall efficiency of the system [31]. There are two main types of seals used in engine applications; namely sealing rings and brush seals. An example of each is given in **Figure 3**[32].

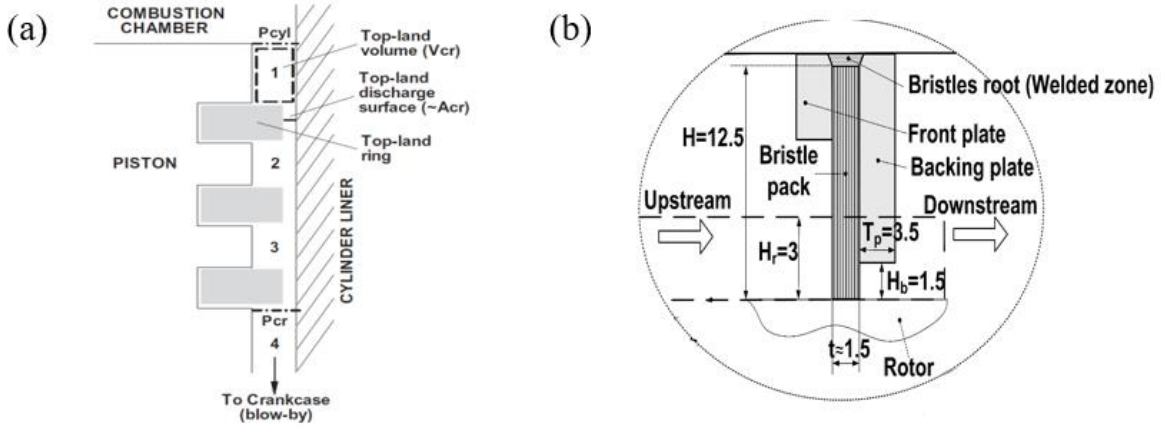

Figure 3: *The two different types of seals namely (a) piston rings and (b) brush seals* [33]

Sealing rings function like springs and are used to seal rotating shafts. The most well-known application of sealing ring is a piston ring [32]. For sealing rings to function, stress relaxation at elevated temperatures needs to be minimised. A brush seal consists of thousands of very fine bristles, with a diameter of 100 µm each, which is very effective in hindering oncoming flow [33]. These are only used for low-pressure applications, or where the difference between upstream and downstream pressure is lower than a factor of 2.

1.3 Oxide based Ceramic Matrix Composites

To cater to the challenges and demands currently being faced by the engineering world, there is a growing need to develop stronger and tougher structural materials that can maintain structural integrity

in high-temperature oxidising environments. Ox-CMCs offer excellent physical and mechanical properties at temperatures in access of a 1000°C, making them ideal candidates for such applications. These consist of three main components; the fibre, the matrix, and the interface (**Figure 4**). The fibres are embedded in the matrix with an interface between them to allow for crack deflection [34].

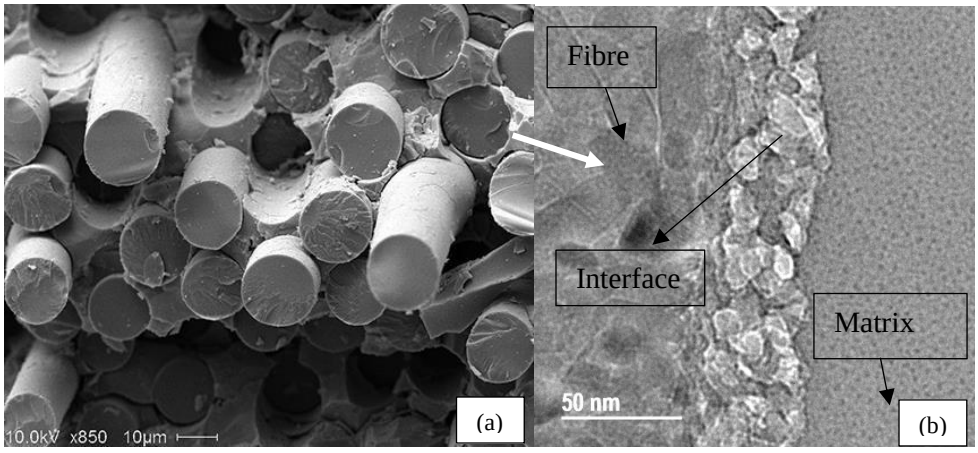

Figure 4: *(a) Cross section of an Ox-CMC, (b) the matrix fibre and interface have been labeled clearly [34].*

1.3.1 Fibre

The fibre provides excellent mechanical properties, due to its high strength and stiffness and acts as a strengthening agent in most Ox-CMC material systems. Fibres can be woven in different cloth configurations, such as 4 or 8 harness satin weave, with each fibre having a diameter of 10-20µm. The fibres are made of ceramic materials that need to be stable above the processing temperature. Depending on mechanical requirements of the application, these fibres can be optimised for strength or creep, by altering the microstructure [20].

1.3.2 Matrix

The matrix, on the other hand, consists of a mixture of different ceramic compounds, which usually are compositionally similar to the fibre. These compounds are chosen to ensure that the matrix and the

fibre have the same coefficient of thermal expansion to avoid cracking when exposed to heat. The matrix has some inherent porosity, which can be increased or decreased depending on the final application. This porosity can serve as a crack deflector and in turn, increase the fracture toughness of the material [8].

1.3.3 Interface

An interface is present in between the fibre and the matrix, which serves as a low strength boundary between the two. When the tip of a crack, which originated from the matrix, reaches the interface, de-bonding takes place, which deflects the crack around the fibre. This, in turn, increases the fracture toughness of the material. If the interfacial layer is strong, the crack would break through the fibre and cause sudden failure. The balance between the amount of porosity, the microstructure of the fibre and the matrix, and the interface oxidation properties determine the overall macro properties of the bulk CMC material [8].

1.4 Mechanical Properties of Oxide based CMCs

One of the main reasons for manufacturing Ox-CMCs is to achieve the desired mechanical properties, having a proportional stress limit of 25MPa or above. Although ceramics can provide excellent mechanical, thermal and oxidation properties, they do not provide the desired fracture toughness or ductility which is paramount for most industrial applications [35].

The bulk hardness of an Ox-CMC is a function of the fibre hardness and the matrix hardness. The fibre hardness is dependent on the microstructure of the fibre, and so can be controlled by the processing parameters during manufacture [36]. Depending on how the matrix was produced, the level of porosity and the crystallinity can have a major effect on the bulk hardness [37]. The hardness of the matrix is

directly proportional to the compressive strength of the material [38]. The higher the hardness of the ceramic the greater the wear on the contact surface. Hence to minimise the wear rate a tribological coating might be applied on the surface of the Ox-CMC fibre [39].

Fracture toughness is the ability of a material to absorb energy before fracture. It is mainly a function of the matrix porosity/additions and the interfacial debonding strength [40]. The de-bonding mechanism present between the fibre and the matrix would increase the fracture toughness of the material, as it would also deflect the crack [40]. CMC's fracture mechanisms help absorb some of the energy associated due to crack. Energy can be absorbed by plasticity around the crack tip. Crack branching which is mainly a function of subsequent microcracking or crack deflection would also absorb crack energy. Friction between interlocking sections of crack faces during fibre pullout along with elastic deformation stored in intact crack bridges would also absorb energy. Volume changes due to stress induced phase transformation could also dissipate some of the energy. All these mechanisms help improve the fracture toughness of the material system.

The strength of an Ox-CMC depends on the percentage volume fraction of the fibre and the matrix. In comparison to the matrix, the fibre usually has a higher tensile strength due to minimal defects and porosity. The matrix and the interface would play a role in defining the strength of the material. It should be kept in mind that the properties required for excellent fracture toughness are inversely proportional to the ones required for strength. Minimal porosity and no de-bonding would give higher load bearing capability but would adversely affect the fracture toughness of the material. Therefore a balance needs to be struck between the two to optimise the properties needed for a good seal [41].

1.5 Thermal Properties

One of the factors that play a major role in selecting an Ox-CMC component is its structural integrity at elevated temperature. The properties of a material change at elevated temperature, as different creep and oxidation mechanisms, come into play [42]. One of the limiting factor is the oxidation of the interfacial layer between the fibre and the matrix [43]. The oxidation of this interface results in fibre matrix bonding which in turn decreases the fracture toughness of the material [44]. The other mechanism that affects the structural integrity of the CMC is creep. The creep strength at elevated temperature changes and is a function of the fibre, interface and the matrix properties [45]. Grain boundary creep can be overcome by utilising an amorphous fibre [41] and matrix system, whereas nanoparticle additions can also improve the creep properties by instigating dislocation pinning. All these factors can be addressed during the manufacturing of the material.

1.6 Properties Required for Sealing

High-temperature mechanical stability

The materials should be mechanically stable at elevated temperature, 1000°C to 1300°C.

The coefficient of thermal expansion

The coefficient of thermal expansion of the seal should match that of the housing it sits in.

Fracture toughness

The seal should be able to absorb energy before fracture.

Tensile strength

The seal should have high enough tensile properties at room temperature and operating temperature, 1000°C to 1300°C, to overcome any fitting stresses and structural loads.

Tribological Properties

The seal should have the right tribological properties to ensure that the wear of the housing can be minimised.

Stress relaxation

The seal should have enough creep resistance at temperatures between 1000°C to 1300°C for it to not lose its shape and stay rigid during service.

Corrosion/Oxidation Resistant

The seal should have enough oxidation resistance to perform adequately at temperatures between 1000°C to 1300°C

Table 1 gives a comparative analysis between Oxide based CMCs and traditional superalloys currently being used in aerospace applications.

Comparison		
Properties	Aerospace Super Alloys (Nickel/Cobalt based)	Ox-CMCs
Density	High	Low density, around 1/3 of aerospace alloys
High-temperature mechanical stability	Stable up to 1000°C	Can survive temperatures of upto 1500°C.
The coefficient of thermal expansion	Have a higher expansion rate (~13 10^{-6} $m.m^{-1}$ K^{-1})	Low, needs to match the housing expansion coefficient (~3 10^{-6} $m.m^{-1}$ K^{-1})
Fracture Toughness	Adequate fracture toughness (~50 $MPa.m^{1/2}$)	Low fracture toughness but can be improved (~10 $MPa.m^{1/2}$)
Tensile Strength	Very high (~1000MPa)	Low (<400MPa)
Tribological properties	Good if an oxide is present on the surface	Inherently poor but can be improved
Stress relaxation	Poor creep resistance above 900°C	High creep resistance at temperatures above 1000°C
Corrosion/Oxidation Resistance	Low corrosion resistance above 1000°C	Very high corrosion resistance up to 1500°C

Table 1: *Difference between aerospace alloys and ceramic matrix composites*

1.7 Creep behaviour in Ceramics

To design a component for long-term operation under high stress and temperature the following parameters need to be taken into consideration

- Permanent strain should not cause excessive distortion over the planned service life.
- Creep failure should not occur within the required operating life

Creep is defined as the time dependent increase in permanent (in-elastic) strain at a constant stress condition. Creep is plastic deformation in a material system which occurs at elevated temperature at stresses lower than the material's yield strength. With time damage starts to develop in the material system which increases the rate of deformation. When the damage reaches a critical value failure occurs due to creep [46]. For ceramics, creep plays a role above $0.66T_{melt}$ temperature. Stress rupture tests give the values for time to failure, $t_{f,}$ and steady strain rate, $\acute{\varepsilon}$, associated with the steady state creep region labelled as secondary creep in **Figure 5**, at a fixed stress and temperature. **Figure 5** below shows the three stages of Creep as a function of time [46].

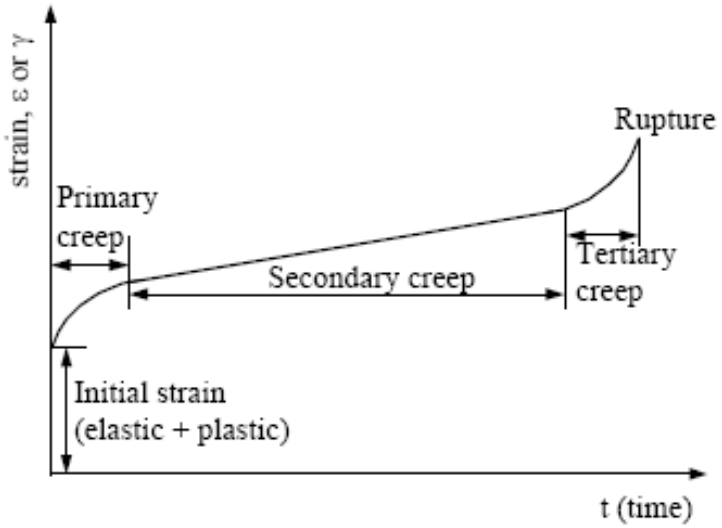

Figure 5: *The three stages of creep namely primary, secondary and tertiary as a function of time* [46].

The initial strain is a virtually instantaneous increase in length due to *elastic-plastic deformation.* After initial loading the creep rate decays with time during the *primary stage,* it then maintains a constant creep rate during the *secondary stage,* after which it increases again in the *tertiary stage,* which leads to failure. The most significant parameter is the steady-state creep, which takes place in the *second stage*. Steady-state creep rate is only dependent on stress and temperature and not time [8]. The equation that governs the steady state strain rate, $\acute{\varepsilon}_{ss}$, has been given below.

$$\acute{\varepsilon}_{ss} = B\sigma^{n} \qquad 1$$

Where B is a constant, σ is the applied stress, n is the stress exponent, Q is activation energy, and R & T are the gas constant and temperature.

1.7.1 Permanent strain in Ceramic Matrix Composites

There are two main ways that could result in permanent strain taking place in ceramic matrix composites. Also known as the classic creep mechanism, the first is due to the presence of microstructural dislocations or vacancies in the fibre or the matrix. The second, and the main cause of

permanent strain in CMCs, is due to the cracks developing and opening permanently in the matrix or via interfacial sliding. At temperature cracks could result in generating extra strain due to elastic unloading which is a function of loss of stifness due to matrix cracking, fibre failure or fibre debonding. If the stiffness of the sample decreases for the same amount of stress there would be extra strain generated within the sample. Interfacial sliding between the different fibre bundles could also result in generating permanent strain within the material system [47].

1.7.1.1 Classic Creep mechanisms in CMCs

There are two types of atomic level mechanisms by which creep deformation is observed at macroscopic level in ceramics. It could either occur due to dislocation motion or through diffusion either through the bulk or at the grain boundaries.

1.7.1.1.1 Dislocation Creep (Power Law Creep)

Creep could occur due to the motion of dislocations. Dislocations can move within a material due to glide of dislocations along slip planes, at an applied shear stress [48]. At high stress and low temperature conditions, plastic deformation occurs by glide of dislocations along the slip planes. At high temperatures the dislocations could climb out of a slip plane as a function of diffusion transport of atoms between dislocations, hence any deformation is a function of both glide and climb [49]. The strain rate determined due to power law creep is determined by the following equation

$$\acute{\varepsilon}_{PLC} = A\frac{\sigma^n}{RT}D_o e^{\left(-\frac{Q_V+Q_{ex}}{RT}\right)} \quad 2$$

Where A is power law constant, D_o is the diffusion constant, Q_v is activation energy associated with vacancy formation, Q_{ex} is activation energy associated with vacancy migration.

1.7.1.1.2 Diffusion Creep (Nabarro-Herring or bulk)

Diffusion creep occurs mainly at high temperatures and low stress conditions. It's mainly a function of vacancy diffusion which gives rise to plastic deformation [48]. Under a known applied stress grain boundaries which are loaded in tension would become sources of vacancies, whereas the grain boundaries that are loaded in compression absorb vacancies. The vacancy flux flows through the grain from the grain boundary in tension to grain boundary in compression. The equation governing steady strain rate due to Nabarro-Herring creep is

$$\dot{\varepsilon}_{NH} = A_{NH} \frac{\sigma \Omega}{RT} \frac{D_v}{d^2} \quad 3$$

A_{NH} is the Naboarro Herring constant, stress exponent in this case is 1, Ω is the atomic volume, D_v is the volume diffusivity which is diffusion through the bulk of the grain, and d is the grain size.

1.7.1.1.3 Diffusion creep (Coble Creep)

Instead of the vacancy flux flowing through the grain, it can also move along the grain boundaries from the grain boundary in tension to grain boundary in compression [48]. The equation governing steady strain rate due to Coble creep is

$$\dot{\varepsilon}_C = A_C \frac{\sigma \Omega}{RT} \frac{\delta D_{GB}}{d^3} \quad 4$$

Where A_C is the Coble constant, stress exponent in this case is 1, Ω is the atomic volume, D_{GB} is the grain boundary diffusivity, δ grain boundary thickness, and d is the grain size. Coble Creep can occur at lower temperature because there is an easier path for atoms and vacancies to move, as the diffusivity of the grain boundary is higher than through the bulk [48]. Dislocation mechanism maps can be used to

identfy the dominant deformation mechanisms in a material under different stress and temperature conditions.

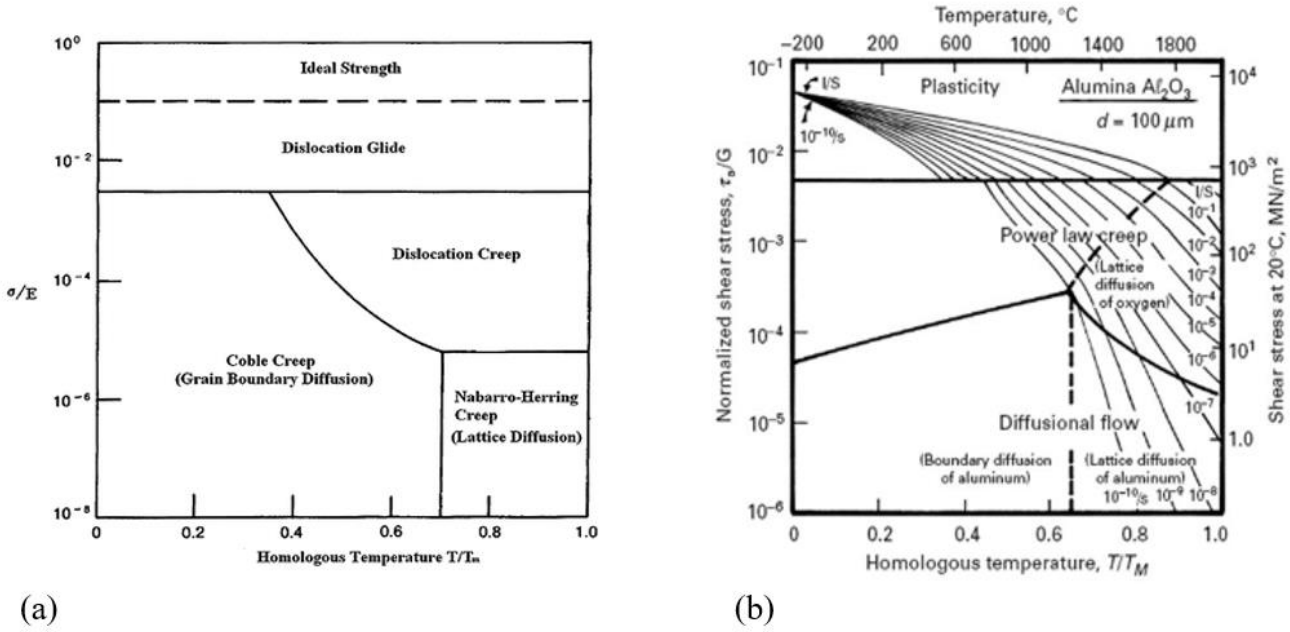

***Figure 6**: Deformation mechanism map of (a) any material (b) of Al_2O_3* with an average grain size of 100 μm [50]

Figure 6 shows a deformation mechanism map for pure alumina with grain size of 100 µm. The map represents the dominant deformation mechanism at different temperatures and loads. Dislocation and vacancy generated permanent strain plays a role in the overall permanent strain within a CMC. CMCs with alumina matrix, could undergo creep deformation at 1100°C due to diffusional creep. In reality alumina based ox-CMC have much finer grain sizes that 100µm, in the range of < 1µm which means that both diffusion creep mechanisms would result in the high magnitude of creep strains at lower stresses than the one predicted in the deformation map.

1.7.1.2 Permanent strain due to damage and interfacial sliding

Permanent time dependant strain could also develop in a CMC as a result of existing damage. Different types of microcracks were identified in a C_f/SiC CMC, and their impact on permanent strain was

investigated by Boitier et al. [47]. Different types of microcracks were present in the system including transverse microcracks (1) transverse bundles (2), longitudinal microcracks in the longitudinal bundles (3) in the transverse bundles (4) and interply microcracks (5) as seen in **Figure 7**.

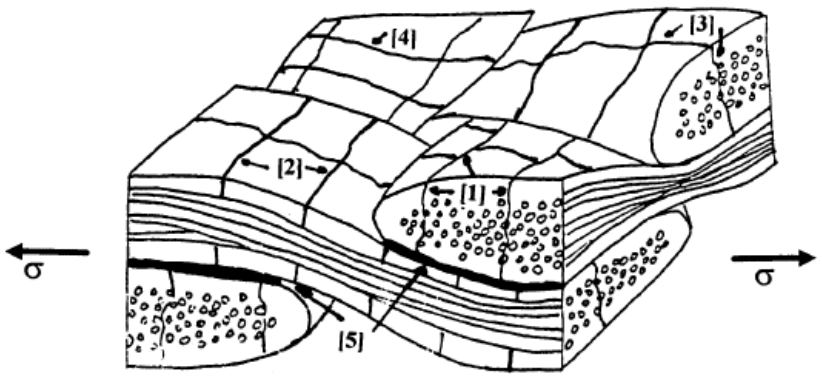

Figure 7*: Schematic illustration of the damage modes encountered in 2.5D C_f-SiC composite* [47]*, including transverse microcracks (1) transverse bundles (2), longitudinal microcracks in the longitudinal bundles (3) in the transverse bundles (4) and interply microcracks (5)*

Under temperature and stress conditions transverse microcracks (1) and (2) were observed with a wider opening than after step loading at the same temperature. As the temperature is increased both types of transverse microcracks 1 and 2 are observed with a wider opening. When the stress is increased the cracks not only initiate at macropores, they also develop at the transverse cracks in the transverse bundles as seen in **Figure 8**.

The damage accumulation via matrix microcracking coupled with interfacial sliding can be assimilated to slow crack growth. The interfacial sliding mechanism, at the microscopic scale, may be due to two types of time-dependent mechanisms at the nanometric scale, dry friction and viscous friction. Microscopic deformation is a result of five modes of matrix microcracking and two modes of interfacial cracking and would result in a change in elastic modulus. All these mechanisms were found to be time and stress dependent.

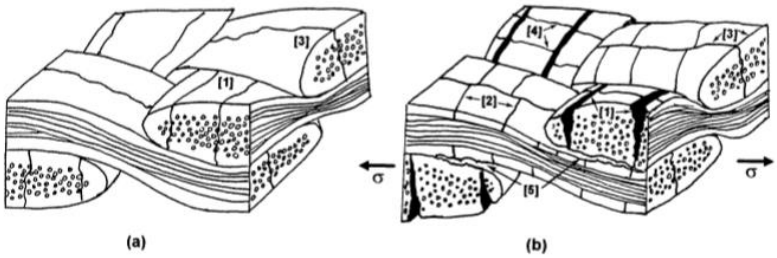

Figure 8: *Five modes of matrix micro-cracking developed in a 2.5D C_f-SiC composite: (a) as-received material; (b) creep tested material* [47]*. Each number depects a type of cracking mode which has been defined in the previous figure*

1.7.2 Modelling creep in CMCs using Andrade's law

Andrade's law [51] can be used to model the primary and secondary creep of a wide range of material systems. It is a completely empirical technique and is extensively used to model creep in ceramics. It states that creep exhibits a transient state in which strain is proportional to the cube root of time, followed by a steady state regime in which strain is proportional to time. A lot of work has been carried out to theoretically explain why the cube root over time is suitable to map the transient creep [52] but no general agreement has been reached so far as to why this is the case [53]. **Figure 9** shows the primary and secondary creep rates with ε_t being the transition point [54]. The equation below shows how creep rates can be quantified.

$$\varepsilon = \varepsilon_{primary} + \varepsilon_{secondary} \quad (5)$$

$$\varepsilon = \beta t^{\frac{1}{3}} + \alpha t \quad (6)$$

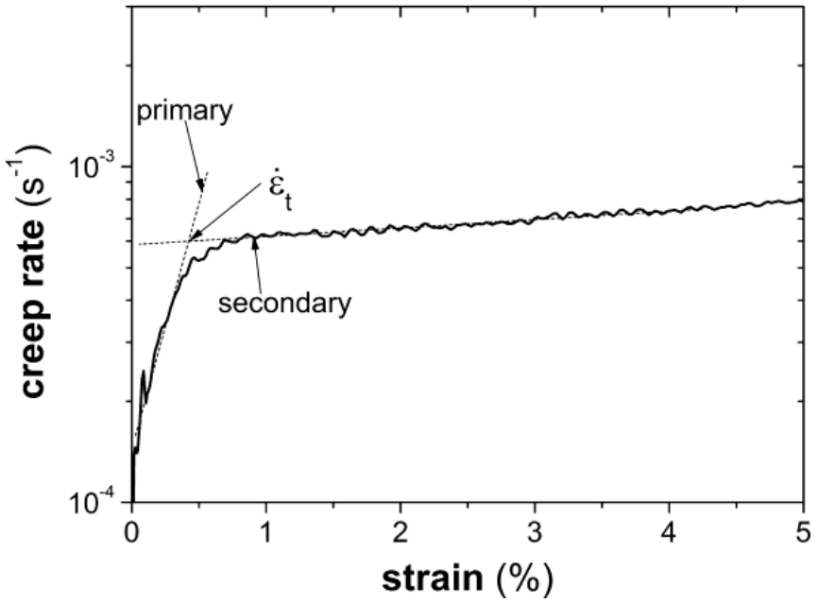

Figure 9: *The two creep rates determined by finding out the gradient of the best fit line with ε_t being the transition point* [54].

Andrade's law offers a good model to compare the primary and secondary creep rates in ceramic matrix composite beams, manufactured under different processing conditions with varied microstructure.

1.8 Summary

This chapter covers how the gradual rise in engine operating temperatures presents a need for seals that function at increasingly high temperatures. Oxide based ceramic matrix composites were looked at in order to understand their key constituents and their mechanical properties. Two different material systems were selected which according to literature offered promising properties for their use in gas turbine sealing applications. Thermal properties, along with failure mechanisms, were also studied for these materials. Time dependant permanent strain mechanisms were studied in detail to understand how they occurred at elevated temperature in Ox-CMCs. It was concluded that permanent strain formation in oxide ceramic matrix composites was both a function of classic creep mechanisms, like dislocation and diffusion, and a function of in-elastic strain due to cracking and interfacial sliding. Creep models,

such as Andrade's law, have been looked at which could be used to quantify the performance of different CMC systems.

CHAPTER 2. Review of the Composite Systems under Investigation along with the main characterisation techniques

2.1 Introduction

Oxide-oxide ceramic matrix composites are CMCs which have an oxide-based fibre and matrix. A family of oxide-based fibres known as Nextel is used in this study. There are six different types of Nextel fibres currently available, two of which have been studied in this work [55]. **Table 2** details the chemical composition, thermal properties, mechanical and morphological properties along with the cost for the four most widely used Nextel fibres [55].

Property	Units	Nextel 312	Nextel 440	Nextel 610	Nextel 720
Chemical composition	wt%	62.5 Al_2O_3 24.5 SiO_2 13 B_2O_3	70 Al_2O_3 28 SiO_2 2 B_2O_3	>99 Al_2O_3	85 Al_2O_3 15 SiO_2
Melting Point	°C	1800	1800	2000	1800
Fibre Diameter	µm	8-12	10-12	11-13	12-14
Crystal size	nm	<500	<500	<100	300-500
Thermal expansion (100-1100C)	ppm/°C	3.0 (25-500°C)	5.3	8	6
Filament Tensile Strength	MPa	1630	1840	2800	1940
Filament Tensile Modulus	GPa	150	190	370	250
Costs per (lbs)	£	137	324	448	448

Table 2: *Composition and properties of Nextel fibres.* [55].

Nextel 312 and 440 contain B_2O_3, which is used to form an interfacial layer between the fibre and the matrix. Nextel 610 is pure alumina, which provides excellent mechanical

properties, whereas Nextel 720 contains 15% SiO_2 which results in bigger grains which in-turn provide better creep resistance at 1100°C, whilst compromising on the tensile strength by 900MPa in comparison to N610. **Figure 10** shows the strength retention of each type of Nextel fibre at temperatures ranging from 600-1400°C [56]. The two fibres selected for this study were Nextel 312 due to its capability up to a range of 900°C and is one third the cost of other fibres and Nextel 720 with the highest temperature capability of around 1400°C.

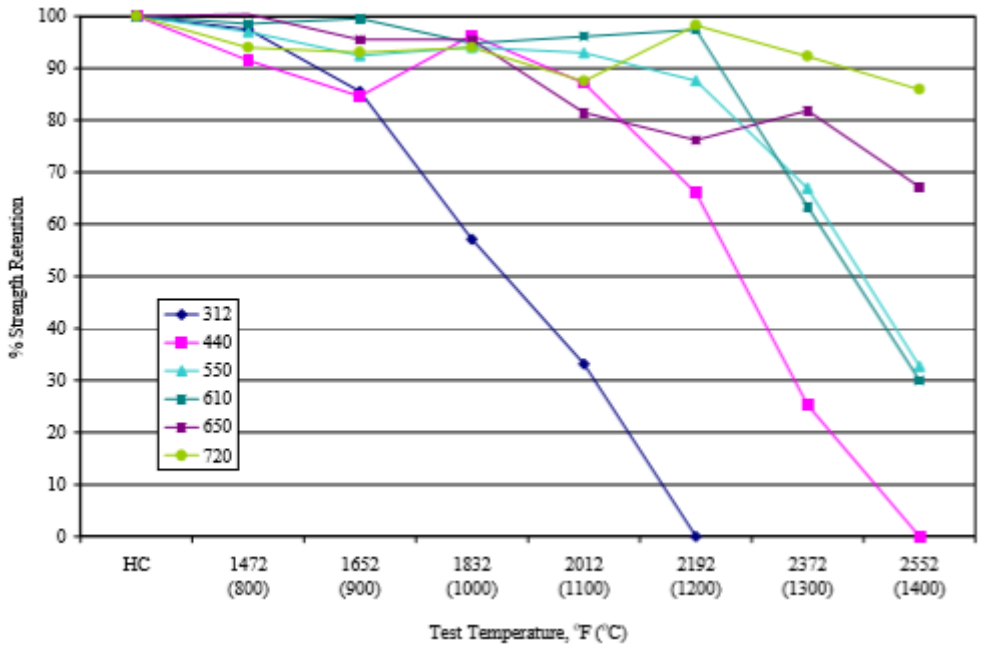

Figure 10: *Strength retention of the 6 different oxide fibres produced by Nextel* [55].

There are two types of material systems under investigation in this study:

- Nextel 312 fibre-based system with SiCO matrix and boron nitride as the interface coating.
- Nextel 720 fibre-based system with porous alumina matrix with no interface coating.

2.2 Nextel 312/SiOC (Lancer Systems)

Manufactured by Lancer systems, the first material system was formulated from SiCO with highly doped silicon carbide nano-particulates as filler material. It was reinforced by Nextel 312 fibre with 5 harness satin weave structure. An interfacial coating of BN was applied between the matrix and the fibre [57]. The Nextel 312, fabric reinforcement used in this CMC, is a commercially available polycrystalline metal oxide ceramic fibre. The reinforcement is made from alumina–silica–boria fibre, and has a composition of 62% $A1_2O_3$, 24% SiO_2, and 14% B_2O_3 (percentage by weight) [58]. Nextel 312 has a fibre diameter of approximately 10 μm, density of 2.8 g/cc, a coefficient of thermal expansion of approximately 3 ppm/°C [58], and retains its strength at 900°C for extended periods [20]. It offers a major cost advantage over other Nextel fibres. The SiCO matrix, known as 'Blackglas', has a chemical composition of 42 wt. % Si, 20 wt. % C, and 38 wt. % O_2. The matrix precursor is a mixture containing polysiloxane monomers, which when heated in the presence of a hydrosilylation catalyst, produce a rigid transparent cross-linked thermoset polymer. When the polymer is exposed to high-temperature pyrolysis, decomposition and redistribution of various elements occur, and the matrix is transformed into SiCO. The coefficient of thermal expansion matches very closely with that of the fibre and can be controlled by varying the carbon content, cure time and avoiding the evolution of reaction gases during the curing process.

2.2.1 Manufacturing Process

The BN interfacial layer is produced by diffusing boria (B_2O_3), inherently present in the Nextel 312 fibre, to the surface [57]. This is done by exposing the fibre to 1300ºC in an ammonia atmosphere, which results in the production of BN on the surface of the fibre. This *in situ* BN coating process results

in the formation of a uniform coat on every fibre, something which cannot be achieved by other methods [59]. To produce the material a pre-ceramic slurry is impregnated into a chosen fabric, thus creating a "prepreg fabric". The prepreg fabric is then laid out into 0-90° composite stack of plys, followed by cure in an autoclave (pressure and heat). The autoclave cure is carried out at 207KPa which results in limited fibre breakage. The curing was carried out for 60 minutes at a temperature of 150ºC and a pressure of 207KPa in full vacuum [60].

2.2.1.1 Initial pyrolysis

Pyrolysis was performed to convert the green state polymer into the initial porous ceramic composite. The Polycarbosiloxane is thermally transitioned into a silicon oxy-carbide matrix, under the protection of an inert-gas atmosphere. Two different gases, ammonia or argon, can be used to carry out pyrolysis at temperatures between 850ºC and 1200ºC. Depending on the required properties of the end product the optimum conditions for pyrolysis are selected [60]. In the sample pyrolysed in ammonia, carbon is displaced in the chemical structure by nitrogen resulting in a lower dielectric constant and possibly a more thermo-oxidatively stable oxy-nitride matrix at higher temperatures than an oxy-carbide one [60].

2.2.1.2 Reimpregnation and cure

The densification and cure cycle is significantly different from the prepreg resin cure cycle. This process is carried out at a higher pressure of 507KPa at 150ºC in vacuum [58]. This step removes any liquid media present in the polymer mixture. In order to develop the thermomechanical properties fully, the panels were subjected to four additional infiltration-densification and five pyrolyses as described above.

2.2.2 Previous studies on high temperature testing and optimisation of Nextel 312/SiOC

Previous work on glass-ceramic with Nextel 312 fibre indicated that [61] the glass-based ceramics could be fabricated into a net-shape with the matrix in a glassy state. Results indicated that interfacial strength should be in the region 1-10MPa for adequate crack deflection. It was found that in comparison to polycrystalline matrices, glassy (amorphous) matrices can help in fabrication, produce near net shape and achieve high matrix densities. To increase the temperature capability, the composite is subsequently heat-treated to convert the matrix into a fine polycrystalline material. This brings the operational capabilities to 1000ºC.

Pyrolysis of SiCO at 1100°C results in a pyrolyzate that is more oxidatively stable than that pyrolysed at 900°C [62]. When this cured polymer is exposed to high-temperature pyrolysis, decomposition and redistribution of the various elements occur, and the polymer is transformed into a black ceramic material product; hence the name Blackglas. The coefficient of thermal expansion (CTE), 3.4ppm/°C, of Blackglas is very close to that of the Nextel 312 fibre 3ppm/°C. Previous experiments conducted using a BN coating have shown that after 100 hrs of exposure at 600ºC the strength and strain bearing capabilities are reduced due to fibre interface oxidation [63].

X-ray diffraction studies [64], summarised in **Figure 11**, indicate that Si-C matrices derived from polycarbosilicane begin to crystallise at 1100-1200ºC, whereas the Si-C-O systems appear to remain amorphous and refractory at 1300-1400ºC. The benefit of using Polysiloxane resins (Blackglas) to produce glassy Si-C-O ceramics is the achievement of high ceramic yields of up to 85% with only 1-2% free carbon.

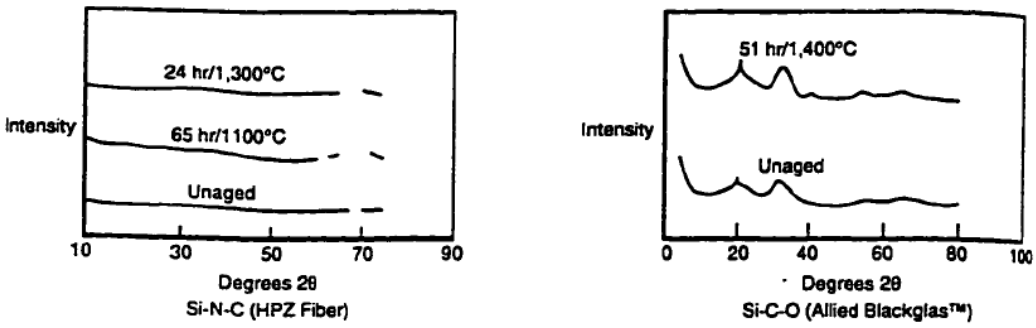

Figure 11: *XRD spectra for Si-N-C and Si-C-O matrices*[64].

Thermogravimetric Analysis (TGA) was conducted for four different Nextel 312(BN)/Blackglas CMCs samples, pyrolysed at different temperatures with exposure to air for 25 hrs at 700ºC and 1000ºC [58]. Pyrolysis was conducted in two different atmospheres, namely Ammonia and Argon, the results of which have been presented in **Table 3**.

Pyrolysis Temperature and Atmosphere	Weight Loss After 25 Hours at 700°C (%)	Weight Loss After 25 Hours at 1000°C (%)
872°C Argon	0.4	0.5
982°C Argon	0.2	0.7
872°C Ammonia	1.9	1.5
982°C Ammonia	0.4	1.1
Nextel 312(BN)	1.0	1.1

Table 3: *Thermogravimetric data, at 700°C and 1000°C, for samples produced at different temperature and atmospheric conditions* [58].

Oxidation behaviour of the composites at 1000 ±ºC indicates that the argon pyrolysed CMCs lose more weight due to decomposition of the pyrolytic carbon, whereas, NH_3 pyrolysed CMCs are stable as both the N and C are bonded to Si in the matrix.

Pyrolysis temperature and atmosphere also had a major effect on the porosity of the CMC produced. **Table 4** shows the measured porosity for each condition. The table shows that samples pyrolysed in ammonia contained higher porosity at the fully densified ceramic state than the argon pyrolysed panels. Chemical analysis revealed that Blackglass ceramic pyrolysed in argon contains approximately 25% carbon, and the amount increases with an increase in pyrolysis temperature. On the other hand, the material pyrolysed in ammonia contained about 13-20% nitrogen and 3-6% carbon [58].

Pyrolysis Temperature and Atmosphere	Apparent Porosity (%)
872°C Argon	4.99
982°C Argon	4.05
872°C Ammonia	8.27
982°C Ammonia	7.88

Table 4: *Approximate porosity of the sample produced using different pyrolysis temperature and atmosphere* [58].

Oxidation analysis was conducted at 700ºC and 1000ºC for 500 hrs duration. The 500 hrs duration was selected to provide a long-term material durability data point [61]. The weight loss percentage as a function of exposure time at 700°C indicated that for argon pyrolysed composites, the ceramic pyrolysed at 872ºC had the greatest weight loss after 500 hrs. The visual appearance of the samples indicated a successive increase in matrix oxidation with time. The weight loss flattened out completely after the first 24 hrs of exposure. The fractographic analysis indicated that the ammonia pyrolysed Blackglas ceramic did not produce as much oxidation in comparison to the argon pyrolysed material. Samples were also exposed to a temperature of 1000ºC for 500 hrs. The same trend of major weight loss in the first 24 hrs was observed, as redrawn in **Figure 12** [61]. It can be concluded that [61] the

composite pyrolysed in ammonia gave the lowest weight loss after 21 days of oxidation. Weight loss of the four materials can be described as follows:

$$872°C\ Ar > 982°C\ Ar > 872°C\ NH_3 > 982°C\ NH_3$$

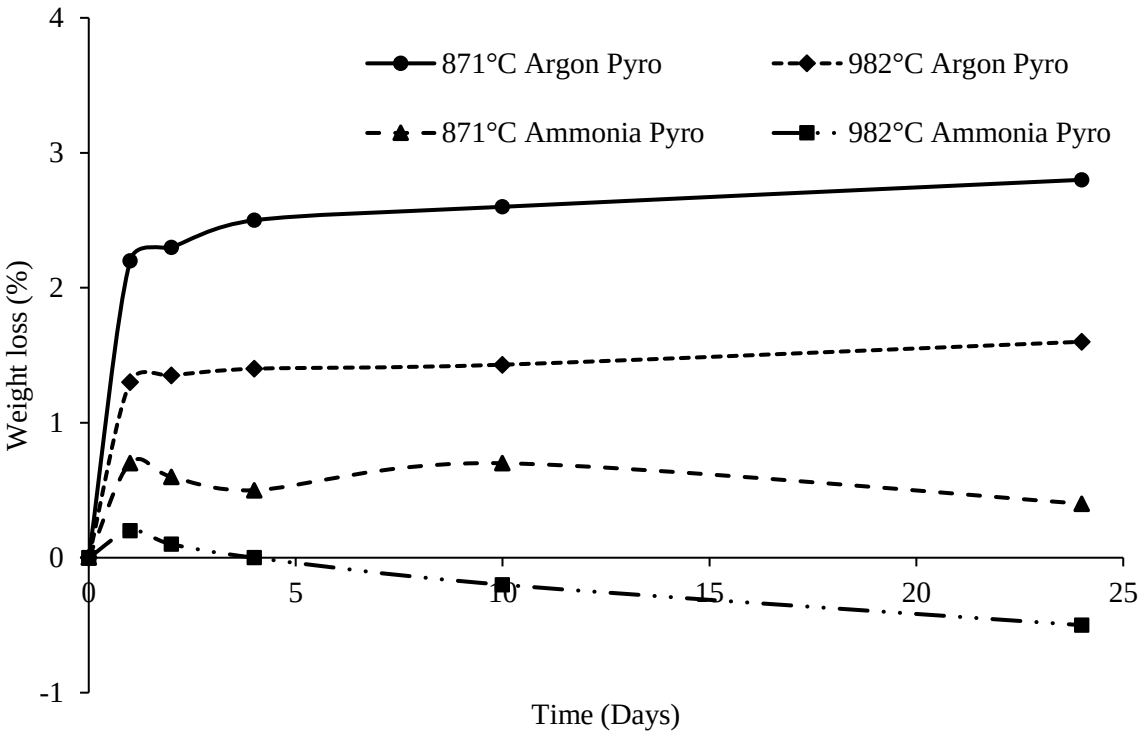

Figure 12: *Is a redrawn figure of change in weight at 1000°C plotted against the exposure time for 4 different samples (from the following paper*[61]*).*

Mechanical properties of Nextel 312(BN)/Blackglas were determined by Rangarajan [61]. **Table 5** indicates the flexural properties of the material when exposed to different temperatures. The highest flexural strength at RT was offered by the sample processed in Argon at 872°C. The flexural strength decreased as the pyrolysis temperature was increased. As the samples were exposed to temperature and tested subsequently, samples processed in ammonia atmosphere lost around 40% of its strength whereas samples processed in argon lost around 70% after 500 hours of exposure.

Processing Condition	Exposure Temperature (°C)	Flexural Strength (Mpa)/Strain (%) As a Function of Exposure Time			
		0 hrs*	25 hrs	100 hrs	500 hrs
872-Argon	700	179.9 ± 12/0.34	137.8 ± 3/0.45	112.0 ± 2/0.49	57.6 ± 6/0.32
	1000		39.9 ± 1/0.06	4.28 ± 5/0.07	NP**
872-NH_3	700	152.6 ± 8/0.46	118.0 ± 2.3/0.25	118.8 ± 3/0.32	96.3 ± 3/0.25
	1000		41.7 ± 3/0.11	45.4 ± 2/0.7	NP
982-Argon	700	117.4 ± 8/0.18	146.9 ± 12/0.27	117.2 ± 9/0.21	51.5 ± 3/0.12
	1000		48.1 ± 1/0.09	39.0 ± 4/0.07	NP
982-NH_3	700	133.5 ± 2/0.27	NP	NP	71.7 ± 4/0.16
	1000		NP	NP	NP

Table 5: *Flexural strength of the Nextel 312/SiOC samples produced under four different processing conditions, as different temperatures and exposure times* [61].

2.2.3 Summary and discussion

To satisfy seal design requirements at high temperature, an oxide based ceramic matrix composite has been selected that is composed of Nextel 312 fibre with a SiCO matrix. One of the main reason for selecting this system is the cost advantage over other ox.ox cmc systems. Previous work on optimising the manufacturing parameters to produce a Nextel 312/SiCO composite for high temperature applications [65,66] showed it could be net-shape fabricated with the matrix in a glassy state. Both pyrolysis temperature and atmosphere are important factors in processing. Pyrolysis at 1100°C has been shown to produce a more oxidatively stable sample in comparison to pyrolysis at 900°C [67,68].

In a study of the oxidation behaviour at 1000°C of Nextel 312/SiCO samples, pyrolyzed at different temperatures and in different atmospheres (ammonia and argon) [60], it was demonstrated that the argon pyrolyzed composite lost more weight due to decomposition of the pyrolytic carbon, whereas the ammonia pyrolyzed composites were stable as both the N and C were bonded to Si in the matrix.

Samples pyrolyzed in ammonia also contained higher porosity than those pyrolyzed in argon. Oxidation analysis conducted at 700ºC and 1000ºC for 500hrs duration [61] indicated that beyond the initial loss in mass, which happened in the first 24 hours, the material system was gravimetrically stable. The highest flexural strength at RT was offered by the sample processed in Argon [61]. The flexural strength decreased as the pyrolysis temperature was increased. As the samples were exposed to temperature and tested subsequently, samples processed in ammonia atmosphere lost around 40% of its strength whereas samples processed in argon lost around 70%.

Tensile tests of Nextel 312/SiCO composites [57] at room temperature and 760°C found no significant change in failure strength over this range. The average failure strains on the other hand was twice as much for high temperature than the room temperature sample. This increase was attributed to relaxation of residual stresses at temperature in the composite that develop after processing during the cooling down phase. As the elevated test temperature of 760°C was close to the PIP temperature, the composite was mostly stress free. Post-mortem analysis suggested that the damage initiated from macro-pores present in the warp and weft yarn. This was followed by matrix cracking, interfacial debonding and fibre cracking.

The BN coating of the fibre can be affected by the operating environment. After 100 hrs of exposure at 600°C, the strength and strain bearing capabilities of a Nextel 312/SiCO were reduced due to fibre interface oxidation [60,69]. In a comparative study [70], composites with either Nicalon or Nextel 312 fibre in a SiCO matrix were manufactured using vacuum assisted resin transfer moulding. The SiC-based Nicalon fibre had a carbon coating, whereas the Nextel 312 fibre were BN coated. After high temperature exposure at 800°C in air, the Nicalon composite had lower strength and displacement

to failure in comparison to the Nextel 312 composite, due to the presence of BN coating on Nextel 312 fibre.

This review suggests that a change in pyrolysis temperature could be used to optimise the high temperature capabilities of Nextel 312 with SiOC matrix. The processing temperature and atmosphere should be taken into consideration when designing composite systems for high temperature application as they have a major impact on the mechanical and thermal stability of the system. Literature suggests that the higher the PIPs temperature the more thermally stable the system would be. In comparison to argon, samples processed in ammonia provided a greater oxidative stability due to the amount of free carbon present in the argon samples. The samples pyrolyzed in ammonia had a higher porosity in comparison to the ones pyrolyzed in argon. The highest flexural strength was achieved by the sample pyrolysed in ammonia at 872°C. All this information will be used to design a material system using Nextel 312, which offers a major cost advantage, which could provide the highest thermal stability and the optimum flexural strength needed for sealing applications.

2.3 Nextel 720/Alumina (Composite Horizons)

The second material system under investigation was manufactured by Composite Horizons Ltd, with Nextel 720 fibre (Al_2O_3 with 15% SiO_2 addition) and Alumina (Al_2O_3) matrix. The fibre had a diameter of 10-12 µm with no interfacial layer between the fibre and the matrix. This was balanced by the high level of porosity in the sample which assisted crack deflection [50].

2.3.1 Manufacturing Process

The material was manufactured by slurry infiltration [71]. Two different weave patterns, namely EF 19 and EF 20 are available. EF 19 has a weave architecture with 50% fibres in the warp and 50% fibre in the weft direction can be used to manufacture Nextel 720/Alumina CMCs [72]. It uses a 3000 denier fibre tow which is woven into 8 harness satin weave pattern as seen in **Figure 13 (a)**. EF 19 has 9 threads per cm in both directions.

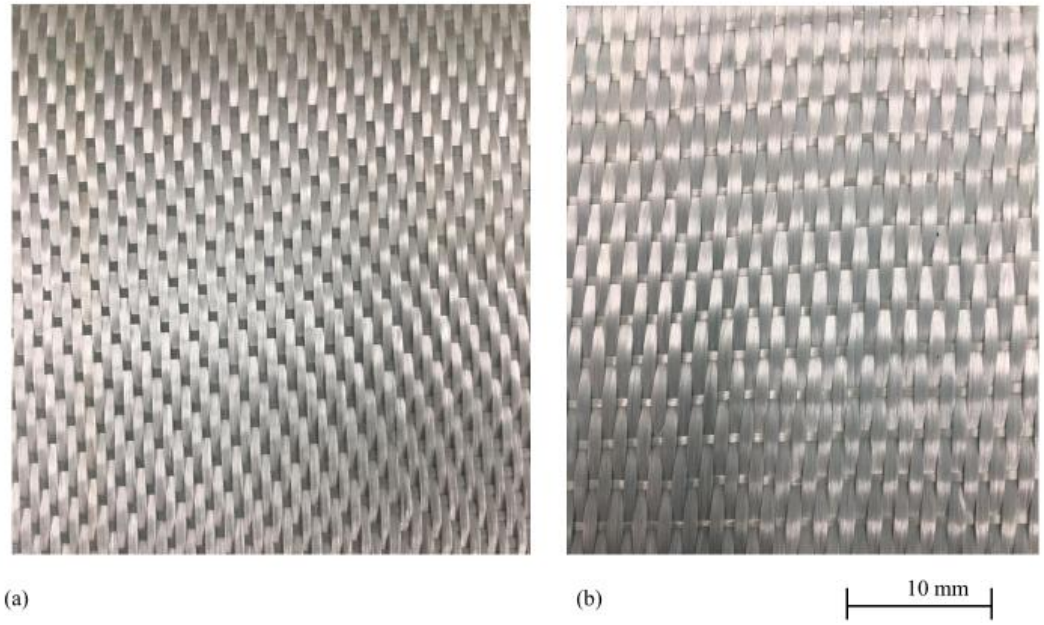

Figure 13: *The weave pattern of (a) EF 19 and (b) EF 20.*

EF 20 is a semi-unidirectional weave that uses two distinct deniers(d) for weaving [72]. 10,000 d is used in the warp direction whilst 1500 d is used in the weft direction, with 6 threads per cm in warp and 4 threads per cm in weft, as seen in **Figure 13 (b).** This equates to around 80% fibre in the warp and 20% fibre in the weft.

The amount of matrix pickup by the fabric, is a function of the speed and toughness of the rollers as shown in **Figure 14** [34]. These prepregs are stacked onto tooling or within a mould and consolidated using vacuum bagging at warm (~150°C) temperatures. The warm temperature is used to drive off water

and remaining solvents. This pregging process has the ability to form near-net shape, complex parts with relatively inexpensive tooling. The material, now in the green state, is pressureless sintered at high temperatures (~1300°C) for the Al_2O_3 matrix particles to fuse together. No interfacial coating was applied during the process.

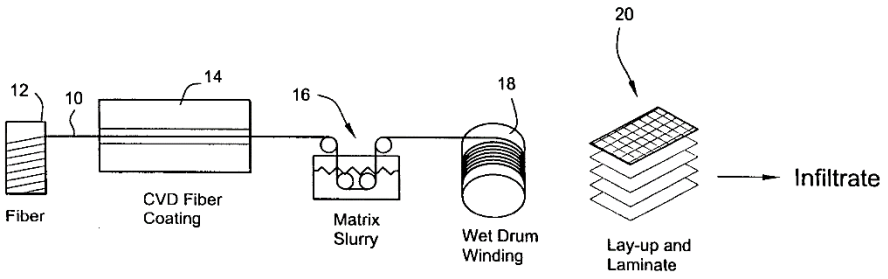

Figure 14: *Schematic for an Ox-CMC pre-pregging line*[34].

2.3.2 Previous comparative studies on testing and optimisation of Nextel 720/Alumina with other oxide CMC systems

2.3.2.1 Mechanical properties

Nextel 720 with mullite matrix CMCs were fabricated by infiltrating filaments with a precursor slurry followed by 1D and 2D winding up the fibre bundles on mandrels. The CMCs in their green state were then sintered in air at 1300°C [19]. **Figure 15** shows the schematic of the fabrication route used to produce these CMC systems.

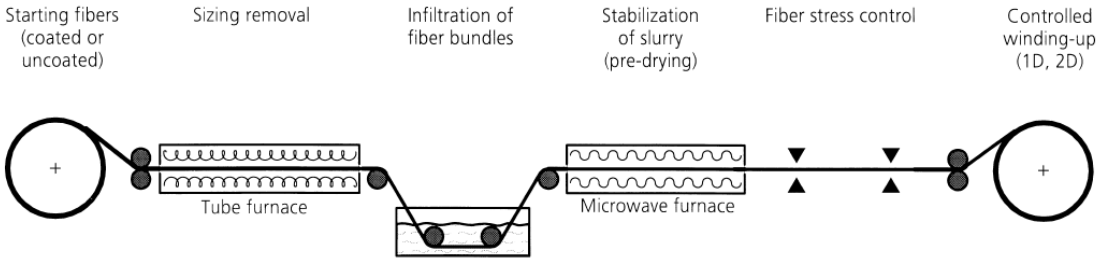

Figure 15: *Schematic view of the fabrication route of the aluminosilicate fibre/mullite matrix composite* [19].

The stress-deflection curves of the material system were obtained for room temperature and at 1200°C using three-point bend test regime as seen in **Figure 16**. Both room temperature and 1200°C showed a very similar failure pattern with a flexural strength of around 160MPa. Long term exposure of the samples at 1250°C for 400hrs and 1500°C for 3 hrs, (see **Figure 17**) resulted in a minor drop in the flexural strength.

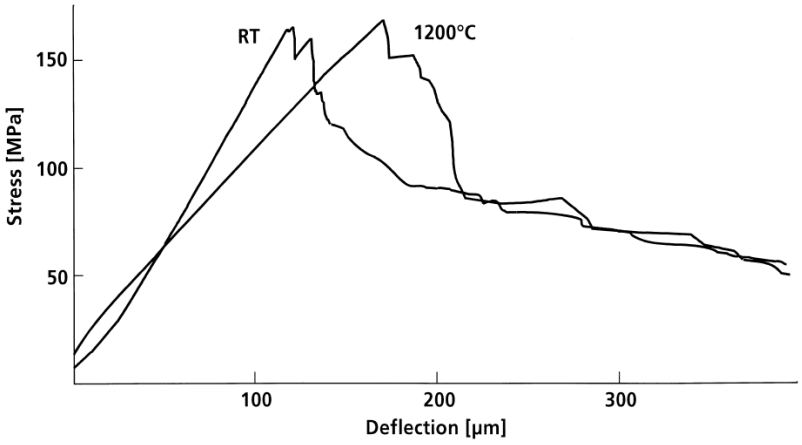

Figure 16*: Stress-deflection curves of 1D aluminosilicate fibre/mullite matrix composites at room temperature (RT) and at 1200°C obtained from three-point bending tests* [19].

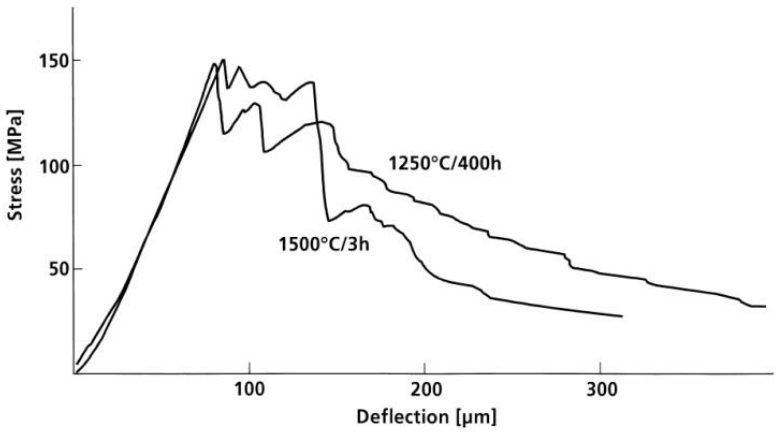

Figure 17: *Three-point bend test results of 1D aluminosilicate fibre/mullite matrix composites at 1250°C and 1500°C* [19].

2.3.2.2 Matrix variation

Three different types of matrix are currently available for high-temperature Ox.Ox CMCs with Nextel 720 fibre. The strength retention of each of these three alumina, mullite and aluminosilicate have been presented in **Figure 18** below [36].

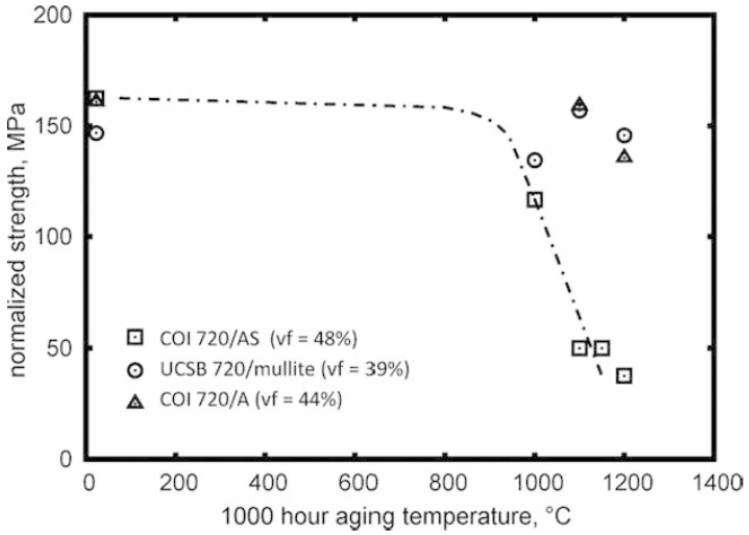

Figure 18: *The strength retension of Nextel720 fabric with three different matrices namely Alumina (A), Aluminosilicate (AS) and Mullite, after 1000 hours ageing. The dashed line indicates the trend for the silica-containing matrix, which is presumed to be stable up to 800°C* [36].

Mullite is resistant to sintering up to 1300ºC. The alumina in the matrix serves to bond the mullite particles together, but because the mullite forms a continuous network, there is no global shrinkage for long duration high-temperature exposure.

All alumina matrices perform well at high temperature, up to 1300°C, by employing a high initial matrix porosity as well as a heterogeneous alumina particle formulation to enable long-term stability against densification. It is completely silica free which may be important in certain atmospheres. The aluminosilicate on the other hand starts to deteriorate above a 1000°C. This is due to the presence of silica, which is glassy in nature and starts to change phase at elevated temperatures.

Property/ID	U090	W30	O090
Material	UMOX	WHIPOX	OXIPOL
Manufacturing	PIP	Slurry based filament winding	PIP
Lay up	0/90 Cross ply	±30° Wound	0/90 Twill fabric
Reinforcement	Nextel 610	Fe_2O_3/0.35% SiO_2	
Matrix	Mullite/SiCO	Alumina	SiCO
Interface	Fugitive	None	Fugitive
Fibre volume content in %	50	37	43
Porosity in %	12	25	15
Raw density in g/cm^3	2.46	2.72	2.36

Table 6: *Summary of the three different material systems being tested* [73].

Mechanical performance of three ox.ox CMCs based on Nextel 610 fibre and SiOC, alumina, and mullite/SiOC matrices respectively, were evaluated by Tushtev et al. [74]. This study looked at how different matrix systems behaved when tested at elevated temperatures. Tensile strength and stiffness of all materials decreased at 1000°C and 1200°C, probably because of degradation of fibre properties beyond 1000°C [73]. **Table 6** gives a summary of the three material systems being tested.

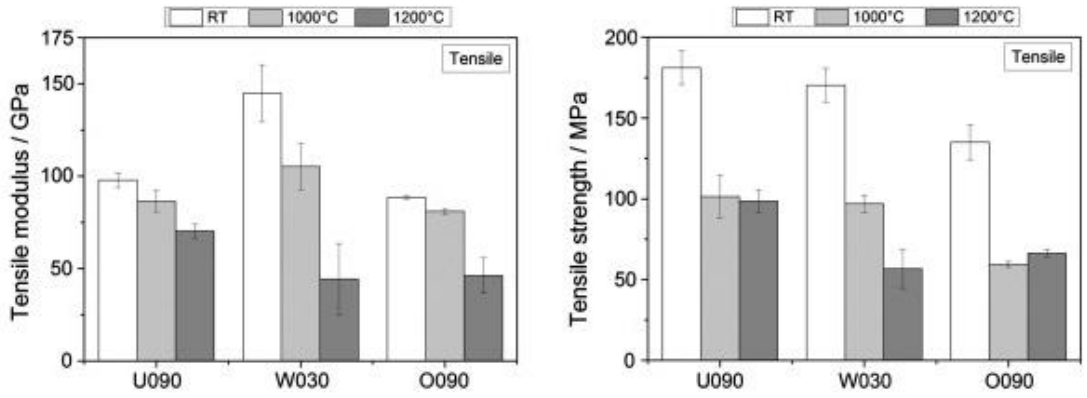

Figure 19: *Tensile Modulus and strength of the samples at different temperatures* [73].

The three materials were then exposed to elevated temperature to understand their mechanical behaviour. The trend showed that an increase in temperature would result in a decrease in tensile and modulus values **Figure 19**. **Figure 20** shows the effect of high-temperature on the bending strength of the samples [73]. An increase in flexural strength was observed at 1000°C in comparison to RT samples. This was mainly due to the residual stress relaxation within the sample at 1000°C. Above 1000°C although the residual stresses would be relaxed but due to the degradation of the fibre the flexural strength of the composite decreases.

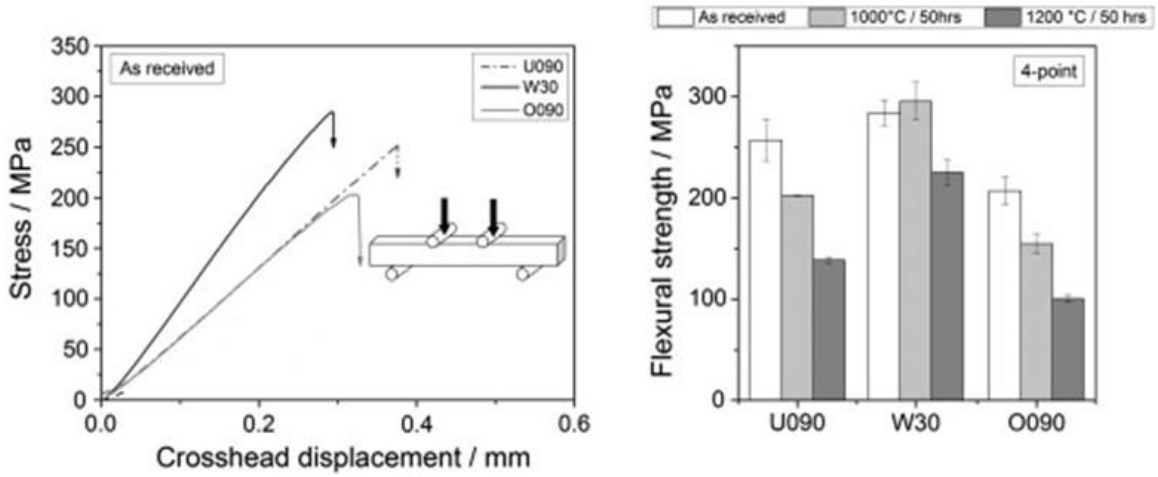

Figure 20: *Effect of temperature on the bending strength of the samples* [73].

Microstructural changes in the composites during exposure at 1000°C and 1200°C for 50 hours reduced their flexural strength, fracture toughness and work of fracture. The results indicated that the tensile strength and stiffness of all materials decreased with increasing temperature because the fibre properties degraded at temperatures beyond 1000°C. The grain growth-related to lower strength of the N610, accompanied by the higher interfacial adhesion in the PIP composites, resulted in lower values of flexural strength, fracture toughness and work of fracture of the composites at elevated temperatures.

2.3.2.3 Fibre variation

Nextel 610 and 720 fibres are used for application of above 1000°C. Nextel 610 provide higher tensile strength than Nextel 720, but N720 has superior creep resistance at high temperatures. Single crystal alumina fibre, sapphire, have been used in the past but has suffered from a minimum production diameter of 100 μm. This fibre cannot be woven easily due to its diameter [74,75]. The use of yttrium aluminium garnet fibre, $Y_3Al_5O_{12}$, provides the best creep resistance [76] along with excellent tensile properties.

The optimum fibre architecture utilised by Nextel fibres is eight harness-satin weave. 3D weaving results in improved properties, but the start-up costs associated with the manufacturing of 3D preforms would require substantial volume production to bring the cost down.

2.3.2.4 Fibre orientation

Elevated temperature testing of Nextel 720 oxide fibre ceramic composite systems with aluminosilicate matrix was performed to understand the effects of fibre orientation and temperature on the mechanical properties [77]. Thermal degradation of the material systems was studied in tandem with notch sensitivity and effects of tensile properties on centre hole panels [77].

For 0/90° fibre orientation, some strength was lost when the sample was heat-treated at 1000°C. Exposure to 1100°C for 100 hours resulted in embrittlement of the material which was visible by substantial decrease in strain to failure. The strength also fell to one third of its original value, but the stiffness of the system increased after 100 hours at 1100°C.

For ±45° fibre orientation an increase in strength after heat-treatment at 1100°C was observed. Analysis of the fracture profile using electron microscopy indicated an abrupt and violent fracture with limited pullout as compared to the as-received fracture which was a gradual process, indicating embrittlement

after heat-treatment. No significant change in porosity was observed after exposure to 1000°C, whilst a small increase in the micro-hardness of the matrix on the other hand increased with treatment temperature and time at 1000°C and 1100°C.

Two different matrix systems, namely alumina and aluminosilicate, with Nextel 720 fibre were investigated by Triplicane et al. [24] in order to quantify the effects of fibre orientation on the strength and creep resistance. The results indicated that the orientation of the fibre affected the high-temperature strength. It was observed that in ±45° orientation the strength was affected by temperature, **Figure 21**.

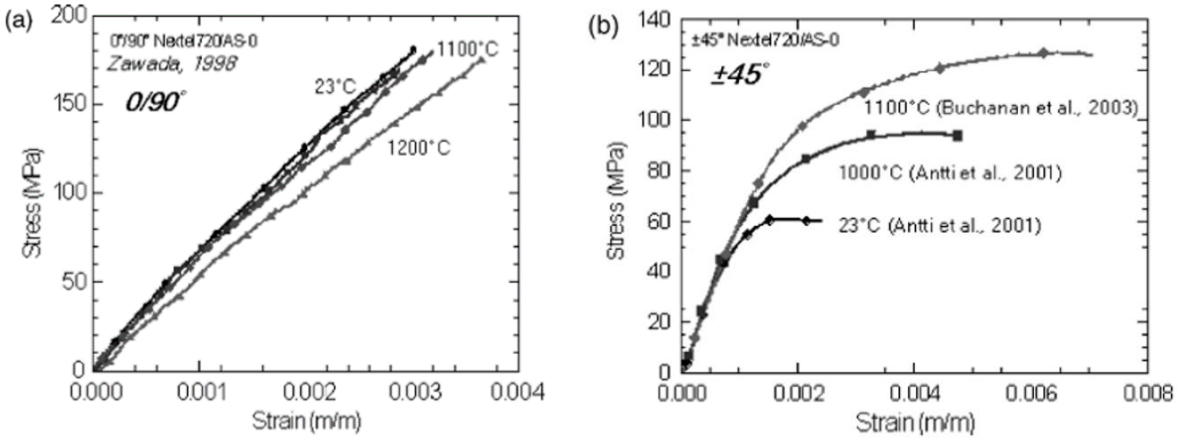

Figure 21: *Effect of fibre orientation namely 0/90° and ±45° on the strain rate of the CMC* [24].

In terms of creep, the orientation had a much more significant effect, the anisotropy of this material has been reported to be much more significant. A difference of three to four orders of magnitude was observed in the creep rate between the 0/90° and ±45° orientations as observed in **Figure 22**.

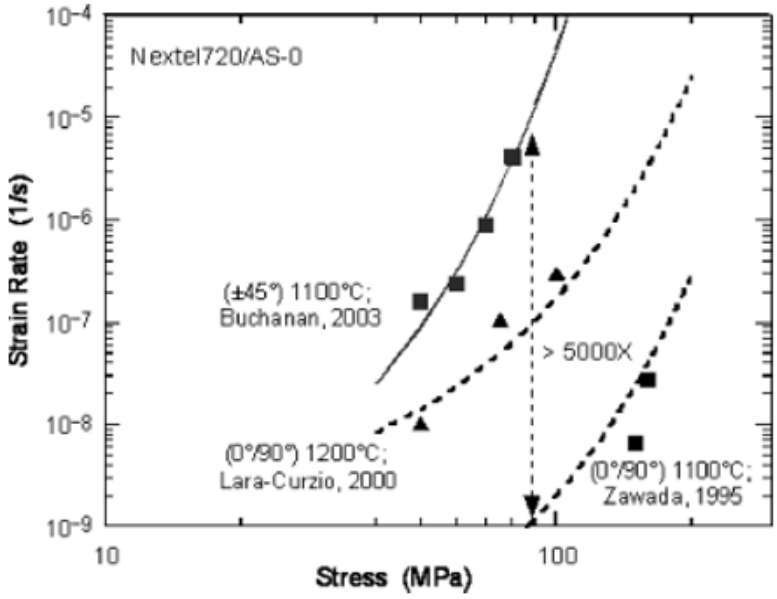

Figure 22: *Creep behaviour of the Nextel 720/aluminosilicate composite measured and reported by different investigators* [24].

Shankar et al [78] investigated the behaviour of notched N720 with Alumina matrix ceramic matrix composites at 1200°C. As the stress level increased the creep rate also increased as a function of time**.** **Figure 23** shows creep strain as a function of time for different stress levels. SEM analysis of the damaged samples indicated excellent fibre pull-out of the sample as seen in **Figure 24**. The initial damage was primarily matrix cracking concentrated in a plane along the weak fibre–matrix interface in the transverse (90°) plies.

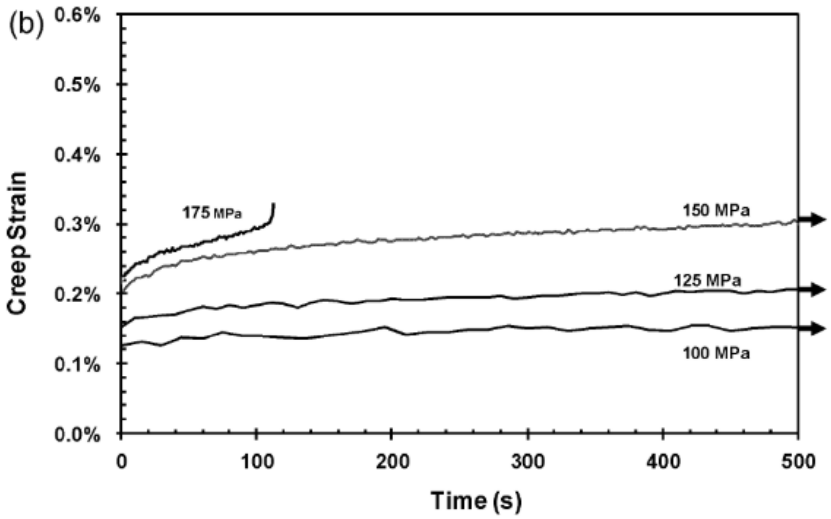

Figure 23: *Creep strain vs time for a notched N720/A.*[78]

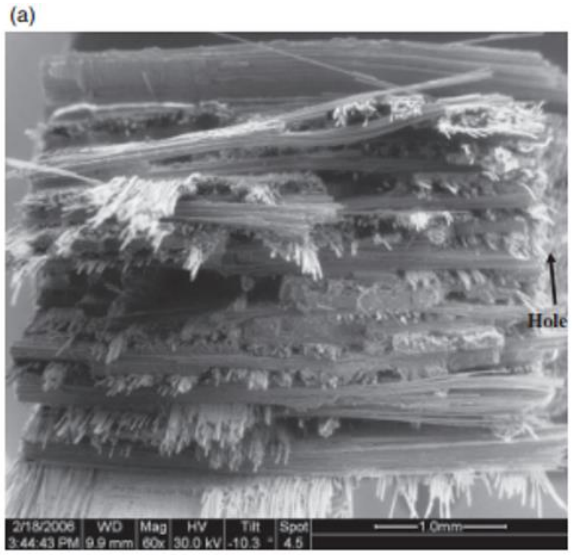

Figure 24: *Overall view of the fractured surface of a notched N720 with Alumina matrix ceramic matrix composite at 1200°C* [78].

2.3.2.5 Effect of processing parameters

The thermal stability of alumino-silicate Nextel 720 fibre in a porous mullite matrix was investigated in the temperature range between 1300°C and 1600ºC. Temperature-controlled reactions between the silica-rich glass phase of the matrix and α-Al_2O_3 at the rims of the fibre were observed accompanied by

the formation of mullite. This process is initiated at shorter time intervals (2hrs) at 1500°C and at longer time intervals (1000hrs) at lower temperatures 1300°C, as seen in **Figure 25** [79] .

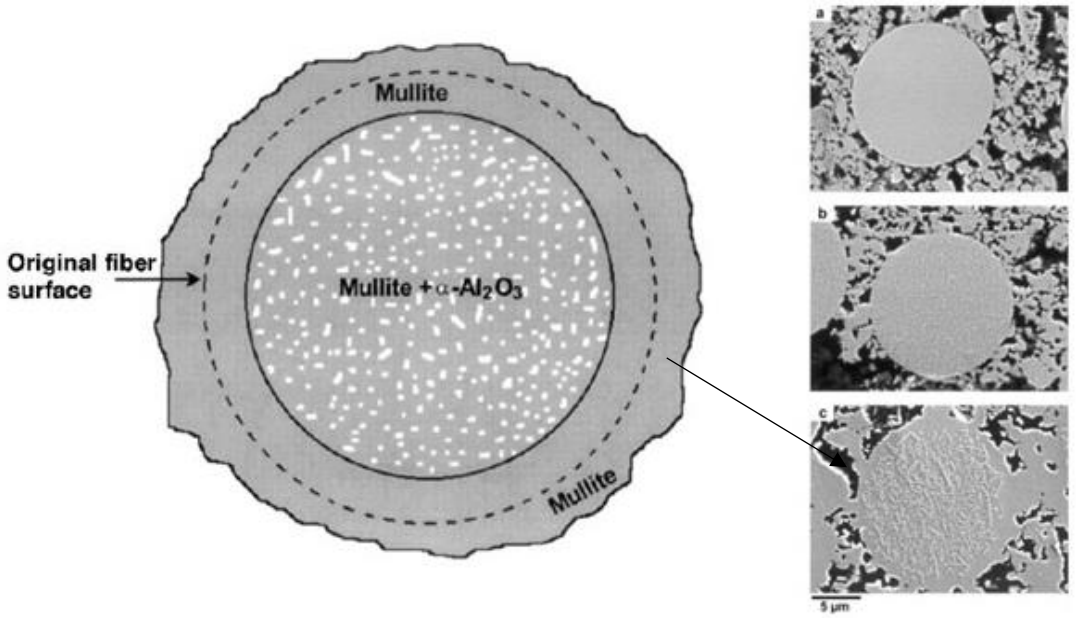

Figure 25: *Schematic presentation of the mechanism of fibre/matrix interaction in Mullite+Al_2O_3 composite. Microstructural changes of alumina-silicate fibre/porous mullite matrix composite caused by thermal treatment. (a) as-prepared; (b)1500°C, 2 h; (c) 1600°C, 2 h. Note that with increasing temperature, gradual coarsening of the fibre compounds occurs. At 1600°C, a depletion of a-Al_2O_3 in the fibre rim area is observed* [79].

Tensile testing was performed on Nextel 720 fibre at room temperature and high temperature in inert atmosphere. The tensile strength equals ~1100 MPa at room-temperature and ~650 MPa at 1200°C [80]. **Figure 26** shows the effect of temperature on the strength of the fibre bundle. High-temperature degradation is mainly a function of silica, due to degradation in high-temperature water and fuel-rich environments.

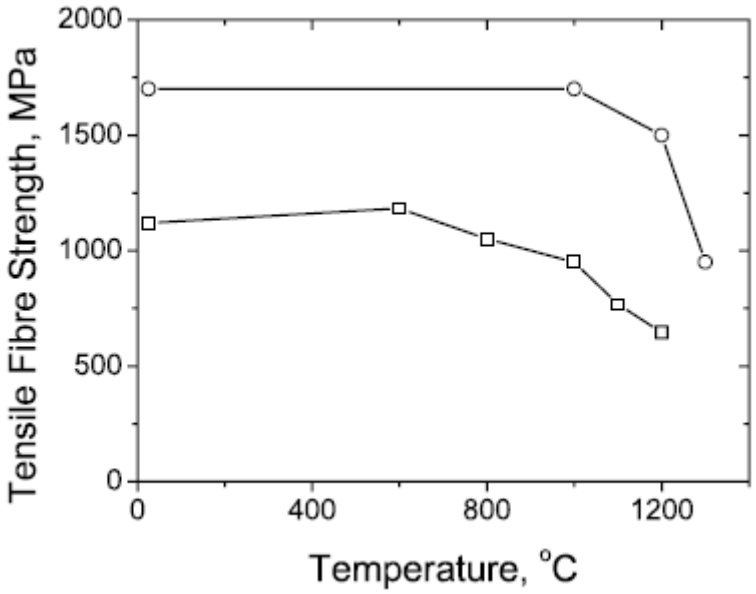

Figure 26: *The mean tensile strength of Nextel 720 fibre (projected to a 25 mm gauge length) as a function of temperature. Square and circle symbols represent results from this study and the reference work by Wilson et al.* [80].

The introduction of a small amount of yttrium alumina garnet (YAG) significantly slows the sintering of fine (0.2 μm) alumina in the composite [81]. ATFI (Applied Thin Films Inc.) have developed an alumina phosphate-based matrix (Cerablak) that contains no silica. This matrix system offers thermal stability up to 1315ºC and are also ultra-lightweight.

Another relatively mature porous matrix composites called 'wound highly porous oxide ceramic composite (WHIPOX)' were developed by the German aerospace centre (DLR) [82]. These materials utilise either Nextel 720 or 610 fibre filament wound into highly porous mullite or alumina matrix. These materials are sintered at atmospheric pressure and exposed to temperatures up to 1300°C, and the resulting components contain 25-50% vol fibres. Sintering at 1300°C can result in grain growth in Nextel 610 fibre which can be detrimental, but this can be minimised by the addition of silica in the matrix [83].

Yang et al. [38] looked at the sol-gel temperature dependent ductile to brittle transition of aluminosilicate fibre, ALF 3025T, reinforced in a silica matrix. Techniques like nano-indentation and push out tests were used to quantify the micro-mechanical properties of the CMC. Temperatures in-between the range of 600-1200ºC, in argon atmosphere, were studied to observe if any phase transition took place. **Figure 27** shows the XRD spectra of the as-received fibre (a) and the AS/SiO_2 composite fabricated at different temperatures (b). Heat treatment up to 1000ºC did not alter the fibre microstructure, but higher heat-treatment temperatures like 1200ºC triggered severe phase transformation of the AS fibre by the formation of the crystallised mullite phase ($3Al_2O_32SiO_2$) through the reactions between the γ-Al_2O_3 and the α-SiO_2.

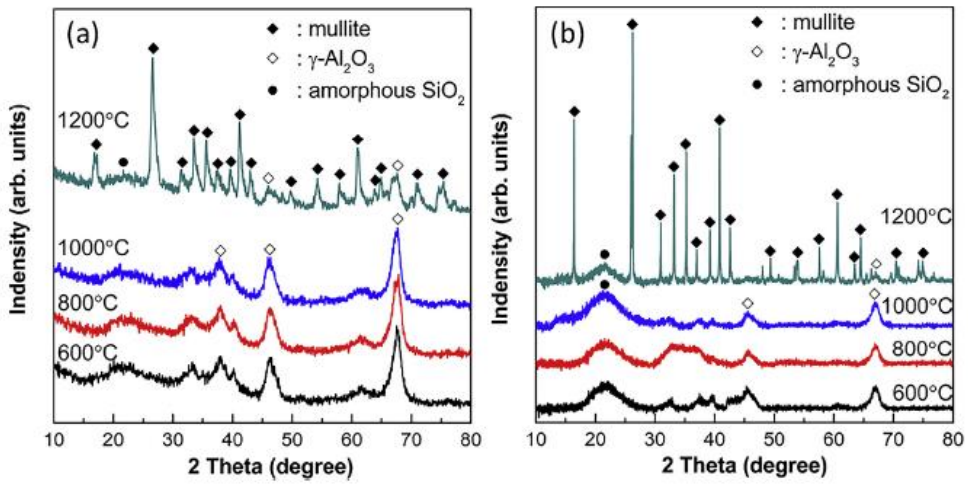

Figure 27: *XRD spectra of the (a) AS fibre and (b) AS/SiO_2 composites fabricated from 600-1200°C* [38].

Microstructural changes at different sol-gel temperatures led to changes in the fibre's mechanical properties, which were quantified using nano-indentation. **Figure 28** shows the result of the sol-gel manufacturing temperature on Young's modulus and hardness of the fibre. Drastic change in the mechanical properties were observed for both the fibre and the matrix beyond 1000°C.

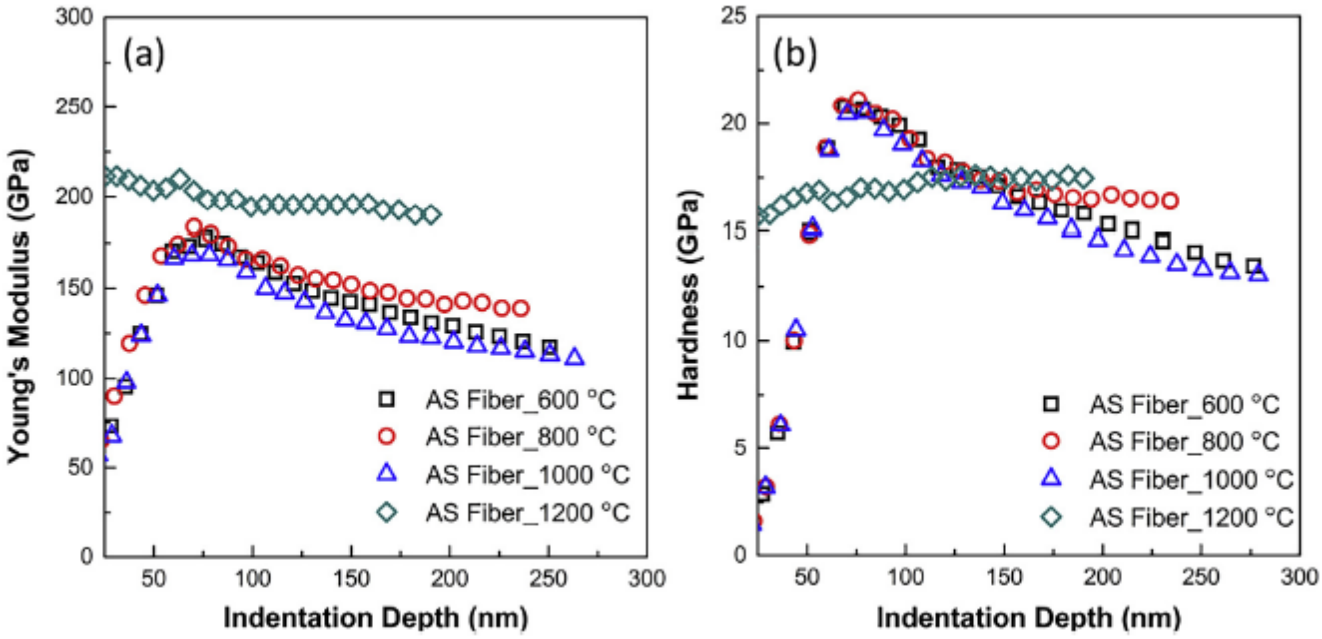

Figure 28: *(a) Young's modulus and (b) hardness of the AS fibre as a function of penetration depth* [38].

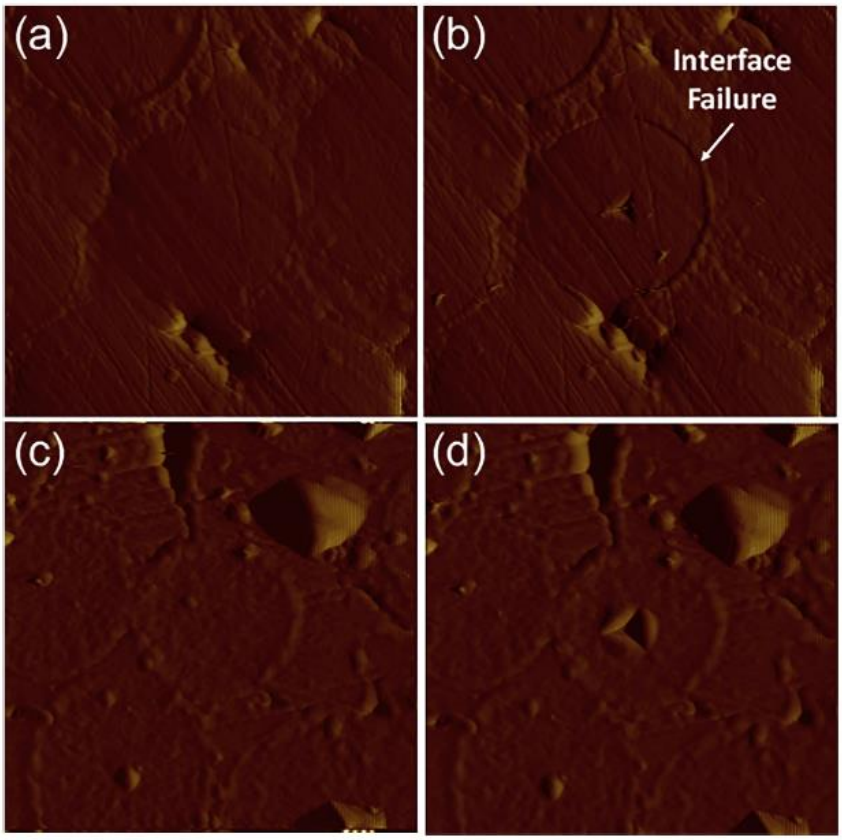

Figure 29: *SEM images of nano-indentation imprints of the AS/SiO_2 composites fabricated at: (a, b) 600°C and (c, d) 1200°C* [38]..

To understand the fibre-matrix interface behaviour fibre-pushout testing was performed. It can be observed that fibre/interface bonding had taken place in **Figure 29 (d)**. The AS/SiO_2 fabricated at 1200ºC showed a different nano-indentation response. The data presented in **Figure 30** showed the deviation in mechanical properties at 1200ºC in comparison to samples produced at 1000ºC and below.

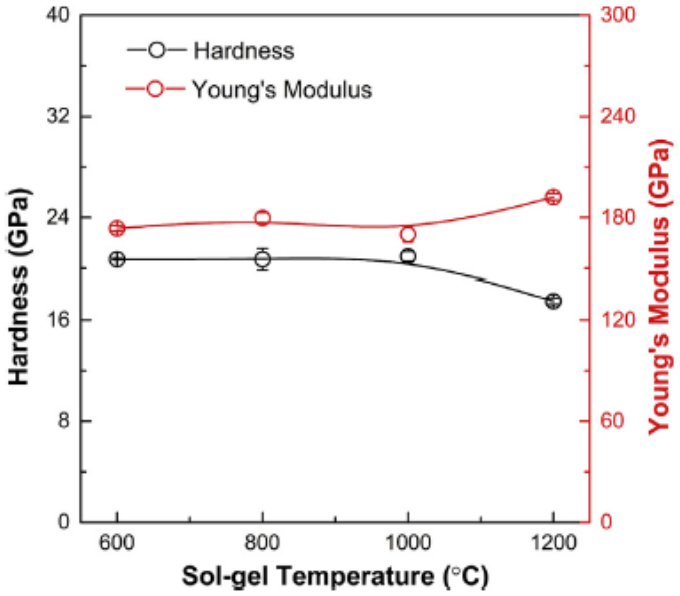

Figure 30: *Young's modulus, and hardness of the AS fibre versus sol-gel temperature in the AS/SiO_2 composite fabricated from 600-1200ºC* [38].

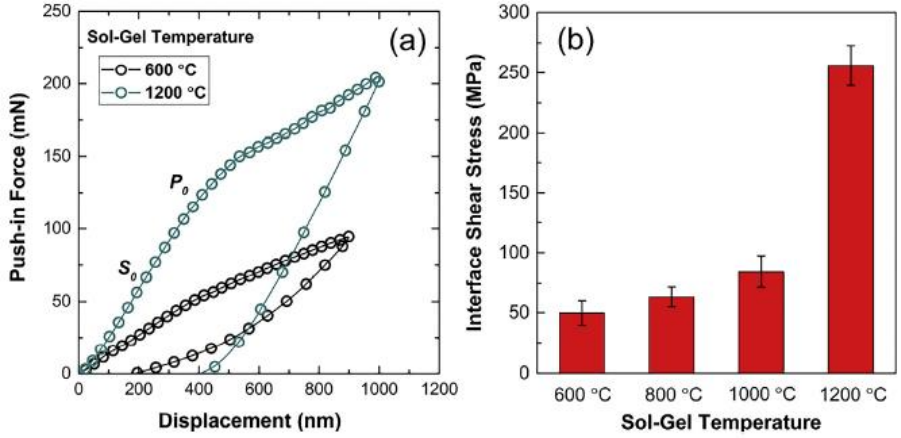

Figure 31: *The typical fibre push-in results of the AS/SiO_2 composite fabricated at 600 and 1200°C; (b) interfacial shear strength of the composite evolved as the sol-gel temperature* [38].

The interfacial shear stress increased massively from 1000°C to 1200°C as seen in **Figure 31**. Mechanical properties of SiO_2 matrix fabricated at different temperatures varied greatly. The properties

of AS/SiO_2 composite means more content of SiO_2 can be formed at higher sol-gel temperatures, which consequently leads to the enhancement of Young's modulus and hardness, as observed in **Figure 32**. **Figure 33** shows how the flexural strength of the sample decreases with an increase in processing temperature. Micro-analysis of the damaged surface, as seen in **Figure 34 (b)**, indicated that no de-bonding had taken place in the sample exposed to 1200°C.

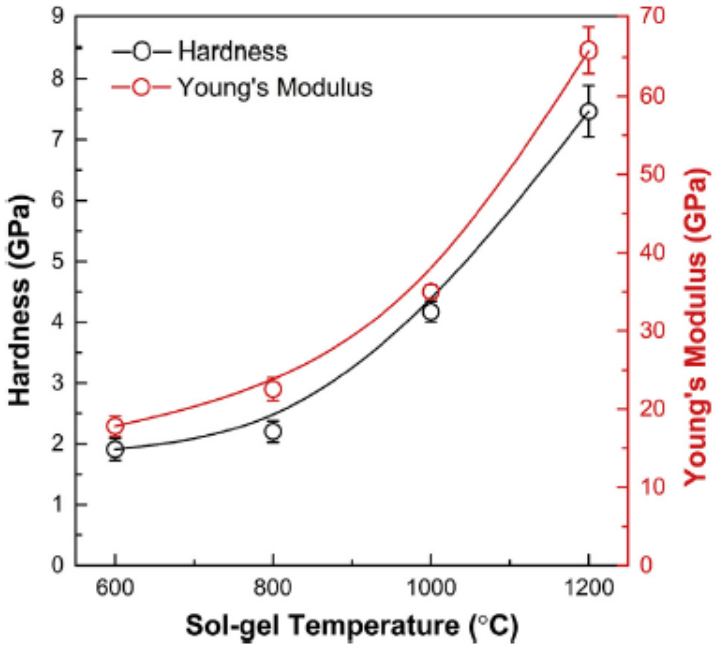

Figure 32:*Young's modulus and hardness versus sol-gel temperature in the AS/SiO_2 composite fabricated from 600-1200°C*

[38].

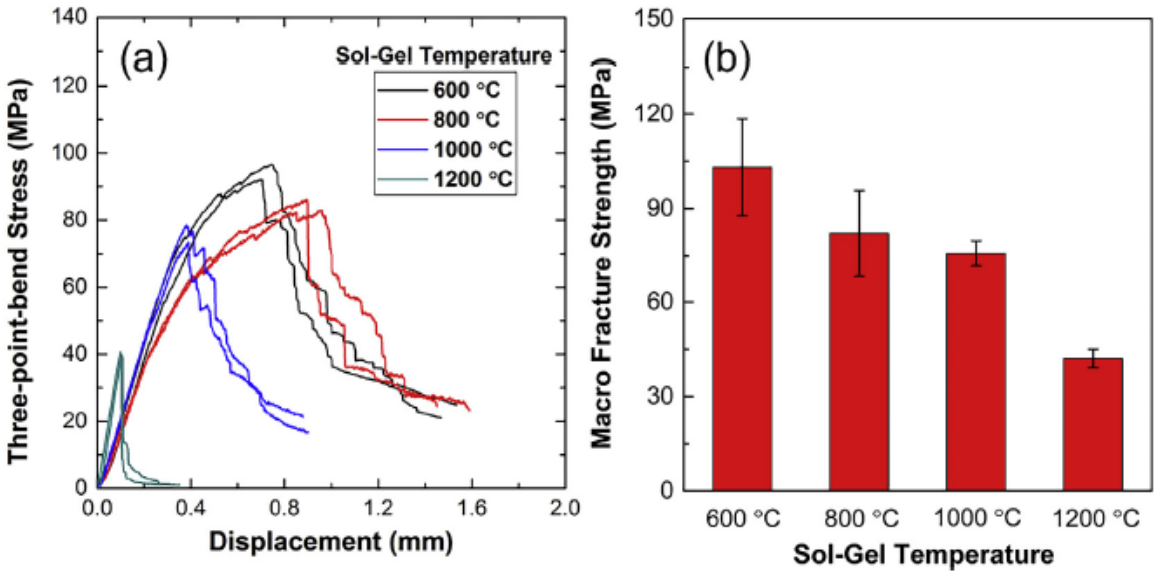

Figure 33: *Three point bend tests of the AS/SiO_2 composite fabricated from 600°C to 1200°C; (b) TPB fracture strength versus sol-gel temperature in the AS/SiO_2 composite* [38].

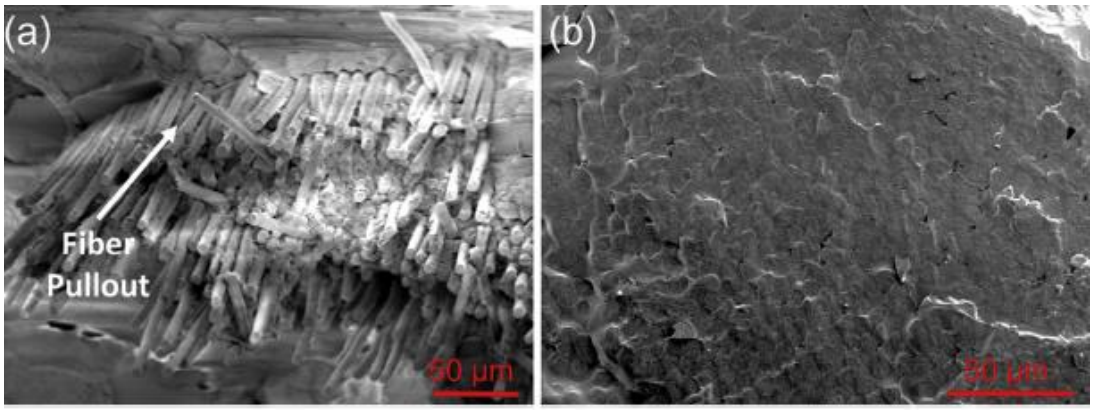

Figure 34: *SEM images of the fracture morphologies of the AS/SiO_2 composites after the three-point bend tests: (a) 600°C and (b) 1200°C* [38].

2.3.2.5.1 Creep

Tensile creep behaviour of Nextel 720 fibre with alumina-mullite matrix with ±45°orientation was studied at 1200°C in *air, steam and argon* [10]. **Figure 35** shows the comparative strength between the 0/90° and ±45° orientation tested at 1200°C.

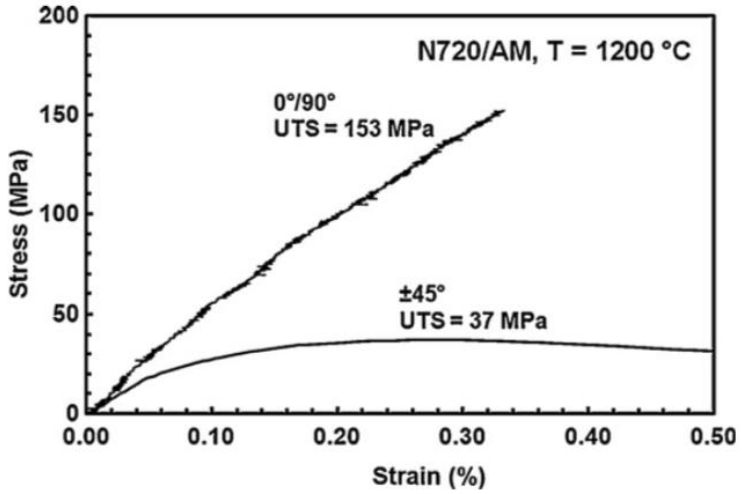

Figure 35: *Tensile stress-strain curves obtained for N720/AM ceramic composite at 1200°C. Data for the 0°/90° fibre orientation* [10].

For a stress range between 13MPa to 30MPa the largest creep strain developed in argon, followed by steam and air [10]. For creep stress levels ≤26MPa environment had little effect on creep rate. Above a stress level of 26MPa, a sharp increase in creep rates in steam and argon environments is observed, while the creep rate in air remains below 10^{-5} s^{-1}. At 30MPa, creep rates in steam and argon environments increase by nearly two orders of magnitude. At 32MPa, creep rates produced in steam and in argon are around three orders of magnitude higher than the rates produced in air.

Vacuum infiltration was used to produce continuous fibre ceramic composites for high temperature applications. Nextel 610 and 720 fibres were investigated in mullite-alumina slurries [84]. The mechanical performance was found to be comparable to SiC/Carbon and Carbon/Carbon CMCs. The materials containing the N720 fibre have excellent high temperature characteristics. Although the small alumina particles sinter themselves to the N720 fibre, this does not result in degradation of fibre strength significantly. The matrix was also observed to provide excellent resistance up to 1200°C.

The creep behavior of inter-laminar shear of Nextel 720/ alumina CMC was evaluated at 1200°C in air and steam using double-notch shear test specimens [85]. The inter-laminar shear stresses were measured

in the range of 4-6.5MPa. Primary and secondary creep regimes were observed in all tests conducted in air. Under shear loading, tertiary creep was also observed with a run-out defined after 100hrs. Steam resulted in a creep performance deterioration of over 50%. The main cause of this was attributed to matrix degradation. **Figure 36 (b)** shows the creep strain that developed in samples tested in air and steam.

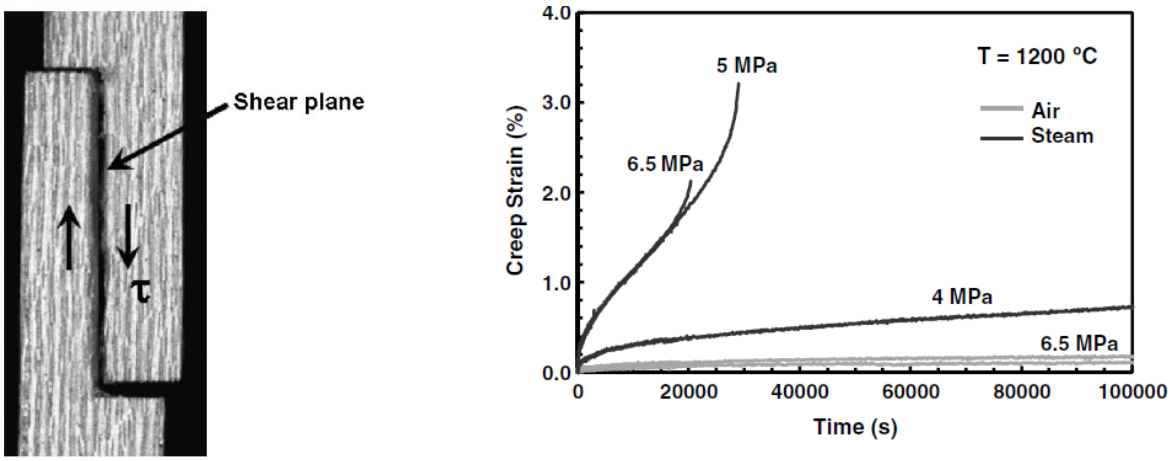

(a) (b)

Figure 36: *(a) the failed sample after undergoing shear loading (b)the creep strain that developed in samples tested in air and steam* [85].

2.3.3 Summary and discussion

Three different oxide matrices are currently available for high-temperature oxide CMCs [36]: alumina, mullite (the only chemically stable intermediate phase in the SiO_2-Al_2O_3 system) and aluminosilicate (compounds of aluminium, silicon and oxygen with substitution by other elements). Literature shows that above 1000°C alumina silicate matrix lost its strength whereas mullite and alumina matrix maintained their strength. The strength of composites comprising Nextel 720 fibres within a mullite matrix [9] or alumina matrix generally remains unchanged after aging at 1200°C for 1000 hr, although significant weakening can occur in the aluminosilicate matrix system at temperatures

of ~1200°C. Electron microscopy investigations have shown that this was due to aluminosilicate matrix beginning to sinter at 1100°C, whereas the microstructure of the fibre remains unchanged [86].

Two different matrix systems, namely alumina and aluminosilicate with Nextel 720 fibre, were investigated by Triplicane et al [24]. The results indicated that CMCs which used aluminosilicate as the matrix instead of alumina, although stronger, cracked much more quickly. Experiments carried out by researchers on Nextel 720/Mullite indicated that the mechanical properties of samples tested at room temperature (RT) and elevated temperature were very similar [19]. The results indicate that the composite exhibited a damage-tolerant behaviour and retained RT maximum bending strength (160MPa) up to 1200°C. Long-term heat treatment at 1250°C and short-term heat treatment at 1500°C had no effect upon RT behaviour. Due to weak fibre/matrix bonding, the use of fibre-coating was not necessary. The FEA analysis indicated that failure occurred due to the residual stresses as a result of creep during service. The analysis included anisotropy of both materials during thermal loading.

Due to the orthotropic nature of the material systems, the strength and stiffness depend on the load direction relative to the fibre directions. For example, the stress-strain behaviour of a Nextel 720/aluminosilicate sample, tested in bending, was found to be stable up to 1100°C with 0/90° ply orientation [86]. As the ply orientation was changed to ±45° significant anisotropy in the mechanical properties was observed. This was attributed to the generation of a tensile stress along the ±45° orientation relative to the weak fibre/matrix interface. There was also a difference of three to four orders of magnitude in the creep rate at 1100°C, in between samples with 0/90° and with ±45° orientations [24].

The matrix properties can be optimised to improve high temperature performance; for instance, the introduction of a small amount of yttrium aluminium garnet (YAG) significantly slowed the

sintering of the alumina at 1300°C [81] and helped maintain its strength at elevated temperatures. Nanoparticles may also be added to the matrix to modify its properties. For instance, with the additions of SiC nanoparticles the tensile creep rate of a mullite matrix composite was reduced to a significantly lower value, roughly four times less than that of the monolithic mullite [39]. Different oxide fibres can perform optimally under different conditions.

The type of fibre has a major impact on the high temperature mechanical properties of the CMCs. In a study of the long-term tensile creep behaviour of oxide ceramic-matrix composites [87] tested at temperatures up to 1100°C, the materials with Nextel 610 fibre exhibited higher strength and stiffness [17], whereas the materials with Nextel 720 fibre had lower strength and stiffness but performed better in terms of creep at 1100ºC. Although it must be noted that the creep resistance of Nextel 720 fibre/alumina matrix CMCs can degrade at temperatures higher than 1100°C in steam environments [88].

Mechanical properties of SiO_2 matrix fabricated at different temperatures varied greatly. The Young's modulus and hardness at 600°C enhanced greatly with an increase in sol gel temperature [38]. At 1200°C, the Young's modulus and hardness increased more than three folds.

It can be concluded that alumina and mullite matrix can both be used at 1100°C. The material systems exhibit significant anisotropy in mechanical properties in bending and creep. The strength of the material systems with N720 and Alumina or Mullite matrix is very similar at RT and 1100°C. Due to the inherent porosity in the material system fibre strength is 3-4 times more than the matrix strength, which suggests that the CMC would fail due to matrix damage. Literature also shows that fabrication at different temperatures had a major effect on the mechanical properties of the CMCs. The orientation of the fibres played a major role on the creep resistance of the material systems. This information would

be used to design material systems which could provide the most optimum creep resistance and maximum elastic strain at 1100°C. Different testing procedures have also been identified including XRD, nanoindentation and fibre pushout [38] that could be used to study comparative performance of material systems fabricated under different processing conditions.

2.4 Main experimental techniques

2.4.1 X-ray tomography

X-ray computed tomography is a non-destructive testing technique that can be used to monitor crack propagation by carrying out 3D visualisation of the sample. It uses numerical computation to process a set of X-ray radiographs, each of which represent a slice through the sample, at different angles. The technique uses X-rays, generated by a radiation source, which interact with the sample and are collected by a detector positioned behind the sample, as seen in **Figure 37** [89]. The X-rays are produced using an electrical X-ray source, where accelerated electrons are bombarded on a metal target to produce X-ray photons [90]. The technique uses a computer to reconstruct an image of a cross-sectional plane through the object. The image generated is a quantitative map of the linear x-ray attenuation coefficient, μ, at each point in the plane. The linear attenuation coefficient is a function of the X-rays being scattered and absorbed whilst interacting with the sample, which is a function of atomic number and density of the absorbing medium. Attenuation increases with the density and thickness of the material.

The change in intensity of a monochromatic incident X-ray can be mathematically expressed in Beer-Lambert Law, and is proportional to the object's thickness (x):

$$\frac{dI}{I} = -\mu dx \qquad 3$$

where I is the intensity of the incident X-ray and μ is a material (atomic number and density) dependent linear absorption coefficient. The integration of equation 2.3 can lead to the description of penetration though a heterogenous material:

$$I = I_o e^{-\int \mu(s) ds} \qquad 4$$

Radiographs are collected at different angular positions which can be reconstructed to generate the virtual slices which can then be viewed in 3D. The contrast, expressed as the grey level in the images, is essentially the distribution of the linear absorption coefficient in the object as seen in **Figure 38**. In order to increase the quality of the signal and decrease the noise, the accusation time can be increased.

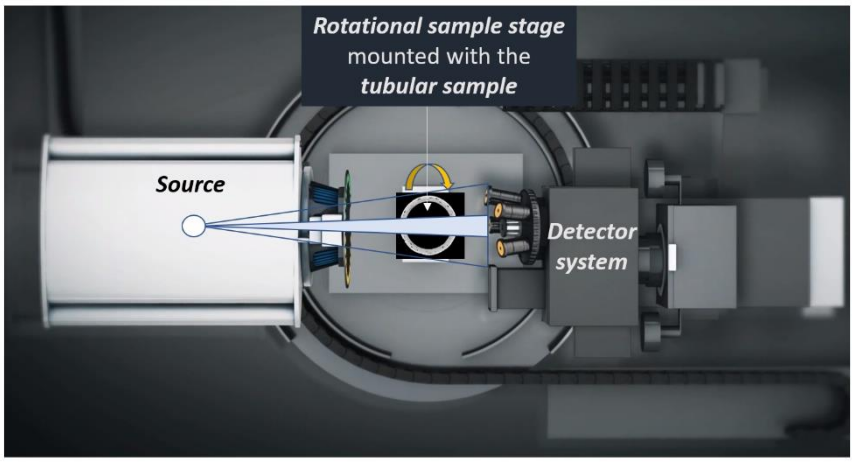

Figure 37: *A schematic of the experimental apparatus for characterization in the laboratory X-ray tomography, Xradia Versa 510. The blue line highlights the cone X-ray beam from the source* [89].

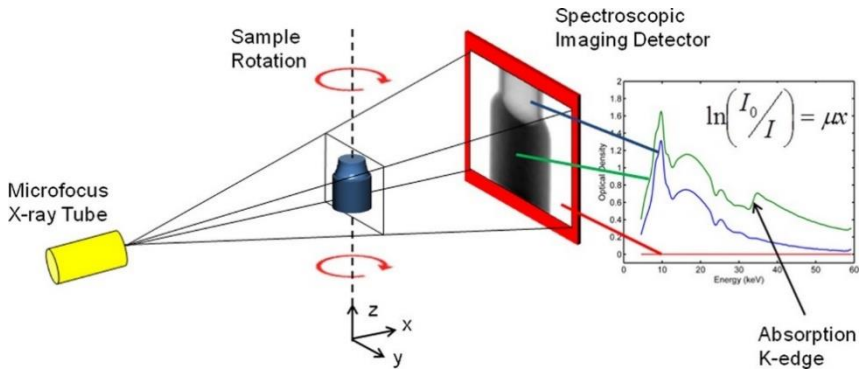

***Figure 38**: The absorbed X-ray spectrum in each pixel can be measured. The geometric magnification can be increased by moving the sample closer to the X-ray source enabling micrometer scale resolution. By recording projections at different angles of sample rotation, a 3D dataset of the sample object can be mathematically reconstructed* [91].

X-ray tomography has been used to study damage development in composites [92]. This technique was used during the thermomechanical cycles to quantify damage, oxidation and healing phenomena. **Figure 39** shows the evolution of cracks in the middle of a utile section of the sample for the seven different loading steps.

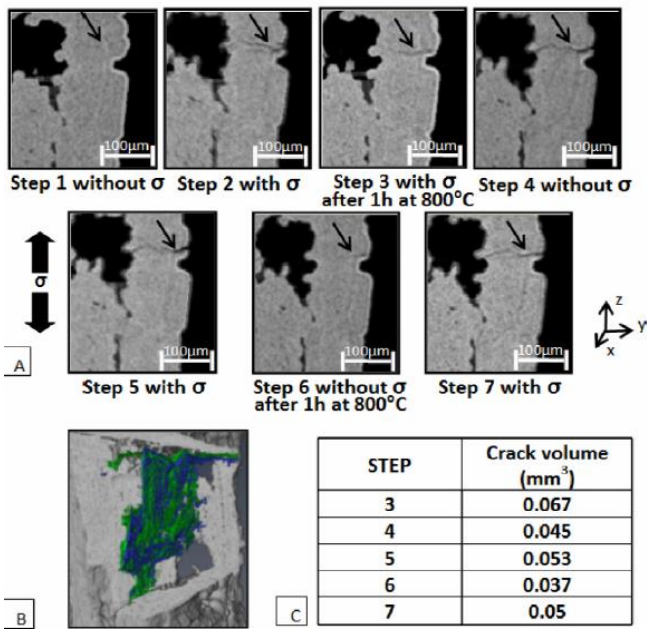

STEP	Crack volume (mm^3)
3	0.067
4	0.045
5	0.053
6	0.037
7	0.05

***Figure 39:** The evolution of a crack captured by µXCT, (a) tomographs of cracks developed (b) 3D visualization of the crack (c) Seven states of the thermomechanical sequence described* [92].

XCT has been used by Vincent et al. [18] to quantify failure events taking place in a melt-infiltrated SiC/SiC composite. In-situ X-ray micro-tomography tensile tests were performed at room temperature and 1250°C. **Figure 40** shows the crack propagation taking place in the sample [18]. Cracks initiate near the free surfaces and propagate perpendicularly to the loading axis. Once a crack forms, multiple microcracks nucleate in the vicinity. The location of the final failure is labelled using a black ellipse in the initial volume.

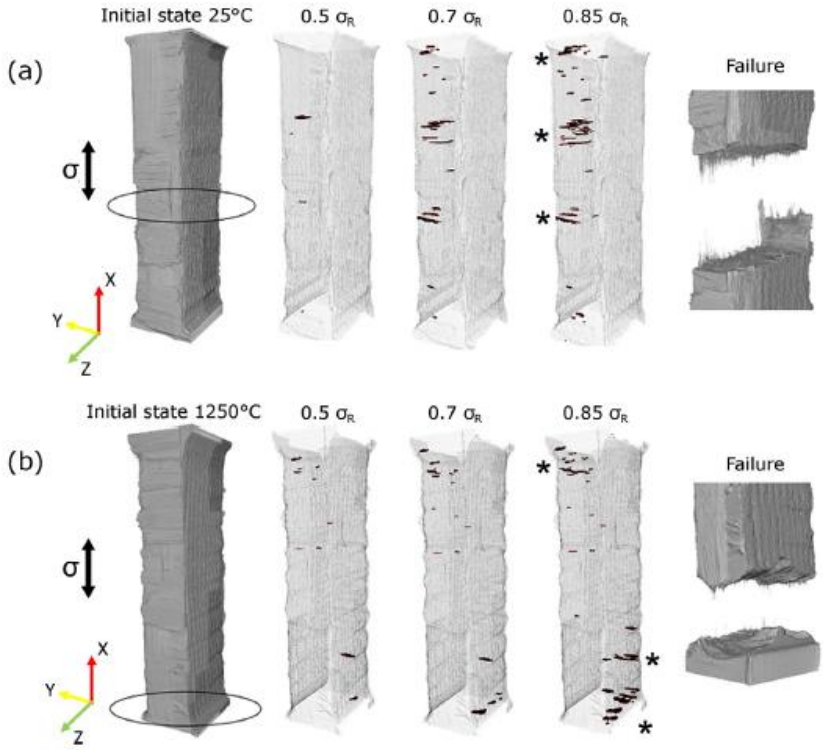

Figure 40: *Tomographs of the melt-infiltrated SiC/SiC composite at different stresses both at (a) RT and (b) 1250°C* [18].

Studies have been carried out to understand matrix cracking and damage progression in SiC/SiC ceramic matrix composites using XCT [93]. It was used to quantify the volume of damage through the employment of greyscale threshold techniques. **Figure 41** shows damage development with loading. Damage is clearly visible in sample b, c and d.

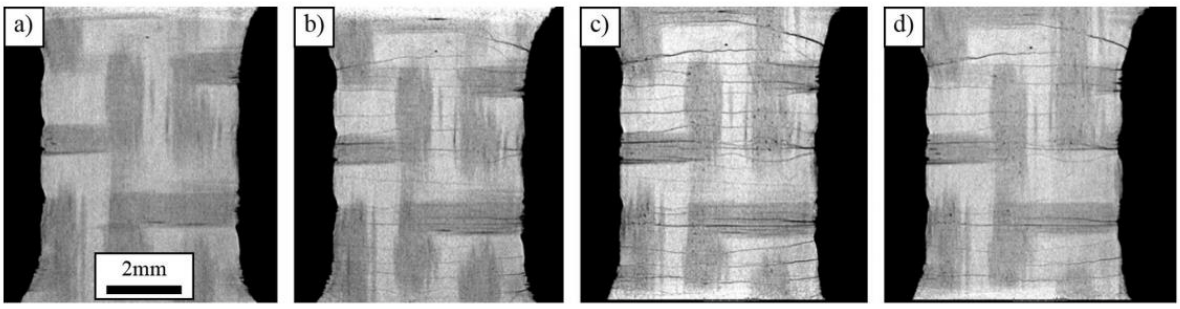

Figure 41: *surface damage observed on a common plate (a) prior to loading (b) first loading cycle, P_{max} (c) 650 loading cycles, P_{max} (d) 650 loading cycles, P_o*

Combination of ex-situ and in-situ computed X-ray tomography observations can be used to study SiC-SiC CMC tube [94]. The visualisation of the SiC-SiC tube was carried out using lab based μCT, **Figure 42** (**a) and (b)** at medium resolution of ~17μm and **(c) and (d)** at ~2μm resolution. **Figure 42 e** shows the segmented porosity of the sample using image intensity thresholding. To measure the porosity correctly pores need to be at least an order of magnitude larger than the voxel size to be measured reliably. XCT in tandem with image visualisation software is an excellent way of quantifying porosity within a system.

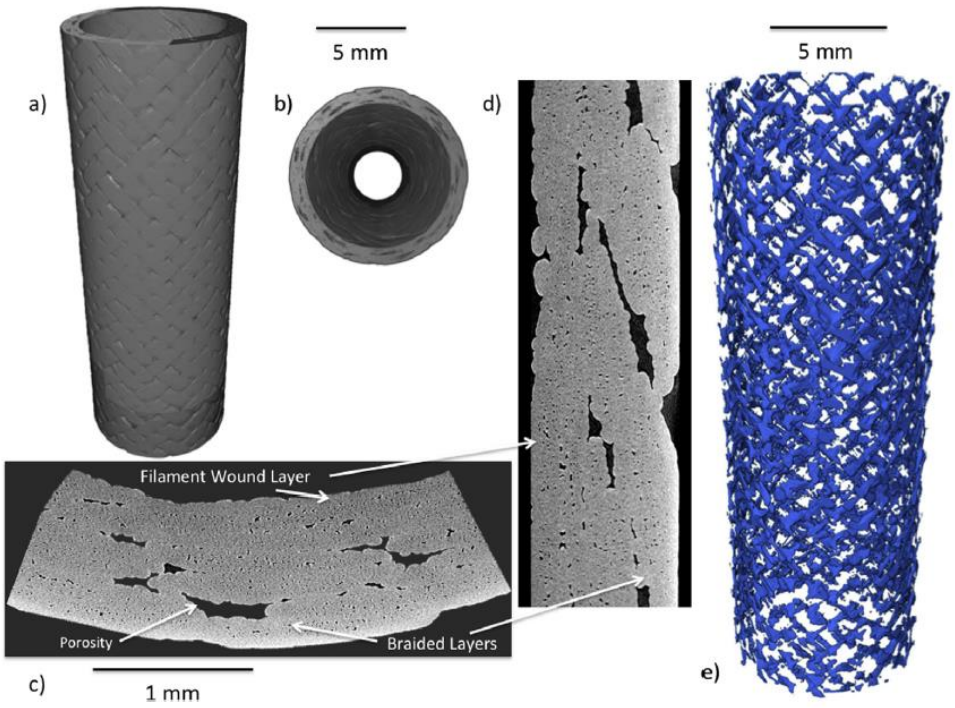

Figure 42: *X-Ray tomography images of a SiC/SiC tube in different orientation (a) (b) (c) (d), and resolved in Avizo* [94].

Figure 43 shows the microstructure characterisation of the structure carried out using medium resolution (17.5µm voxel) laboratory tomography. **Figure 43** shows the porosity of the sample measured in Avizo, at different axial positions **Figure 43 (a)**, along with pore populations measured at different resolutions **Figure 43 (b)** [94].

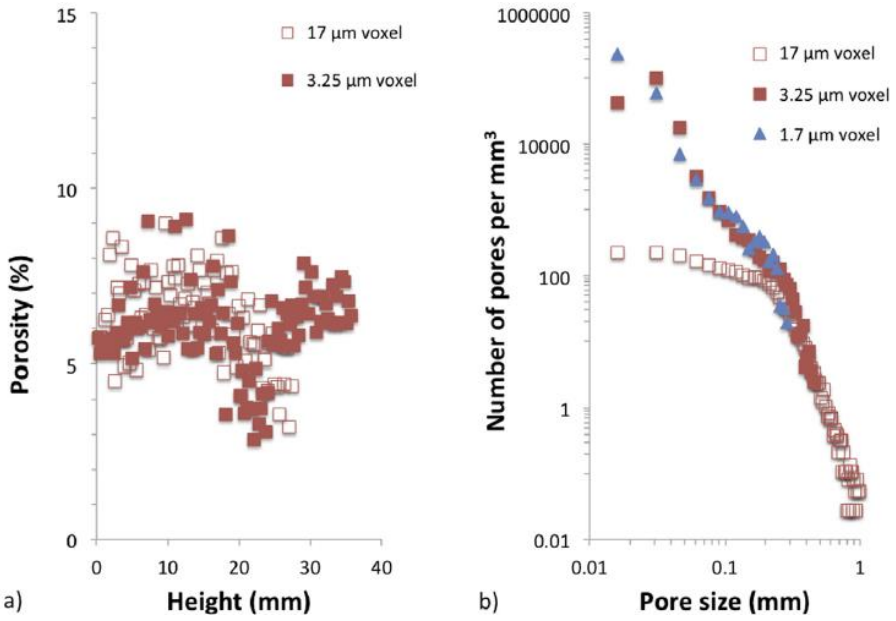

Figure 43: *Porosity % and average pore density using avizo a) variation of total porosity with axial position (i.e. height); b) pore populations measured at different voxel resolutions* [94].

This technique was used extensively throughout the study to identify the formation and growth of cracks, and quantify the nature and volume of those cracks. It can also be used as a technique to study the step by step formation of microstructural cracks both in-situ and ex-situ. Imagine visualization software, such as Avizo, could be used on the tomography data to approximate the combined open and closed porosity of different composite samples. Certain limitations associated to the technique including the imaging resolution of the tomography machine which determines the size of the defect that can be visualised. Tomography is a very time intensive technique, with each volumetric tomograph taking over 8-10 hours.

2.4.2 High temperature three-point bend test

High temperature three-point bend tests can be used to measure the difference in magnitude of flexural strength and flexural strain development at room temperature (RT) and elevated temperature. This can be used to understand how the failure mechanism changes with the elevation of temperature. It can also

be used to quantify creep strains that develop in samples at constant stress at elevated temperature. The technique employs a load cell to apply load on the sample and using either the machine deflection or an linear variable differential transformer (LVDT) the displacement of the sample is measured. This displacement can then be used to calculate strain, and consequently calculate the Flexural Modulus.

High temperature three-point bend tests were carried out on C/SiC composites by Feng et al. [95]. The technique was used to calculate the flexural strength and fracture toughness of different material systems. **Figure 44** shows the sample being tested at 1400ºC. The spallation area initiates from the top surface to the bottom surface.

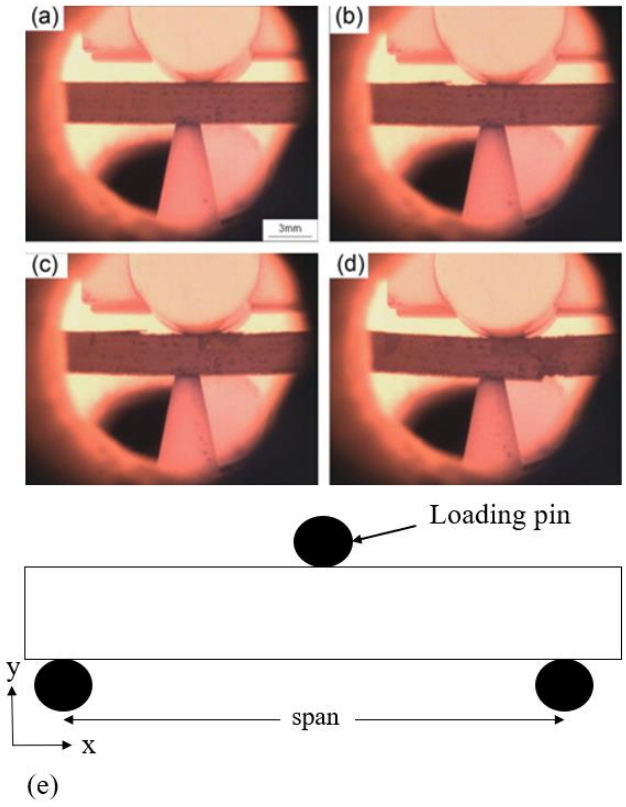

Figure 44: *Fracture process of C/SiC composites at 1400°C as a function of time: (a) t =1.0s; (b) t = 3.0s; (c) t = 4.5s; and (d) t =6.5s* [95] *(e) three point bend test setup for high temperature testing*

The shaft underneath the sample was used as an LVDT to measure beam deflection. Using this technique crack propagation was captured in real-time by using bandpass filtering method, assisting in

enhancing the understanding of material fracture at elevated temperature. Single layer silicon carbide cloth reinforced glass composites were fabricated and subjected to three point bending [96]. High temperature three point bend tests were used to quantify the flexural strength of zirconia toughened alumina (ZTA) matrix CMCs [97]. In comparison to RT the flexural strength at 1200°C was around 20% lower for both material systems.

This technique can be used to quantify the flexural modulus and the proportional limit stress of the composites under investigation. It could be used to compare the strength and modulus changes of CMCs, processed under different conditions, at high temperature. It could also be used as a technique in tandem with X-ray tomography to study the crack initiation in the microstructure at RT and elevated temperature. This technique could also be used to compare the creep behaviour of different CMCs under constant stress at elevated temperature. The biggest limitation of this technique is measuring the strain correctly. Most high temperature flexural setups would not have an LVDT hence accurate displacement measurements might not be possible.

2.4.3 Digital Image Correlation

One of the approaches used to study in-situ damage in fibrous CMCs at RT and high temperature is Digital Image Correlation (DIC). This technique studies surface displacement and strain fields developed during motion or deformation, in order to predict the failure modes in the sample. A reference image of the undeformed sample is taken along with a sequence of test images which are acquired during deformation. The DIC software splits the image into an array of subsets, with a percentage of overlap. The software is then used to maximise the cross-correlation coefficient between each subset of

the reference and the test image in order to quantify the displacement field. **Figure 45** shows the reference image with the subset size. The movement of the subset in x and y axis of the reference sample can be seen in the target image identified as the displacement vector.

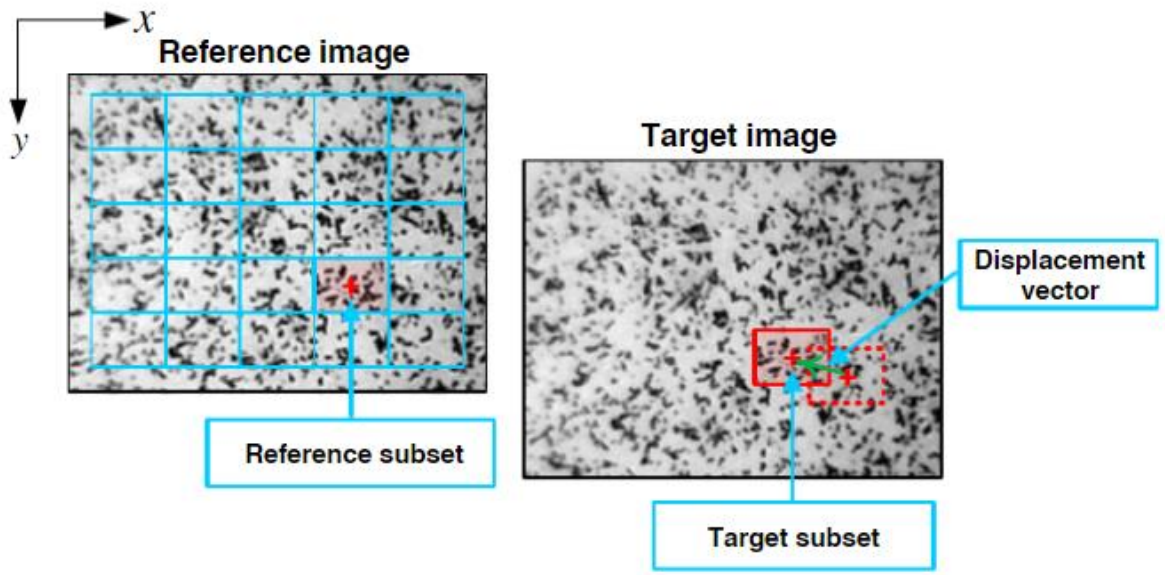

Figure 45: *The schematic illustration of the undeformed subset and the corresponding deformed subset in 2D*

In order to achieve good accuracy sources of noise need to be minimised. This is done by insure that the

- camera system is complete stationary
- no variation in lighting
- high contrast images
- randomness in speckle pattern
- Selection of the appropriate subset size

The selection of subset size is key to DIC analysis. An increase in subset size would result in better displacement resolution, which is a function of standard deviation of displacements. This has a

drawback of compromising on the spatial resolution, which is defined as the smallest resolvable displacement feature. A balance needs to be struck to ensure that the subset size gives both the optimum displacement and spatial resolution.

Jared et al. [98] used this in tandem with SEM to produce full strain field maps to characterise damage evolution from crack initiation to final failure. Being a non-contact method, DIC can be used for measuring full field deformations on the surface of the material. This is achieved by calculating the relative displacement of the features of a tracking pattern. High temperature (800ºC) tests were conducted using an FEI Quanta 3D scanning electron microscope using an in-situ stage heater. **Figure 46** [98] shows the full field quantitative maps of damage progression at 795ºC, as a crack initiates at a notch and propagates through a SiC/SiC CMC.

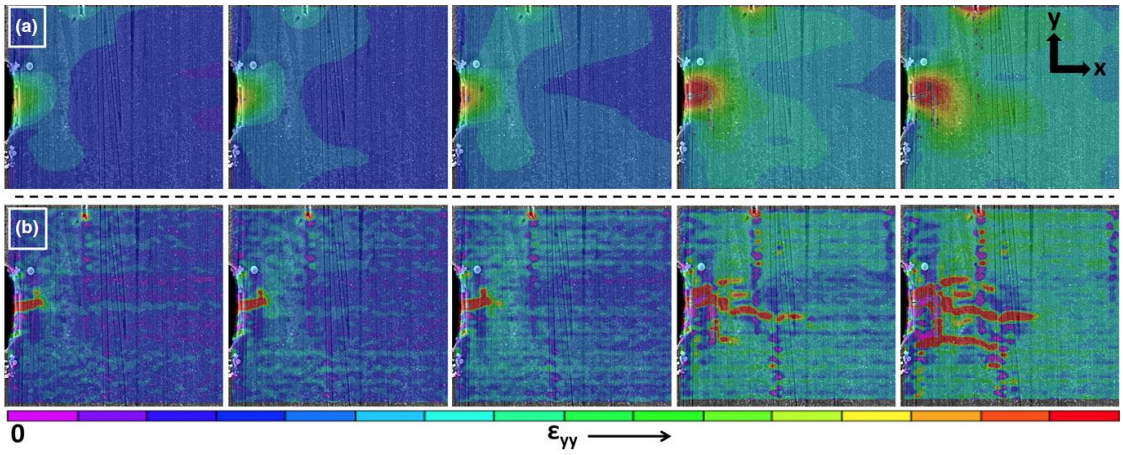

Figure 46: *Panel sequence indicates crack growth from left to right. In (a) the strain filter is 7x the subset size whereas in (b) it is 1.5x the subset size. The smaller filter does not mitigate artefacts of image noise; however, it does reveal more damage, especially the multiple cracks propagating from the crack tip* [98].

Accurate characterisation of de-bond lengths in fibrous composites can be used to determine crack bridging tractions, which in turn can be incorporated into cohesive zones. Images for DIC were captured over a field of view (FOV) consistent with three distinct length scales: (1) constituent length scale (FOV B 100um), (2) lamina length scale (FOV several hundred microns wide), and (3) laminate length scale

(FOV 1 mm) [99]. Each scale provides a unique perspective of the damage evolution in the CMCs, making the multiscale analysis essential to understand the failure patterns.

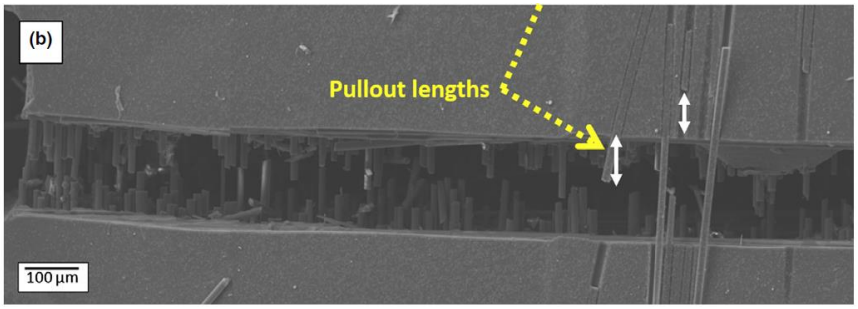

Figure 47: *SEM image of fibre pullout lengths are of similar magnitude as de-bond lengths* [98]

Mechanical tests were conducted in a miniature load frame capable of operating in an SEM **Figure 56** [99]. DIC requires a high contrast speckle pattern, accomplished using gold nanoparticles with a particle size of 30 to 150 nm. Damage assessment was focused on determining where and when cracks initiate. Indications of cracking in the thicker regions of transverse fibre coatings in un-notched tensile coupons were observed in DIC data significantly below the proportional limit [100]. **Figure 48** shows that cracking is contained to small, localised areas of fibre coatings, and the stress in each frame is smaller than the failure load. The data was used only to assess the damage areas qualitatively.

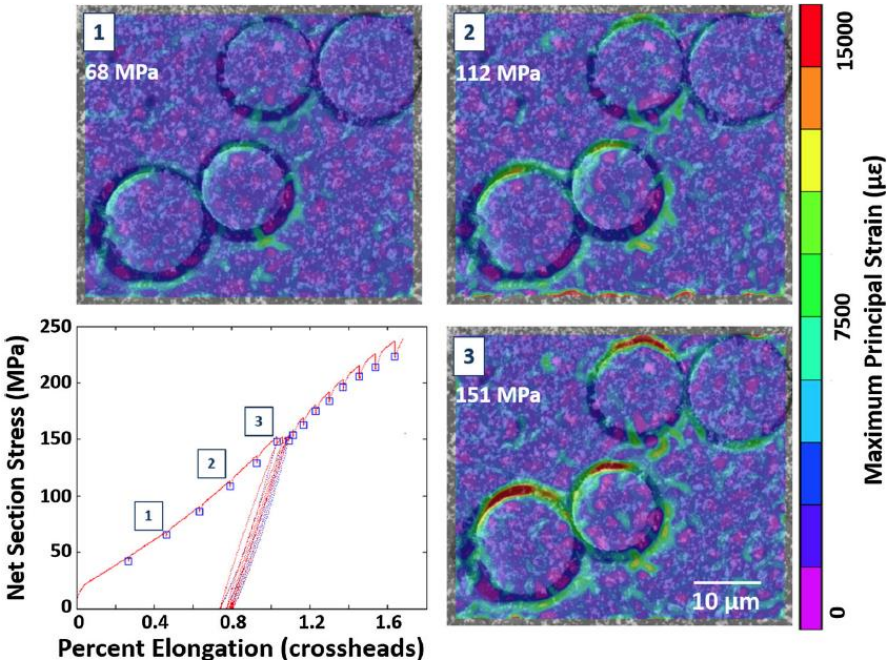

Figure 48: *Full-field maximum principal strains overlaid on SEM images of transverse SiC fibres in SiC matrix at three load increments as shown in the graph* [99].

Figure 49 shows strain localisation in transverse fibre coatings for a separate tensile coupon for which SEM images were captured at a FOV that sampled numerous fibres. It shows that strain localisations appear in the coatings of nearly every fibre, which, within each coating, are distributed primarily along the loading axis. As the applied load increased, the cracks at the fibre-coating-matrix interface grew to openings on the order of tens of nanometres.

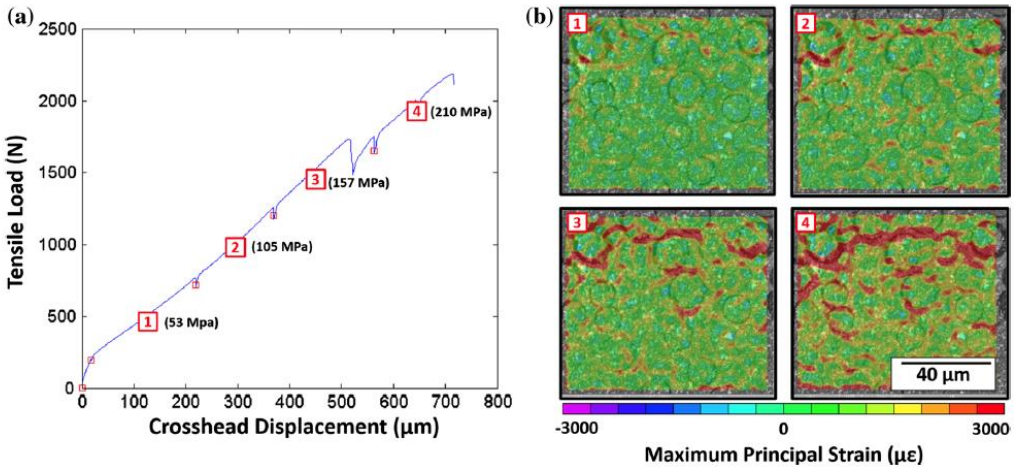

Figure 49: *Strain localisation in transverse fibre coatings for a separate test coupon where (a) is the load displacement curve (b) the maximum principal strain developing close to the fibres* [99].

Increasing the FOV although adversely affects the spatial resolution, but instead of the microstructural damage, macro-structural damage can be quantified with more clarity. At the laminate length scale, the most observable damage takes place above the proportional limit. The primary purpose of laminate-level tests was to observe the matrix crack population under mechanical loading. **Figure 50** shows the longitudinal strain fields for three separate tensile coupons loaded vertically in the plane of the page.

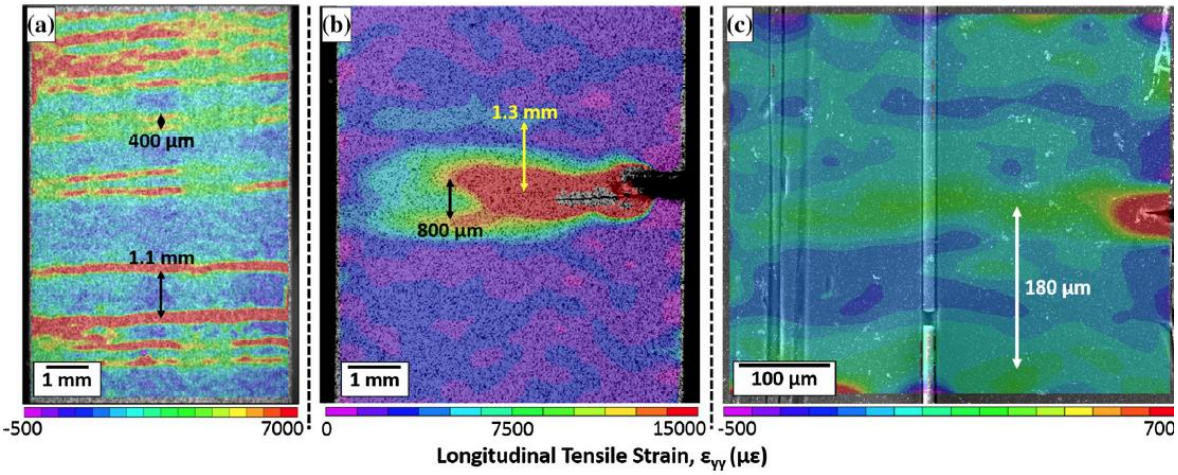

Figure 50: *Longitudinal strain fields at multiple length scales at applied stresses near the tensile strength (a) an edge-notched coupon (b) smallest resolvable crack spacing at the macroscale was 400 μm (c) shows that crack spacing can be around 180 μm* [99].

Figure 50 a and b were imaged macroscopically, whereas **c** was imaged microscopically. All three samples had the same ply structure, but **b** and **c** had edge notches. The density of macroscopically resolvable matrix cracks is greater for the un-notched sample [99]. **Figure 51** shows the comparison of the damage evaluation at the micro and the macro scale. It identifies the advantage of using multi-scale DIC in CMC applications, in order to understand the strain fields that are produced around local microstructural features. The main advantage of macroscale full-field deformation fields is that they graphically depict the evolution of large cracks over broad fields of view. In conclusion, the microscale investigations showed that damage in transverse fibre coatings occurred below the proportional limit. Damage was confined to small, localised areas of fibre coatings and mostly situated along the loading axis.

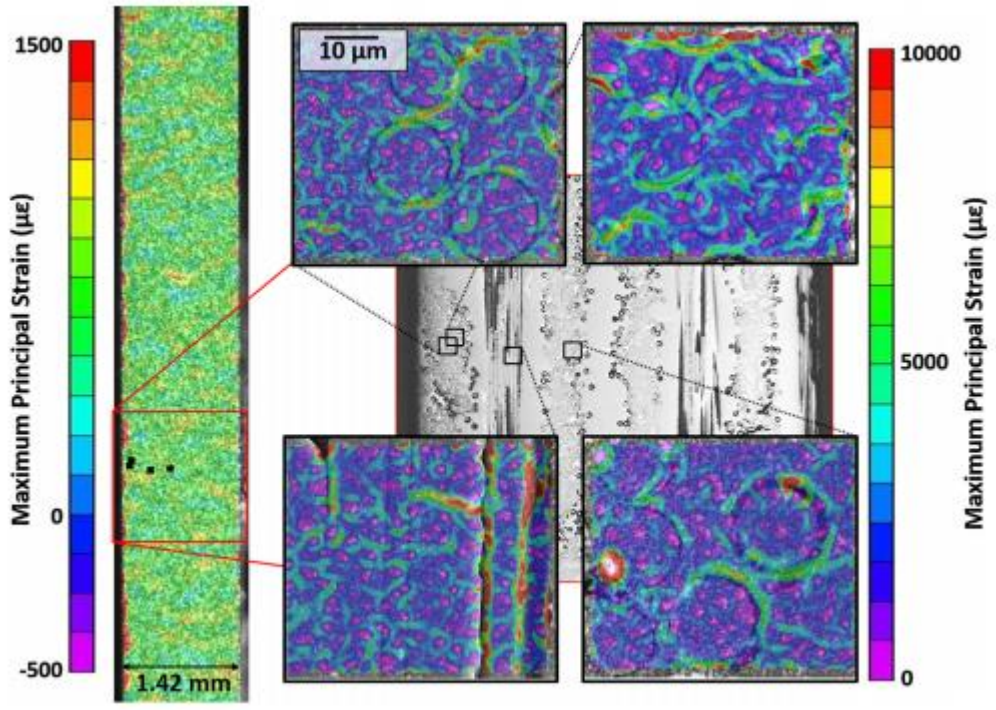

Figure 51: *Comparison of damage evolutions at microscopic and macroscopic length scales. On the left is the macro scale deformation field. On the right are four microscale deformation fields corresponding to positions on the macroscale field.*

DIC has been used as a technique to accurately quantify the elastic modulus of the specimen. The main problem with DIC surface strain which consists of both the axial strain and the bending strain caused

by the bending moment. Using 2D-DIC and dual-reflector imaging technique, which takes the two strains on the opposite surfaces can eliminate the bending strain of the specimen with initial bending moment and out of plain motion. This helps determining the elastic modulus with high measuring accuracy [101]. The DIC technique can be used at different scales, offering the capability of analysing microcracks along with understanding the fracture behaviour across a wider field of view, to understand how ceramic matrix composites interact with different stress profiles. It can be used to carry out a comparative study of different manufactured samples to see which one provides optimum crack deflection. DIC technique doesn't take into consideration the in-plane movement of the sample. This however can be overcome by rigid body moment correction.

2.4.4 Digital Volume Correlation

Digital volume correlation (DVC) is a 3D visualization technique that looks at strain development in the component whilst applying stepped loading conditions on the sample. This technique can be used to study the failure mechanisms that develop in a sample along with understanding which microstructural features act as stress concentrators under load. The results generated from X-ray tomography experiments are in the form of digital volumetric images. In-situ X-ray tomography experiments offer the opportunity to carry out further displacement analysis by comparing each volumetric dataset with a reference dataset at unloaded conditions[102]. DVC is a significantly more detailed form of DIC, which extends the 2D analysis into a 3D displacement measurement analysis [103]. The technique involves [104,105]:

I. A series of in situ volumetric images are divided into smaller grid units called correlation windows

II. The displacement in x, y and z of the correlation windows is calculated by comparing the reference image with the loaded image

III. The 3D displacement fields are converted into strain fields using differential analysis [105,106]

The choice of the correlation window size is key to the accuracy of the DVC analysis. The correlation window needs to be small enough for essential features to be resolved, whilst keeping in mind the computational time. The strain is then calculated as the change (gradient) of the displacement vectors along certain directions, hence the distribution of the localized deformation can be mapped within the entire 3D volume. **Figure 52** shows the relationship between the reference volume and the deformed volume as a function of the displacement vector.

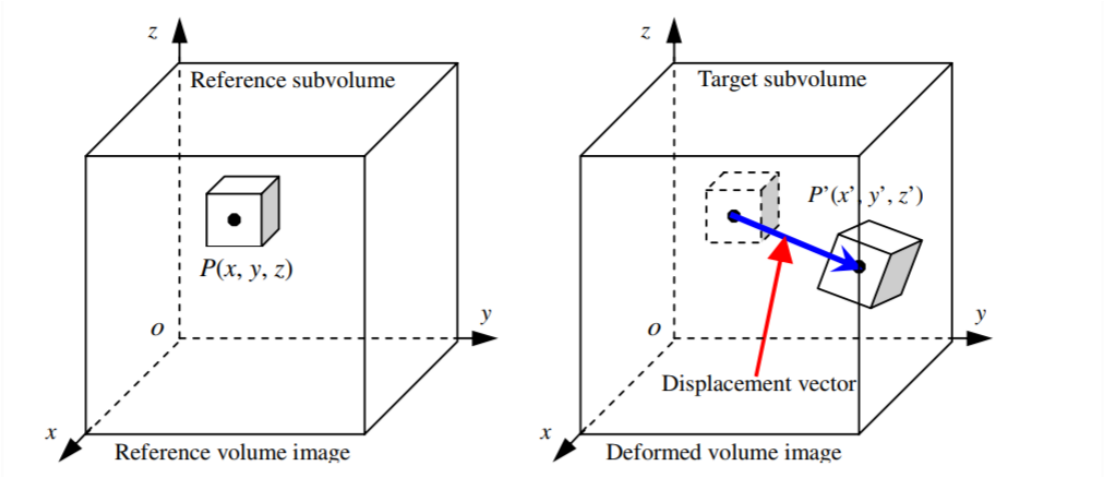

Figure 52: *Principles of DVC: the sub-volume at the position P in the reference image and tracked at P' in the deformed image; the coordinate difference between the P' and P gives the displacement vector* [107].

Vincent et al. [18] looked at the failure events taking place in a melt-infiltrated SiC/SiC composite. DVC was used to understand the damage mechanisms within the material at increasing loads. Previous studies have indicated that the matrix cracks initiate in weft tows in the matrix-rich regions [108,109]. DVC residuals were analysed at RT, as shown in **Figure 53**, to characterise the localised damage events. Initial crack propagation was observed to initiate in the *weft yarns*, which was barely visible in the

deformed tomographs, but was very visible in the corresponding residual fields. As the load increased, other cracks initiate in the crossing within the yarns and propagate into the matrix rich regions, finally merging into a thick continuous crack.

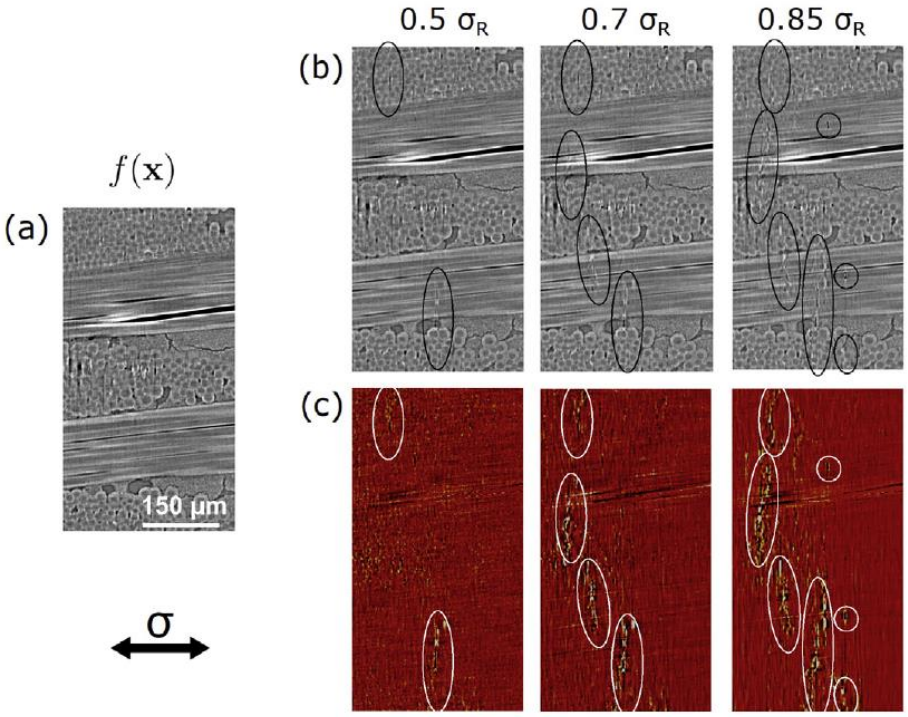

Figure 53: *mCT slice of the sample tested at room temperature; (a) reference image, (b) deformed images at several load steps corrected by a DVC displacement field and (c) the corresponding residual fields* [18].

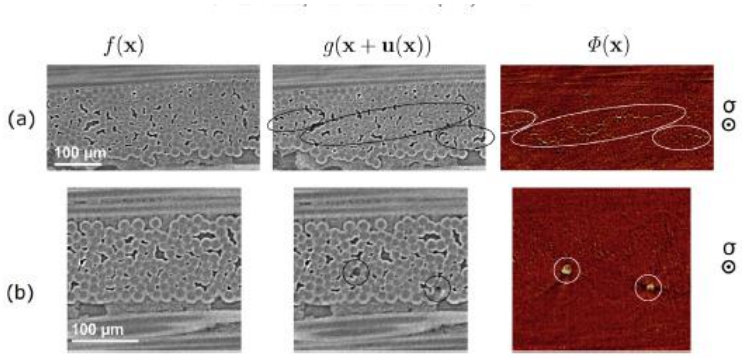

Figure 54: *µCT slices of reference images (left), deformed images corrected by a DVC displacement field (middle) and corresponding residuals (right). They show (a) debondings in longitudinal yarn (black ellipse) at 1250°C and (b) fiber failures (black ellipse) at room temperature* [18].

Debonding between the fibre and the matrix was detected at 1250°C in between the longitudinal tows in **Figure 54 a**. The residual fields offer a very good way of detecting fibre failure both at RT and elevated temperature as seen in **Figure 54**. At high temperature fibres mostly break in the main crack plane, while at room temperature they are spread over 200 mm around the crack. This has been confirmed by post-mortem SEM observations that clearly show a smoother fracture surface at 1250°C than at room temperature, which indicates limited delamination taking place at elevated temperature [18]. In both cases, the oxidising species can penetrate in the material due to the crack network at high damage level. However, the oxidation kinetics become more significant at elevated temperature [110], which results in a more brittle failure at 1250°C than at room temperature, **Figure 54**. This paper confirms a change in failure mechanism between room temperature and elevated temperature samples. Experiments were carried out at a synchrotron source using a 2KN Deben loading rig [94]. Compression along the specimen's vertical diameter produced a tensile strain on the outer surface that was sufficient to cause fracture as the load was increased under displacement control in steps to 1200N. **Figure 55** shows the displacement vectors, generated using DVC analysis, in the horizontal plane under load at 400N and 800N.

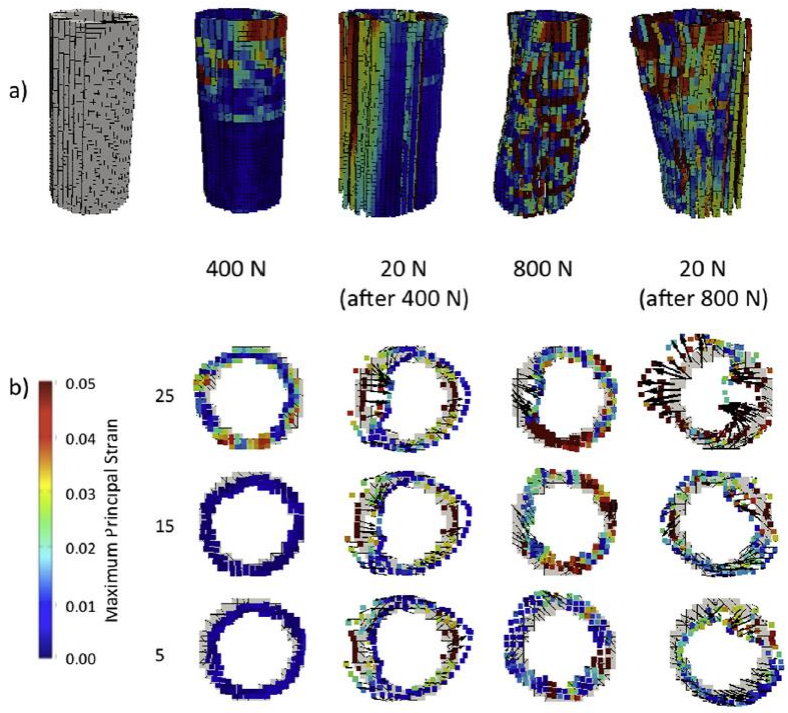

Figure 55: *Deformation of the tensile loaded tube with the magnitude of the maximum principal strain in the background (a) deformation of the tube in 3D, (b) the maximum principal strain as a 2D slice of the cross-section* [94].

The deformation is uniform at 400N, except close to the upper fixture, but as the load increased, the composite tube begins to deform non-uniformly with no recovery when the load is removed. **Figure 56** shows the 3D visualisation of the principal strain in the sample. Permanent principal strains were observed locally close to the upper fixture at 400N. As the load was increased to 800N, large amounts of principal strains developed across all of the sample, which were still present after the sample was unloaded.

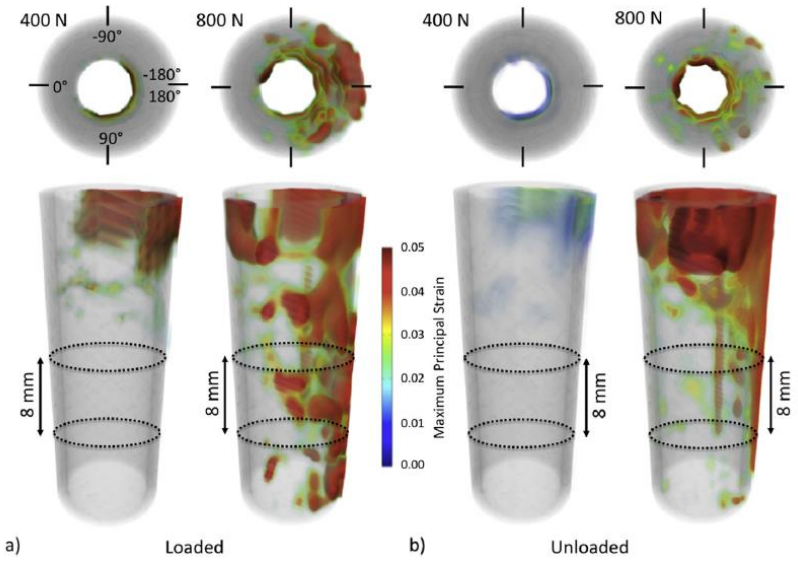

Figure 56: Visualisation with the perspective of the maximum principal strain obtained from the measured displacement fields of the tensile loaded tube [94].

The literature review carried out on DVC technique demonstrates the feasibility of using it as a tool to study damage development in both *in situ* and *ex situ* experiments. DVC can be used to measure three-dimensional deformation behavior of samples in response to different loading conditions. The maximum principal strain profile could be overlaid on the microstructure in order to identify the relationship between different microstructural features and strain concentrators. This technique could also be used to identify where permanent deformation had taken place in the microstructure after creep damage. Care must be taken to ensure a volumetric window is selected such that the relevant strain damage can be observed. If an optimized volumetric window is not selected the results could be skewed in a way that the derived conclusions could be erroneous.

2.4.5 Summary and discussion

X-ray tomography has been used extensively throughout literature to identify the formation and growth of cracks, both in-situ and ex-situ, during different loading configurations, making it ideal for this study. Imagine visualization software, such as Avizo, could be used to approximate the combined open and

closed porosity of composite samples. High temperature three-point bend tests can be used to quantify the flexural modulus and the proportional limit stress of the composites under investigation. It could be used to compare the strength and modulus of CMCs with different fibre orientations, processing temperatures and layup styles used in this study.

Digital Image Correlation DIC technique can be used at different scales, offering the capability of analysing microcracks along with understanding the fracture behaviour across a wider field of view. This helps in understanding how ceramic matrix composites interact with different stress profiles. It can be used to carry out a comparative study of different manufactured samples to see which one provides optimum crack deflection.

Digital Volume Correlation technique demonstrates the feasibility of using it as a tool to study damage development in loaded samples. DVC can measure three-dimensional deformation behavior of samples in response to different loading conditions. The maximum principal strain profile could be overlaid on the microstructure in order to identify which microstructural features act as strain concentrators. This technique could also be used to identify where permanent deformation had taken place in the microstructure after creep damage.

2.5 Conclusion

This chapter presented all the relevant literature on the two ox.ox CMC material systems being investigated in this study. The chapter looked at the manufacturing process, for both systems in detail, to understand how each step effects the mechanical and morphological properties of the system. Detailed literature review gave a picture of the parameters previously used to modify these material systems. It helped quantify the mechanical properties of these materials, and define the base values.

This chapter looked in detail at the key techniques that are extensively used in the study of ceramic matrix composites. A literature review has been carried out on these techniques to understand how they have been used previously, to understand the mechanical behaviour and visualise and characterise microstructure damage in ceramic matrix composites. Both *in situ* and *ex situ*, surface and three dimensional, techniques have been looked at as tools to quantify the deformation and damage evolution in composites. The limitations and benefits of the techniques were understood and all these techniques were used extensively in this study.

Due to lower costs, around on third that of the other Nextel fibres, work has been done on Nextel 312/SiOC systems which highlight the general trends on what effect processing temperature has on the mechanical and thermal properties of this system. Literature suggested that the processing temperature and different atmospheres directly affected the mechanical properties [60]. The higher the PIPs temperature the more thermally stable the system would be. The flexural strength decreased as the pyrolysis temperature increased, whereas tests conducted at 1000°C indicated that the samples processed in ammonia atmosphere lost around 40% of its strength in comparison to the samples processed in argon which lost around 70%. A more detailed summary of the literature review on Nextel 312 based material has been presented in Section 2.2.3.

A systematic study which could compare different PIPs processing temperatures keeping in mind the effects on the thermal stability, porosity, modulus, flexural strength, interfacial shear strength, porosity and mechanical properties of the fibre and the matrix would be useful to assess its applicability for sealing applications. Using the understanding developed after carrying out the literature review, Nextel312/SiOC material system would be optimised for long term use at 900°C. This would be done

by selecting different pyrolysis temperatures. A test matrix will be created that carries out a thorough investigation on each of the key properties that would be applicable for gas turbine sealing application.

Nextel 720 fabric has been used with three different oxide matrices currently available for high-temperature oxide CMC applications [36]: alumina, mullite and aluminosilicate, with alumina found to be stable at 1100°C. Mechanical testing carried out on Nextel 720/Mullite samples tested at room temperature (RT) and elevated temperature (1100°C) showed very similar results [19]. The orientation of the fibres played a major role on the creep resistance of the material systems at 1100°C [10]. A detailed summary of the literature review on Nextel 720 based materials have been provided in Section 2.3.3.

No work has been done till now to assess the failure mechanisms of Nextel720/Alumina material systems at the service temperatures (1100°C). The effect of processing temperature on the mechanical properties of the material system, at the service temperature, has not been studied. Very limited work has been carried out to understand the effect of different fabric types on the overall mechanical performance of these materials at service temperatures. The effect of different types of layups on the mechanical and creep performance of the systems has not been looked at in detail. No work has been done on manufacturing sealing rings from Nextel720/Alumina based material system. This study will look to address the key gaps found in literature, the results of which would then be used to manufacture sealing rings for gas turbine applications.

CHAPTER 3. Experimental Techniques

This chapter looks at different techniques used to quantify the properties and failure mechanisms of CMCs at room and elevated temperatures. The parameters used to carry out each measurement along with the details of who carried it out have also been detailed in this chapter.

3.1 Characterization techniques

This section looks at the parameters that were used to characterize samples using different visualization and measurement techniques, the results of which have been presented in later chapters 4, 5 and 6.

3.1.1 Microstructure Characterisation

3.1.1.1 Optical Microscopy

Optical microscopy of the polished Nextel720/alumina samples, prepared by polishing with 1200 grit SiC paper, then 6 µm, 3 µm, and 1 µm diamond paste, finish with 0.05 µm colloidal silica, studied in **CHAPTER 4**, were undertaken using an Olympus BX51 Metallographic Microscope, **Figure 57**. An extended depth of focus was used, which is part of the inbuilt software, to combine images in z to provide extended depth of focus. A Nomarski contrast objective lens of 10X was used in bright field

mode, with montage images obtained by image stitching using an ImageJ[1] plug-in[2]. Measurements and sample prep were carried out by the author.

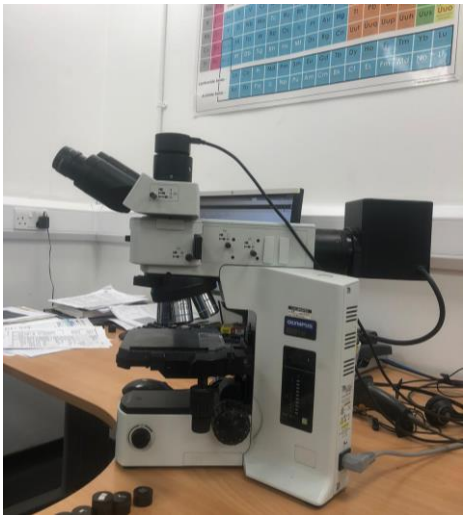

***Figure 57**: Olympus BX 51 optical microscope.*

3.1.1.2 Scanning Electron Microscopy (SEM)

The Nextel312/SiCO samples, studied in **CHAPTER 4**, were prepared by mounting in conductive epoxy resin and polishing with 1200 grit SiC paper, then 6 µm, 3 µm, and 1 µm diamond paste, and finishing with 0.05 µm colloidal silica. This was followed by ion beam polishing using a PIPS II system, **Figure 58 (a),** for 1 hr at 6 kV beam voltage and an average beam current of 0.32 µA with an argon gas flow of 0.1 cm^3 min^{-1}. It was then coating with carbon by a Q150R Plus plasma rotary pump sputter coater. This was done to prevent charging before examination in a Carl Zeiss Merlin Field Emission Scanning Electron Microscope (Carl Zeiss SMT AG), **Figure 58 (b),** at 5 kV with a probe current of

[1] Schneider, C.A., Rasband, W.S., Eliceiri, K.W. "NIH Image to ImageJ: 25 years of image analysis". *Nature Methods* 9, 671-675, 2012.

[2] ImageJ plugin: Preibisch S., Saalfeld S., Tomancak P. "Globally optimal stitching of tiled 3D microscopic image acquisitions", *Bioinformatics*, 25(11),1463-1465, 2009.

100 pA, equipped with an Xmax 150 EDX detector for elemental mapping and analysis. Measurements and sample prep were carried out by the author.

(a) (b)

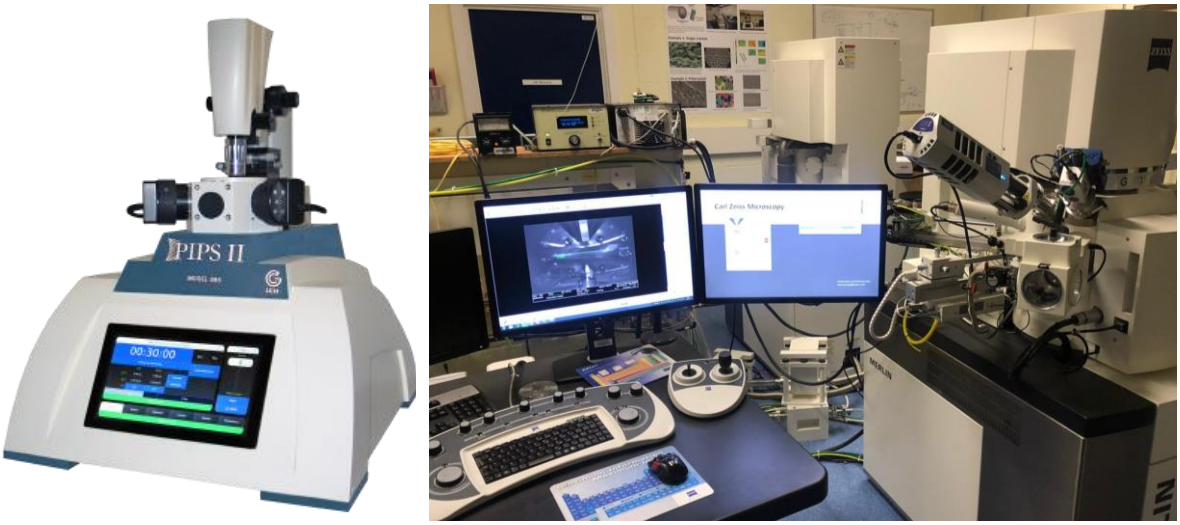

Figure 58: *(a) Gatan PIPS II polishing system and (b) Merlin Field emission microscope by Carl Zeiss.*

The fractured Nextel720/Alumina samples, studied in **CHAPTER 5**, were mounted in conductive epoxy resin and ground with 1200 grit SiC paper followed by successive 6 µm, 3 µm and 1 µm diamond paste polishing, prior to a final polish in colloidal silica (Col-K) with particle size of ~60 nm. The surface was then cleaned by a Gatan PIPS II ion polishing system for 2 hr at 6 kV beam voltage and an average beam current of 0.32 µA with an argon gas flow of 0.1 cm^3 min^{-1}. This was performed to prevent charging before examination in a Carl Zeiss Merlin Field Emission Scanning Electron Microscope (Carl Zeiss SMT AG) at 5 kV with a probe current of 100 pA. Measurements and sample prep were carried out by the author.

3.1.1.3 Transmission Electron Microscopy (TEM)

Transmission electron microscopy was carried out using a JEOL 2100 TEM, **Figure 59 (a)**, with the Nextel312/SiCO sample, studied in **CHAPTER 4**, prepared by thinning a 3 mm disk (cut using a precision saw and ultrasonic cutter) to 50 µm using manual polishing followed by ion beam milling to perforation with a Gatan 691 precision ion polishing system **Figure 59 (b)**. This was done at a beam energy setting of 3keV and a current density of 10mA/cm^2 for 3 hours. Images were obtained at an accelerating voltage of 200kV and a beam current of 105µA. Measurements and sample prep were carried out by the author.

(a) (b)

Figure 59: *(a) JEOL 2100 Transmission Electron Microscope used to carry out transmission imaging (b) Gatan 961 precision ion polishing system..*

A Tescan Lyra3 XMU Focused Ion Beam Scanning Electron Microscope (FIB-SEM) was used to make thin foils for examination of Nextel720/Alumina samples, **CHAPTER 5**, by TEM. A strip of platinum was deposited on the sample to protect the region of interest from material re-deposition during focused ion-beam milling (FIB) [111]. Trenches were cut to define the foil using a FIB voltage of 30 kV and a

current of 4 nA, then at 30 kV/1 nA for surface cleaning. Each foil, with a width of ~1 µm, was then cut free, transferred and mounted on a copper grid and then further thinned from both sides progressively to 300 nm at 30 kV/1 nA, to 100 nm at 30 kV/160 pA and then at 2 kV/20 pA to 50–60 nm thickness with the foil inclined at 2.5° from the optimal tilt angle. A polished sample, coated with carbon, was produced by the author and sent over to Czech Academy of Sciences. A JEOL 2100 TEM was used for imaging which were obtained at an accelerating voltage of 200kV and a beam current of 105µA. The Focused Ion Beam work was carried out by Ivo Šulák, at the *Institute of Physics of Materials, The Czech Academy of Sciences, Czech Republic.*

3.1.1.4 X-ray Tomography

The microstructure of the Nextel312/SiCO specimens, **CHAPTER 4**, were examined by computed tomography with an Xradia Versa 510 X-ray microscope, **Figure 60**, operated at 80 kV energy, and 7 W power. The analysed specimens were 15 mm long with a cross-section of 4 x 5 mm. Each tomograph was reconstructed from 2001 projections recorded over a 360° rotation about the specimen's longest axis, with 2x binning of the 2048 x 2048 pixel camera, to obtain an image volume with a voxel size of 3.1 μm^3. The tomographs were reconstructed (16-bit greyscale) using the Xradia software. The Avizo 9.5 image visualization software was used to quantify the observed porosity using segmentation by greyscale thresholding. Measurements and post-processing were done by the author.

Figure 60: *(a)Zeiss Xradia 510 Versa 3D X-ray tomography microscope used to carryout lab based µCT analysis (b) a ring sample loaded in a µCT holder.*

Prior to the in-situ experiments, the microstructure of a rectangular Nextel 720/Alumina specimen (15 × 4 × 5 mm), **CHAPTER 5**, was first examined with laboratory tomography using a Zeiss Xradia 510 Versa 3D x-ray microscope, operating at 80 kV energy with 7 W power. The tomograph was reconstructed from 2001 projections (11s per projection) recorded over a 360° rotation, with 2× binning of the 2048 × 2048 pixel camera, to visualise a cylindrical region of interest (~2.7 mm diameter × 2.7 mm height) at a voxel size of 2.7 × 2.7 × 2.7 μm^3. The specimen's longest dimension was parallel to the rotation axis to minimise the X-ray path length. The tomograph was reconstructed using the instrument software, and then visualised and post-processed using the Avizo software (Version 9.5.0b). Measurements and post processing were carried out by the author.

Nextel720/Alumina beams specimens of size (20 × 4 × 5 mm), were µXCT scanned, before and after creep tests, CHAPTER 6, with laboratory tomography using a Zeiss Xradia 510 Versa 3D x-ray microscope, operating at 100 kV energy with 7 W power. The tomograph was reconstructed from 2001 projections (13 seconds per projection) recorded over a 360° rotation, with 2× binning of the

2048 × 2048 pixel camera, to visualise the centre of the sample at a voxel size of 5.6 × 5.6 × 5.6 μm^3. Measurements were carried out by the author.

Nextel 720/Alumina EF 19 and EF 20 sealing ring specimens, as seen in **Figure 60 (b),** approximately 140mm in diameter, having a cross-section of size (~ 5 × 5 mm), were μXCT scanned, before and after creep tests, CHAPTER 6, with laboratory tomography using a Zeiss Xradia 510 Versa 3D x-ray microscope, operating at 100 kV energy with 7 W power. The tomograph was reconstructed from 2001 projections (14 seconds per projection) recorded over a 360° rotation, with 2× binning of the 2048 × 2048 pixel camera, to visualise a section of 20 × 5 × 5 mm at a voxel size of 6.9 × 6.9 × 6.9 μm^3 180° away from the gap. Measurements were taken of the area opposite the gap. Table 1 shows the parameters used to carry out the X-ray tomography measurements. All measurements and processing were carried out by the author.

Scans	Chapter 4	Chapter 5	Chapter 6	
			Beam specimens	Ring specimens
Voxel Size	3.1 μm^3	2.7 μm^3	5.6 μm^3	6.9 μm^3
Approximate	15 × 4 × 5 mm	2.7 × 2.7 × 2.7 mm	20 × 4 × 5 mm	20 × 5 × 5 mm
No of projections	2001	2001	2001	2001
Sample rotation	360°	360°	360°	360°
Binning	2	2	2	2
Time per projection	12s	11s	13s	14s
X-ray energy	80 KeV	80.0 KeV	100 KeV	100 KeV
Power	7W	7W	7W	7W

Data Type	16 bits	16 bits	16 bits	16 bits

Table 7 *Summary of the scanning parameters used for lab based XCT*

3.1.1.5 Elevated Temperature Tomography

In situ x-ray tomography experiments, **CHAPTER 5**, were conducted at beamline 8.3.2 on the Advanced Light Source, at the U.S. Lawrence Berkeley National Laboratory [112]. During the experiments, a unique device (**Figure 61**) that permits mechanical loading at elevated temperatures was used [113]; details of the device are found in the following reference [114]. Its central part is an aluminium chamber (~150 mm in diameter) where the heating is provided by six ellipsoidal 150 W halogen lamps which illuminate a uniform hot zone region (~0.5 cm^3). The test specimen was positioned in the hot zone, and in line with a 300 µm thick aluminium window to allow X-ray transmission from the source (white beam, 6 - 43 keV) to the detector. The field of view on the detector (PCO Edge 2× CCD camera, 2560 × 2560 pixels) was 8 × 4 mm (voxel size: 3.25 μm^3); for higher resolution characterisation, it was reduced to 3.2 × 2.6 mm (voxel size: 1.3 μm^3). Rectangular beam specimens, with dimensions of approximately 4 × 5 × 20 mm were tested at the lower resolution, with dimensions of 1.75 × 1.75 × 20 mm at the higher resolution. These were loaded using a three-point bending configuration with a 16 mm span (the diameter of the loading rollers was 3 mm).

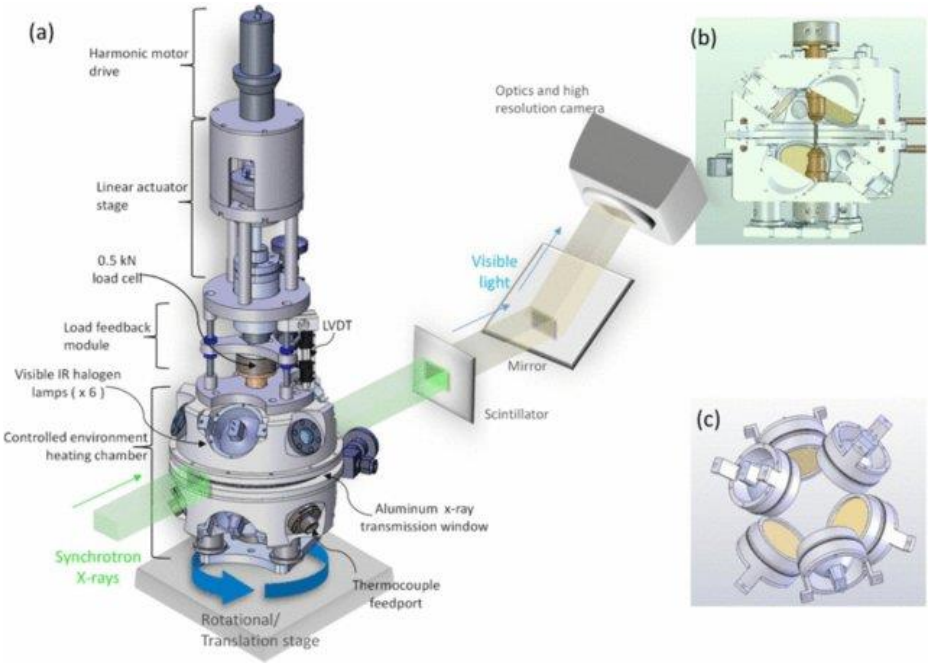

Figure 61: *(a) Schematic of in situ tension/compression test rig. (b) Cross sectional view of heating chamber with a view of the test sample along with the halogen heat lamps (c) The location of the six halogen lamps in the loading chamber* [114].

Tests were conducted at two temperatures: RT (nominally 25°C) and 1100°C. Two samples were tested at each temperature, with one of these observed by tomography for RT at 3.25 µm voxel size. Two samples observed by tomography for 1100°C at two different voxel sizes: Sample S1 was imaged at 3.25 μm^3 voxel size, and Sample S2 was imaged at 1.3 μm^3 voxel size. A thermocouple was placed in contact with the side of the sample to control the temperature via the lamp current. For each *in situ* tomographed sample, several scans were performed from the pre-load (effectively load-free) condition until fracture. In each scan, 1969 projections were collected over a rotation of 180°, with an acquisition time of 30 ms for each projection. The reconstruction was performed using the Gridrec algorithm [115] with the centre of rotation of each scan individually identified. This was necessary to eliminate artefacts caused by deformation, especially for the elongated vertically oriented samples under bending. Conventional flat field correction was used to normalise the acquired projection images to reduce the detector's fixed pattern noise. The experiment was designed by the author, along

with producing all the samples that were used in this experiment. The experiment itself along with the image reconstruction was carried out by Dr. Dong Liu, School of Physics, University of Bristol, UK.

3.1.1.6 Digital Image Correlation (DIC) with 3 point bend test

Digital Image Correlation was carried out in tandem with three point bend test sample using a Shimadzu universal testing frame with a 5 kN load cell, CHAPTER 4. Each specimen was tested in the 0°/90° ply orientation with the 0° fibres aligned in the longitudinal direction. The specimen thickness and width were nominally 5 mm and 4 mm, measured to ±0.01 mm. The span was 60 mm with loading and supporting pin diameters of 4 mm. A displacement rate of 0.1 mm min^{-1} was used.

A single camera optical system was used to observe the specimens during the bend tests, with an image pixel size of 6 μm and a 15 x 18 mm field of view centred on the central loading pin. Each specimen was prepared by first coating the surface with Hycote matt white paint, which was then sprayed with a very fine speckle pattern of acrylic black ink, diluted with acetone and applied with an airbrush from a distance of 50 cm to achieve an average speckle size around 1-10 μm. The images, recorded at a frequency of 1 Hz, were processed with the LaVision Davis 8.3.1 digital image correlation software using the least square and time series approximation methods. A final subset size of 40 pixels was selected along with a step size of 5. Sample preparation, measurements and processing were carried out by the author.

3.1.1.7 Digital Volume Correlation

Digital volume correlation was carried out using LaVision DaVis software, version 8.4.0, using direct correlation procedure, with an upgraded workstation, OUMS-ARES, with 512 GB memory and an Intel Xeon E5-2699 processor. The software works by creating subset which are then processed in accordance to the reference scan and loaded scan. A few techniques can be used to increase the resolution of the processed data. Overlapping interrogation subsets can result in improving the spatial resolution by smoothening the changing fields. Although a smaller subset size might offer better resolution, it comes at the cost of increasing noise. This could be overcome by either using a larger interrogation window or by increasing the number of passes per subset size. A sequence of overlapping, number of passes and subset sizes are selected in order to optimize the precision and spatial resolution of each displacement field dataset. In order to check if the DVC analysis has been able to resolve the displacement fields successfully, the correlation coefficient of the analysed data is looked at. A correlation coefficient of 0.8 or above indicates that the error present in the calculated displacement only minutely affect the displacement measurements, **Figure 62**.

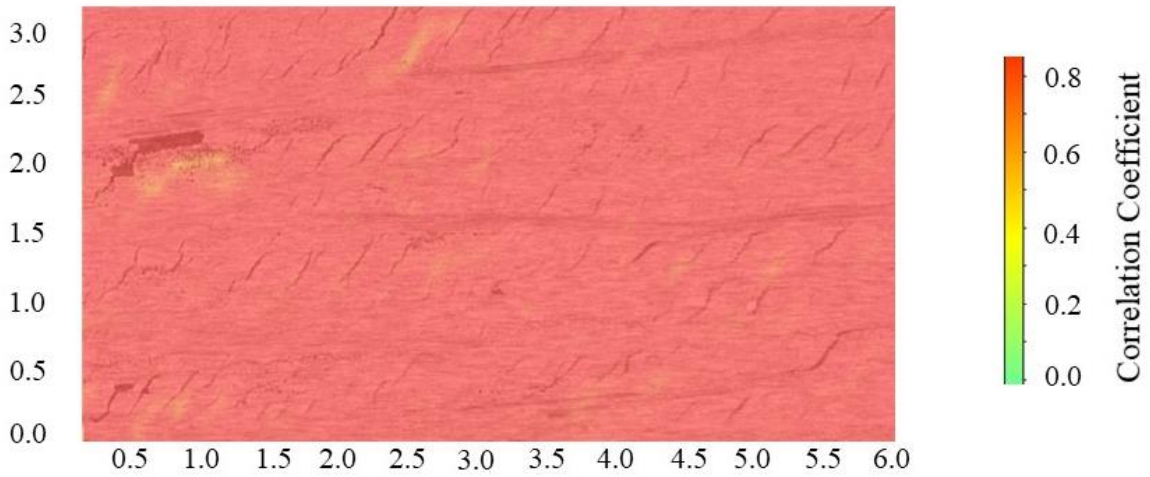

***Figure 62**: The correlation coefficient value of 0.8 present across the sample. A value lower than 0.8 would suggest a high error in the DVC calculated displacements.*

DVC of the synchrotron X-ray tomographs, **CHAPTER 5**, was carried out with the LaVision DaVis software (version 8.3.1) using the Direct Correlation procedure and the pre-loaded tomograph as reference. The analysis of loaded tomographs from the room temperature experiment and the 1100°C sample S1 was carried out with a final subset size of 32 × 32 × 32 voxels (*i.e.*, 32^3) at 75% overlap, using the pre-load tomograph as reference, after two passes each at successive cubic subset dimensions of 256^3, 128^3, 64^3 and 32^3 voxels. For the sample S2 tested at 1100°C, it was necessary to carry out the DVC analysis only to a larger subset size of 64^3 voxels at 75% overlap to reduce the noise that is inherent at smaller subset sizes. Post-processing of the three-dimensional displacement fields was performed using Matlab (Version 2017a).

Lab based X-ray tomography was used to carry out DVC of the beam samples, creep tested in three-point bend configuration at constant stress, **CHAPTER 6**, with LaVision DaVis software (version 8.3.1) using the Direct Correlation procedure. Datasets of pre- and post-creep tests were first registered using visual matching in x, y and z axes. This was followed by a rigid body moment correction process performed in the LaVision Davis 8.4 software. This involved carrying out an initial DVC analysis with a large interrogation subset size, 128x64x64 with a 50% overlap, and rotating one of the datasets using precise rotational angles obtained by this analysis. This was followed by carrying out digital image correlation analysis at a final subset size of 20x20x20 with 70% overlap for 2 passes, where the pre-creep test was taken as the reference scan and compared with the post-creep test scan

Lab based X-ray tomography was used to carry out digital volume correlation (DVC) of the two sealing ring samples, creep tested in constant deflection configuration (Chapter 6) with LaVision DaVis software (version 8.3.1) using the Direct Correlation procedure. The analysis of the crept sample was

carried out with a final subset size of 20 × 20 × 20 voxels (*i.e.*, 20^3) at 75% overlap, using the pre-crept tomograph as reference, after two passes each at successive cubic subset dimensions of 64^3, 48^3, $36^3$and 20^3 voxels. 3D visualisation and segmentation were subsequently undertaken using Avizo.

A summary of the parameters used to carry out DVC analysis have been presented in the **Table 8**. All DVC and Avizo post processing was carried out by the author of this thesis.

DVC Analysis	Chapter 5		Chapter 6	
	RT and S1 beam specimens	S2 beam specimen	Beam specimens	Ring specimens
Subset size	256^3, 128^3, 64^3 and 32^3 voxels	64^3	64^3, 48^3, $36^3$and 20^3 voxels	64^3, 48^3, $36^3$and 20^3 voxels
Number of passes	2 passes at each subset size	2 passes at each subset size	2 passes at each subset size	2 passes at each subset size
overlap	75%	75%	75%	75%

Table 8: *Summary of the parameters used to carry out the DVC analysis*

3.1.1.8 Thermo-gravimetric analysis

Thermo-gravimetric analysis was carried out in an open alumina pan under a constant flow of air at 20 ml min^{-1} using a Perkin Elmer Pyris 1 TG/DTA instrument, **Figure 63**. The Nextel312/SiCO specimens, **CHAPTER 4**, were each approximately 15 mg of material (measurement precision 0.005 mg) and were heated from 30°C to 975°C at a rate of 3°C min^{-1}. The measurements were carried out by **Nicola Flanagan,** Oxford Materials Characterisation Service, University of Oxford.

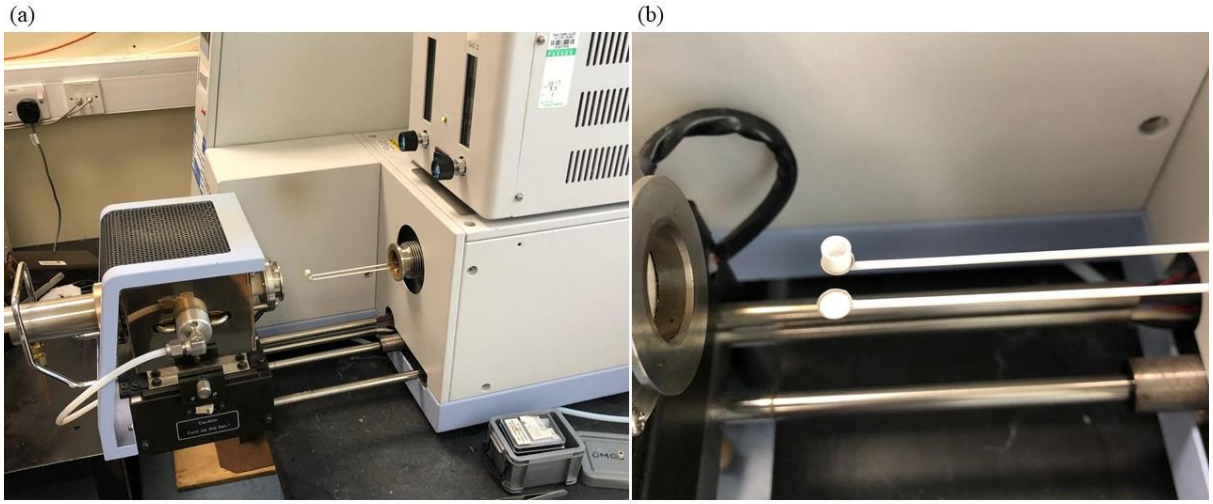

Figure 63: *(a) Perkin Elmer Pyris thermo-gravimetric analysis machine used to carry out the gravimetric measurements (b) the crucible that contains the sample to be tested.*

3.1.1.9 X-ray Diffraction (XRD)

X-ray diffraction (XRD) analysis was performed on powdered Nextel312/SiCO specimens, **CHAPTER 4**, using a Bruker D8 ADVANCE eco powder diffractometer employing copper K_α radiation (λ=0.15406 nm) and a LYNXEYE XE detector. Each specimen was continuously spun during data collection and scanned using a step size of 0.02° (2θ) over the range of 10°-80° (2θ) at ~0.5° min^{-1}, with the baseline subtracted from the raw data to define the characteristic peaks. The measurements were carried out by **Dr Phil Holdway,** Oxford Materials Characterisation Service, University of Oxford.

A JEOL 2100F STEM (200 kV) system with point-to-point resolution of 0.23 nm was used for observations of Nextel720/alumina samples, **CHAPTER 5**, in both bright field (BF) and annular dark field (DF-HAADF) STEM modes (2048 × 2048 pixels at 30 µs per pixel). Diffraction images of fibres sectioned in both longitudinal and transverse directions from the room temperature sample were obtained using a camera length of 800 mm. The polished sample used to produce the lamillas was produced by the author. The lamillas were then produced at the Czech Academy of Sciences and the

diffraction measurements were carried out by Ivo Šulák**,** *Institute of Physics of Materials, The Czech Academy of Sciences, Czech Republic*.

3.1.2 Mechanical Testing

3.1.2.1 Three-point flexural bend tests

Three-point flexural bend tests were performed on Nextel312/SiCO samples, **CHAPTER 4**, using a Shimadzu universal testing frame with a 5 kN load cell. Each specimen was tested in the 0°/90° ply orientation with the 0° fibres aligned in the longitudinal direction. The specimen thickness and width were nominally 5 mm and 4 mm, measured to ±0.01 mm. The span was 60 mm with loading and supporting pin diameters of 4 mm. A displacement rate of 0.1 mm min^{-1} was used. Three specimens from each sample material were tested. Measurements were carried out by the author.

3.1.2.2 Micromechanical testing

Nano-indentations were performed using a Berkovich tip on a Nano-indenter XP (Agilent Technologies, USA), **Figure 64**. The Nextel312/SiCO specimens, **CHAPTER 4**, were polished to sub-micron level using diamond polishing media followed by colloidal silica, then ultra-sonicated in an acetone bath for 10 minutes before attachment to an aluminium stub with Crystalbond™ adhesive. A nano-indenter penetration depth of 800 nm was selected for the matrix, and a penetration depth of 200 nm was selected for the fibres due to their smaller dimension. An average of 40 indents were made in both fibres and matrix for each material. These measurements were carried out by the author of this thesis.

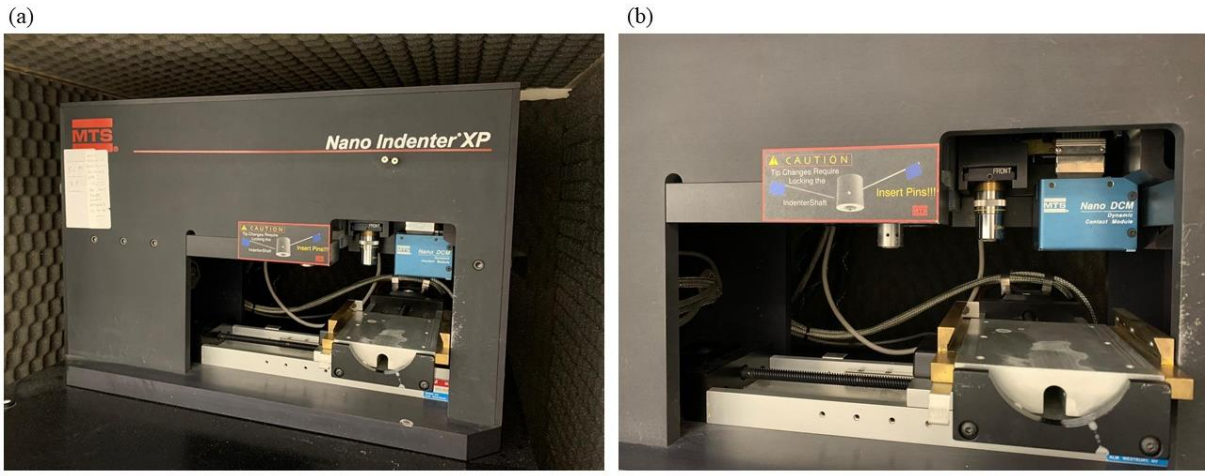

***Figure 64**: (a) Nano-indenter XP (Agile technologies, USA) with a Berkovich tip, used to carry out nano indentation on the fibre and the matrix (b) a picture of the stage used to mount the sample.*

Nextel 312/SiCO specimens, **CHAPTER 4**, for fibre pushout tests were ground to an average thickness of 200 µm, polished on both sides to sub-micron level using diamond polishing media followed by colloidal silica and then ultra-sonicated in an acetone bath (10 minutes duration) followed by two ethanol baths (5 minutes duration each) to remove surface wax that had been used to fix the specimens during polishing. The specimens were then attached with minimal amount of wax to a holder [116] that was designed to enable pushout without bending of the test specimen. The pushout tests used a NanoG200 nano-indentation instrument, **Figure 65**, equipped with a 40x objective lens and a 5 µm radius flat-tip punch that could achieve a maximum pushout displacement of 6 µm. 15 measurements of the cross-section of the fibre were made using a Carl Zeiss Merlin Field Emission Scanning Electron Microscope (Carl Zeiss SMT AG) to determine its dimensions. The average fibre dimensions were calculated with a fibre thickness of 6.5µm and a fibre width of 10.5µm. Measurements of the specimen cross-sectional thickness was carried out using a micrometre. Sample prep was done by the author of the thesis. Measurements were carried out by Robin De Meyere, Department of Materials, University of Oxford.

(a) (b)

Figure 65: *(a) Nano G200 nano-indentation instrument was used with a flat-tip punch to carry out fiber pushout tests (b) stage used to mount the sample*

3.1.2.3 High temperature three-point bend tests

Three-point bend tests were performed, at the Department of Engineering, Imperial College London, using a custom-built rig consisting of a 25 kN universal test frame (Instron) and a tungsten-element vacuum furnace (Materials Research Furnaces Inc.), **Figure 66**. The vacuum was maintained at $<5x10^{-4}$ torr with a Varian Agilent DS102 rotary vacuum pump. The sample was placed between graphite push rods, with SiC spacers either side of it to prevent any sample-push rod reaction. The spacers were sprayed with hexagonal BN to minimise friction. Samples were heated at 20 °C min^{-1} to the test temperature and held isothermally for 10 min to allow the furnace to reach thermal equilibrium.

Testing modes

Constant strain mode (Flexural strength test)

Nextel720/Alumina cmc samples, **CHAPTER 5**, were loaded to 20N and put under vacuum after which a ramp up rate of 15°C per minute was used to heat the sample to 1100°C. A load of 20N was applied

on the sample to hold it in place. Once the sample was at 1100°C a ramp rate of 0.05mm/min was used to perform the flexural test.

Constant Stress mode (Creep test)

Nextel720/Alumina cmc samples, CHAPTER 6, were put under a preload of 20N under vacuum and heated to 1100°C using a ramp rate of 15°C/min. A stress of 25MPa was then applied on to the sample over a period of 2 minutes. The sample was then kept under constant stress with an increase in strain measured over a period of 120 minutes. After 120 minutes the load was ramped down to 10N over a period of 60 seconds. In both configurations the samples were cooled down to 10°C using a ramp rate of 60°C/minute. Measurements were carried out by the author.

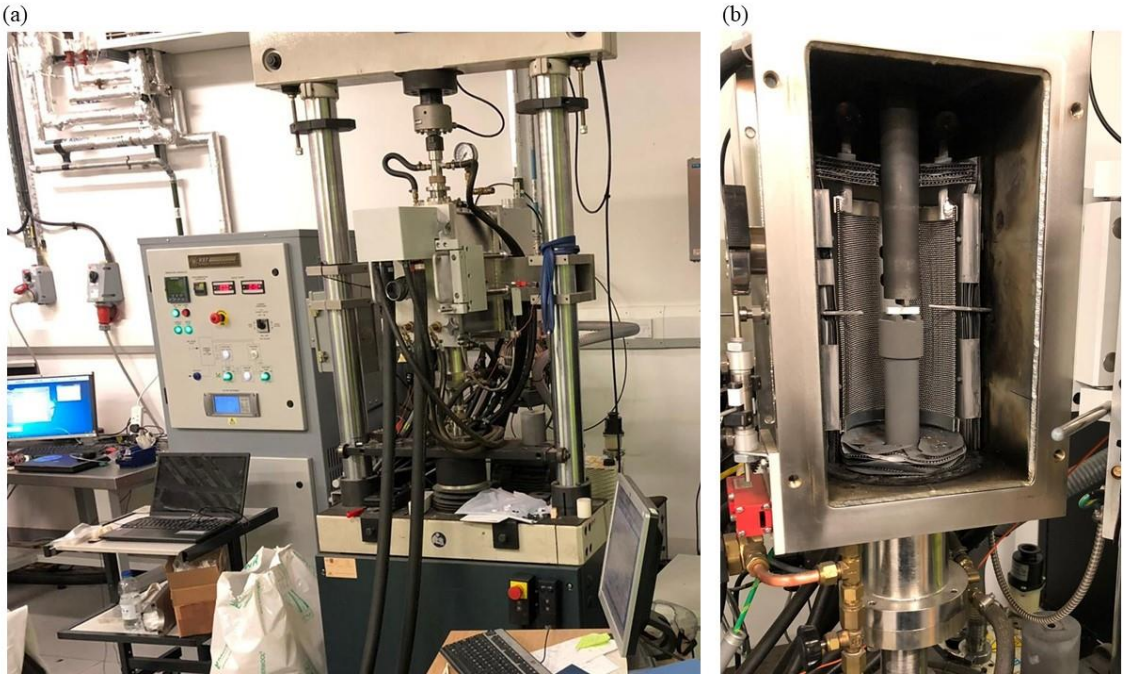

Figure 66: *(a) 25KN Instron universal frame, with a tungsten-element vacuum used to carry out high temperature three-point bend tests (b) the three point bend test setup with the sample in the test condition.*

3.1.2.4 Stress relaxation ring tests

Stress relaxation tests were performed by loading a 140mm diameter ring, CHAPTER 6, in a ceramic, Al_2O_3, pot and heating up to 1100°C in a LH 15/12 – LF 120/14 chamber furnace. At each time interval

the free and fitted gap of the ring was measured using a shadowgraph, Starrett HB400 Shadowgraph, **Figure 67**, with a machine accuracy of 0.254 µm and a measurement accuracy of 2.5 µm. The ring was placed square into the ring gauge and clamped to the shadowgraph. The gap of the ring was aligned with the measuring plane and measured at a height (radial distance) of 250 µm from the outer diameter (O/D) of the ring to give a result for the fitted gap size. The process was repeated with the ring in free state (not in gauge) to obtain the free gap result. Measurements were carried out by the author.

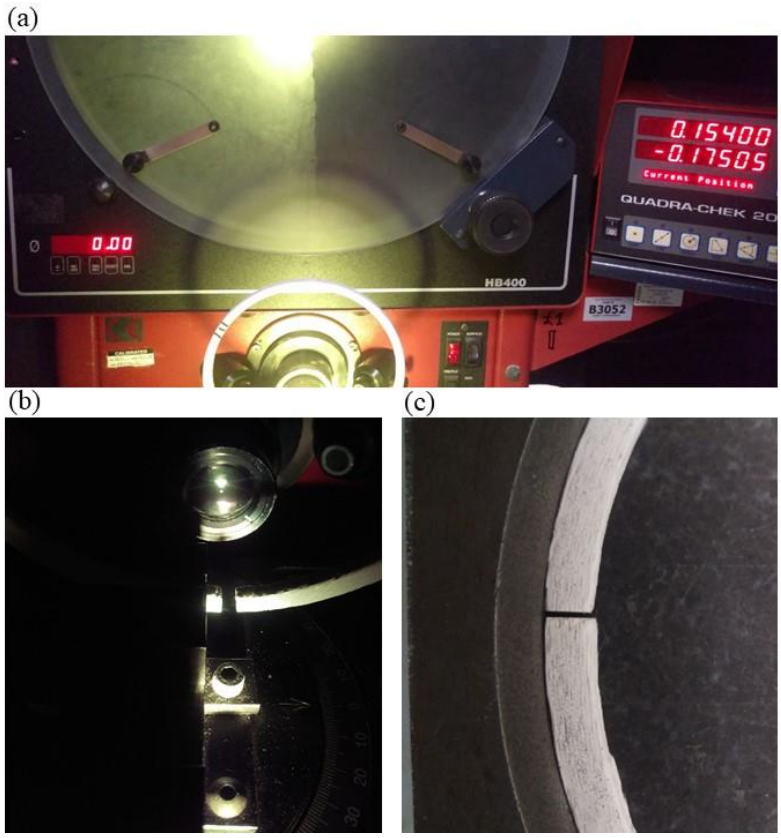

Figure 67: *(a)Starrett HB400 Shadowgraph used to carry out measurements of free and fitted gap (b) the gap in its free condition (c) the gap in its fitted condition.*

Load measurements were carried out on the ring using a Mecmesin multitest 2.5-i load testing machine **Figure 68 (a)** [117]. The ring was closed to the gauge diameter and load measurements were carried out using a 250N load cell. Care was taken to ensure that the gap was at 0°. Five measurements were

carried out on each ring and averaged to get the final value. Measurements were carried out by the author.

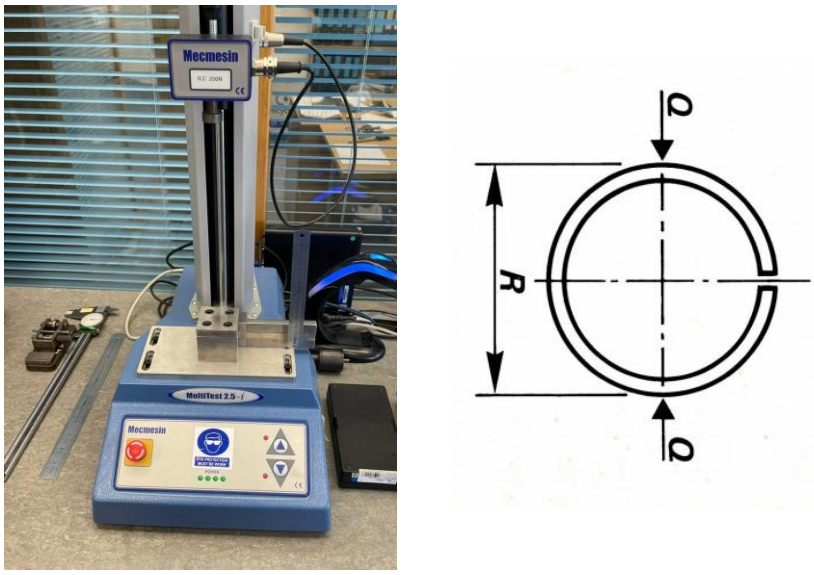

(a) (b)

Figure 68: *The setup used to carry out load measurements (a) the Mecmesin load testing machine (b) the ring in its closed condition where R is the gauge diameter and Q is the force required to keep it at gauge diameter* [117].

3.2 Summary

The chapter provides the parameters used to carry out measurements for each characterization technique used in this study, the results of which have been presented in Chapter 4, 5 and 6. The chapter presents all the techniques from literature review that were found relevant to understand the material systems in this thesis.

The chapter has been divided into two sections. The first section looks at the techniques used to carry out microstructural characterisation which could give an in depth understanding of effects of the layup and processing parameters on the microstructure. This included not only understanding the microstructure in 2D and 3D, it also looked at X-ray diffraction characterisation along with studying the thermal stability of the systems.

Mechanical characterisation was also carried out on the samples. Three-point bend tests were carried out to quantify the bulk flexural strength and modulus of different composites. Micromechanical testing was carried out in order to quantify the properties of the fibre, matrix and the interface separately. High temperature mechanical properties are critical for understanding how the system will behave in service conditions. Hence high temperature 3-point bend tests were carried out to quantify the flexural properties of the system. Creep tests were carried out by applying a constant load at temperature and measuring time dependant strain development in the sample. The results were used to compare the high temperature performance of different configurations to see which weave style and sintering temperature provided the least amount of plastic strain under loading. X-ray tomography was carried out in tandem with the creep tests to identify which microstructural feature acted as stress concentrator. Stress relaxation tests were carried out at 1100°C on sealing rings, produced using Nextel 720/Alumina fabric, to study their high temperature performance. X-ray tomography was used through the mechanical testing to understand how strain developed within the microstructure under load and/or temperature.

CHAPTER 4. Effects of polymer infiltration processing (PIP) temperature on the mechanical and thermal properties of Nextel 312 Fibre SiCO ceramic matrix composites

4.1 Introduction

To satisfy seal design requirements at high temperature, an oxide based ceramic matrix composite (Ox-CMC) has been proposed that is composed of Nextel 312 fibre with a SiCO matrix [20]. The fibres have a boron nitride (BN) coating, which is obtained by exposure of the fibres to an ammonia atmosphere at high temperature [57].

This chapter looks at optimising Nextel 312/SiCO composites for sealing applications at service temperatures up to 900°C, using repeated matrix impregnation and pyrolysis (polymer infiltration processing, PIP). The effects of the polymer infiltration temperature on the mechanical, morphological and thermal properties will be studied. The microstructures will be analysed using SEM, TEM, XRD and X-ray computed tomography in order to quantify the differences arising from the manufacturing process. The materials will be tested mechanically to determine their strength, ductility and fracture behaviour. Nano indentation will be used to quantify the elastic modulus and hardness of the fibre and the matrix, and micro-mechanical fibre pushout tests will be performed to measure the interfacial shear strength. The thermal stability of the composites will be investigated using thermo-gravimetric analysis (TGA).

The objective is to identify the PIP temperature that could provide the optimum combination of properties of high elastic flexural deflection, thermal stability, low interfacial shear stress for toughening and low mass loss up to the intended service temperature. Future studies may examine the

gas permeability of these material systems, long term exposure at operating temperature and the effects of mechanical damage on this.

4.2 Materials and Methods

4.2.1 Material Processing

The manufactured composites were composed of Nextel 312 fibre, woven in an 5-harness satin weave structure, **Figure 69 (a)**, AF-20, with a denier size of 1800 [118] and a layer thickness of 0.53mm, with SiCO matrix and a boron nitride (BN) interface. **Figure 69 (b)** shows the cross-section of thickness 5 mm. The sample has 8 layers in total, 4 orientated at 0° and 4 orientated at 90°. The fibre coating of BN was achieved by diffusing boron, from the boria (B_2O_3) that inherent within Nextel 312, to the fibre surface by heating the fibres in an ammonia atmosphere at temperature above 1000°C. A pre-ceramic slurry of polycarbosiloxane, with highly doped silicon carbide sub-micron particulates as filler material, was then impregnated into the fabric to create a prepreg. The prepreg fabric was laid out in a 0°/90° composite stack and autoclave cured at 825 kPa and a temperature between 150-200°C for 240 minutes. All processing was done in an argon atmosphere.

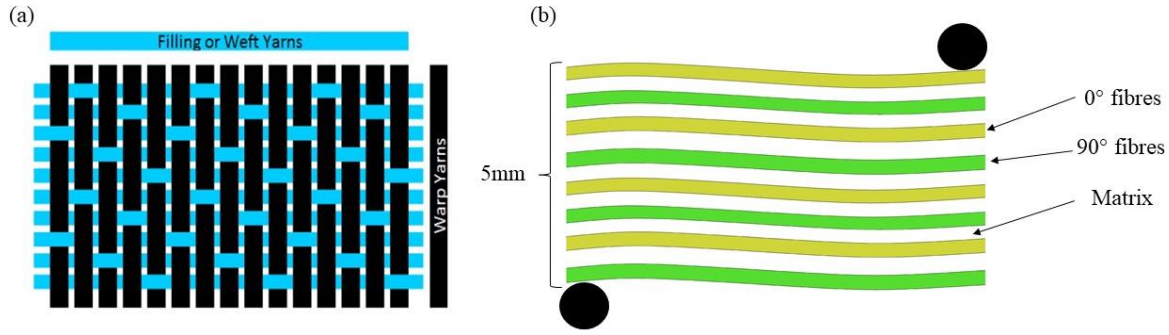

Figure 69: *(a) 5 Harness Satin weave (b) layup of the composite with 0° and 90° layers labelled*

Pyrolysis, to convert the green-state polymer into a silicon oxi-carbide matrix by thermal transition of the polycarbosiloxane, was performed at temperatures between 850°C and 1050°C under protection of an argon atmosphere. Each cycle of reimpregnation of the porous matrix was carried out in vacuum (75 kPa) and ambient temperature. In addition to the initial pyrolysis, each material was subjected to five additional infiltration-densification cycles (**Table 9**) to produce four sample materials for testing and characterisation.

Sample Number	Manufacturing Parameters
1	6 x PIP at 850°C
2	6 x PIP at 950°C
3	6 x PIP at 1050°C
4	5 x PIP at 950°C then 1 x PIP at 1050°C

Table 9: *Summary of the manufacturing parameters for the four sample materials.*

4.3 Results

4.3.1 Microstructure Characterisation

Figure 70 presents SEM images of the overall structure of the material and shows the 0° and 90° fibre tows within the matrix. Details of the measuring parameters have been presented in section **3.1.1.2**. The microstructures of all four samples are indistinguishable, hence only example images for sample 1 are shown. Matrix defects (pores with a size of approximately 200 µm) are observed (**Figure 70a**). The fibre bundles are embedded in the matrix, which tends to be crack orthogonally to the fibre layers. Individual fibres have an elliptical cross-section, oriented at various angles within the fibre bundles (**Figure 70b**). TEM imaging (**Figure 70c**) reveals the 30-40 nm thick BN interface between the matrix

and the fibre. The matrix also contains nano-particles, similar in appearance to those identified in the literature as SiC [58], as expected from the processing.

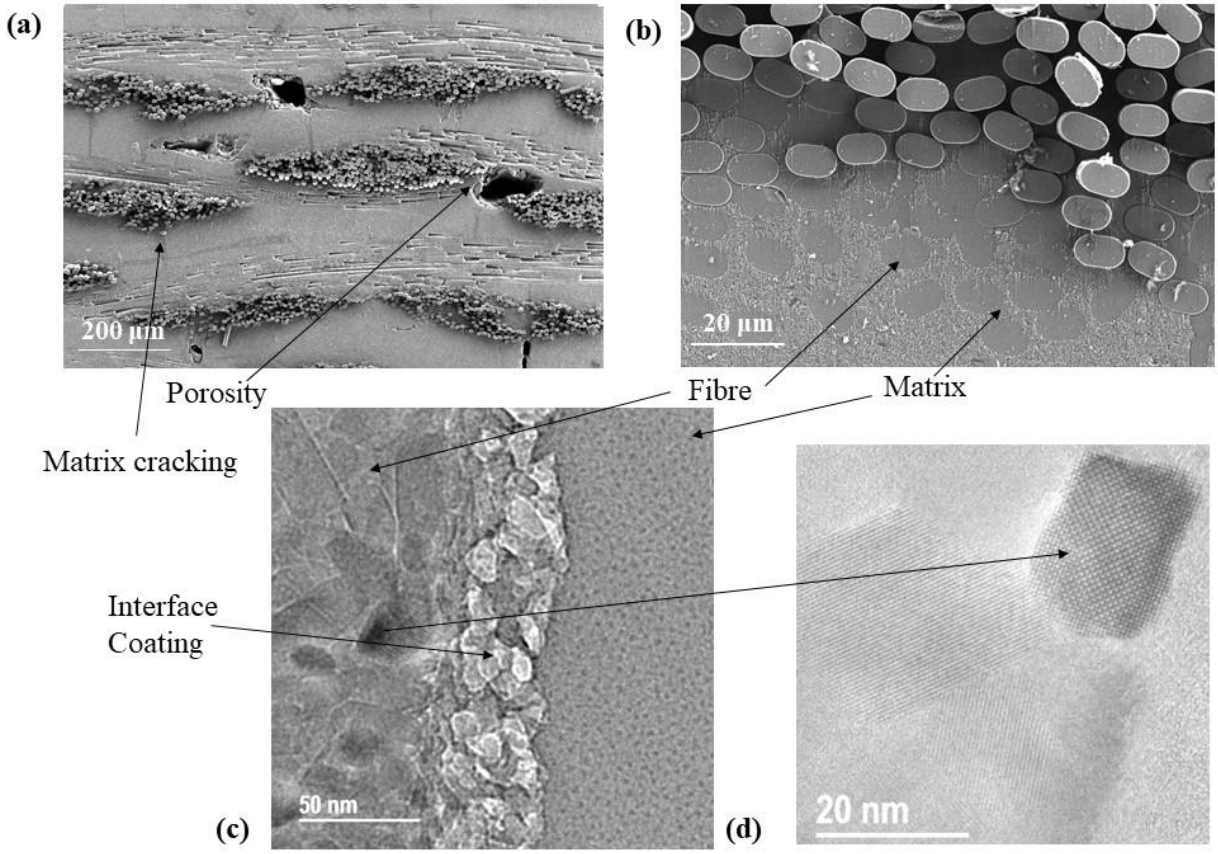

Figure 70: *(a) SEM image of the bulk structure of the CMC (sample 1) with inherent defects from matrix cracking and porosity, (b) SEM image of the elliptical cross-sections of the fibres embedded in the matrix, (c) TEM bright field image of the fibre and the matrix with the BN interface in between, (d) a higher resolution lattice image, using objective aperture, of the fibre structure.*

The XRD data (**Figure 71**), measured in accordance to **3.1.1.9**, for the four samples are indistinguishable, with any differences in the crystalline structure being below the resolution of this technique. The XRD pattern was processed using Bruker 'DIFFRAC' software [119]. The software uses a match routine which compares peak positions in the pattern with those in the International Centre for Diffraction Data ICDD database [120]. The data was plotted in Origin and all the possible crystal structures that could be present were investigated one by one. It was observed that the crystalline content

is predominantly boron-mullite ($Al_9BSi_2O_{19}$), with smaller contributions from silicon carbide (SiC), and aluminium boron oxide ($Al_4B_2O_9$). The boron-mullite and the aluminium boron oxide are the expected crystalline phases in these fibres, and the matrix has been reported as amorphous and containing crystalline SiC [58].

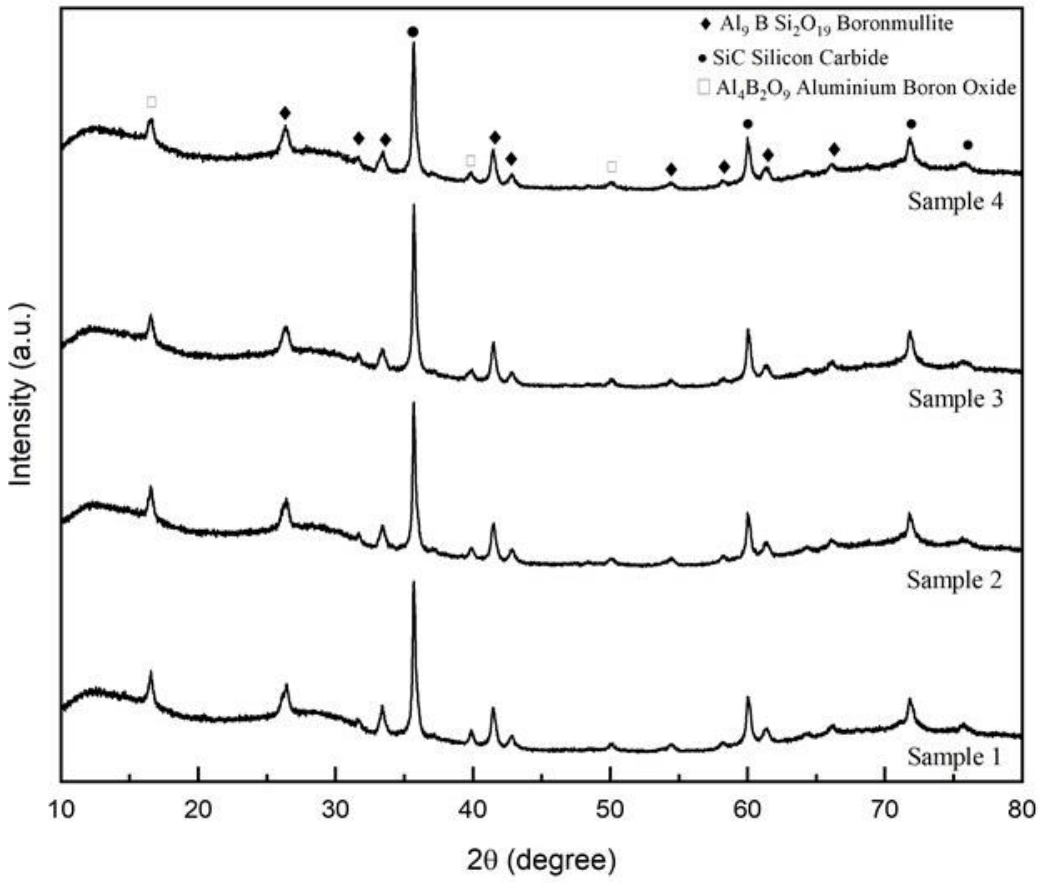

Figure 71: *X-ray diffraction spectra for the four sample materials.*

X-ray tomography (**Figure 72**), **3.1.1.4**, shows the three-dimensional arrangement of the fibres and matrix, and clearly shows the distribution of the matrix cracks that are significant contributors to the internal porosity of the material. An orthoslice of the tomograph reveals the cracks and micropores in more detail (**Figure 72 a**). The vertical matrix shrinkage cracks are clearly visible in the matrix (either

perpendicular to, or parallel to, the fibres) and porosity (mainly in the matrix and at the fibre bundle/matrix interface). The matrix cracks are mainly a function of cooling during processing [121].

3D visualisation was carried out in Avizo to determine the sensitivity of the measured porosity to the segmentation threshold. **Figure 73 (i)** shows data for a sub-volume of 27 mm^3 that is a typical region of interest. A sensitivity study determined the optimum segmentation threshold to quantify the observable porosity and to estimate the measurement error. The optimum threshold was observed to be 140, with a porosity measurement error of 0.13% within the plateau around this threshold. The porosity measurements obtained by threshold segmentation of the μXCT images (**Table 10**) show the total amount of porosity increased with PIP temperature; the porosities of samples 3 and 4 are indistinguishable. The measurement uncertainty was estimated as the sample standard deviation of 5 measurements at different non-overlapping locations for each sample, each with volume ~27 mm^3. This is significantly lower than the variability of the total porosity observed in different regions of interest. Examples of segmentation below, at and above the optimum threshold are shown in **Figure 73 (ii).**

The bulk density for each material was obtained by measurement of the mass (precision of 1 mg) and external dimensions (precision of 0.01 mm) of rectangular specimens. The bulk density measurements (**Table 10**), showed a similar decrease in density with increase in PIP temperature from a specific gravity of 2.4 ± 0.012 in sample 1 (850°C PIP) to 2.2 ± 0.010 in samples 3 and 4. The open porosity was measured in sample 1 (850°C PIP) using the Archimedes principal. After measuring the dry weight, the sample was submerged in a brine solution and put under pressure of 25inHg (0.8 bar). This allowed the fluid to seep into the open pores and the sample was left in the solution under pressure for 3-5 minutes. The sample was then taken out and access solution on the sides was dried out on a paper towel. The saturated sample was then weighed. Using the density of brine and the volume

absorbed, the porosity of the sample was calculated. This technique was only able to quantify the open porosity of the sample and hence wasn't very accurate in measuring the sample's bulk porosity. For the highest density material, processed by PIP at 850°C, the brine penetration measured an open pore volume of 8.33 ± 1.18 mm^3 for a sample with dimensions of 19.35 x 4.01 x 4.99 mm. The open porosity of 2.15 ± 0.30 % is approximately 20% of the total porosity observed by µXCT. This indicates that the majority of the porosity is closed, which is beneficial for low gas permeability.

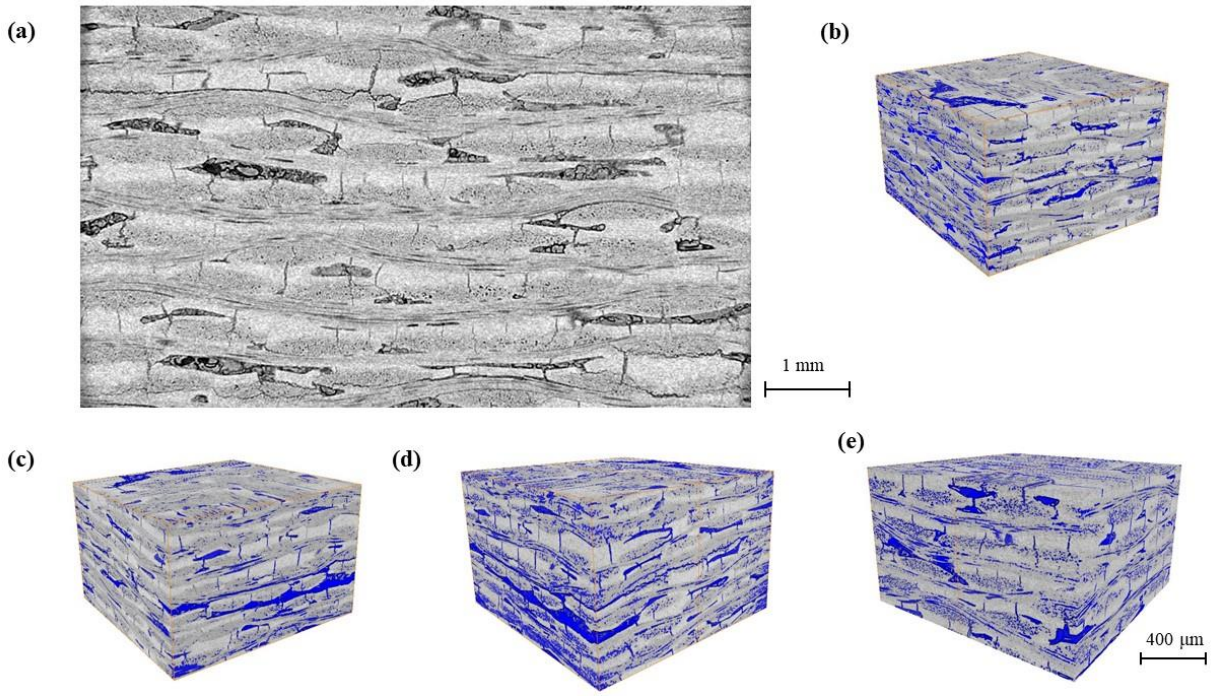

Figure 72: *X-ray computed tomographs, with porosity visualised by image grey-scale segmentation: a) vertical slice across the 0°/90° plies; (b) to (e) show 3D visualisations with threshold segmentation of pores and cracks for samples (1) to (4) respectively.*

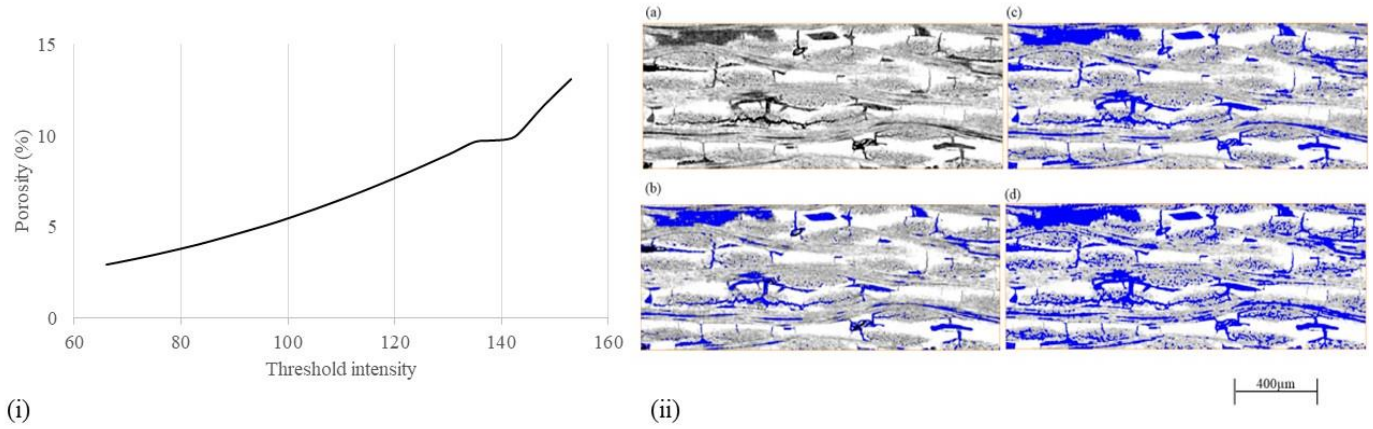

Figure 73: *(i) Threshold intensity against measured sample porosity (ii) 2D slices of the microstructure of sample 1 (850°C PIP): (a) raw image (8 bit, 0 to 256 grey levels of threshold intensity); and segmented at different threshold intensities of (b) 130 grey; (c) 140 grey; and (d) 150 grey.*

Sample Number	Pore Volume Fraction (%)	Density (specific gravity)
1	9.4±0.9	2.35±0.012
2	11.2±1.1	2.30±0.013
3	15.2±1.4	2.19±0.011
4	14.6±1.2	2.21±0.10

Table 10: *Total observed porosity by threshold segmentation of X-ray tomographs (mean ± sample standard deviation for 5 measurements).*

Thermo gravimetric analysis was used as a technique to study the thermal stability of the 4 different samples. The parameters used to carry out these measurements have been detailed in section **3.1.1.8.** Example traces of the relative mass change in the thermo-gravimetric analysis (TGA) from 25°C to 975°C are shown in **Figure 74**. They show a two-step weight loss process. The data, summarised in **Table 11**, report the total mass change (%) and the changes within intervals up to 300°C; between 300 and 600°C; and between 600 and 900°C. Sample 1, with the lowest PIP temperature, shows the greatest mass loss (6.5% total). Sample 2 and 3 show similar weight loss profile with a total weight loss of 4.5%.

Sample 4 which experienced the highest PIP temperature was thermally the most stable with the lowest weight loss of 4%. The most significant weight loss occurred above 600°C.

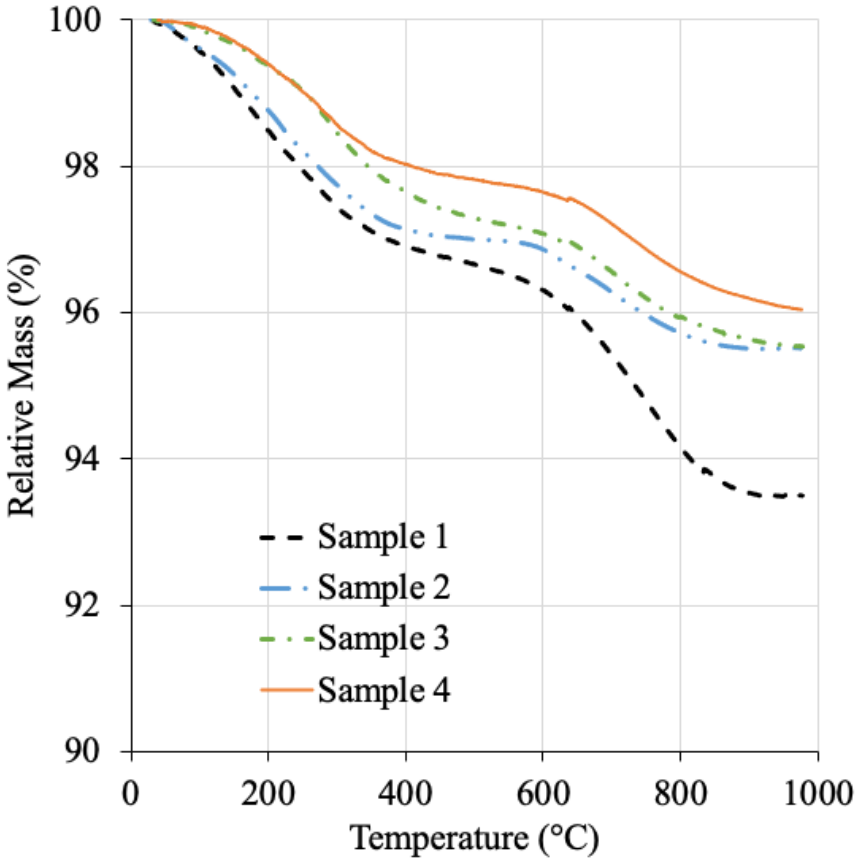

Figure 74: *Thermo-gravimetric analysis (in air), showing relative mass loss with temperature.*

Sample Number	Total %	up to 300°C	300-600°C	600-900°C
1	6.5	2.6	1.4	2.7
2	4.5	2.2	0.7	1.4
3	4.5	1.5	1.7	1.4
4	4.0	1.5	0.9	1.6

Table 11: *Mass change (%) up to 900°C: the total mass and mass loss in ranges of i) up to 300°C; ii) between 300° and 600°C; and iii) between 600°C and 900°C. The measurement uncertainty is 0.05%.*

4.3.2 Mechanical Testing

Figure 75 shows the nominal (i.e. effective) flexural stress vs flexural strain curves from the tests of three specimens of each sample, measured using the technique detailed in section **3.1.2.1.** The average number of plys that comprised the sample thickness were around 7 to 8. The flexural stress was calculated using the following equation.

$$\sigma_{flex} = \frac{3FL}{2bd^2} \quad 9$$

Where F is the load

L is the length of the support span

b is the width

d is the thickness

The effective strains were calculated using the cross-head displacements and simple Euler–Bernoulli beam theory, which assumes constant, homogeneous and isotropic elastic properties. For clarity, unless otherwise stated, the stresses, strains, stiffnesses and elastic moduli referred to in this work are effective values that are derived with this assumption.

$$\varepsilon_f = \frac{6Dd}{L^2} \quad 10$$

Where

D is the maximum deflection at the centre

d is the width of the tested beam

L is the support span

The flexural strength (maximum flexural stress) and nominal flexural moduli, obtained using a linear fit between 0.1 and 0.2% strain, are summarised in **Table 12**. All specimens showed similar stiffness, with some non-linearity at high strain. The largest strains to failure were observed for specimens from sample 1.

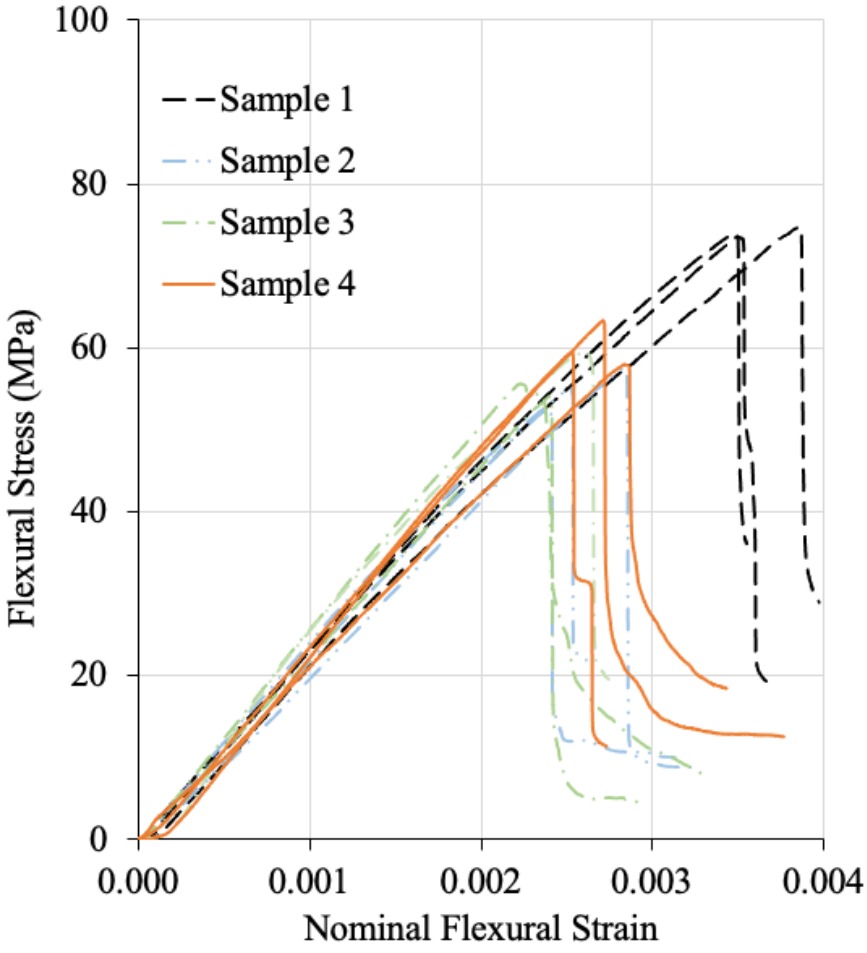

Figure 75: *Flexural stress vs nominal flexural strain (from cross-head displacement) for three tested specimens of each of the four sample materials.*

Sample Number	Flexural Strength (MPa)	Effective Flexural Modulus (GPa) (cross-head)	Effective Flexural Modulus) (GPa) (strain gradient)		Effective Flexural Modulus) (GPa) (load-line)	
			20 N	60 N	20 N	60 N
1	70.9±3.6	22.0±1.2	27.3±1.6	20.4±0.4	29.2±1.6	23.3±0.6
2	55.2±2.4	22.2±0.8	31.4±1.6	24.5±0.4	30.8±1.7	25.6±0.7
3	56.5±3.2	23.7±1.3	33.4±1.8	31.8±0.6	33.6±1.8	34.1±0.9
4	60.3±3.1	23.8±2.5	26.6±1.4	24.9±0.4	27.9±1.6	26.3±0.7

Table 12: *Flexural strengths and flexural moduli (using cross-head displacement between 0.1% and 0.2% strain) obtained from three-point bend testing (mean ± maximum deviation from the mean of 3 measurements). The flexural elastic moduli are also obtained from the strain gradient (mean ± standard error) and load-line displacement (mean ± maximum deviation from mean) at 20 N (~18 MPa) and 60 N (~54 MPa) load.*

Examples of the surface strain fields obtained by the DIC analysis are presented in **Figure 76** using the maximum 2D principal strain, ε_{max}, which is sensitive to discontinuities of the displacement field that are caused by cracks [122–125] and governed by equation 11.

$$\varepsilon_{max} = \frac{\varepsilon_{xx} + \varepsilon_{yy}}{2} + \sqrt{\left(\frac{\varepsilon_{xx} - \varepsilon_{yy}}{2}\right)^2 + {\gamma_{xy}}^2} \qquad 11$$

Where

ε_{xx} is the maximum normal strain in x direction

ε_{xx} is the maximum normal strain in y direction

γ_{xy} is the maximum shear strain in x and y direction

This finds no evidence of cracking up to 0.9σ (i.e. 90% of σ, the flexural strength that is the flexural stress at maximum load). At the flexural strength, cracks are observed to propagate from the tensile surface in all samples. The fracture tends to be deflected parallel to the lamination of the microstructure,

particularly in sample 1. In each sample the crack branches out into a number of cracks with maximum crack branching observed in sample 1. Details of how DIC technique was carried out have been given in **3.1.1.6.**

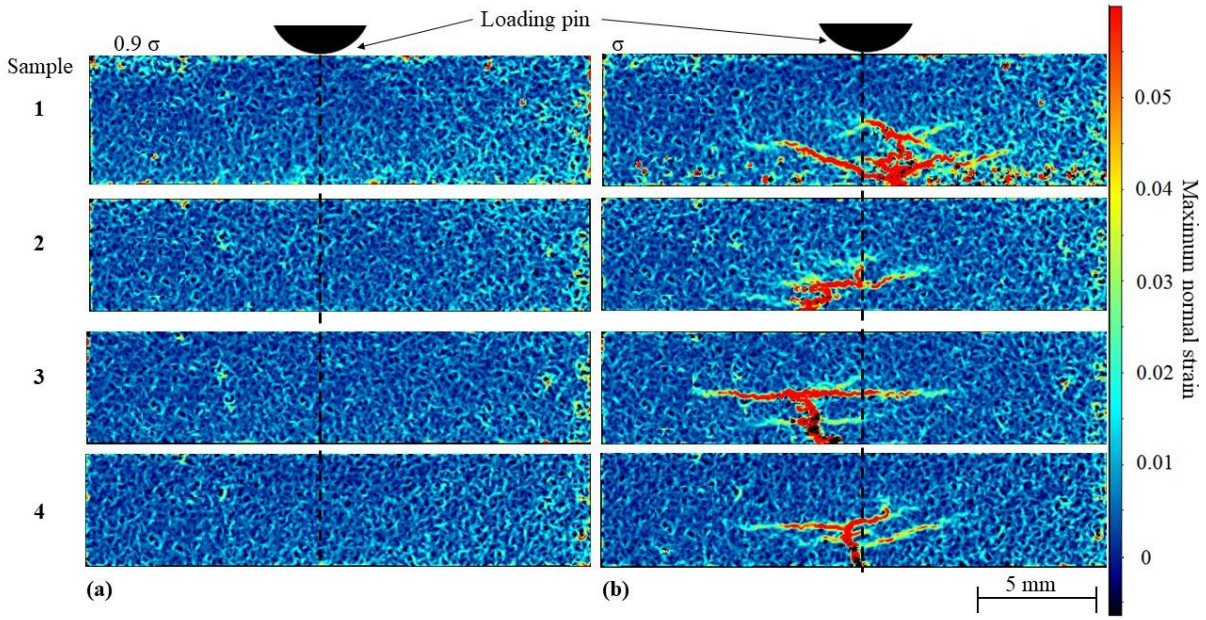

Figure 76: *Maximum normal surface 2D strain, obtained by digital image correlation (DIC) in flexural bending, at a) 0.9 σ and b) σ (i.e. 90% and 100% of the failure stress)*

The load-line displacements were estimated by DIC measurement of the vertical movement of the specimen underneath the load pin (the support pins were not imaged and were assumed to be rigid), with an uncertainty obtained using the sample standard deviation of 5 displacement vectors within 0.12 mm of the pin. This load-line deflection, d, was then used to calculate an effective flexural modulus $E_{flexural}$ using equation 12,

$$E_{flexural} = {L^3 F}/{4wh^3 d} \qquad 12$$

where L is the span length, F is the maximum load applied, w and h are the width and height of the specimen, and d is the load-line deflection at maximum load.

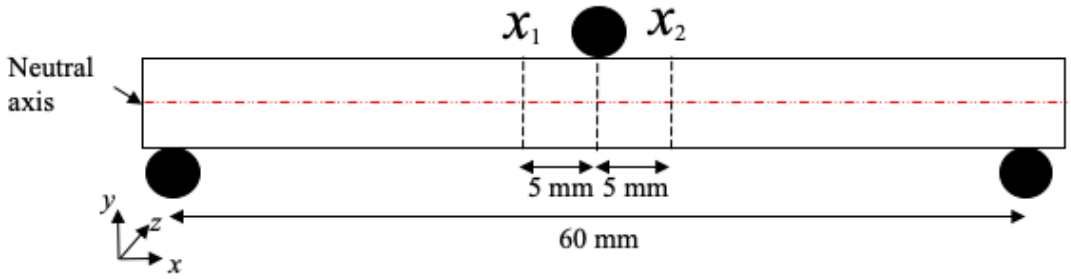

Figure 77: *Schematic illustration of the y-z planes between which relative x-displacements were measured using DIC.*

The DIC-measured displacement fields also allowed the effective flexural modulus of the specimens to be quantified via the sample curvature. This was done by measuring the relative differences in x-displacement between points on two vertical (y) planes, positioned on either side of the central loading pin and separated by a gauge distance of 10 mm (**Figure 77**); in this region, the bending moment is within 5% of its maximum value. The average strain ε_x in this region was therefore obtained as a function of position, y. Euler–Bernoulli beam theory was then used to estimate the effective elastic modulus. The analysis assumed no movement of the neutral axis, and used the linear gradient of the strain, $\frac{d\epsilon_x}{dy}$, to estimate the beam's radius of curvature, r, thus [126]:

$$M = {}^{E_{eff}I}/_{r} \text{ where } \frac{d\epsilon_x}{dy} = -{}^{1}/_{r} \qquad 13$$

where M is the bending moment, I is the second moment of area of the beam, and E_{eff} is the effective elastic modulus.

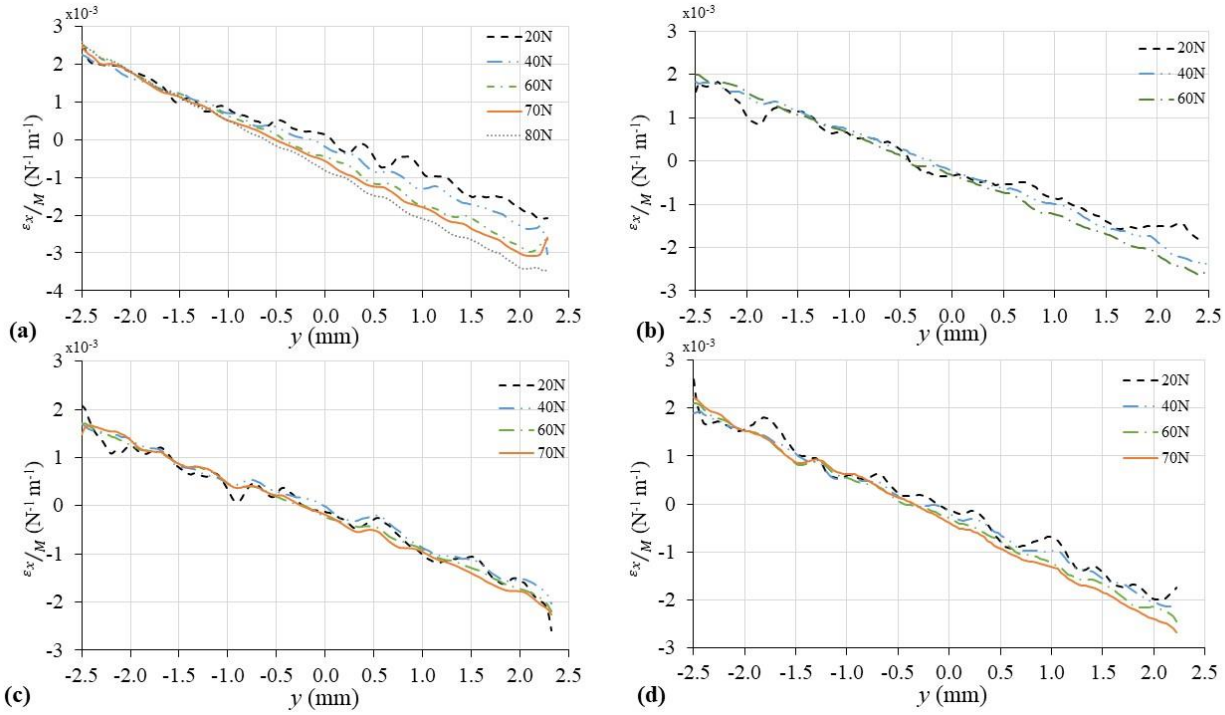

Figure 78: *The normalized flexural strain* $\left(\epsilon_x/_M\right)$ *as a function of distance from the beam centre for different loads in example specimens from (a) sample 1, (b) sample 2, (c) sample 3, and (d) sample 4.*

The normalized flexural strains $\epsilon_x/_M$ as a function of distance from the beam centre for load are shown in **Figure 78**. For sample 1, which had the lowest PIP temperature, there is a clear increase in the gradient with increasing load, which indicates a reduction in effective flexural modulus, together with a shift in the position of the neutral axis by ~0.5 mm towards the tensile surface. Similar, but smaller, reductions in modulus are observed at high load in the other samples. The effective flexural moduli, obtained via the load-line deflection (Equation 12) and the specimen curvature (Equation 13, fitted via linear regression), are presented in **Figure 79 a** and **b**. The load-line flexural moduli decrease with increasing load for samples 1, 2, and 4, and are practically constant for sample 3 that had the highest modulus. The moduli measured via the strain gradient all decrease with increasing load; sample 3 has the highest modulus. The moduli obtained at 20 N (~18 MPa) and 60 N (~54 MPa) using both strain gradient and load-line displacement are summarised in **Table 12**. The strain gradient moduli,

relative to that obtained at 20 N, are presented in **Figure 79c** as a function of flexural strain (calculated using the load-line displacement). All samples show a relative decrease in effective flexural modulus with increasing strain; samples 3 and 4 are least affected and maintain similar and higher relative moduli than samples 1 and 2 to a strain of at least 0.1%.

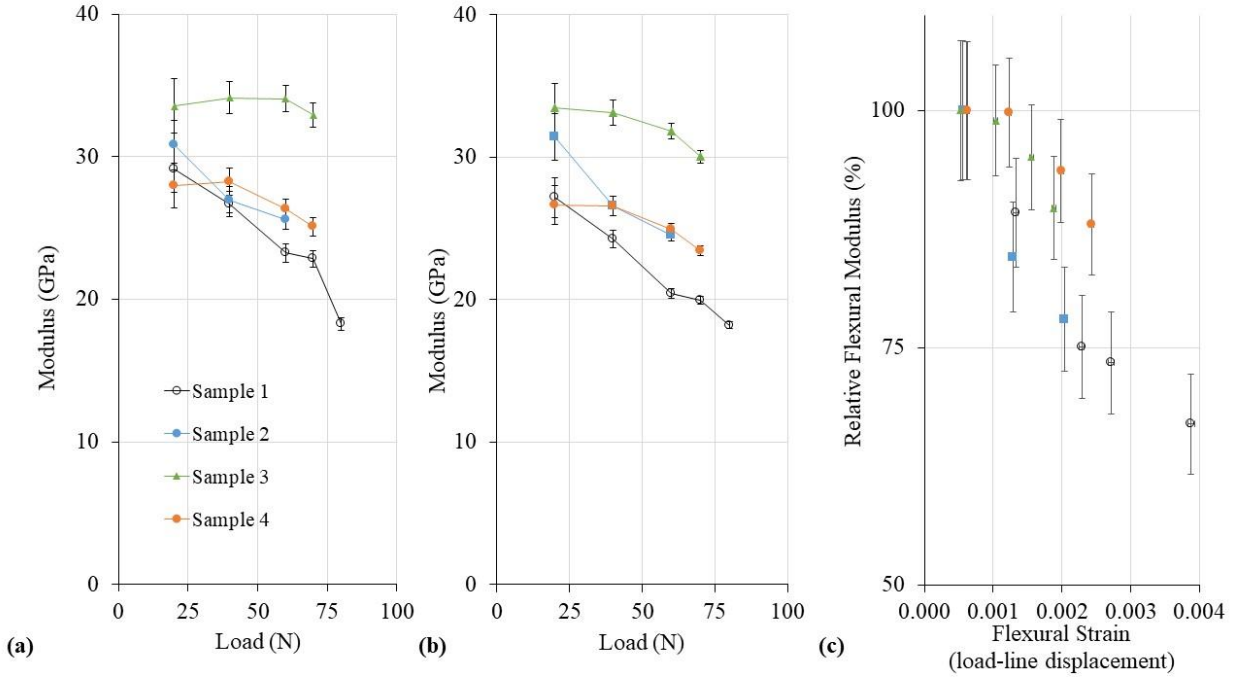

Figure 79: *The effective flexural modulus values obtained using (a) the load-line displacement, (b) flexural strain gradient. The effective flexural modulus (strain gradient), relative to that at 20 N, is shown in (c) as a function of the flexural strain (from load-line displacement).*

4.3.3 Micromechanical Testing

Nano indentation is carried out to characterize the mechanical properties of the fibre and the matrix separately, using the methodology specified in section **3.1.2.2**. The load vs displacement profile was used to calculate the final depth h_f (the residual depth of the hardness impression after final unloading) labelled in the **Figure 80**. Oliver et al [127] found that the final depth h_f, provided a better estimate for the contact area than the depth at peak load. The hardness was calculated using the following equation

$$H = \frac{P_{max}}{A} \quad (14)$$

Where

A is the projected area of the elastic contact

P_{max} is the peak load

The modulus, E_r, was calculated using the stiffness of the upper portion of the unloading curve.

$$E = \frac{1}{\sqrt{4A}} \frac{dP}{dh} \sqrt{\pi} \quad (15)$$

Where

dP/dh is the stiffness of the upper portion of the unloading curve

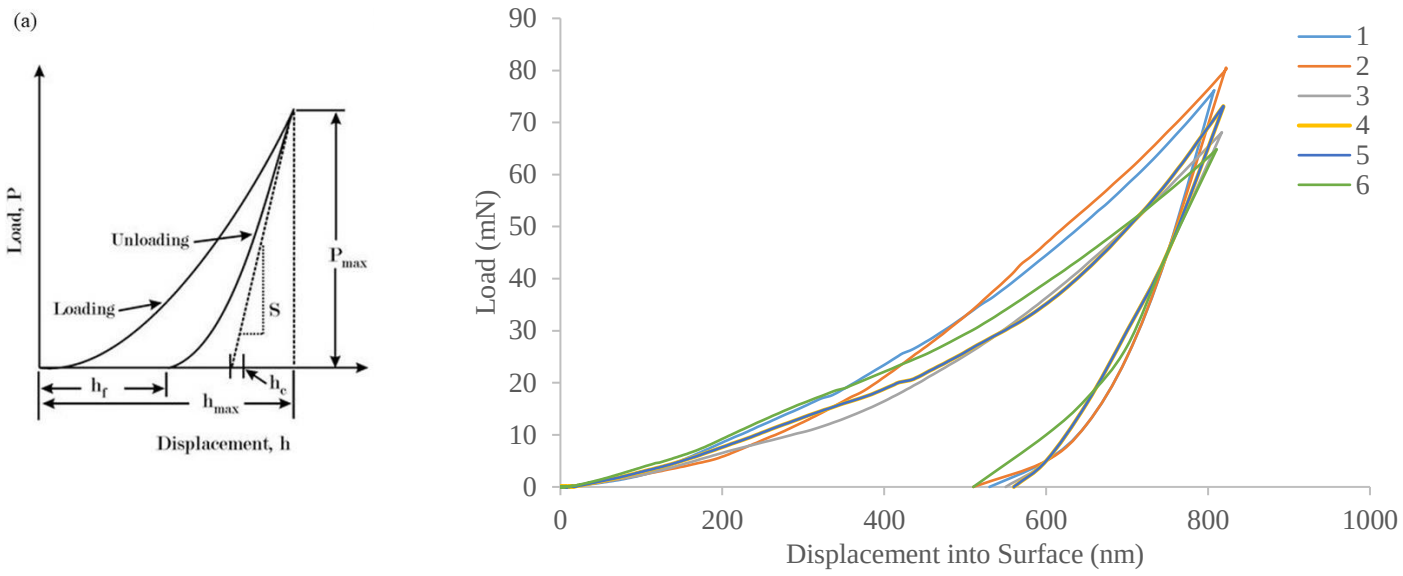

Figure 80: *(a) schematic representation of the load versus indenter displacement data for a nano-indentation measurement* [127] *(b) load vs displacement data of indentation in sample 4 matrix.*

Figure 81 shows the hardness and modulus profile of the matrix in sample 4. It could be observed that the data was very noisy for the first 300 nm after which the hardness and modulus values stabilised. The hardness and modulus values were calculated by averaging the data value between 300 - 800 nm.

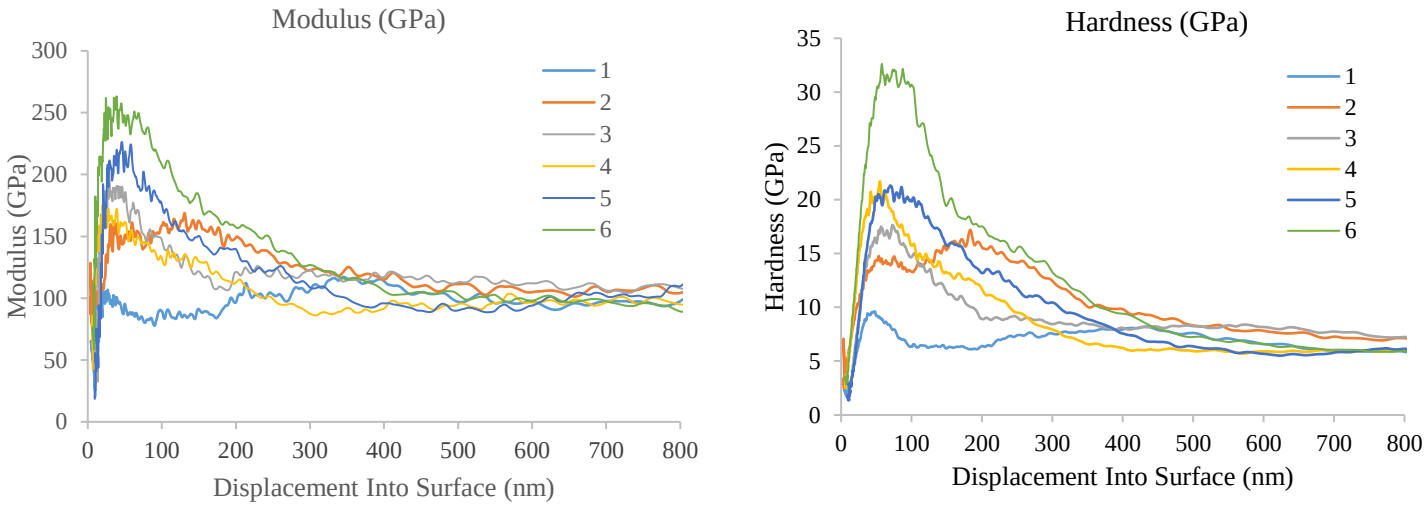

(a) (b)

Figure 81: *The displacement profiles of 6 indents placed in the matrix in sample 4 (a) Modulus vs depth of the indent (b) Hardness vs the depth of the indent*

The nano-indentation data (**Figure 82**), after rejecting those indents that did not fully sample matrix or fibre, show the four samples have a fibre modulus of ~120 to 140 GPa and hardness of ~10 GPa, while the matrix modulus was ~100 to 115 GPa with a hardness 6 to 7 GPa. The uncertainties are the 95% confidence intervals of the mean (**Table 13**). The number in the brackets, n, represents the number of measurements used to generate the average value. A Welch's t-test was used to quantify whether the difference amongst the hardness and modulus, between samples was statistically significant. The t-tests assumes a normal distribution for both data sets with different variance. It is calculated by quantifying the difference in the means and dividing it by the standard error of their difference, using equation 16.

$$t = \frac{X_1 - X_2}{\sqrt{\frac{{s_1}^2}{n_1} + \frac{{s_2}^2}{n_2}}} \qquad 16$$

This is a suitable method to be used on the indention data as the number of tests, n, vary for each sample. The tests conducted test the null hypothesis which states that both groups have the same modulus or hardness. The p-value is the probability of attaining the observed values when the null hypothesis is true. A small p value signifies that the observed difference in between the values would not be a function of random sampling. Using a p value of 0.05 the null hypothesis is rejected when the value of $p < 0.05$. The analysis ($p=0.05$) concludes the differences in the means for both modulus and hardness are statistically significant, with the exception of the matrix hardness for samples 1 to 3; these have means that are not significantly different from each other and are higher (~20%) than sample 4. There is no clear trend in the modulus data for fibre or matrix and though statistically significant the differences between sample means are small (<16% for both). There appears to be a weak trend for decreasing fibre hardness with increasing PIP temperature (<7% change).

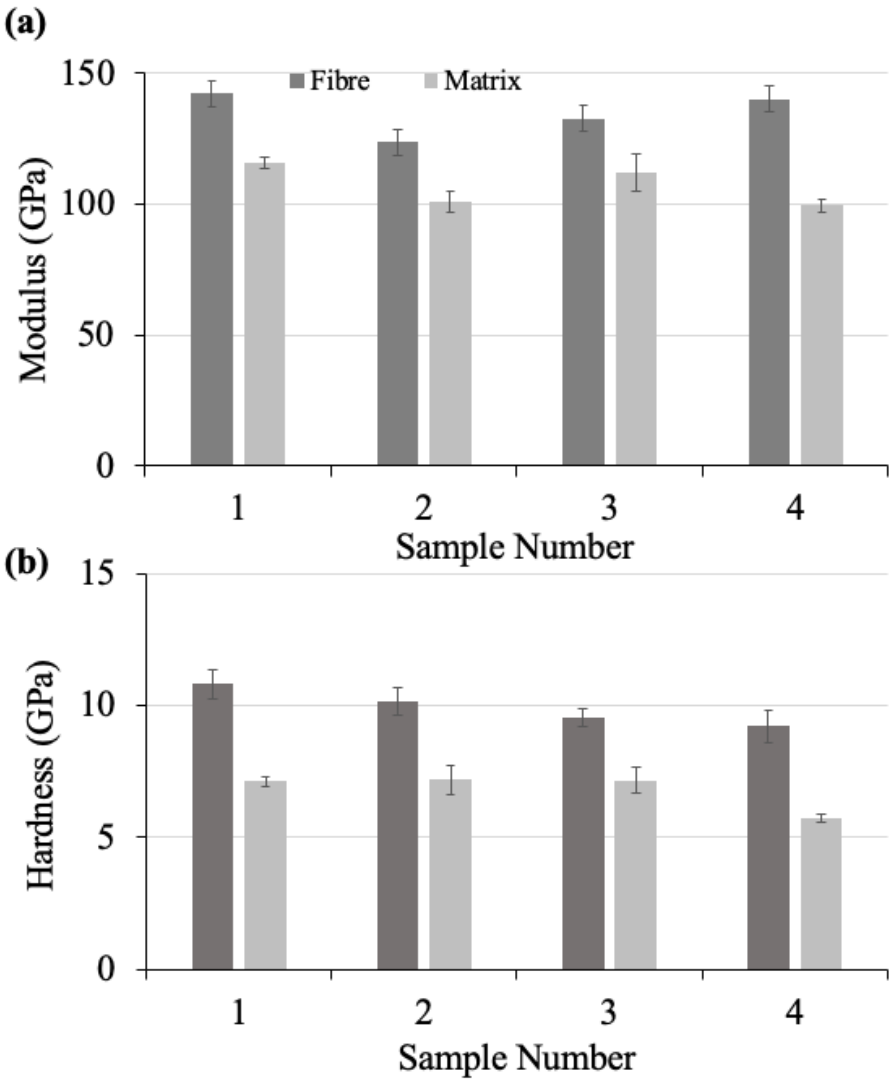

Figure 82: *Nanoindentation measurements for matrix and fibre: a) modulus and b) hardness (mean and 95% confidence interval). Data are summarised in Table 13**:** Fibre and matrix modulus and hardness, measured by nanoindention (sample mean ± 95% confidence interval [n is the number of measurements]).*

Sample	Hardness (MPa)		Modulus (GPa)	
Number	Fibre	Matrix	Fibre	Matrix
1	10.8 ± 1.1 [18]	7.1 ± 0.5 [24]	142.6 ± 11.6 [18]	116.0 ± 4.9 [24]
2	10.1 ± 1.1 [21]	7.2 ± 1.3 [24]	123.8 ± 12.2 [21]	101.1 ± 9.6 [24]
3	9.5 ± 0.8 [23]	7.2 ± 0.9 [14]	132.8 ± 10.8 [23]	112.0 ± 12.4 [14]
4	9.2 ± 1.3 [20]	5.7 ± 0.2 [10]	140.0 ± 10.6 [20]	99.6 ± 3.5 [10]

Table 13: *Fibre and matrix modulus and hardness, measured by nanoindention (sample mean ± 95% confidence interval [n is the number of measurements]).*

Fibre push out tests were carried out in order to quantify the interfacial shear strength of the fibre matrix interface, using the method detailed in section **3.1.2.2**. The maximum load was calculated using the load plateau observed in the load vs displacement graph plotted for the indent. The theoretical fibre displacement during pushout was set to be 2µm. In order to calculate the shear stress the surface area of the fibre that was in contact with the matrix was calculated by first finding out the circumference of the fibre and then multiplying it with the thickness of the sample, H. The pushout configuration schematic has been presented in the **Figure 83** (b). For each indent, load vs displacement graph was produced as seen in the **Figure 83 (c)**. The plateau load represents the load at which the crack is fully propagated and the fibre starts to slide. The shear stress at this load applies to the entirety of the interface.

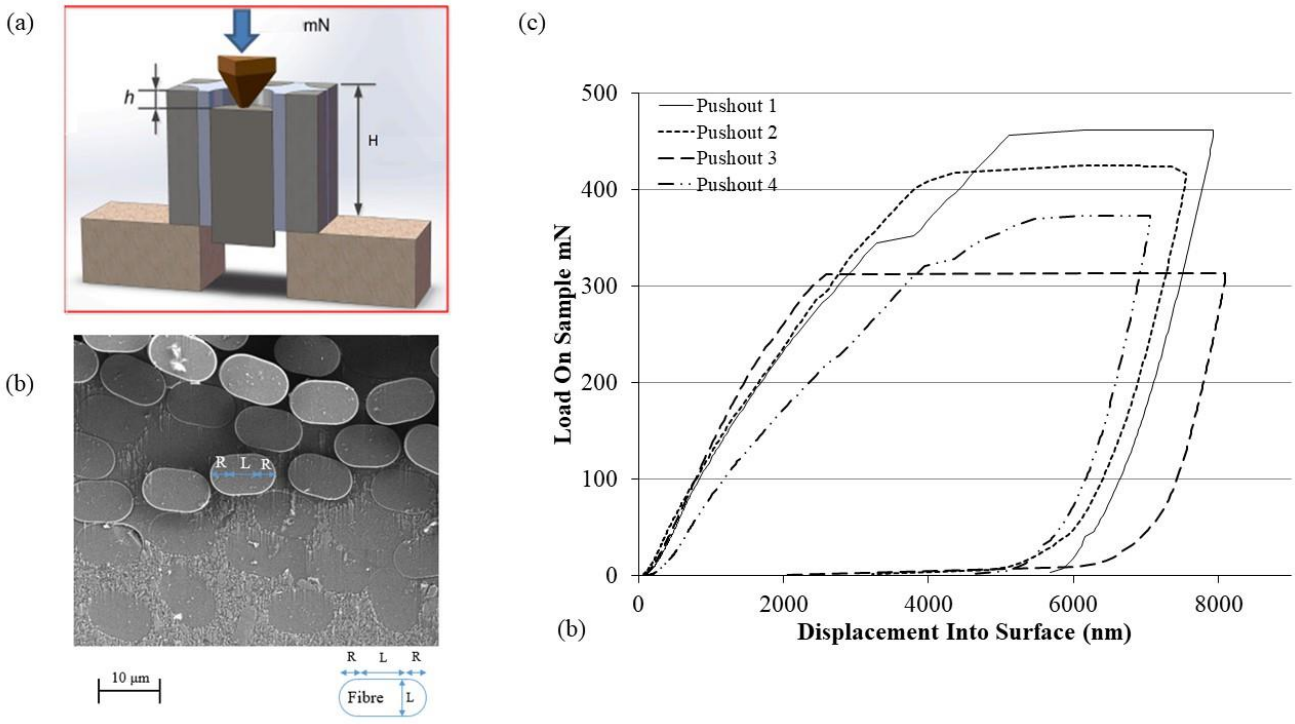

Figure 83: *The fibre pushout tests carried out on the samples (a) the schematic of the arrangement were H is the thickness of the sample and mN is the applied force (b) the fibre shape with the dimensions R & L labelled on the fibre (c) the load vs displacement curves of the pushout,, the plateau load was used as the pushout load value in equation 17.*

The fibre pushout tests were analysed to calculate the interfacial shear stress for pushout, τ_{is}, using equation (17) [128],

$$\tau_{is} = \frac{F}{(2\pi R + 2L)H} \qquad 17$$

where F is the push-out load, R and L are the dimensions of the fibre as seen in **Figure 83 (b)**, and H is the sample thickness. The load vs displacement data was processed by Robin De Meyere, Department of Materials, University of Oxford, to generate interfacial shear stress data using equation 17. Cross-hair calibration was performed on the surface of the sample to ensure x-y in-plain accuracy. The indents were visually inspected using the in-built optical microscope, in G200, to ensure that they all landed in the centre of the fibre and resulted in achieving a clean pushout.This test method results in producing data with varied levels of interfacial stress and in order to successfully quantify the level of stress the distributions of strengths measured in successful tests are reported in **Figure 84** and summarised in **Table 14**. The number in the brackets, n, represents the number of measurements used to generate the average value. Sample 1 has the lowest interfacial shear strength, with an average that is approximately half that of samples 2 to 4. The shear strength distributions, which have similar ranges in samples 2 to 4, were compared using the unequal variances (Welch) t-test, described earlier: the means of samples 3 and 4 are statistically indistinguishable ($p=0.98$); the mean of sample 2 is approximately 25% higher than 3 and 4 with statistical significance ($p<0.05$).

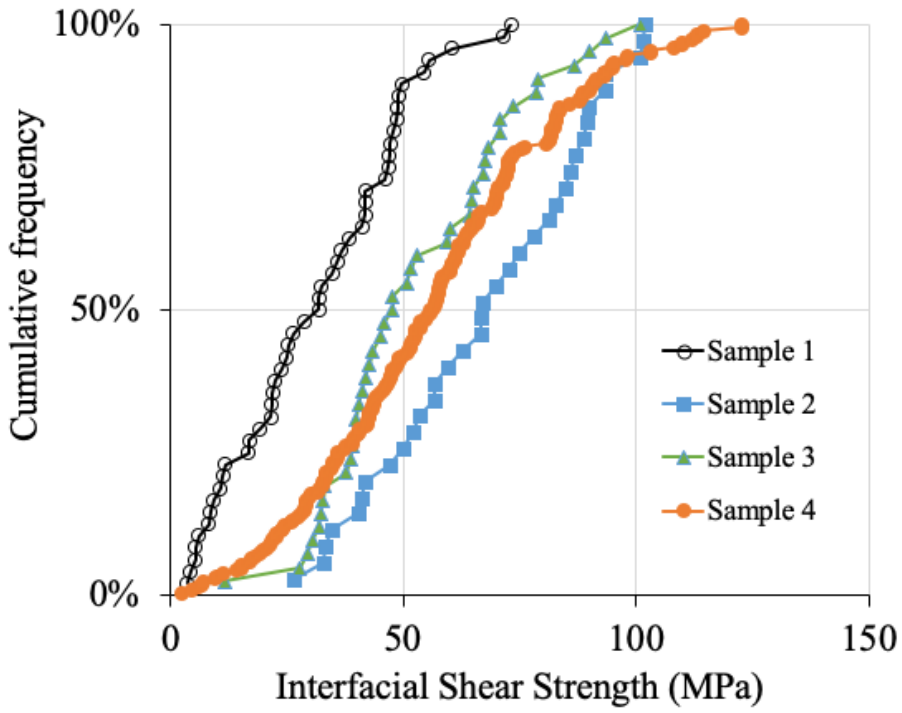

Figure 84: *Cumulative frequency for the interfacial shear strengths measured for the four sample materials by fibre pushout*

Sample Number	Interfacial Shear Stress (MPa)
1	31.4 ± 18.3 [48]
2	67.6 ± 22.1 [35]
3	53.2 ± 20.3 [42]
4	56.2 ±26.2 [200]

Table 14: *Interfacial shear stress (mean ± sample standard deviation) obtained by fibre pushout testing [n measurements].*

4.4 Discussion

All the samples have visually similar microstructures (**Figure 70**) with fibre bundles in the 0 and 90° with pores visible in the matrix. A BN interface was observed in between the fibre and the matrix with a measured thickness of around 30-50nm. The proportion of defects (cracks and porosity) were observed to increase with PIP temperature (**Figure 72, Table 10**). Samples 3 and 4, which had the same and highest PIP temperature in their final stage, had very similar total porosity. This is consistent with the differences in coefficients of thermal expansion, CTE, of the Nextel fibre (3 ppm $°C^{-1}$ [60]) and aluminosilicate matrix (3.4 ppm $°C^{-1}$ [58]). These cause tensile thermal strains due to post-processing shrinkage that would be relaxed by matrix cracking. The higher the processing temperature the higher the effect of the shrinkage due to the CTE mismatch. The trend is also observed in the density measurements carried out for each sample, with the specific density observed to decrease with increase in processing temperature indicating an increase in the level of microstructural porosity. No differences in the constituent phases of the microstructure were measurable by XRD, with all four samples exhibiting a crystal structure containing boron mullite, Silicon carbide and aluminium boron oxide. Any difference that might be present in the crystal structure is well below the resolution of this technique [129]. There are differences between the fibre and matrix properties of the samples, measured by nanoindentation, but these are small and do not show clear trends (**Table 13, Figure 82**). The most significant difference due to processing is observed in the matrix of sample 4 (5 cycles at 950°C and one at 1050°C) that is ~20% softer than the other samples, which have the same matrix hardness.

Increasing the PIP temperature increased the thermal stability, measured as the mass loss in TGA (**Figure 74 and Table 11**) with sample 1, processed at 850°C, being the least stable. Sample 4 (5 cycles at 950°C and one at 1050°C) has the highest thermal stability. The two-stage behaviour is consistent

with the observation that the 'Blackglas' matrix contains free carbon [130], which burns off at temperatures above 400°C, as well as free silicon and SiO_4 and SiC_4 domains [60]. Increasing the pyrolysis temperature significantly increases the amount of SiC_4 and reduces the amount of less thermally stable SiO_4 [131,132], which tends to oxidise above 850°C. The short term TGA analysis provides a crude measure of thermal stability, and more detailed studies of the long term thermal stability of these systems would be required before application of these materials.

The fibre-matrix interfacial shear strength in ceramic matrix composites can be affected by both the mechanical strength of the interface and the action of residual stresses [133]. The relative thermal contractions of matrix and fibre, and the observed process-induced cracking between matrix and fibres (**Figure 72**), indicate that compressive interfacial residual stresses are unlikely. Hence, the measured interfacial shear strengths represent the mechanical strength of the fibre/matrix interface. The fibre pushout tests (**Figure 84**) show that sample 1, with the lowest process temperature of 850°C, had significantly the lowest interfacial shear strength. The interfaces in sample 2, processed at 950°C, are slightly stronger than samples 3 and 4, which had the same final process temperature of 1050°C and presented the same shear strength. The mechanical properties of the interface microstructure depend on both the PIP temperature and the sequence of PIP treatments, which affects the development of the matrix as demonstrated by the nano-indentation hardness. The low PIP temperature of 850°C leads to a weak interface; the effects of PIP processes at higher temperatures are more complex but lead to stronger interfaces. It must be noted that the local environment could have an effect on the measured interfacial shear strength [134]. As the material system had an interfacial thickness of around 50nm the location of the fibre within the tow might have very limited effect on the interfacial shear strength measurement.

The highest flexural strengths and maximum displacements to failure were measured in sample 1 (**Figure 75 and Table 12**), which had the lowest processing temperature of 850°C. The flexural failures of specimens from the other samples were similar to each other. All showed a tendency for crack deflection parallel to the fibre plies (**Figure 76**), consistent with low interfacial shear strength between fibre and matrix, particularly sample 1 that has the weakest interfaces (**Figure 84**). This encouraged greater delamination, leading to higher strains to failure, with a consequent increase in the maximum flexural stress. This also confirms that fibre debonding mechanism is fully active after processing for all samples and even though the interfacial shear strength has increased with higher PIP's temperature fibre matrix bonding has not taking place and the fracture toughness mechanisms are still fully active in the composite.

The effective flexural moduli can be used to monitor the development of mechanical damage, since the development of cracking in brittle materials reduces the elastic modulus [135,136]. The relative change in modulus with increasing load shows that the spatial resolution of strain imaging by DIC was not sensitive enough to observe damage below $0.9R\sigma$. The effective flexural moduli that were measured using the sample curvature (**Figure 78**) are most sensitive to this **(Figure 79**), but may not provide an absolute measure of the sample compliance as only surface measurements are used that may be affected by sample alignment (i.e. non-parallel surfaces). The effective moduli obtained via the load-line displacements would be less sensitive to these factors but are affected by the assumption that the non-observed support pins were rigid. The effect of this is judged to be small, due to the relatively low stiffness of the small and slender test specimens, hence the effective load-line moduli measured at low load (i.e. no damage) allows the relative moduli of the composites to be compared, finding that the modulus tends to increase with PIP temperature, with sample 4 being less stiff than sample 3 (**Table**

12). The PIP temperature has competing effects on the similar fibre and matrix moduli (**Table 13**) and porosity (**Table 10**), so clear correlations between these and the flexural modulus cannot be discerned. Nonetheless, the effect of the different PIP processing is small, and all samples have similar elastic properties.

The direct measurement of the specimen curvature assumes isotropic homogenous behaviour, which is not strictly correct for a composite material. Hence the reported modulus is only an effective modulus for this test geometry. Nonetheless, it gives a quite sensitive assessment of relative changes in modulus (**Figure 79c**). For the comparison, this is presented as a function of the surface flexural strain, obtained using the load-line displacements and the assumption of simple beam theory. Samples 1 and 2 show a significant decrease (up to 33%) with increasing tensile strain. Samples 3 and 4 retain their modulus up to higher strains before declining similarly, with sample 4 showing the highest effective modulus. The modulus decline occurs before the observation of delamination, which is only observed above 90% of the failure load (**Figure 76**). The modulus decline is attributed to propagation of defects from the matrix, which ultimately coalesce to cause delamination at the failure stress. The composites demonstrate a better tendency to resist the onset of mechanical damage with increasing tensile strain with increased PIP temperature. However, after the onset of delamination, there is greater delamination exhibited in sample 1, which was processed at the lowest PIP temperature. This has the lowest interfacial shear strength, which encourages fibre pull-out and a more graceful failure. By calculating the modulus using beam bending theory and relative flexural profile of the sample and quantifying the change in modulus values provides a very good way of detecting crack development in the sample with increasing load. To identify these microcracks would be very difficult and would require a very high resolution DIC or

X-ray tomography measurements of sub-micron. The effective modulus calculations used in this study offer an excellent way of detecting microstructural damage.

In terms of the design requirements for spring retention, these measurements conducted at ambient temperature indicate that although sample 1 that was PIP processed at 850°C had the highest density and flexural strength, it had lower thermal stability. Samples 3 and 4, processed at the highest PIP temperature of 1050°C had slightly lower density due to increased closed porosity, good resistance to mechanical damage from tensile strain and good thermal stability, and could be useful for sealing applications around 900°C for short periods of time. The open porosity measurements carried out in this study indicate that most of the porosity is closed insures that the material is suitable for sealing applications. Further investigation must be carried out to quantify their long term capability at service conditions.

4.5 Conclusion

Nextel 312 fibre/SiCO matrix ceramic matrix composites have been manufactured using repeated PIP (polymer infiltration and pyrolysis), with pyrolysis at temperatures between 850°C and 1050°C. All samples had similar microstructures with no consistent effect of process conditions on the fibre or matrix properties, measured by nano-indentation. The porosity is mostly from closed pores and increased with final PIP temperature.

The effective modulus decreases with increasing flexural strain, with greater resistance to mechanical damage at higher PIP temperature. The highest flexural strength was observed in the sample with the lowest PIP temperature. This had the lowest interfacial shear strength, and graceful failure due to increased delamination increased the maximum flexural strain and strength. Processing at 950°C or above gave good resistance to mechanical damage from tensile strain and good thermal

stability. This material although performed adequately at 900°C for the period of time it was investigated, doesn't fulfil the design requirement of producing a sealing ring at temperatures above 1000°C. The temperature capability of this material system, as studied in literature or by carrying out experiments in this piece of work, suggests that this material system would not be able to perform adequately as a seal at temperatures ≥ 1000°C hence it was not investigated further in this study.

The results of the experiments and analysis presented above were published in Composites Part A: (https://www.sciencedirect.com/science/article/pii/S1359835X20304346)

CHAPTER 5. *In situ* observation of the deformation and fracture of an alumina-alumina ceramic-matrix composite at elevated temperature using x-ray computed tomography

5.1 Introduction

In situ observations of damage development within ceramic composites is essential in providing an in-depth understanding of the mechanical interactions between the matrix, fibres and porosity [137], as these cannot be accessed by surface observations. The application of high-resolution computed x-ray tomography (μXCT) allows new insights into damage development within ceramic composite microstructures, and when such *in situ* studies are coupled with digital volume correlation (DVC) [94] it is possible to quantify the deformation and strain states [102,138] and their interactions with the architecture of the composite [138]. High temperature *in situ* observations are also feasible [114] to investigate fracture propagation through the woven microstructure, including the influence of oxidation.

The objective of this work was to adopt this *in situ* approach to study failure in a Nextel 720 fibre / alumina matrix CMC at ambient temperature and at 1100°C, and document the evolution of damage with particular attention to the initiation of cracks and their subsequent propagation within the microstructure.

5.2 Material system

The material under study was an oxide ceramic-matrix composite with an alumina (Al_2O_3) matrix and Nextel 720 fibre with EF 19 weave style, 8 harness satin weave as seen in **Figure 85 (a)**, with no interfacial layer between the fibre and the matrix. The prepreg cloths were then stacked following the conventional 0/90° layup and consolidated using vacuum bagging, followed by a drying process, which

drives out water and remaining solvents, at a temperature of around 150°C followed by pressureless sintering in the range of 1000-1250°C. Details of the process has been presented in **2.3.1.** The thickness of each layer was measured to be around 0.58mm with roughly 8 layers of fabric in a 5 mm sample as seen in **Figure 85 (b)**.

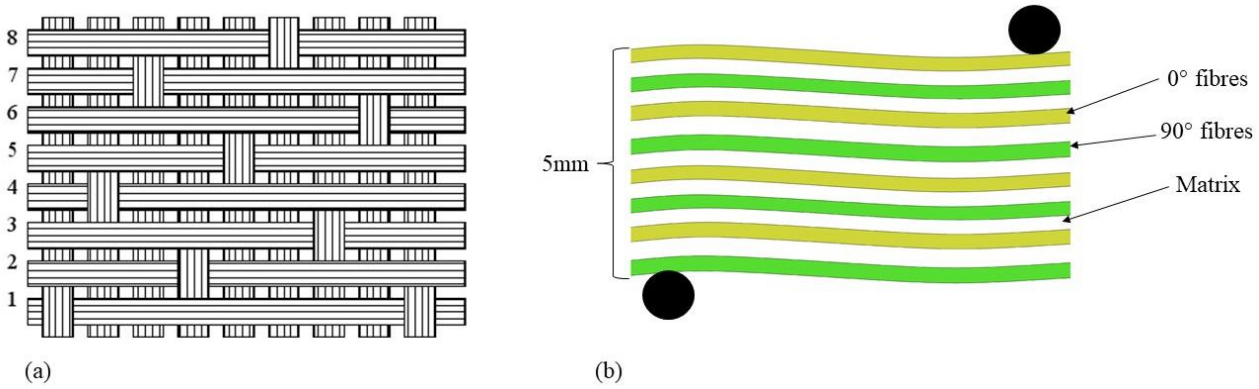

Figure 85: *The weave structure of the fabric, (a) 8 Harness satin weave (b) layup of the composite with 0° and 90° layers labelled*

5.3 Results

5.3.1 Microstructure

Laboratory based X-ray tomography was carried out as a pre characterisation of the microstructure before the in-situ high temperature X-ray tomography experiments at Advance Light Source (ALS) Berkley. It was to ensure than the smaller ALS samples were representative of the composite microstructure. The microstructure of a rectangular specimen (15 x 4 x 5 mm) was examined with laboratory tomography using a Zeiss Xradia 510 Versa 3D X-ray microscope, as described in experimental in **3.1.1.7.** The laboratory X-ray tomograph of an as-fabricated sample **Figure 86 a** shows the fibre bundle orientations in the 0°/90° woven structure, where 0° fibres have been defined as being parallel to x axis and 90° fibres are parallel to the z axis. There are pre-existing matrix shrinkage cracks (either perpendicular to, or parallel to, the fibres) and porosity (mainly in the matrix and at the fibre

bundle/matrix interface) (**Figure 86 a, b**). The matrix cracks are caused by cooling during processing [121]. The SEM images show the close packing of the fibres within the tows (**Figure 86 c**), and fine pores (**Figure 86 d**) in both the fibres and matrix. In order to quantify the detectable open and closed porosity of the material system, a 3D visualization tool is used, similar to the technique presented in CHAPTER 4. The 3D visualisation is carried out in Avizo using the threshold difference between the sample and the pores. A study was carried out to find the optimal threshold, which is where the detected porosity showed an approximate plateau over a range of threshold values, **Figure 87**. This was selected as the total porosity of the tomographed sample (**Figure 86 a**) and was estimated to be around 24 vol.%. The uncertainty in the measurement is of the order of the range of the plateau (0.58%). The measured porosity is towards the lower end of measurements in literature of similar composites which were between 24-40% [86].

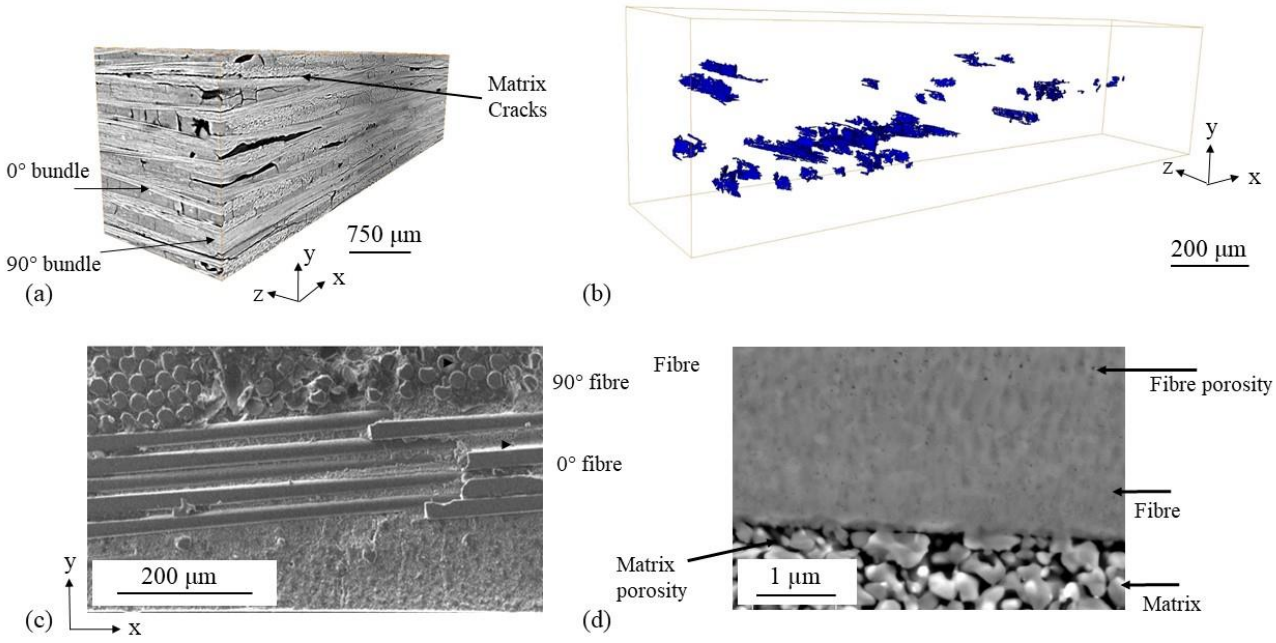

Figure 86: *Microstructure of as-fabricated oxide-oxide ceramic-matrix composite sample: a) 3D x-ray tomography visualization (2.7 µm voxel); b) Pore segmentation and visualization from x-ray tomograph; c) SEM image of polished section; d) SEM image of fibre/matrix interface.*

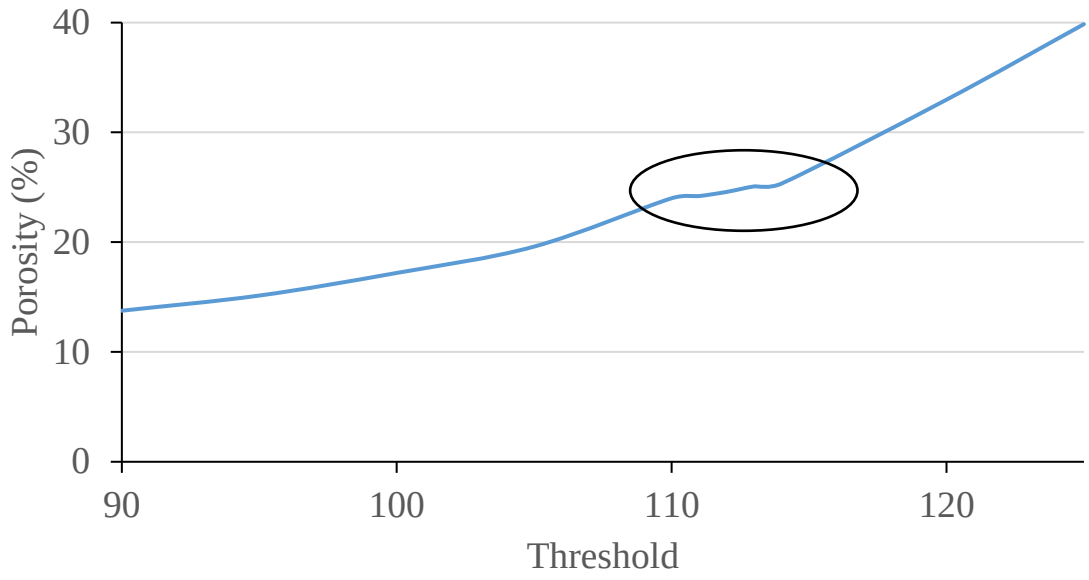

***Figure 87**: 3D visualization carried out in Avizo using the threshold difference between the sample and the pores. The location where the porosity plateaued over a range of different threshold values was selected as the sample porosity, highlighted by a black ring.*

A Tescan Lyra3 XMU Focused Ion Beam Scanning Electron Microscope (FIB-SEM) was used to make thin foils for examination by transmission electron microscopy (TEM). A JEOL 2100F STEM (200 kV) system with point-to-point resolution of 0.23 nm was used for observations in both bright field (BF) and annular dark field (DF-HAADF) STEM modes (2048 x 2048 pixels at 30 µs per pixel) which were carried out by Ivo Šulák, at the *Institute of Physics of Materials, The Czech Academy of Sciences, Czech Republic*. Imaging using transmission electron microscopy (TEM) (**Figure 88**) confirmed the porous interface between the fibre and the matrix, with no difference distinguishable between the interface structures after testing at room temperature and at 1100°C. The TEM images of the fibre show an equiaxed structure with an average grain size of 50-100 nm. Selected area diffraction pattern (SADP) analysis, **3.1.1.9,** was performed on the fibres sectioned in both longitudinal and transverse directions,

as seen in **Figure 89**, from the room temperature sample were obtained using a camera length of 800 mm. Diffraction patterns of the fibre shown in **Figure 90** are obtained from sections parallel (0°, 30°) and perpendicular (60°, 90°) to the fibre axis. The patterns were rotationally averaged using the Difftool [139] which transforms the two dimensional electron diffraction pattern into a one-dimensional profile similar to a normal X-ray diffraction pattern. This involves locating the centre of the diffraction pattern accurately. The software has an in-built tool called "locate SADP Centre" which provides an estimation of the centre of the pattern. This uses a mask of concentric rings about this centre and helps generate the goodness of fit of centre with respect to the diffraction spots. Using the "Rotate and Insert SADP" tool the patterns can be inserted into their corresponding images with a rotation correction applied, which turns the two-dimensional electron diffraction pattern into a one-dimensional profile as seen in **Figure 90 (a)**. The peak locator tool is used to identify the different peaks in hkl. Using crystal tool option present in the Difftool software, and by feeding in the lattice parameters of a particular crystal structure that could exist, the peaks can be tallied with the data to find out if a particular crystal structure is present in the diffraction pattern [140]. The azimuthally integrated diffraction spectra in **Figure 90 a** shows the peaks from cristobalite (SiO_2), mullite ($Al_2O_3.SiO_2$), and alumina (α-Al_2O_3) with the alumina phase dominant. The fibre has a preferred crystalline texture, shown (**Table 15**) by the change in relative integrated intensity of the {113} and {223} alumina peaks with observation angle relative to the fibre axis.

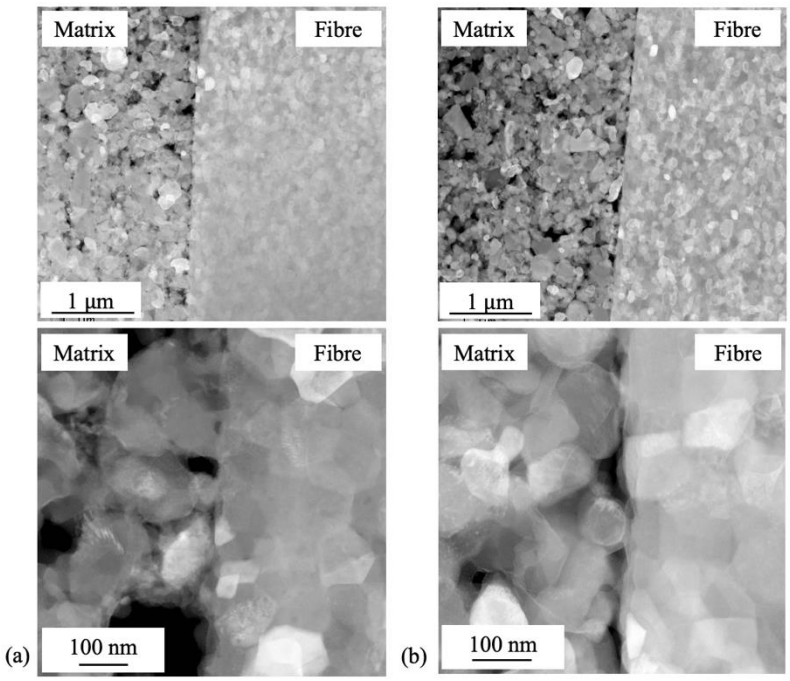

Figure 88: *Scanning transmission electron microscopy (STEM) observations with DF-HAADF dark field (porosity is black) of the matrix/fibre interface of samples tested at (a) room temperature and (b) 1100°C.*

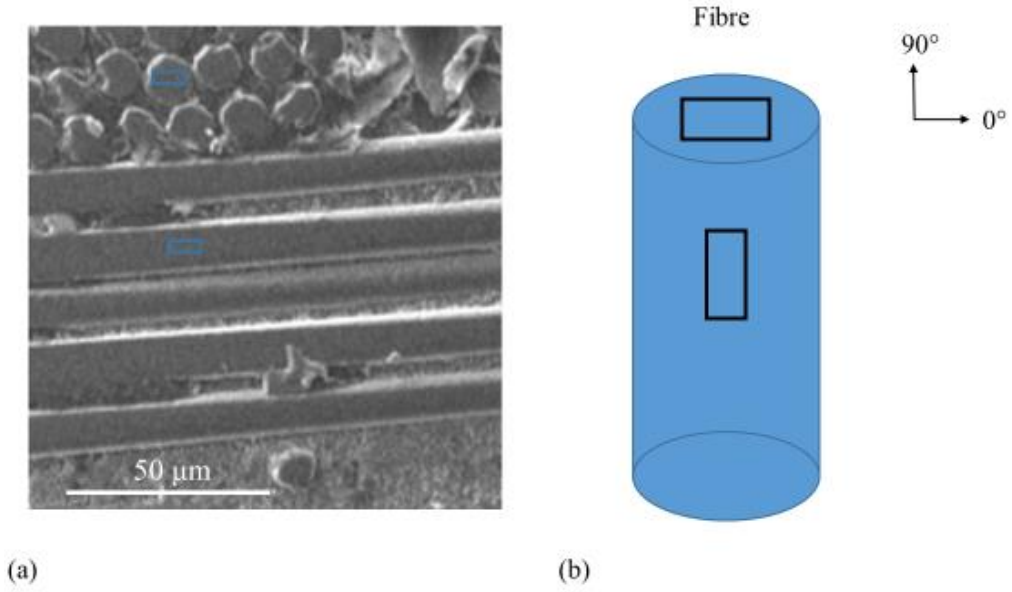

Figure 89: *(a) The weave architecture with fibres in °0 and 90° (b) a schematic of the fibre with two boxes showing the direction in which the two lamellas were cut.*

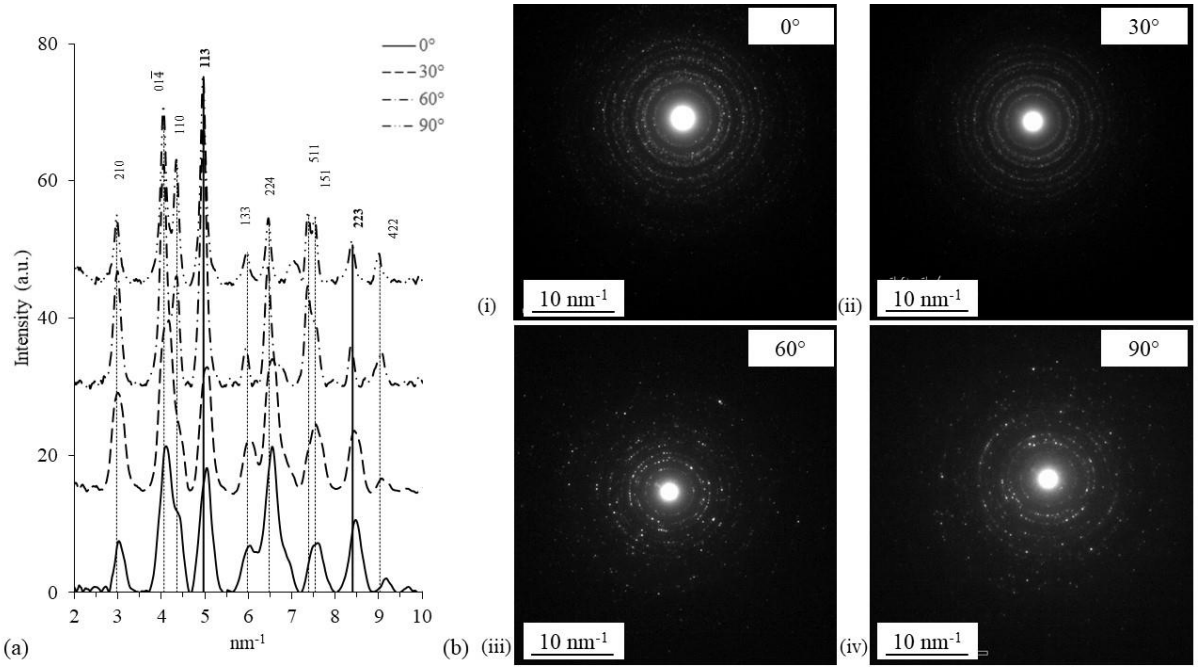

Figure 90: *Diffraction from fibres (sample RT) obtained at different orientations relative to the fibre axis: (a) azimuthally integrated diffraction spectra (vertical lines show the expected location of the α-alumina peaks, with the {113} and {223} emphasised); b) diffraction images obtained with beam oriented at i) 0°; ii) 30°; iii) 60° and iv) 90° relative to the fibre axis.*

Rotation Angle (°)	{113}	{223}	Ratio
0	5.68±0.05	1.31±0.05	4.3
30	7.89±0.05	1.14±0.05	6.9
60	5.71±0.05	2.81±0.05	2.0
90	5.90±0.05	3.49±0.05	1.7

Table 15: *Areas (and mean ratio) of the alumina {113} and {223} diffraction peaks with beam angle relative to the fibre axis.*

5.3.2 Fracture Behavior

Tests were conducted at two temperatures: RT (nominally 25°C) and 1100°C. A thermocouple was placed in contact with the side of the sample to control the temperature via the lamp current. A detailed image of the setup was shown in **Figure 91 (a)**. In addition, a similar zoom-in image is presented in **Figure 92**, including a schematic of the three-point bending and positions of thermocouple [141]. The

hot zone size is sufficiently large to include the whole sample cross-section. A detailed analysis of the hot zone was analysed in [114] and a schematic was included in **Figure 93**. The distributions of temperatures measured by the thermocouple across the cross-section of the sample has been presented in **Figure 93**. For each *in situ* tomographed sample, several scans were undertaken from the pre-load (essentially load-free) condition until fracture, details of the experiment are provided in **3.1.1.5.**The load-crosshead displacement data acquired during the *in situ* synchrotron X-ray tomography tests at ambient and 1100°C provided nominal relationships for stress *vs*. strain, (**Figure 91 b**), which were obtained using the Euler–Bernoulli (slender beam, linear homogeneous elastic properties) analysis for small displacements. The flexural strengths at both RT and 1100°C were similar at approximately 100 MPa (**Table 16**). The flexural moduli were estimated from the linear region of the stress-strain curve (**Figure 91 b**); the low-load region was neglected as it shows the typical bedding-in characteristic of the mechanical testing of composites, whereas data at high stresses may be affected by damage from contact with the loading pins. Sample displacements were calculated by measuring the movement of the bottom most layer of the sample underneath the loading pin, using digital volume correlation. The linear-elastic moduli obtained by this method at room temperature and 1100°C were ~50 GPa and ~40 GPa, respectively (**Table 16**).

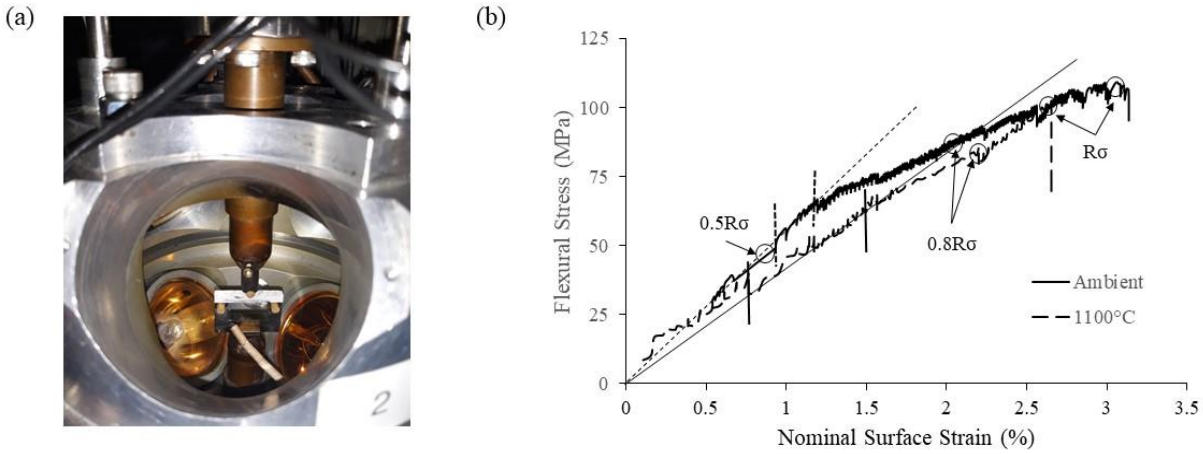

Figure 91: *(a) The setup used to carry out the three-point bend test, (b) Stress strain curve of samples tested using three-point bend test at room temperature and elevated temperature, S2. The straight lines at around 45° angle were used to calculate the modulus of the curve. The vertical lines indicated the region from which the gradient was measured [141].*

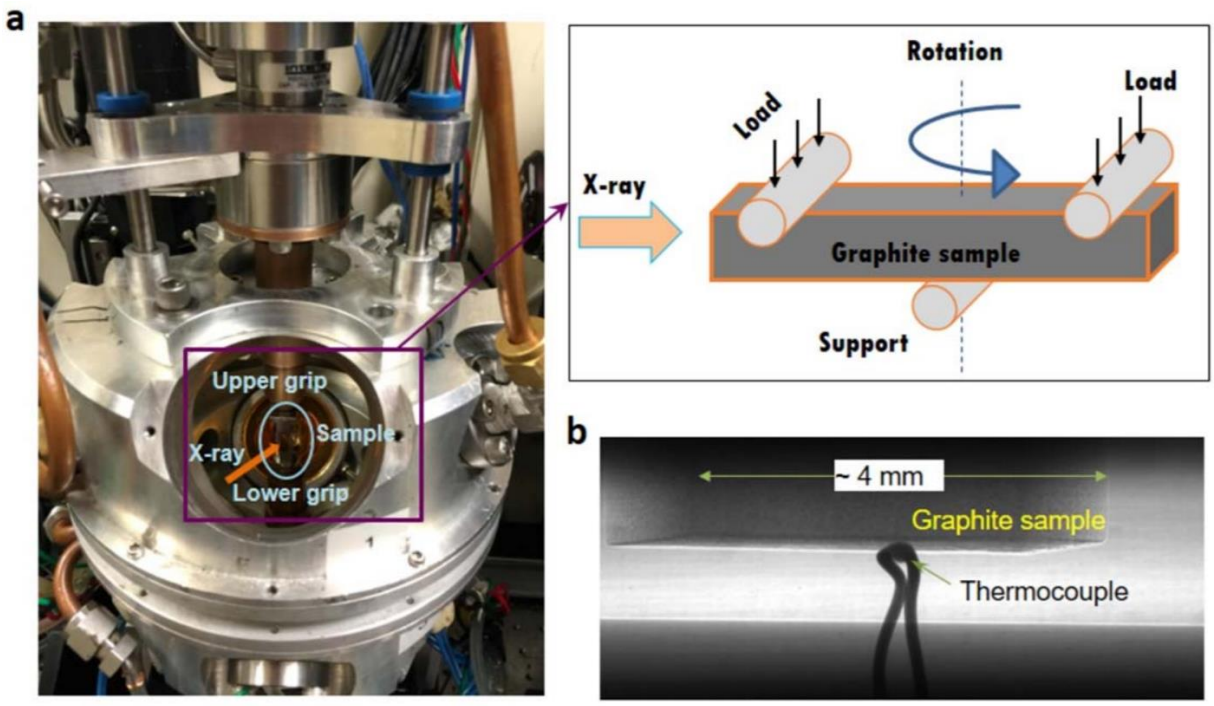

Figure 92: *(a) the high temperature test rig which was used to carry out the three-point bend tests (b) the three-point bend test schematic (c) the location of the thermocouple in reference to the sample* [141].

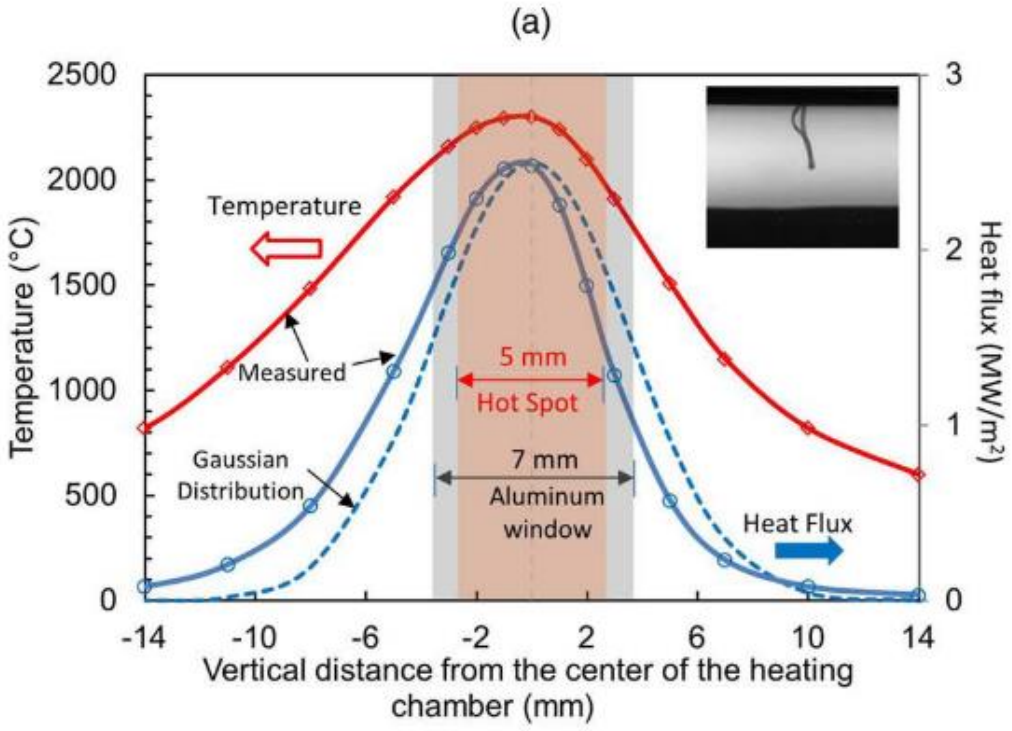

Figure 93: *(a) Distributions of temperature measured by bare thermocouple (red) and calculated heat flux (blue) along vertical axis of chamber. Measurements obtained by moving the thermocouple tip while continuously monitoring position by radiography (inset).* [114]

Table 16*: Mechanical properties obtained from three-point bend tests at room temperature (RT) and 1100°C. Duplicate tests, not observed by tomography, are shown in brackets. The uncertainties are the measurement error, and for the flexural modulus the variance of the best linear fit gradient.*

Test Temperature	**RT**	**1100°C**
Flexural stress at fracture (MPa)	107±0.4 (103±0.7)	100±0.6 (98±0.8)
Flexural modulus (GPa)	51.6±0.8	42.5±0.7

In addition to a reference at the pre-load, tomographs were recorded close to ~80% and 100% of the peak loads. A tomograph was also collected for the RT sample at ~50% of the peak load. These are respectively indicated as 0.5Rσ, 0.8Rσ and Rσ in **Figure 91**. The regions that were observed by tomography are identified in **Figure 94**; the loading pin is visible on the top of the tomograph. A smaller region is indicated that contains the results of the DVC analysis. The nominal shear force and bending

moment profiles that the samples experienced during loading are also shown for reference, assuming Euler–Bernoulli conditions.

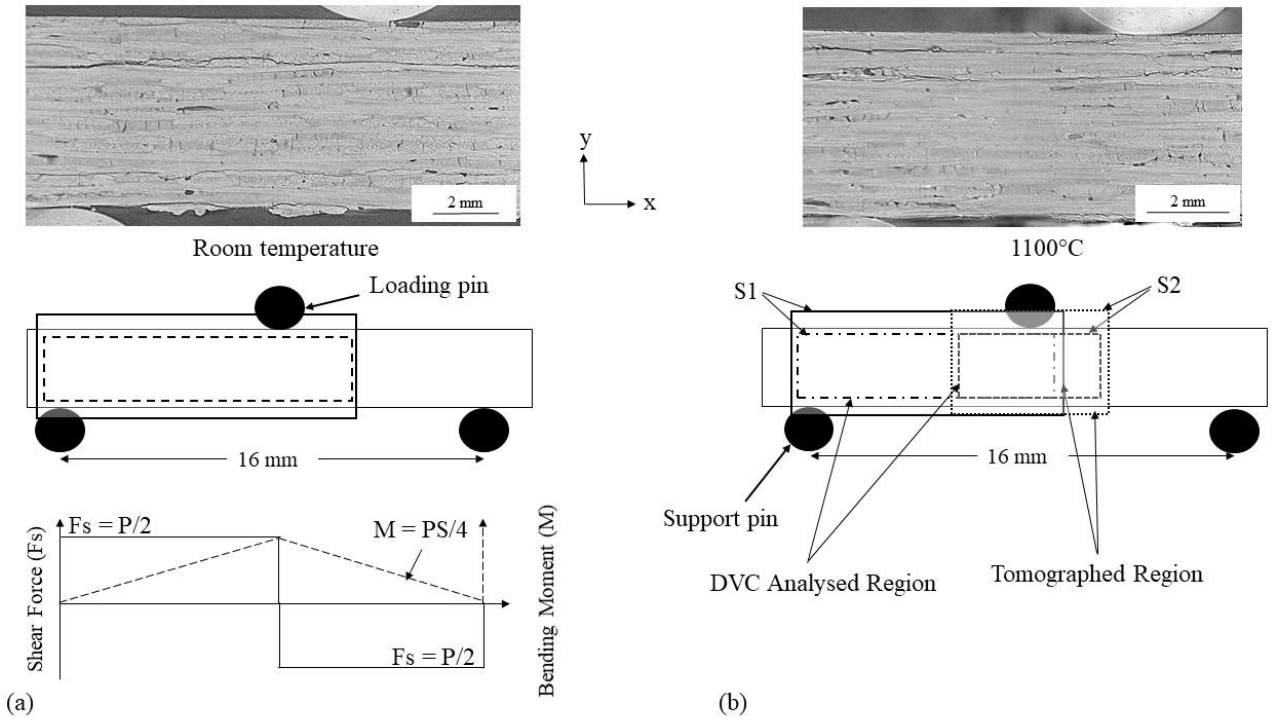

***Figure 94**: Three-point bend test setup showing the regions imaged by tomography (sections are presented at the pre-load) and analysed with digital volume correlation (DVC), in relation to the loading and support pins at a) room temperature and b) 1100°C. (S1 and S2 are the volumes tomographed at different resolutions: a tomograph section from S1 is shown). The theoretical shear force (Fs) and bending moment (M) diagram is also shown, as a function of load, P.*

A *post-mortem* analysis using optical microscopy (**Figure 95 a**), carried out, using the technique detailed in section **3.1.1.1**, shows that at RT, crack propagation was inclined at an angle of approximately 45° to 60° with respect to the loading axis, whereas the samples tested at elevated temperature showed complete delamination (**Figure 95 b**). Scanning electron microscopy confirmed the tendency for the crack to propagate with local paths that were inclined to the loading direction, with crack deflection also at the interfaces of 0° and 90° fibre tows (**Figure 95 c**). At 1100°C, significant delamination can also be seen; the sample also appears to be more prone to breakage and pitting as indicated by the polishing damage in the circled regions in **Figure 95 d**.

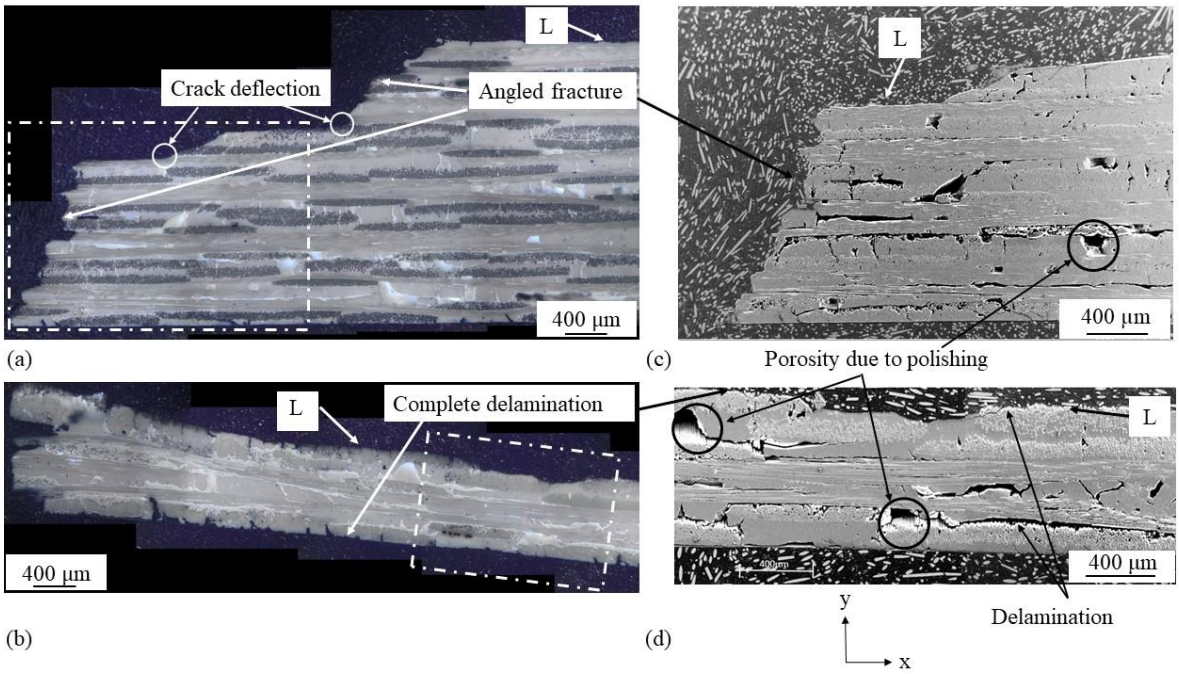

Figure 95: *Cross-sectional examination of tested specimens: Nomarski optical microscopy images of samples tested at (a) room temperature and (b) 1100°C. The dotted box in (a) and (b) shows the area analysed by scanning electron microscopy for samples tested at (c) room temperature and (d) 1100°C. The side labelled 'L' indicated the compressive surface on which the loading pin was located.*

The room temperature *in situ* tomography data are summarised in **Figure 96 a**, using vertical sections ('orthoslices' in the *y-x* plane) across the central region of the sample with the positions of the loading and support pins indicated. In region (i), which is beyond the outer support pin and so outside the zone of maximum shear force, an initial vertically oriented matrix crack was observed to close with increasing load. The formation of new cracks was only observed above 0.8Rσ, within the zone of high shear force; examples are identified in regions (ii) and (iii) and are presented at higher magnification in **Figure 96 b**. The cracks, parallel to the y axis, that were originally present in the matrix did not show any obvious extension. The three-dimensional nature of cracks (ii) and (iii) is visualised in **Figure 97**, which shows crack propagation along the interface between the 0/90° fibre tows, with these inter-tow cracks joined by sectors within the fibre tows at approximately 45°. These cracks extend across the whole width of the sample. The cracks highlighted in red in **Figure 97** are the original vertical matrix

cracks present in the sample prior to loading. 3D visualisation of these cracks, in Avizo, reveal that they extend across the whole width of the sample.

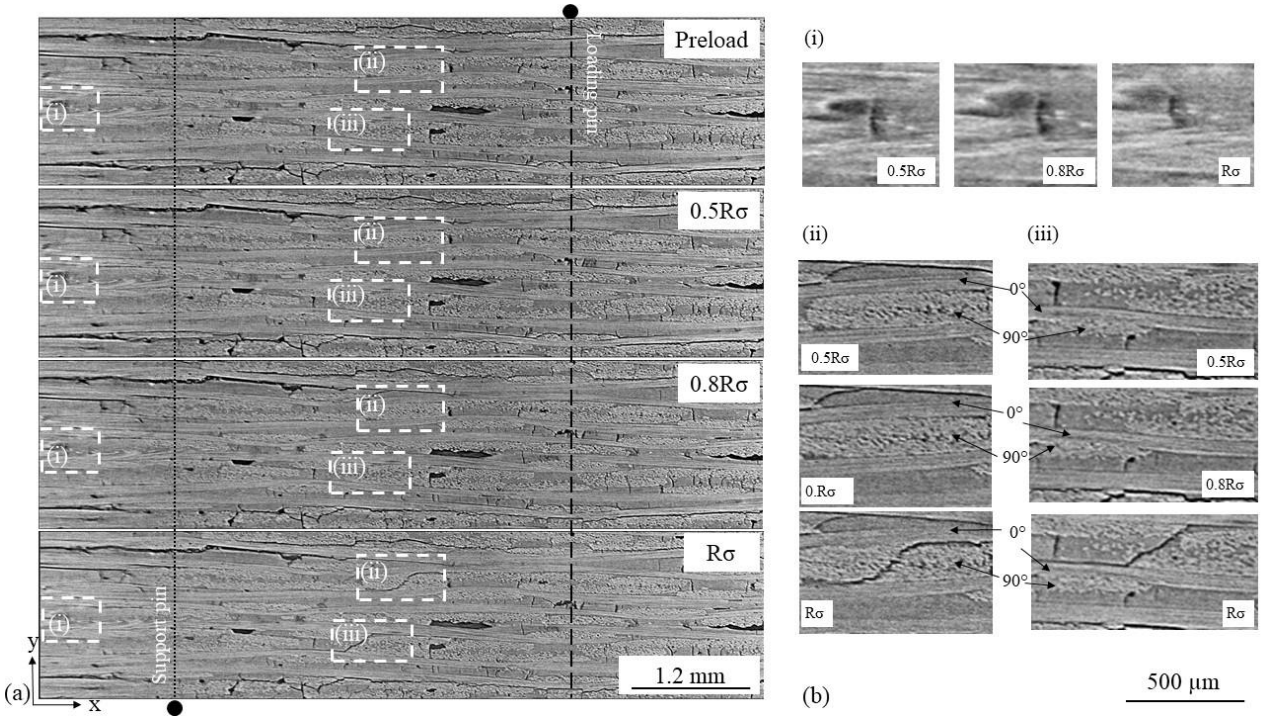

Figure 96: *Central orthoslices (x-y plane) of tomographs at room temperature (3.25 µm voxel); a) with increasing load from the pre-load to Rσ; b) magnified images at selected regions (i) to (iii) with increasing load. The locations of the load and support pins, and the 0° (parallel to x-axis) and 90° (parallel to z-axis) fibre bundles, are indicated.*

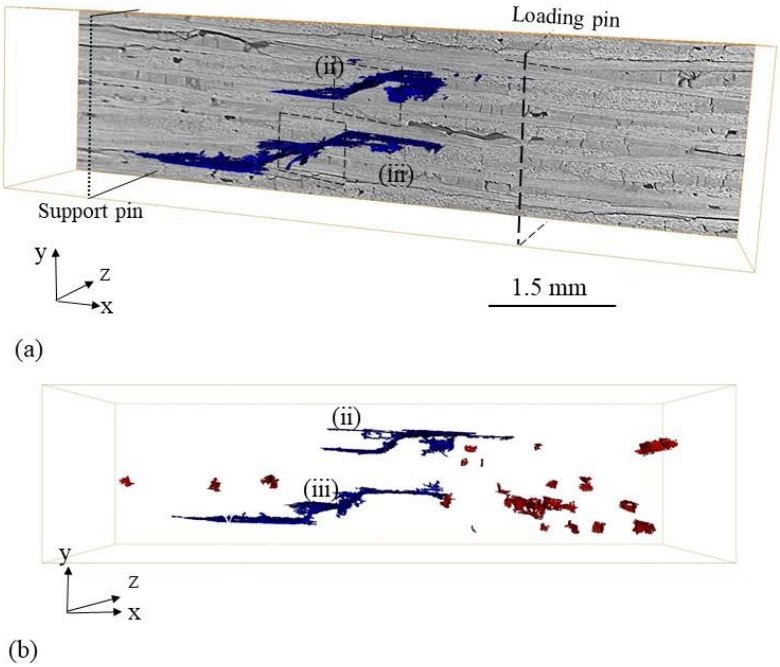

Figure 97: *3D visualizations from different perspectives (a, b) of the significant cracks developed at Rσ in the room temperature test, observed by X-ray tomography. The locations of the loading and support pins are indicated in (a). The newly developed cracks (ii) and (iii) are shown in blue, with the pre-existing defects in red.*

Results are similarly presented in **Figure 98** for sample S1, which was tomographed at 1100°C with the same 3.25 μm^3 voxel size as the RT sample. **Figure 98** shows inclined cracks at ~45°, labelled (ii) and (iii), and interlayer cracks, labelled (i). The cracks are visualised in three dimensions in **Figure 99**, which shows they also propagated across the whole width of the cross-section, similarly to those observed at RT. The interlayer cracks (i) are needle-shaped; such cracks were only observed at elevated temperature, mainly underneath the loading pin (*i.e.*, at the maximum bending moment) in both tensile and compressive regions, with some cracks also observed close to the support pin. These cracks were visualised separately in **Figure 99 (c & d)**. Volumetric thresholding was carried out, using Avizo, to identify the total volume covered by these cracks. The total volume of the needle shaped cracks was measured to be around 0.3%.

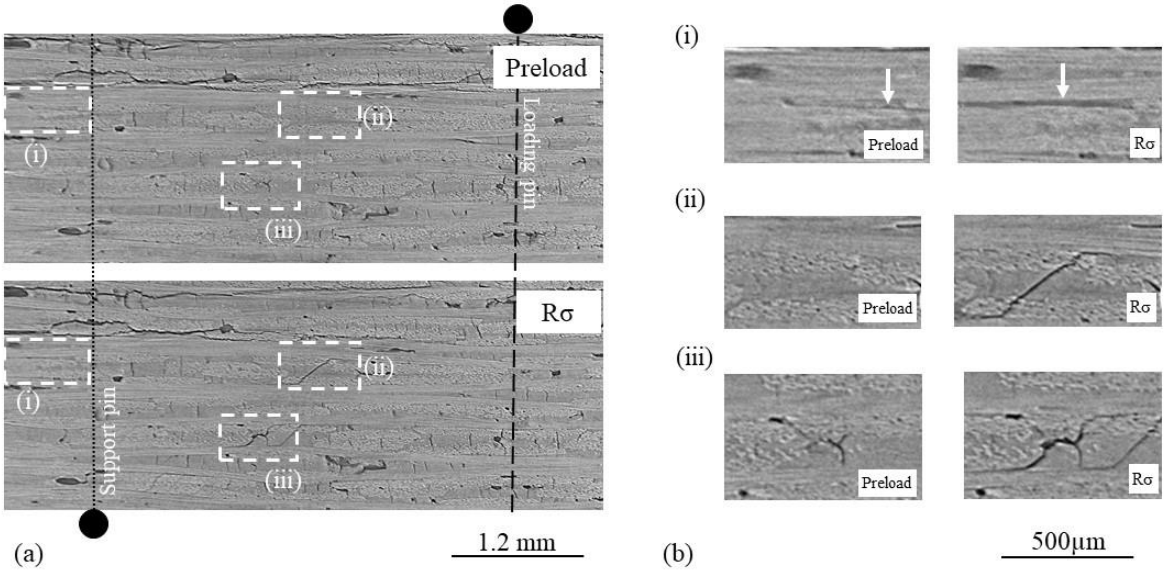

Figure 98: *Central orthoslices (x-y plane) of tomographs at 1100°C (sample S1, 3,25 µm voxel); a) with increasing load from the pre-load to Rσ; b) magnified images at selected regions (i) to (iii) with increasing load. The locations of the load and support pins, and the 0° (parallel to x-axis) and 90° (parallel to z-axis) fibre bundles, are indicated.*

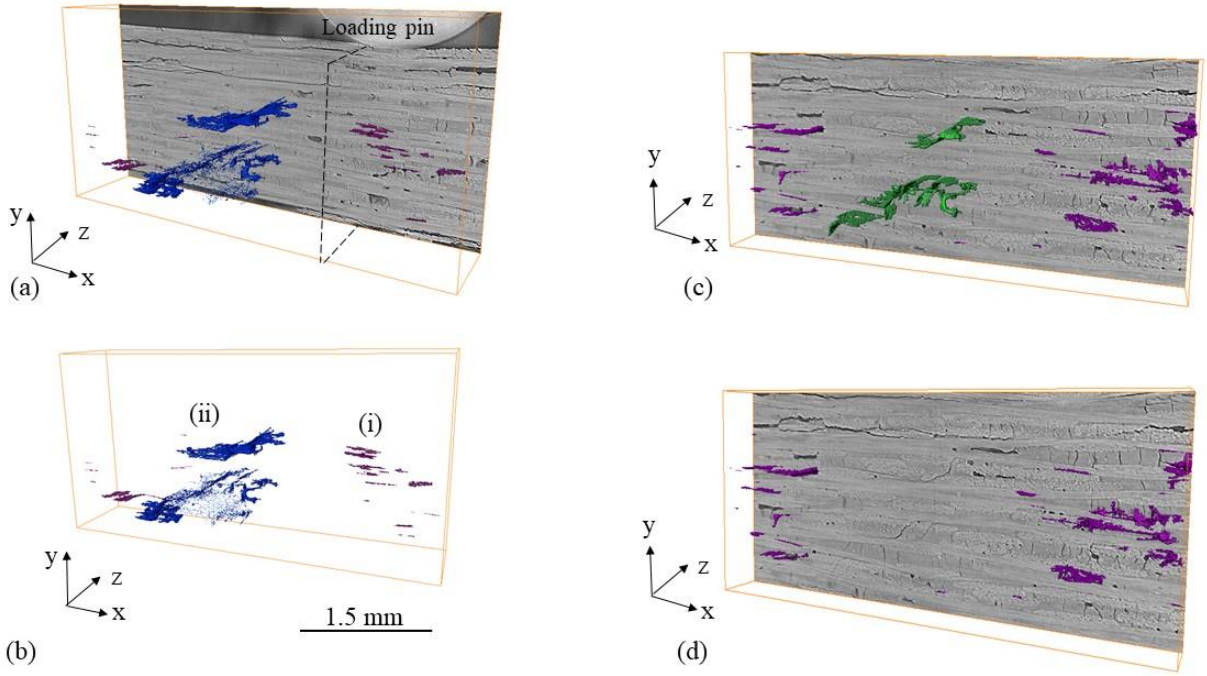

Figure 99: *Visualizations (a , b) of the significant cracks developed at Rσ at 1100°C in sample S1, observed by in situ x-ray tomography. The locations of the loading pin can be seen in (a). The newly developed cracks of two different types are identified: (i) through the cross section (blue) and (ii) needle shaped (purple).Visualizations (c & d) show limited area of the*

sample without the loading pin. This area was selected in order to quantify the net volume of the needle shaped cracks in comparison to the whole sample volume.

In Sample S2 (**Figure 100**) the region of maximum bending moment was tomographed at 1100°C at a voxel size of 1.3 μm^3. A typical pre-existing matrix crack is highlighted in region (i). No new cracks are observed until 0.8Rσ was exceeded. Examples of these new cracks are indicated in regions (ii) and (iii); these interlayer cracks propagate along the interface between the 0° and 90° fibre tows or parallel to the fibres within the tows. A 3D visualisation of the cracks observed at Rσ is presented in **Figure 101**. As observed in sample S1 at 1100°C, they are needle-like in shape, with width between 15-20 μm, and are aligned with the *x*-direction of applied load. **Figure 102**: Schematic illustration of the **proposed damage** sequence. The **yellow** layer represents the 0° fibres (parallel to the loading) and the green layer represents the 90° fibres. The white interlayer represents the matrix. Crack development process (a) Room temperature at 0.5Rσ, (b) Room temperature Rσ, (c) 1100°C 05.Rσ, (d) 1100°C Rσ. **Figure 102 (b)** shows how cracks develop at room temperature Rσ in comparison to **Figure 102 (d)** which shows how additional needle shaped cracks develop at 1100°C Rσ.

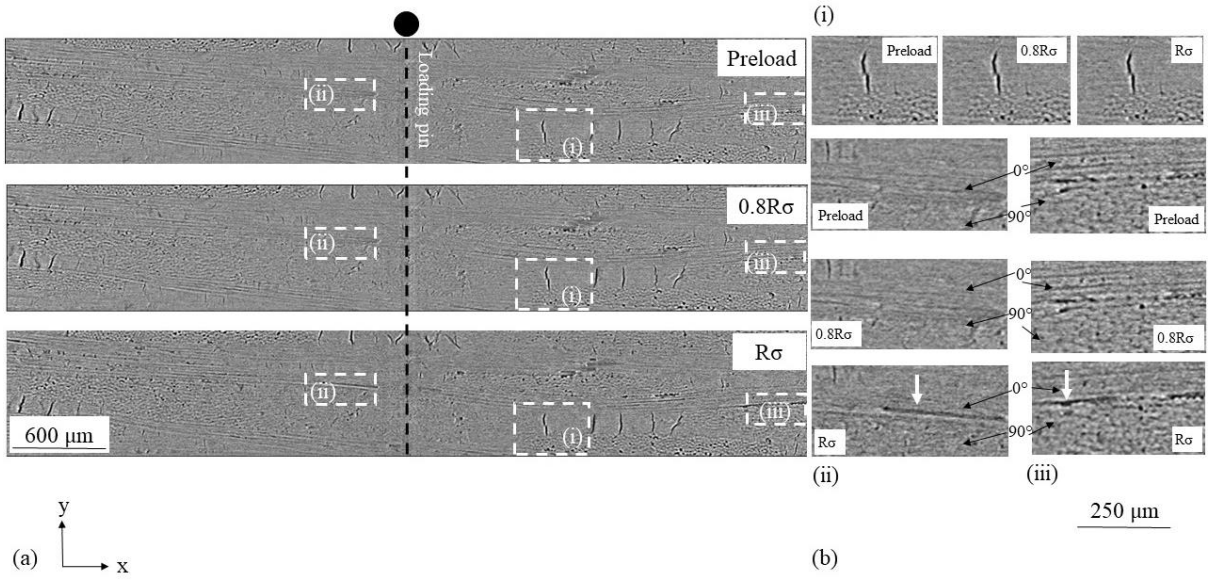

***Figure 100**: Central orthoslices (x-y plane) of tomographs at 1100°C (sample S2, 1.3 µm voxel); a) with increasing load from the pre-load to Rσ; b) magnified images at selected regions (i) to (iii) with increasing load. The locations of the load and support pins, and the 0° (parallel to x-axis) and 90° (parallel to z-axis) fibre bundles, are indicated.*

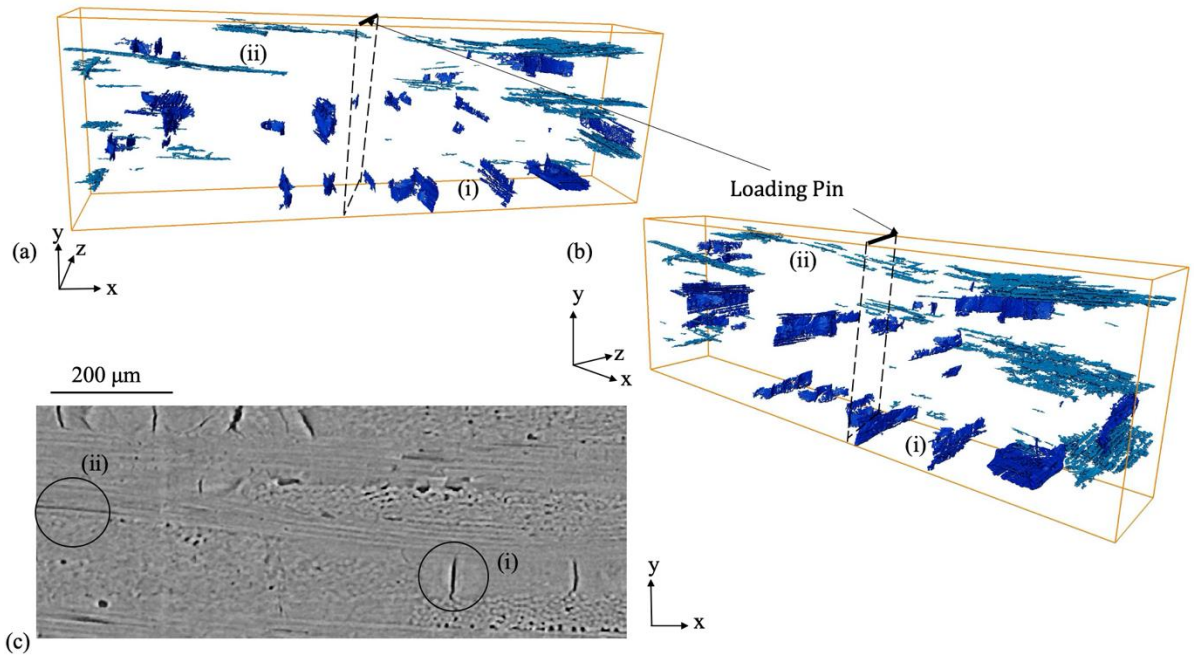

***Figure 101:** Visualizations from different perspectives (a , b) of the significant cracks developed at Rσ at 1100°C (sample S2), observed by in situ X-ray tomography. The location of the loading pin is indicated. An orthoslice (x-y plane) of the tomograph at Rσ is shown in c). The cracks labelled (i) are examples of pre-existing cracks in the matrix, whereas those labelled (ii) initiated prior to failure.*

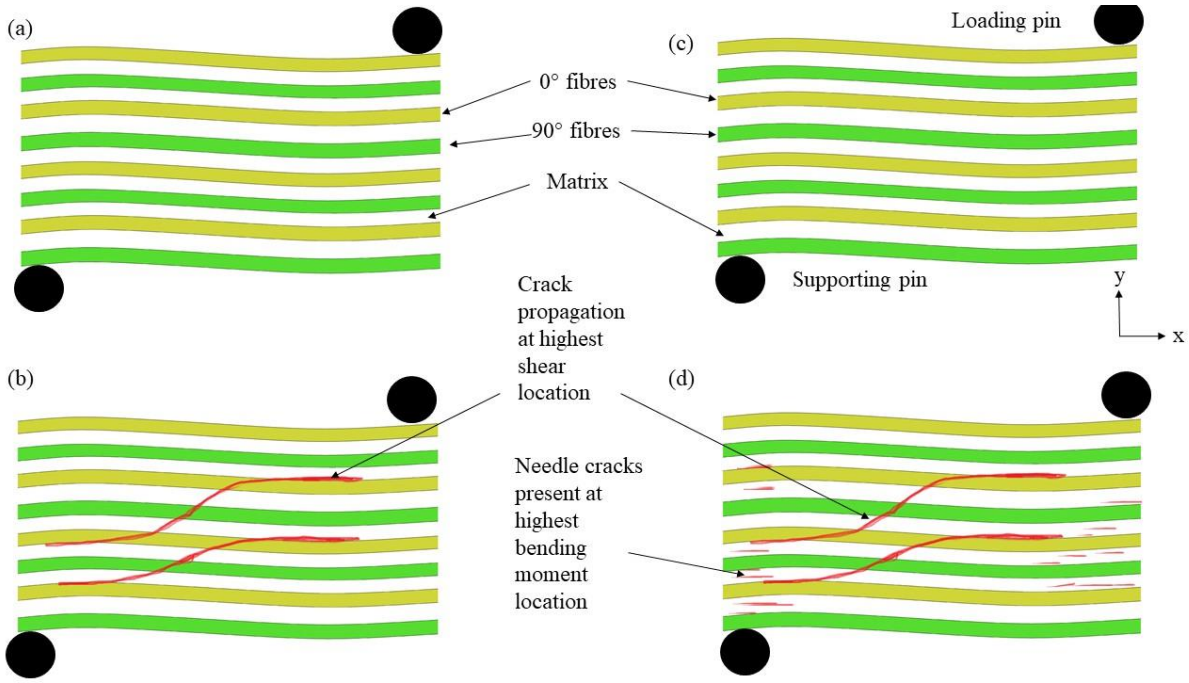

Figure 102: *Schematic illustration of the proposed damage sequence. The yellow layer represents the 0° fibres (parallel to the loading) and the green layer represents the 90° fibres. The white interlayer represents the matrix. Crack development process (a) Room temperature at 0.5Rσ, (b) Room temperature Rσ, (c) 1100°C 05.Rσ, (d) 1100°C Rσ.*

5.3.3 Analysis of Displacement Fields

Digital volume correlation (DVC) of the synchrotron X-ray tomographs was carried out with the LaVision DaVis software (version 8.3.1) using the direct correlation procedure and the pre-loaded tomograph as reference. DVC of tomographs provides three-dimensional displacement fields of the deformation relative to the reference image. The 3D local strain fields were calculated from the displacement fields measured using DVC with 3-point centred differentiation.

The displacement field of the tomograph data set can be used to calculate the strain tensor e_{ij} which defines the strain state for each orthogonal direction for each correlation window.

$$e_{ij} = \frac{\partial V_i}{\partial j} = \begin{bmatrix} e_{xx} & e_{xy} & e_{xz} \\ e_{yx} & e_{yy} & e_{yz} \\ e_{zx} & e_{zy} & e_{zz} \end{bmatrix} \quad (i \in \{x, y, z\}; j \in \{x, y, z\}) \qquad 18$$

The principle strains are determined by calculating the maximum eigenvalues of each plane that are independent of the coordinate system. Principle strains occur when the shear strains are equal to zero. The maximum normal 3D strain is the maximum of the 3 principle strains and was plotted in **Figure 103** and **Figure 106**.

The results obtained at room temperature are presented in **Figure 103 a** as maps of the maximum normal 3D strain, calculated from the local gradients of the displacement field (centred 3-point differentiation). Some quite localised strains are observed at low load (0.5Rσ), but these strains are sensitive to errors in the low magnitude displacement field and may not be reliable. No significant strains are developed until Rσ is reached, and these strains are coincident with the newly developed cracks in regions (ii) and (iii) (**Figure 103 b**). The normal strains, ε_{xx}, ε_{yy} and ε_{zz}, for Rσ were plotted in **Figure 104**, to see which of the three had the most profound effect on crack opening. It was observed that the normal strains in y were coincident to the cracks observed in the tomograph. The area where the rollers were in contact with the sample correspond to the location of maximum compressive strain in ε_{yy}, **Figure 104 (c)**.

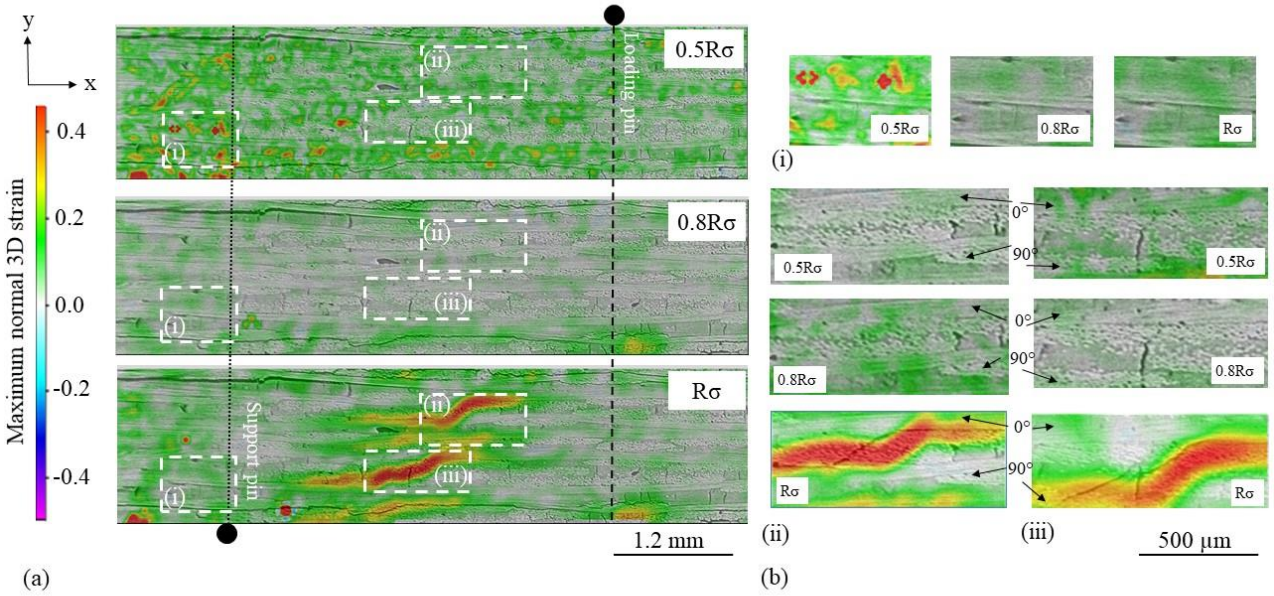

Figure 103: *Central orthoslices (x-y plane) of the maximum normal 3D strain field measured by DVC of in situ x-ray tomographs at room temperature (referenced to the pre-load): a) with increasing load from the 0.5Rσ to Rσ; b) magnified images at selected regions (i) to (iii) with increasing load. The locations of the load and support pins, and the 0° and 90° fibre bundles, are indicated. The backgrounds are orthoslices of the loaded tomograph at the same location. All images have the same strain scale. A high strain threshold was used for visibility. The transparent areas represent strain being well below the noise threshold of 0.02, which is small compared to the strain associated with microstructure cracks.*

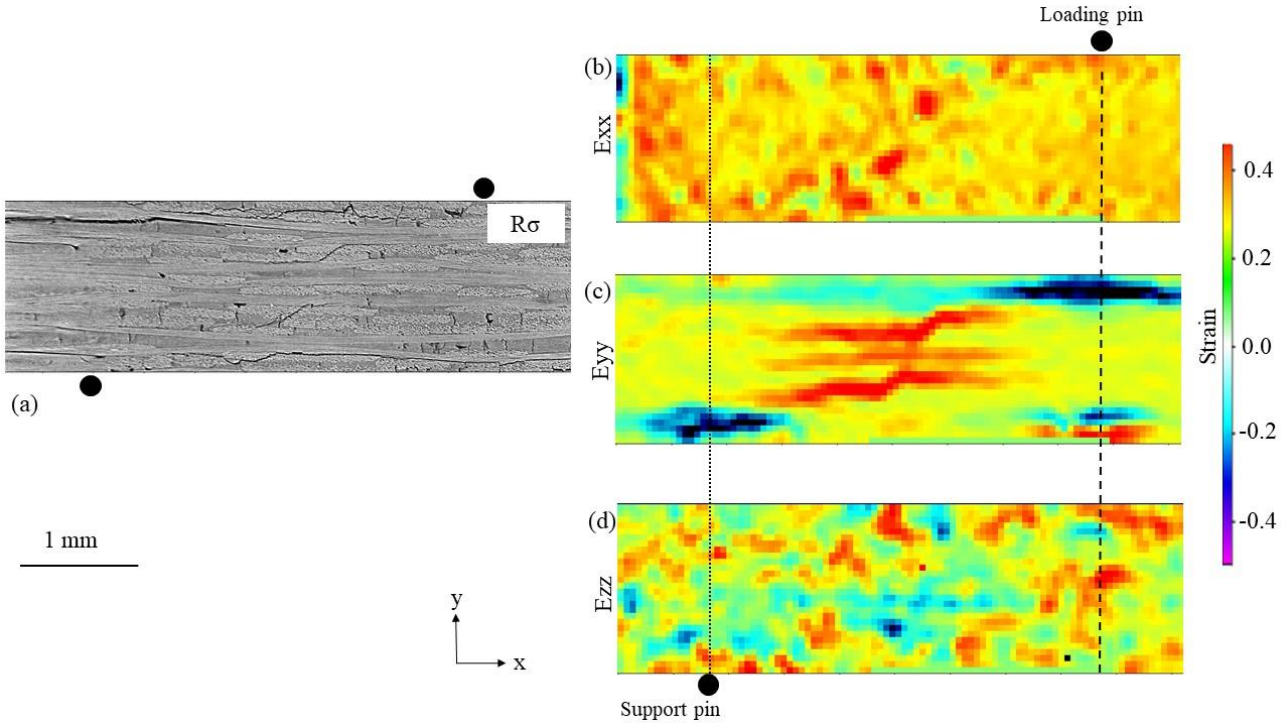

Figure 104: *Central orthoslices (x-y plane)of the three components of strain in the (a) x direction (b) y direction and (c) z direction along with the relevant X-ray tomograph. The locations of the load and support pins are indicated.*

A more detailed analysis of the crack at region (ii) is presented in **Figure 105**, using the relative displacements between points separated by ~100 µm across the crack; the values are averaged over 7 slices in the *z*-direction (~75 µm). This finds significant opening and shear displacements of the crack; within the 45° inclined region (location D), the crack has an opening displacement of about 3.5 µm, and a shear displacement of ~6 µm.

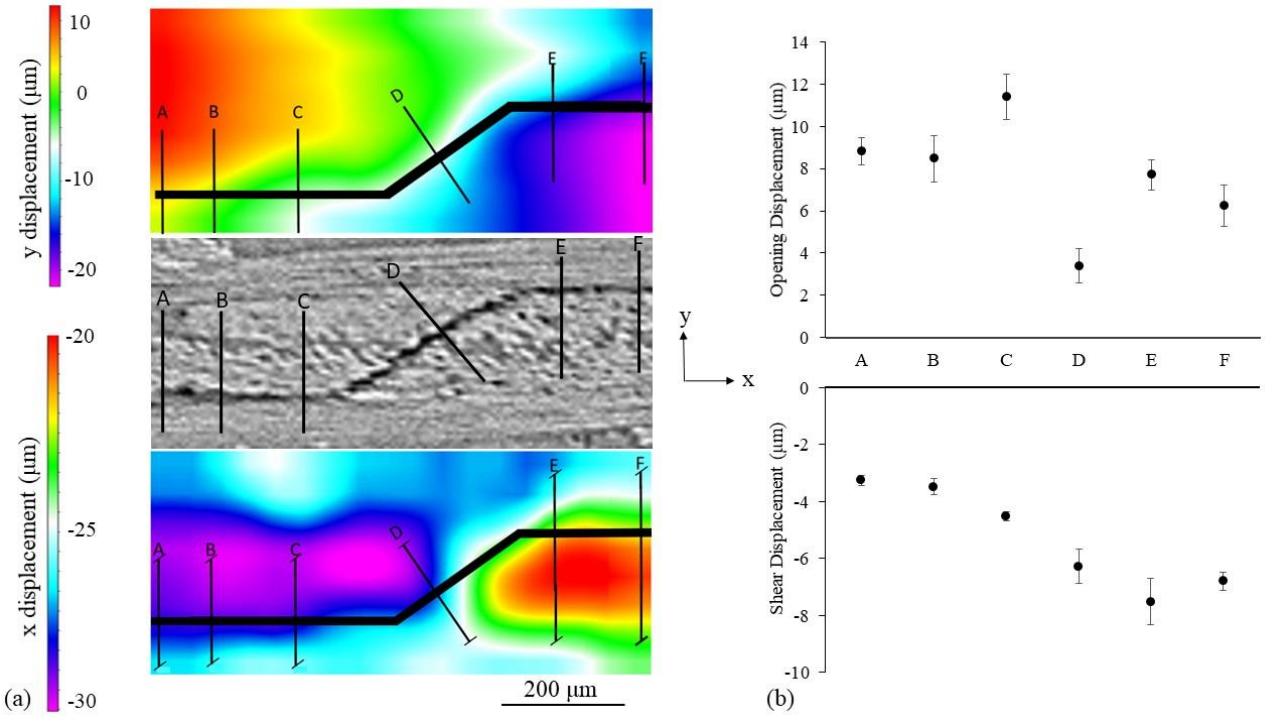

Figure 105: *Analysis of the relative displacements, calculated at Rσ relative to the pre-load, across a major crack developed at room temperature, identified in* ***Figure 103*** *b; (ii): a) sections of the 3D displacement field, showing the components of x- and y-displacement; b) the relative opening and shear displacements measured parallel and perpendicular to traces A to F, which are labelled in (a). The error bars are the sample standard deviation from measurements over a z-distance of 75 µm.*

DVC analysis of sample S2 at 1100°C shows regions of high maximum 3D strain at Rσ (**Figure 106 a**) that are coincident with newly initiated interlayer cracks such as those at regions (i) and (iii); these are presented in more detail in **Figure 106 b**. There are no measurable strains associated with the vertical matrix cracks, which are present in the as-fabricated microstructure (ii), indicating that they do not open significantly. The normal strains, ε_{xx}, ε_{yy} and ε_{zz}, for Rσ were plotted in **Figure 107**, to see which of the three had the most profound effect on crack opening. It was observed that the normal strains in y were coincident to the cracks observed in the tomograph. The cracks were labelled with black arrows in **Figure 107** (a) & (c). The ε_{yy} strains around the crack show compressive and tensile strains. This figure shows the problem of using ε_{yy} because the actual strain are not nicely aligned to the x and y axis. This results in the doubling effect, high and low ε_{yy} values, that are visible around the

crack. This is due to the fact that the strain is acting at an angle to the x and y axis which is easily resolved when plotting the maximum normal 3D strain, which is the maximum principal strain which picks up the location of the maximum strain and is independent of the direction of the strain. This doubling effect seen in **Figure 107 (c)** suggests the presence of shear strain within the sample.

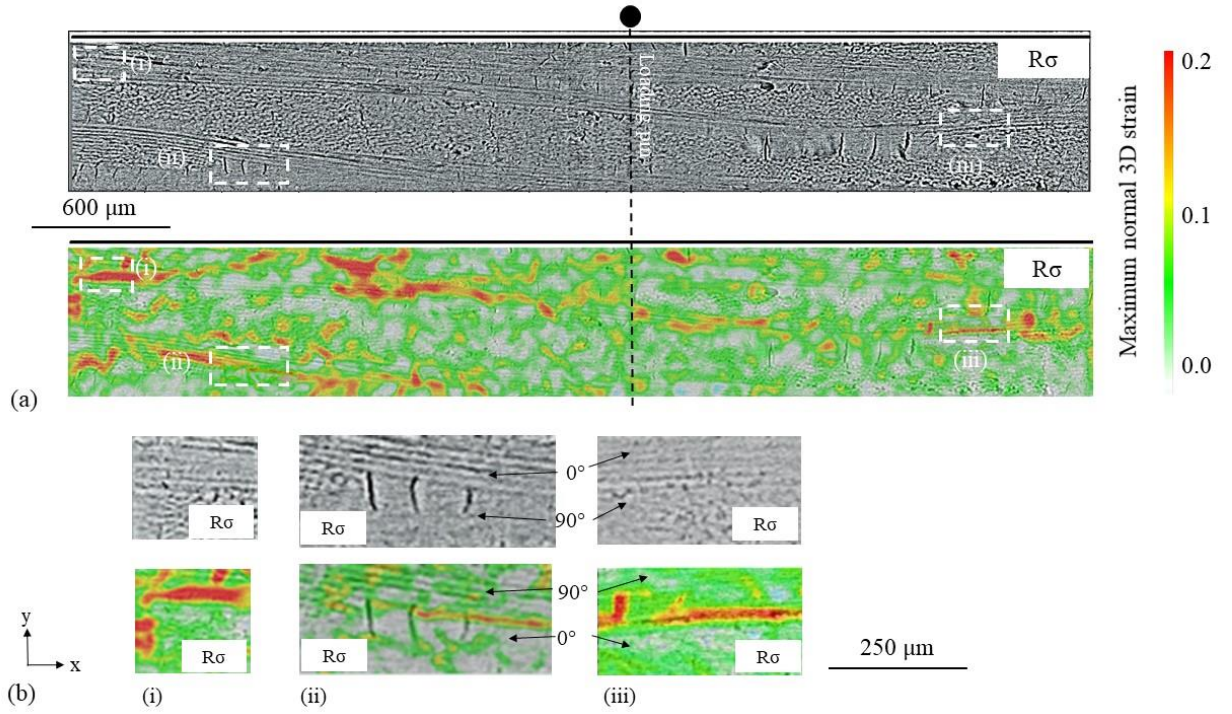

Figure 106: *Central orthoslices (x-y plane) of the maximum normal 3D strain field measured by DVC of in situ X-ray tomographs of sample S2 at 1100°C (referenced to the pre-load): a) at Rσ; b) magnified images at selected regions (i) to (iii) at Rσ. The locations of the load and support pins, and the 0° and 90° fibre bundles, are indicated. The backgrounds are orthoslices of the loaded tomograph at the same location. All images have the same strain scale. A high strain threshold was used for visibility. The transparent areas represent strain being well below the noise threshold of 0.02, which is small compared to the strain associated with microstructure cracks.*

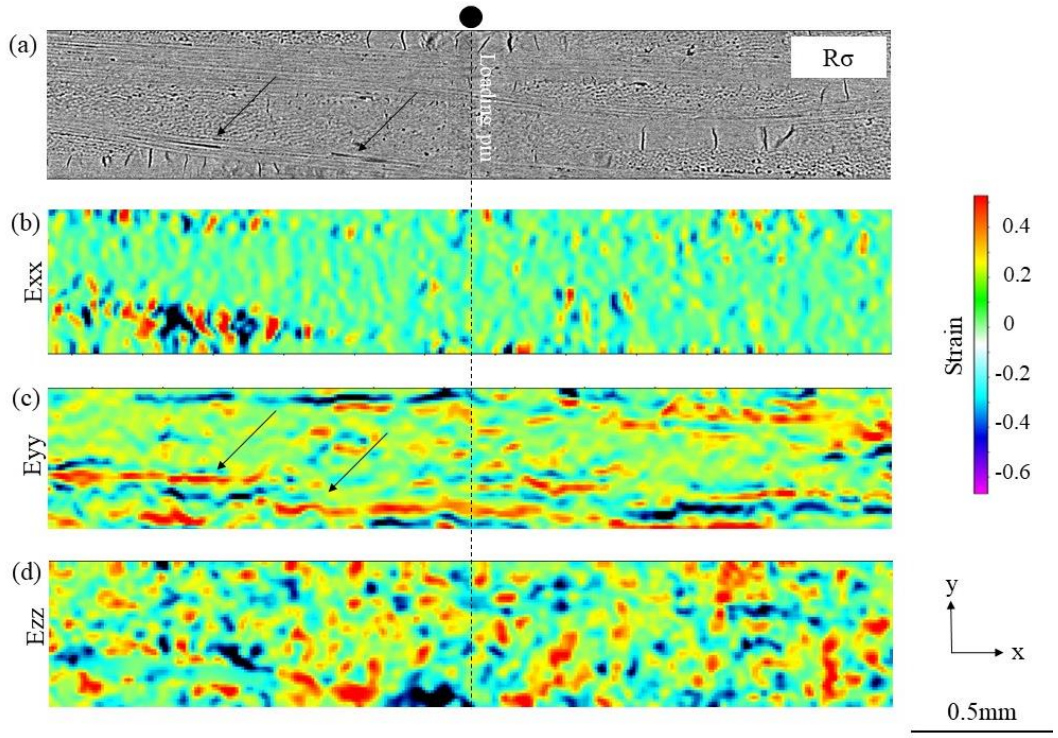

***Figure 107**: The three components of strain in the (a) x direction (b) y direction and (c) z direction along with the relevant X-ray tomographs of sample S2 at 1100°C (referenced to the pre-load). The black arrows labelled in (a) & (c) highlight the location of cracks that developed during loading.*

Analysis of the displacement field around a needle-shaped interlayer crack that developed within a fibre tow and along the fibre tow/matrix interface, following the same method as at ambient temperature (**Figure 108**), shows the crack shears by up to ~10 µm and opens by up to ~7 µm. There is a smaller crack opening magnitude within the fibre tow than at the fibre/matrix interface.

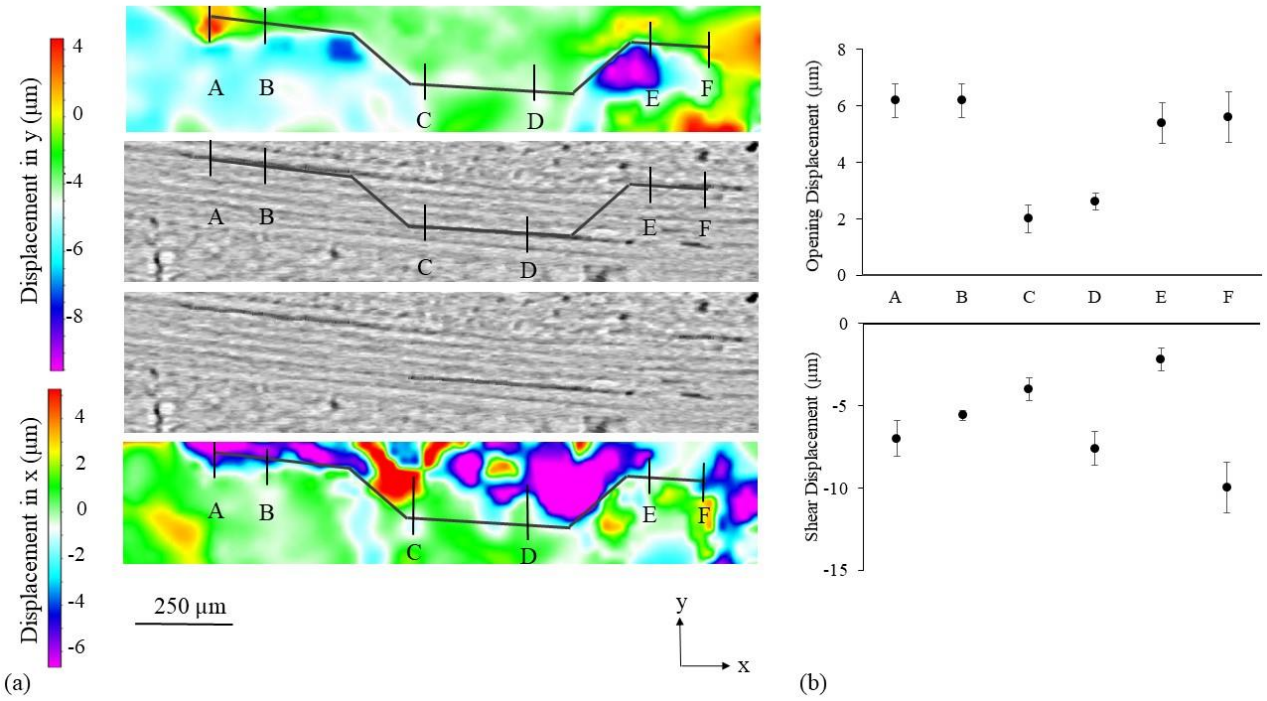

Figure 108: *Analysis of the relative displacements, calculated at Rσ relative to the pre-loaded state, across a crack developed at 1100°C (sample S2): a) sections of the 3D displacement field, showing the components of x- and y-displacement; b) the relative opening and shear displacements measured parallel and perpendicular to traces A to F, which are labelled in (a). The error bars are the sample standard deviation from measurements over a z-distance of 75 µm.*

The DVC-measured displacement fields allow the overall flexural behaviour of the specimens to be quantified. This was carried out by measuring the relative differences in *x*-displacement between points on two vertical (*y*-*z*) planes, positioned on either side of the central loading pin and separated by 0.7 mm (**Figure 109 a**); within this region the bending moment is within 5% of its maximum value. The average strains, obtained from the displacement change over the gauge length between the selected planes, are mapped in **Figure 109 b,** for the RT data. The strains are approximately constant across the sample thickness (*z*-direction), indicating that bending of the specimen is well aligned, and there is a trend from compression to tension over the specimen height (*y*-direction). Measurements obtained for the DVC analysis at 1100°C are more noisy, but show the same trends; the data from all tests are summarised in **Figure 109 c**, averaged across the specimen width and normalised by the ratio of bending moment (*M*) to second moment of area (*I*).

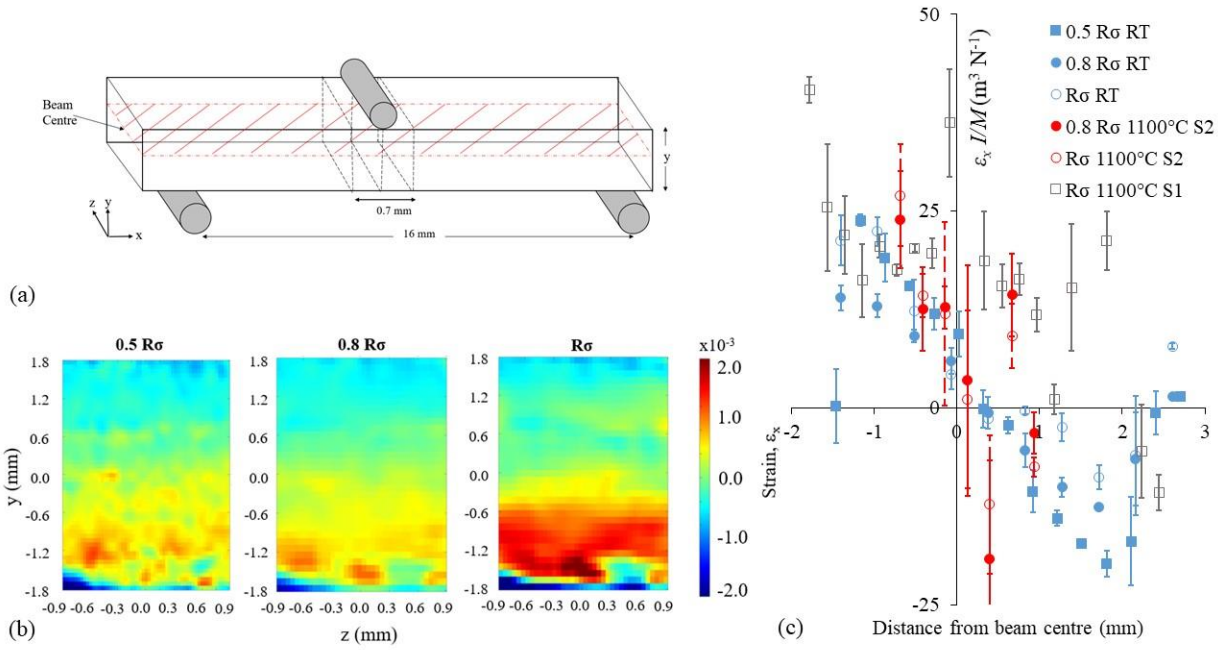

***Figure 109**: Flexural strain gradient measurement: (a) Schematic of the y-z planes, separated by a distance of 0.70 mm, between which the relative x-displacements were measured to obtain the average flexural strains, ε_x, at the location of maximum bending moment; (b) maps of the flexural strain, ε_x, with increasing load up to Rσ at room temperature; (c) the normalized flexural strain, $({}^{\varepsilon_x I}/_{M})$ as a function of distance in the y direction from the beam centre for different loads at room temperature (RT) and at 1100°C (samples S1 and S2). The data are averaged in z, I is the second moment of area of beam cross-section, and M is the change in applied bending moment. The error bars are the standard deviation of the measurements.*

The effective elastic moduli of the beams were estimated from these strain data using the assumptions of simple Euler–Bernoulli bending. This assumes isotropic properties and neglects any movement of the neutral axis and fits a linear gradient to the variation of flexural strains, ε_x, with position *y* to calculate the beam's radius of curvature, R:

$$M = {}^{EI}/_{R} \text{ and } \frac{d\epsilon_x}{dy} = -{}^{1}/_{R} \ , \qquad 19$$

where *M* is the change in the applied bending moment, *I* is the second moment of area of the beam and *E* is the elastic modulus [126]. The effective elastic moduli were calculated using a linear regression analysis of the normalised data, averaged across the specimen width (**Figure 109 c)**; the resulting values are summarised in **Table 17**. The room temperature modulus at 0.5Rσ was ~38 GPa, but it was

progressively reduced with increasing load at 0.8Rσ and Rσ. At 1100°C, the modulus for Sample S2 was approximately 40 GPa at 0.8Rσ and reduced with increasing load at Rσ. Sample S1 had a low modulus of around 27 GPa at Rσ.

Stress (Rσ)	RT	1100°C (S1)	1100°C (S2)
0.5	37.9±1.4		
0.8	34.7±1.9		40.1±2.4
1.0	33.2±3.2	26.6±3.7	35.9±4.1

Table 17: *The flexural modulus (GPa) obtained by linear fit to the normalised flexural strains (**Figure 109**c) for different loads at room temperature (RT) and 1100°C. The uncertainty is from the variance of the best fit gradient.*

5.4 Discussion

The microstructure of the Nextel 720 fibre/alumina matrix ceramic matrix composite is similar to that reported by Tandon *et al*. [142] with each layer having an approximate thickness of 0.58mm. The inherent matrix porosity and defects (cracks, **Figure 86**) are caused either in the evaporation process during the initial drying stage or by matrix shrinkage during the sintering process, when the sample is cooled down to room temperature [121,143]. The elastic moduli in **Table 16** were estimated using the maximum normal displacement in y, measured underneath the loading pin, using DVC, and so are not necessarily accurate, but the relative magnitudes of the flexural strengths and moduli are consistent with similar biaxial oxide/oxide composites, albeit in the lower range [144]. A previous review [24] found no significant effect of temperature up to 1100°C on the strength and modulus for 0°/90° composites of Nextel 720 fibres in an alumina-silicate matrix for tensile loading parallel to the fibre bundles. This is consistent with the data in this study; the measured difference in strength with temperature (**Table 16**) for the small number of samples tested is not statistically significant. In order to increase the accuracy of the values presented in **Table 16**, multiple samples should be tested under each condition. The initial porosity of these composites is high (>24 vol.%), due to matrix and interface cracks, but is similar to

that observed in comparable oxide-oxide composites [145]. Due to oxide based CMC not having an interfacial layer between the fibre and the matrix, the porosity plays a major role in crack deflection and in turn increases the fracture toughness of the material system. Hence porosity is an important microstructural feature that needs to be tweaked and optimised to control strength and maximise crack deflection.

Analysis of the *in situ* X-ray tomographs using DVC to measure local displacements allows discrimination between new cracks and the inherent defects that formed during manufacture; the latter did not open or propagate measurably both at room temperature and at 1100°C, (**Figure 105** and **Figure 108**). It also helps understand the interaction between the microstructure and the cracks formed under loading. The analysis presented in **Figure 105** and **Figure 108** indicate that the cracks had both a shear component and a tensile component as both x and y displacements had significant magnitude. Significant new cracks were observed to initiate and propagate only close to the maximum flexural strength, though the possible formation of fine cracks below the resolution of μXCT cannot be discounted. The effective elastic moduli, obtained by specimen curvature measurement via DVC (**Table 5**), do not measure the actual Young Modulus, due to the gradient of strain and anisotropic properties. Nonetheless they are a measure of the flexural stiffness of the composite specimen. This shows that in the absence of visible new damage (*i.e.*, up to 0.5Rσ at RT and up to 0.8Rσ at 1100°C), the moduli are similar at RT and 1100°C. The reduction in effective modulus observed at higher loads can be attributed to the development of damage, which acts to reduce the composite stiffness. The initiated damage results in generating a higher permanent strain for a given stress hence reducing the bulk effective modulus.

The TEM observations (**Figure 88**) show no observable difference between the structure of the interfaces of samples tested at room temperature and at 1100°C. Close study of the interface between the fibre and the matrix showed no signs of sintering. However, the increase in temperature to 1100°C has significantly changed the failure patterns; at room temperature, the fracture was inclined across the fibre bundles (**Figure 96**, **Figure 97**), whereas at 1100°C the fracture propagated similarly to room temperature, but a new crack mode was observed which resulted in crack propagation between the fibre bundles leading to complete delamination.

At both room temperature and 1100°C, cracks initiated in regions of high shear and low bending moment (**Figure 103**), located between the loading and the support pin, and consequently the crack openings displayed a significant shear displacement (**Figure 105**). The inclined crack path through the 0° fibre bundle, in which the fibres are oriented in the *z*-direction and loaded orthogonally in the *y*-direction, with the E_{yy} orthogonal strain mirroring the crack path, **Figure 104**, indicates that the crack open up and shear as a response to the applied stresses. A significant crack at room temperature (**Figure 103**, region (ii)), which also generated inclined fracture across the 0° fibre bundle, developed in the region below the neutral axis where the *x*-direction loading is compressive. This suggests these cracks may initiate due to the shear loading of the 0° fibre bundles. They then propagate by longitudinal splitting along the bundle interfaces, similarly to delamination from transverse cracking [146]. The normal strain calculated using DVC, **Figure 104,** revealed that the cracks were mainly driven by normal strain in y axis. Similar shear cracking of matrix and interlaminar deflection has been observed in compression testing of a Nextel 610/Alumina composite [145]. The final fracture path is a consequence of the interactions between these propagating shear and delamination cracks with pre-existing defects in the matrix and also at the fibre bundle/matrix interfaces.

When the displacements in x across the depth of the sampled were averaged, **Figure 109**, the microscopic behaviour that should be expected in beam bending, with a well-defined neutral axis, the top surface in compression and the bottom surface in tension, is observed. The strain maps in **Figure 104** and **Figure 107** show localised strain and are unable to reveal the classic beam bending behaviour and are mainly used to show the effects of damage. This proposed sequence of damage development could be confirmed by more frequent tomographs in a future study. A multi-scale analysis [99] could also be carried out in order to observe the sample at smaller voxel size to resolve micro cracks at lower load, which results in changing the effective flexural modulus, which weren't visible at the current resolution.

The cracking observed at 1100°C was similar to that at room temperature, but needle-like interlayer cracks, aligned parallel to the *x*-direction of loading, developed additionally between and within the fibre bundles. These cracks were observed in both the tensile and compressive regions of the flexural specimen, and tended to occur in the regions of highest bending moment, *i.e.*, close to the position of the central loading pin, as well as close to the support pin (**Figure 99**, **Figure 101**). These are the locations where higher shear strains would be expected between lamellae of different compliance in a laminated composite beam [147]. The normal strain analysis of sample S2, **Figure 107**, indicates that the cracks were also driven by normal strain developed in y axis. **Figure 102** shows a schematic of the cracks that developed at RT and at 1100°C highlighting the differences in crack development amongst the two.

The elastic properties of the matrix and fibres are essentially constant at the temperatures investigated, so the stresses that develop within the microstructure due to external loading are not expected to differ at room temperature and 1100°C. On cooling from sintering, misfit strains will

develop due to differential thermal contraction of the matrix and fibres (alumina (7.9×10^{-6} C^{-1}) and the Nextel 720 alumino-silicate fibre (6.0×10^{-6} C^{-1})) [148]. The fibres have the lower expansion coefficient, so a residual compressive misfit stress would be expected at the fibre-matrix interface [149]. The fibre crystallographic texture may cause anisotropic properties, giving additional stress between the 0° and 90° fibre layers [150–152]. At 1100ºC, which is close to the sintering temperature, the thermally induced residual stresses would be significantly relaxed. A reduction in the compressive residual stress between the matrix and fibre would decrease the frictional sliding resistance of the interface, and this may be the cause of the increased tendency for interfacial failure and the needle-like interlayer cracks that are observed at 1100°C at locations of higher shear stress. Interfacial failure could be further encouraged by creep, which has been observed to occur at 1100°C in a Nextel 720/alumina composite at high stress [88]. Repeat tests should be done on a number of samples in tandem with tomography at smaller voxel sizes to see how these micro cracks form and interact with the microstructure at 1100°C.

5.5 Conclusions

In situ synchrotron X-ray observations of flexural bending tests on a Nextel 720 fibre/alumina matrix CMC, conducted at ambient and 1100°C, show there is a change in failure mechanism at the higher temperature. XCT is one of the few techniques that can be used to capture 3D high resolution imaging non-destructively at these elevated temperatures. No change in the interface was observed in both samples, TEM study showed no signs of sintering. Measurements of the strain gradient, using digital volume correlation, demonstrate a reduction in effective flexural modulus that is coincident with the observation of mechanical damage as significant internal cracks initiated and propagated close to the flexural strength. At both room temperature and 1100°C, cracks are initiated by the shear of the fibre bundles that are oriented perpendicular to the loading axis; these cracks are then deflected along

the fibre bundle/matrix interfaces. The cracks were observed to propagate through the whole cross-section of the sample. At 1100°C, interlayer cracks also initiated between, and within, the fibre bundles, and caused significant delamination. These cracks, were needle-shaped and only a few slices thick, were observed in regions of the highest bending moment. The change in failure mode at 1100°C may be explained by relaxation of the thermal misfit stresses to decrease the frictional sliding resistance of the fibre/matrix interface. The presence of texture in the fibre could also give rise to anisotropic properties, resulting in additional stress between the 0° and 90° fibre layer. At 1100°C creep starts to be active in these material systems which could also propagate interfacial failure. Repeat tests at higher tomography resolution would be able to shed more light on how these needle-like cracks develop and how they interact with the microstructure.

CHAPTER 6. Design and experimental evaluation of CMC based sealing rings at 1100°C

6.1 Introduction

Literature suggested that the strength and stiffness of an oxide based CMC is a function of the fibre orientation with respect to the load direction [86]. A difference in orders of magnitude could result as a function of fibre orientation [24]. Studies also suggests that the mechanical properties of CMCs fabricated at different temperatures varied greatly [38]. Hence work needs to be done to optimise the fibre layout and architecture, along with the processing temperature, to produce a Nextel 720 with alumina matrix with highest creep resistance at a service temperature of 1100°C.

This chapter looks at understanding the effects of different combinations of weaves, layups and processing parameters on the mechanical properties of Nextel720/Alumina based composites, at 1100°C. Three-point bend tests were carried out at 1100°C, in an argon atmosphere, in order to understand which particular system provided the highest proportional limit stress.

This chapter then studies the behaviour of different composite designs under constant stress and constant displacement conditions at 1100°C. Using the modulus values calculated for EF 19-1 and EF 20-1, sealing rings with a gauge diameter of 140 mm and 5x5 mm cross-section were designed, roughly 8 plys in thickness. It was estimated a flexural stress of 25 MPa was required to generate enough spring, which is defined as the difference between the free and fitted gaps of a sealing ring, to hold the sealing ring in place and close the gap during service conditions.

Beams, of 4x5 mm cross-section, were hence loaded under a constant flexural stress condition of 25 MPa, and the creep strains were quantified using the permanent displacement generated in each

sample. The samples were kept under load for 2 hours, at 1100°C, in order to be able to quantify the primary and secondary creep regimes. All samples were imaged using X-ray tomography pre- and post-creep tests, in order to evaluate how and where the damage developed during the loading regime. It must be noted that some damage could disappear when the beams are in the unloaded condition due to crack closure. This is because once the load is removed the cracks come together and could be too fine to be observed by tomography. Using the knowledge gained from the beam experiments, two piston rings were designed and subjected to a constant deflection with a nominal stress of 25 MPa, with the objective of producing a fully functional sealing ring. These rings were examined using ex-situ X-ray tomography to quantify the microstructural failure. The stress relaxation tests at 1100°C were used to quantify their sealing performance.

6.2 Material Systems

8 different combinations were used to produce panels with dimensions of 150 x 150 x 5 mm, which were then tested to study the effects of different processing parameters on the mechanical properties of the composites. **Table 18** shows the different combinations used to maximise the elastic deformation of the system. Two different weave patterns, namely EF 19 and EF 20 were used in this study. EF 19 has a weave architecture with 50% fibres in the warp and 50% fibre in the weft direction [72]. It uses a 3000 denier fibre tow which is woven into 8 harness satin weave pattern as seen in **Figure 13 CHAPTER 2 above**. EF 19 has 9 threads per cm in both directions.

EF 20 is a unidirectional weave that uses two distinct deniers(d) for weaving [72]. 10,000 d is used in the warp direction whilst 1500 d is used in the weft direction, with 6 threads per cm in warp and 2

threads per cm in weft, as seen in **Figure 13 CHAPTER 2 above.** This equates to around 80% fibre in the warp and 20% fibre in the weft.

After infiltration of the weave pattern with slurry, two different layups were investigated the first one being the conventional 0/90° layup. In the 0/90° layup, the impregnated weave is laid on top of each other first in longitudinal and then transverse direction. The second type of layup involves the cloth being cut into 20 mm wide strips, which are then laid on top of each other with a 10 mm overlay, as seen in **Figure 110 a**. Once the first layer is laid a second layer is produced on top following the same pattern as seen in **Figure 110**. This is known as the involute layup [153,154], which helped increase the shear strength between the layers. The breaks in the fibre allows it to possibly bend more. It gives rise to a much more complicated stress distribution within the structure. The involute produces a small step in the y direction which could provide a more 2.5 D. effect. The main benefit of this type of layup is experienced in cylindrical applications, which predominantly experiences hoop stress.

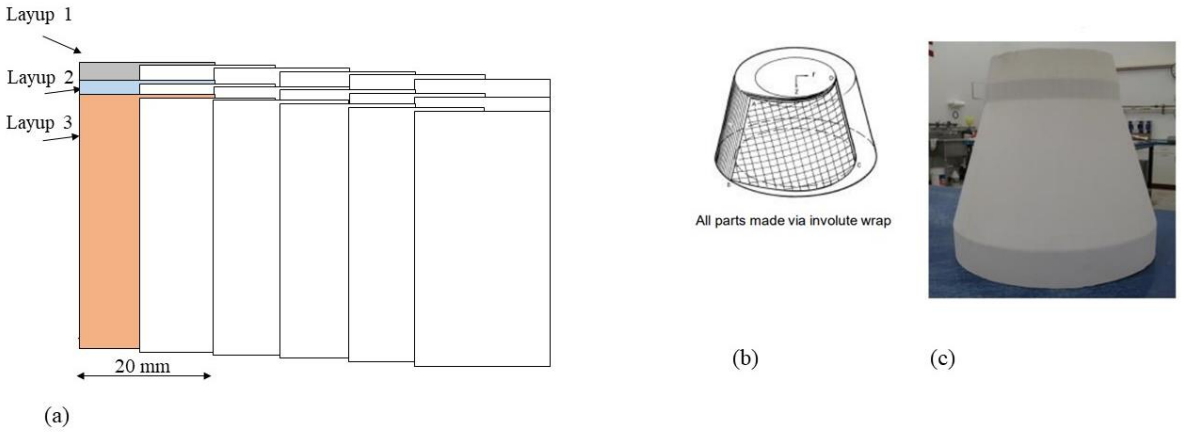

Figure 110: *The involute layup used to fabricate (a) the 20 mm wide strips laid with a 10 mm overlap, (b) involute rapping used for conical designs, (c) a demonstrator manufactured using involute layup* [155].

Sample No.	Weave type	Layup	Temperature
EF 19-1	EF 19	Involute	CHI Temperature
EF 19-2	EF 19	Involute	1250°C
EF 19-3	EF 19	Involute	1200°C
EF 19-4	EF 19	0/90°	1200°C
EF 20-1	EF 20	Involute	CHI Temperature
EF 20-2	EF 20	Involute	1250°C
EF 20-3	EF 20	Involute	1200°C
EF 20-4	EF 20	0/90°	1200°C

Table 18: *Different samples produced for testing.*

The sintering temperatures were varied in order to understand the effects of three different temperature regimes on the mechanical properties. The CHI temperature is proprietary to Composite Horizons Inc, the company that supplied the samples, and has not been disclosed to the author.

6.3 Three-point Bend Tests

6.3.1 Displacement Measurement

Samples were cut into rectangular beams, 25 mm in length, with a cross-section of around 4 mm by 5 mm, which constitutes of roughly 8 layers. The samples were tested using a three-point bend test configuration, **Figure 111**, with graphite grips manufactured in accordance to the drawing provided in **Appendix 1.** The distance between the centres of the support pins was measured to be 16 mm. **Figure 112** shows the load vs displacement curves produced using the raw data.

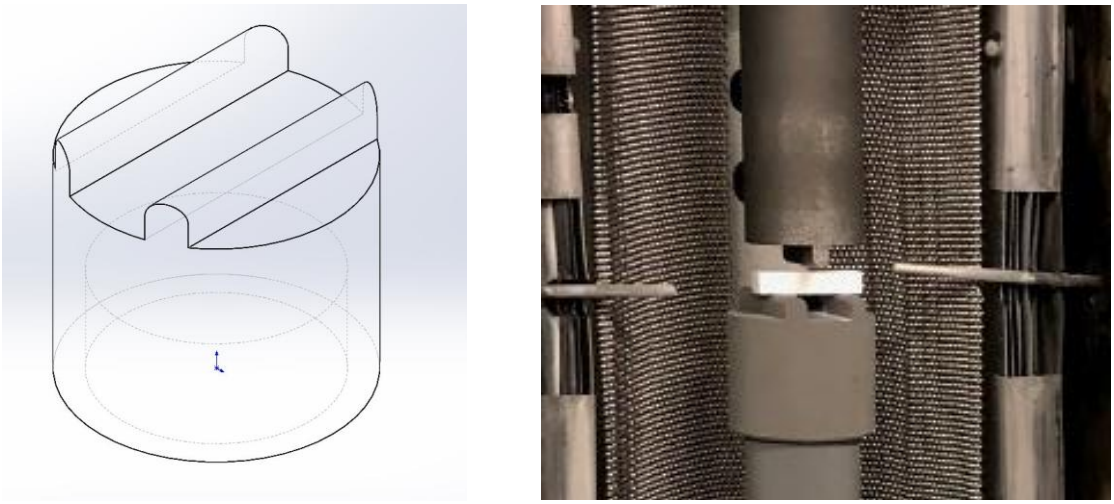

(a) (b)

Figure 111: *Three-point bend test configuration (a) the supporting grip, (b) the loaded sample*.

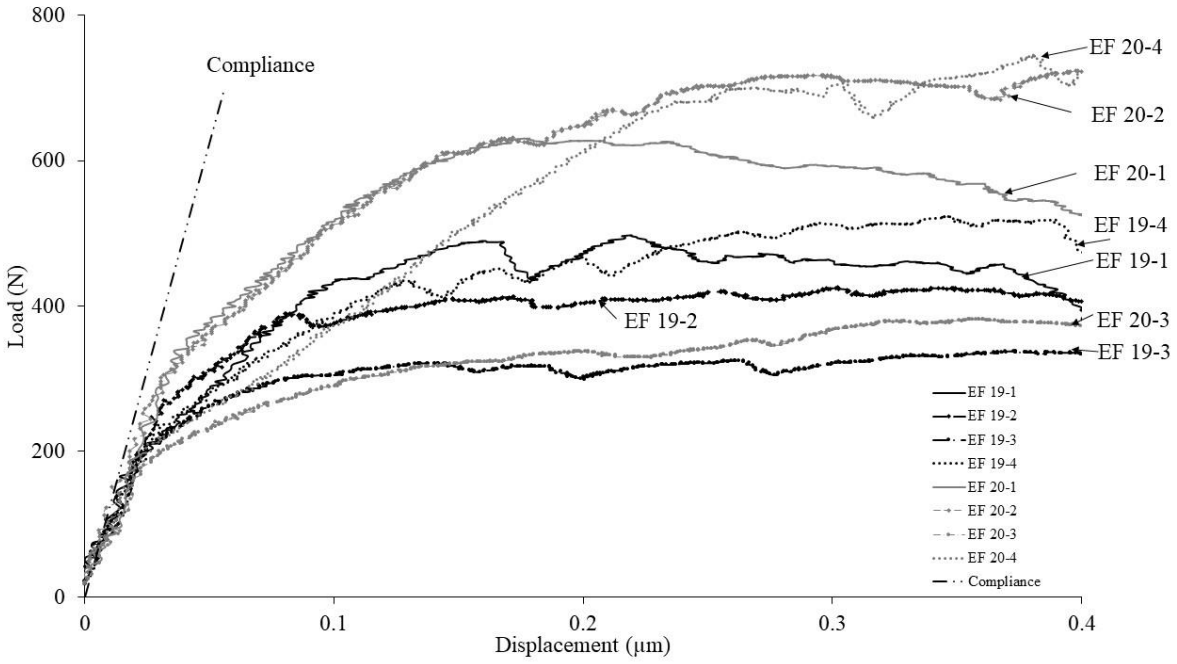

Figure 112: *Load displacement data generated at 1100°C for all eight samples. The machine compliance was calculated using the modulus calculated in the previous chapter and plotted as a function of displacement.*

6.3.2 Actual Displacement

Figure 113 (a) shows a schematic of the total displacement being measured during the three-point bend test, using two springs. The total displacement is the sum of the sample displacement and the machine displacement. Even though the machine displacement was zeroed before the start of the test, the machine had its own compliance, which adds to the total displacement. The effective modulus value calculated in CHAPTER 5, using Digital Volume Correlation, for EF 19 0/90° layup, sintered at 1200°C temperature and tested at 1100°C, was assumed to be the same for EF 19-4 used in this experiment. This assumption was taken keeping in mind not only because of the microstructure being approximately similar, but also the dimensional similarity of the samples and was measured using the exact same test method with the same supporting pin span. Flexural modulus values could be taken from literature using a more accurate measurement procedure. The standard flexural tests would be carried out at a span to thickness ratio in access of 15 [156]. This is done to reduce contact loads and would diminish the effects of transverse compression. The flexural modulus calculated in CHAPTER 5 and 6 were done using the same span width and a similar span to thickness ratio [102]. Hence using the value calculated at 1100°C in tandem with DVC, in **CHAPTER 5**, provides the most feasible flexural modulus estimation value which could be used to calculate the compliance of the machine, which is a constant gradient.

This value was then used to calculate the actual sample displacement, of EF 19-4, at different loads. These sample displacements were then subtracted from the total displacements to find out the machine displacements as a function of load. This can be expressed in the form of a linear fit compliance equation, where compliance is the machine displacement, μm, at a particular load, N.

$$Compliance = 0.00008 * Load - 0.0053 \quad (20)$$

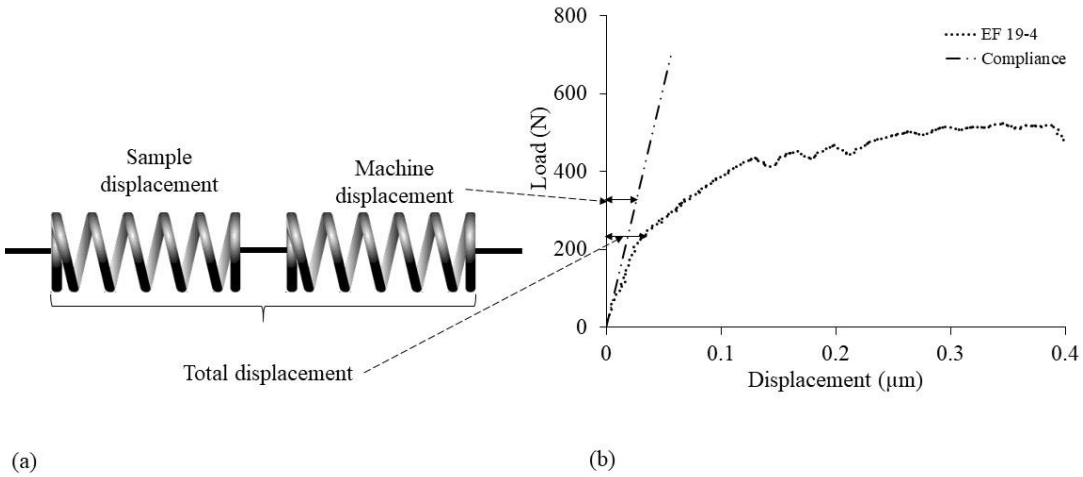

Figure 113: *(a) The schematic of the displacements taking place during loading modelled using two springs, (b) the load vs displacement curve for EF 19-4 plotted along with the machine compliance.*

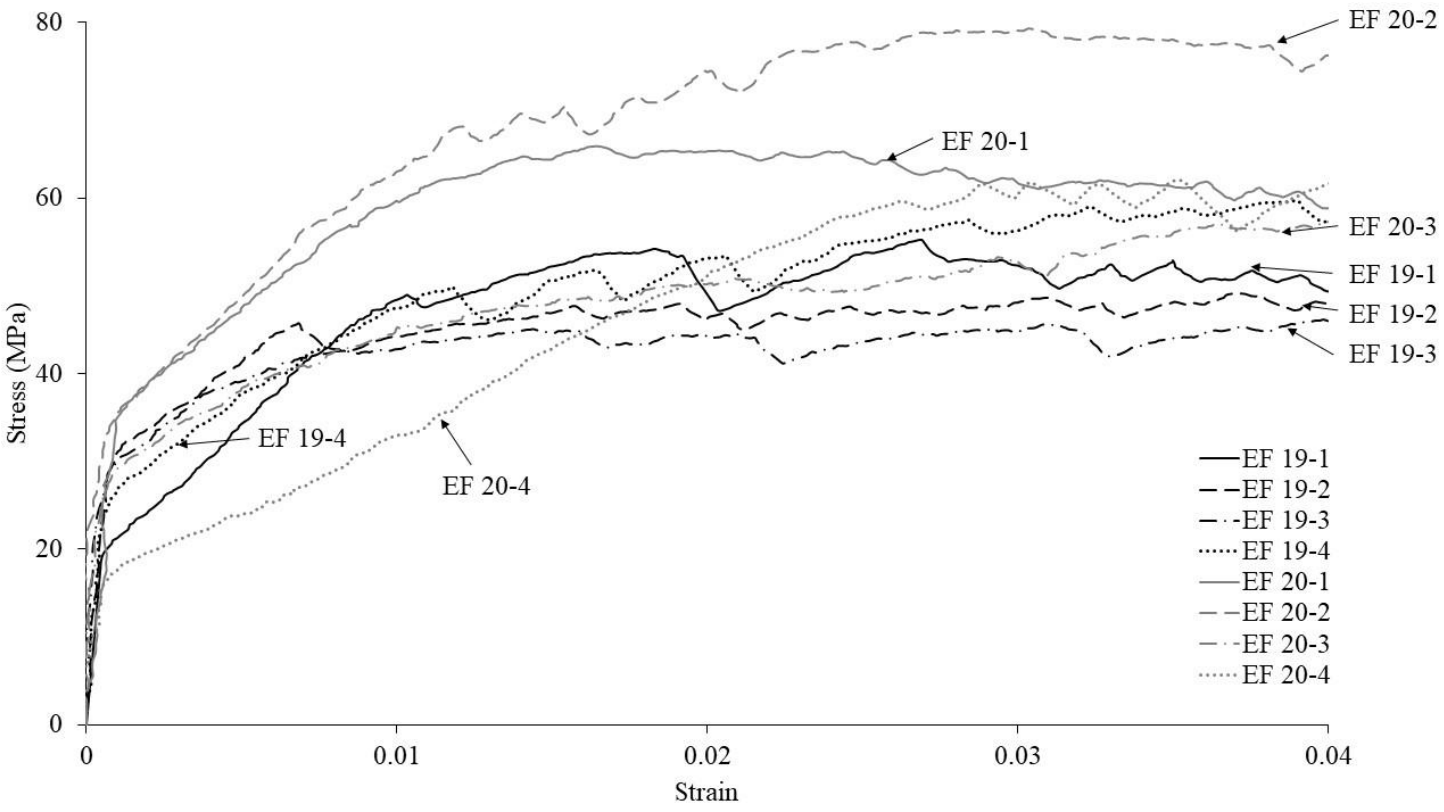

Figure 114: *stress vs corrected strain for each of the eight samples.*

Using the effective modulus value of 42.5GPa to estimate the stiffness for sample EF 19-4, the displacement due to the machine compliance was calculated as a function of load. This was then subtracted from the total sample displacements measured, to get the actual sample deflection due to load at 1100°C. **Figure 114** shows the actual stress vs strain experienced by each sample. The modulus values were calculated using the gradient of the initial straight line using the linest function, presented along with the errors in **Table 19**. The proportional limit stress (PLS) is the first non-linearity in the stress-strain curve that is associated with the development of the matrix microcracks. The proportional limit values, plotted in **Figure 115**, were calculated by identifying the point where the stress value deviated 5% from the gradient value. The error was calculated by taking into consideration the fluctuation in the values, 10 points before and after the proportional limit stress.

Sample No.	Temperature	Modulus (GPa)	Error (GPa)	Proportional Limit Stress (MPa)	Error (MPa)
	CHI				
EF 19-1	Temperature	39.9	±2.6	19.4	±5.7
EF 19-2	1250°C	43.0	±2.9	28.8	±1.9
EF 19-3	1200°C	51.4	±5.4	29.0	±2.4
EF 19-4	1200°C	42.5	±3.8	24.5	±3.8
	CHI				
EF 20-1	Temperature	38.2	±3.7	34.4	±2.7
EF 20-2	1250°C	35.4	±5.4	35.1	±3.2
EF 20-3	1200°C	40.8	±4.1	24.1	±2.4
EF 20-4	1200°C	19.8	±2.6	16.9	±3.4

Table 19: *The modulus and the Proportional limit stress calculated from the stress vs strain data.*

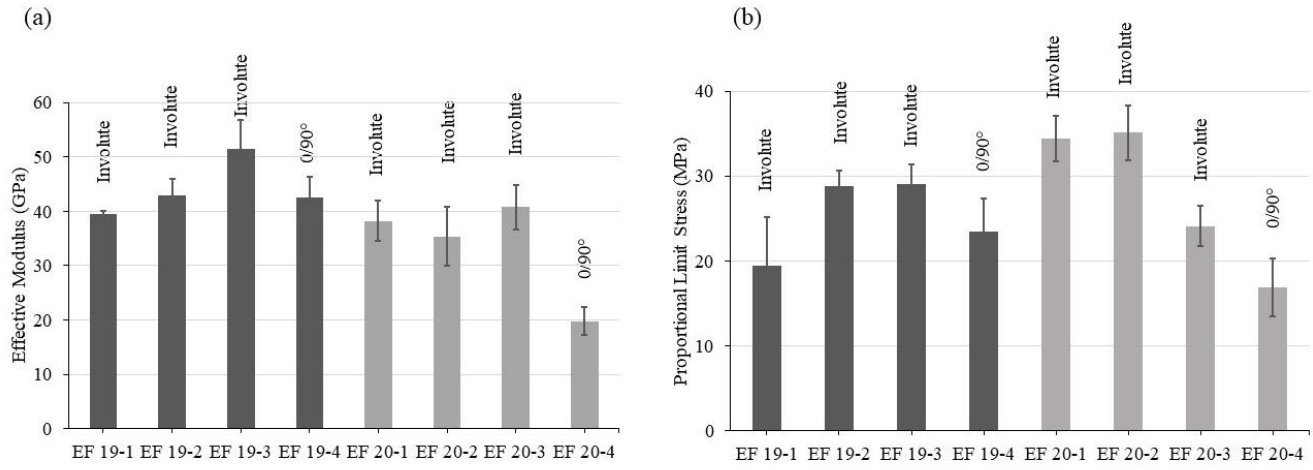

Figure 115: *(a) Effective modulus of the different samples (b) Proportional Limit Stress measured for each sample.*

6.4 Material Systems

Out of the 8 samples evaluated, 7 samples were shortlisted and analysed under creep loading conditions. Sample EF 20-4, which had a PLS of 16.9 MPa, was ignored in this study as its PLS was much lower than the in-service stress condition. The creep experiment in tandem with X-ray

tomography is a very time-consuming process requiring more than 25 hours of experimental time per sample, which equates to a few thousand pounds in equipment cost. Hence EF 20-4 was removed from the experimental plan.

6.5 Results

6.5.1 Creep Tests (Constant Stress)

Samples were cut into rectangular beams, 25 mm in length, with a cross section of around 4 mm by 5 mm(thickness) consisting of roughly 8 layers. Creep tests for each sample were carried out at constant stress conditions. The samples were tested using a three-point bend test configuration, used in the previous chapter, under a 25MPa constant strain. The displacement due to machine compliance, at 25MPa stress level, was removed from the strain data generated during the experiment to quantify actual strain. Andrade's law [51] was used to estimate the primary and secondary creep rates in order to do a comparative study for the 7 samples. The equation below shows how creep was modelled in the samples.

$$\varepsilon = \varepsilon_{primary} + \varepsilon_{secondary} \quad (21)$$

$$\varepsilon = \beta t^{\frac{1}{3}} + \alpha t \quad (22)$$

Where β represents the estimated primary creep rate, α represents the estimated secondary creep rate and t is the time in minutes. Literature [157] shows that for low creep strains a value of $t^{1/3}$ should

be assumed. This value could be replaced with t^n which could be found using numerical simulation in MATLAB. Both 1/3 and n were used to calculate the values of the constants α and β. For both cases, the values came out to be quite similar, hence the assumption of $t^{1/3}$ was used to calculate the primary creep rate. **Figure 116 (a)** shows the creep strain vs time plotted for different samples tested at 1100°C. For each of the samples, the values of α and β were calculated using **Equation 22**. The estimation of α and β fits quite well with the raw data, showing how well the model, represented by the lines labelled primary and secondary for EF 19-4 in **Figure 116 (a)**, fits the primary and secondary creep points. The fits for the rest of the samples have been presented in **Appendix 2. Figure 117** shows the values of primary and secondary creep rates measured from the creep curves using **Equation 22**. The data also shows a major difference between the creep strains developed in EF 19 and EF 20.

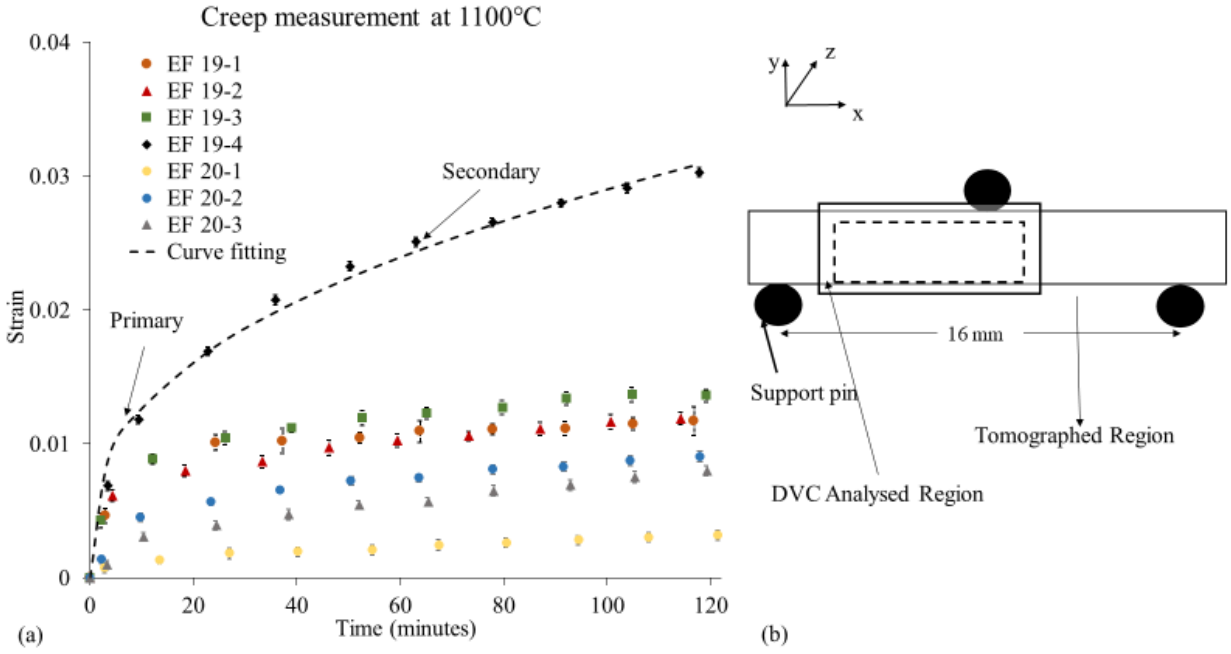

Figure 116: *(a) The creep curves generated at 1100°C at constant stress of 25MPa, (b) Three-point bend test setup showing the regions that were imaged with tomography and analysed with digital volume correlation (DVC) both for the preloaded scan and post creep sample scan.*

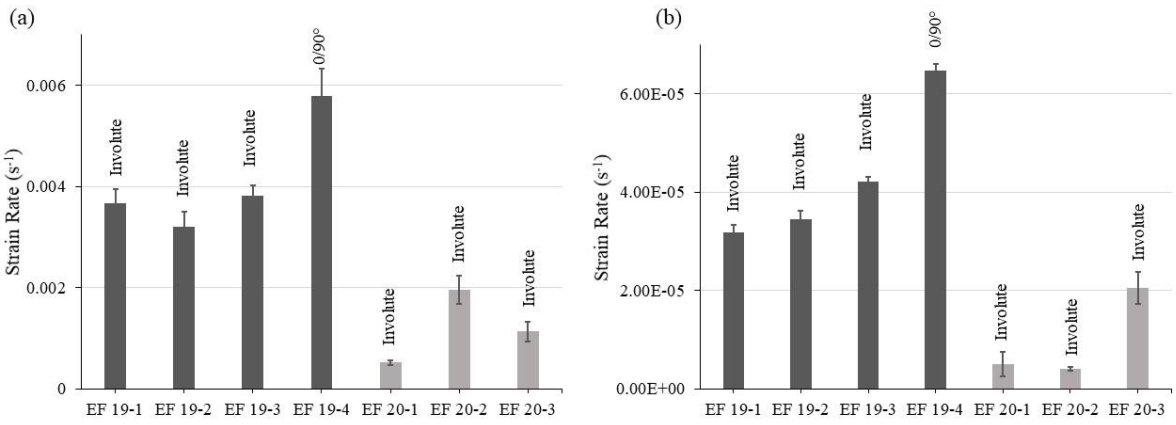

Figure 117: *The creep rate plotted as a bar graph with error bars (a) primary creep (b) secondary creep.*

6.5.1.1 Fracture behaviour

X-ray tomography was carried out on the test samples, pre- and post-creep deformation, in the region showed in **Figure 116** (**b)**. The details of the experimental procedure and conditions have been given in CHAPTER 3**.** The tomographs were looked at to see if damage could be detected after the creep tests were performed on each sample. For EF 19-1, EF 19-2 and EF 19-3 no damage was observed between the reference tomograph, and the crept sample tomograph, that experienced a stress of 25MPa at 1100°C. This could be due to damage development closing up after the load was removed. Hence the μXCT data for these three samples has not been presented in this study. The tomography data for sample EF 19-4, which developed the highest amount of creep strains, showed signs of microstructural damage at different locations, mainly in between the interlayers parallel to the 0° fibre tows. **Figure 118** (**a**) shows the *ex situ* tomography data summarised using vertical sections (‘orthoslices’ in y-x plane) across the central region of sample EF 19-4 that underwent permanent strain. The formation of new cracks were observed within the crept sample tomograph between the fibre matrix layers. All cracking was

observed to be parallel to the 0° tows, examples of which are identified in regions (i) to (iii). This could be a function of the 0/90° layup which is the only difference between EF 19-3 and EF 19-4.

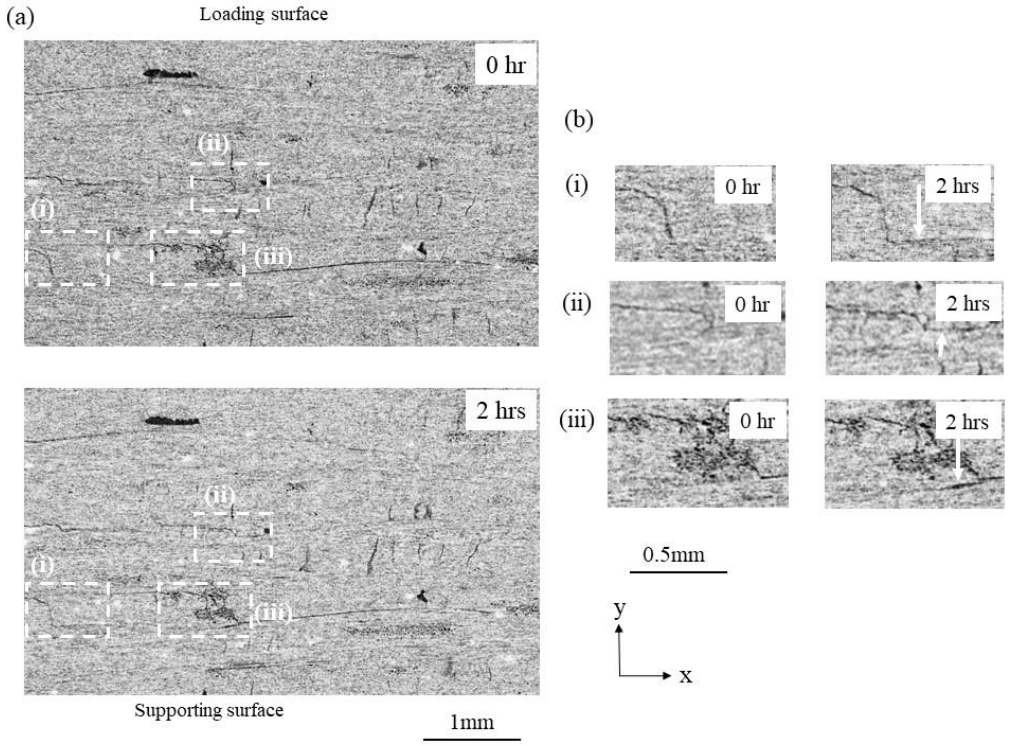

Figure 118: *Central orthoslices of the in situ x-ray tomographs pre- and post-creep analysis of EF 19-4; a) with increasing time from the pre-load, 0 hr condition, to 2 hrs of exposure at 1100°C under 25MPa of stress; b) high magnification images at selected regions (i) to (iii) with increasing time. The locations of the crack development have been labelled using a white arrow are indicated.*

X-ray tomography data for EF 20 samples was also scrutinised to identify if creep tests resulted in matrix cracking. No damage was observed between the reference tomograph, and the crept sample tomograph, that experienced a stress of 25MPa at 1100°C in EF 20-1, and 2. When the tomography data for sample EF 20-3, which developed the highest amount of creep strains amongst the three, was looked at, signs of limited microstructural damage were observed at different locations within the cross-section. **Figure 119 a**, shows the *ex situ* tomography data summarised using vertical sections ('orthoslices' in y-x plane) across the central region of sample EF 20-3. The formation of new faint cracks were observed within the crept sample tomograph. Cracking was observed to be both horizontal, **Figure 119 b (iii),**

and vertical **Figure 119 b (i)**. The only difference between EF 20-2 and EF 20-3 was the sintering temperature, with EF 20-2 having been sintered at a 50°C higher temperature. Crack segmentation was carried out in Avizo with limited success, due to the nature of the cracks being very thin in comparison with the image resolution

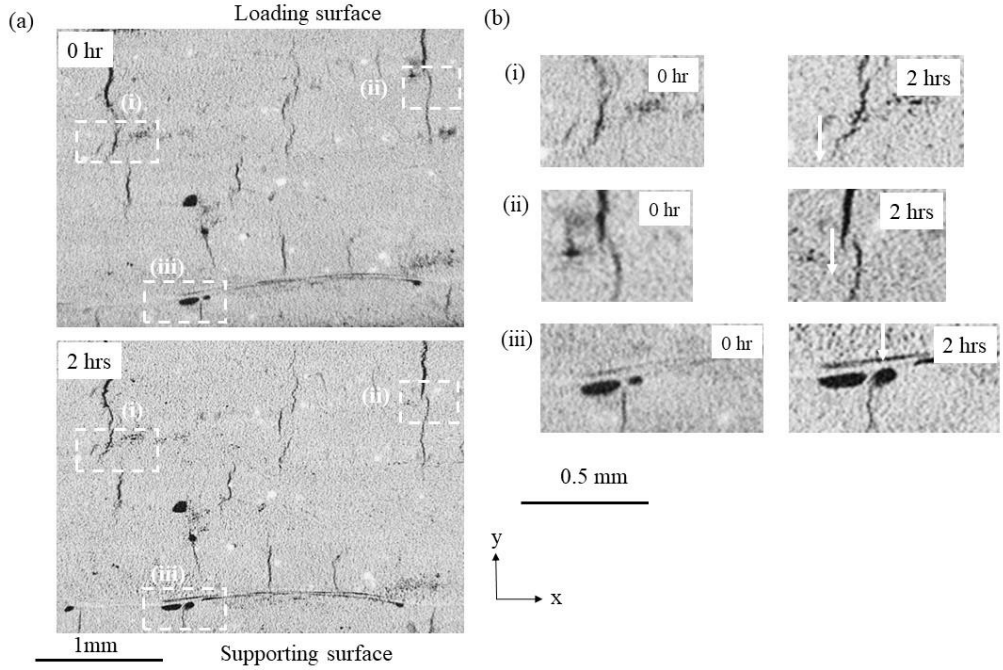

Figure 119: *Central orthoslices of the in situ x-ray tomographs pre and post creep analysis of EF 20-3; a) with increasing time from the pre-load, 0 hr condition, to 2 hrs of exposure at 1100°C under 25MPa of stress; b) high magnification images at selected regions (i) to (iii) with increasing time. The locations of the crack development have been labelled using a white arrow are indicated.*

6.5.1.2 Strain analysis

Datasets of pre- and post-creep tests were first registered using visual matching in x, y and z axes. This was followed by a rigid body moment correction process performed in the LaVision Davis 8.4 software. The pre-creep test was taken as the reference scan and compared with the post-creep test scan. Details of the successive subset dimensions that were used for the DVC analysis have been presented in CHAPTER 3. It was ensured that a correlation value of 0.8 and above was achieved throughout the region of interest before using the DVC results.

DVC of tomographs provides three-dimensional displacement fields of the deformation taken place in the sample due to creep relative to the reference image. The results obtained for the four EF 19 samples were presented in **Figure 120** as maps of the maximum normal 3D strain, calculated from the local gradients of the displacement field (centred 3-point differentiation). Some quite localised strains are observed in samples EF 19-1, 2 and 3, but these strains are sensitive to errors in the low magnitude displacement field and may not be reliable. Significant strains developed in Sample EF 19-4, which are coincident with the newly developed cracks observed in **Figure 118** regions (i), (ii) and (iii).

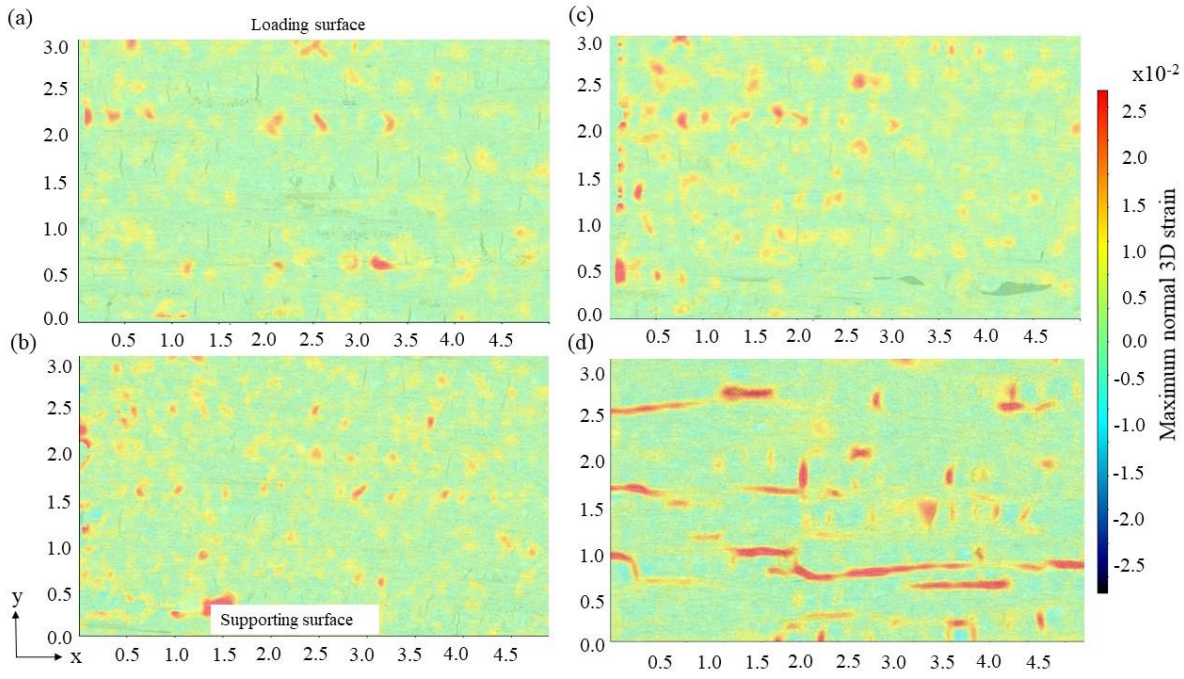

Figure 120: *Maximum normal strain profile in the samples (a) EF 19-1, (b) EF 19-2, (c) EF 19-3, (d) EF 19-4.*

In order to have a detailed understanding of the strains that developed in EF 19-4, normal strains in each axis were plotted separately in **Figure 121**. It can be observed that the normal strain component in y, ε_{yy}, is the main driver contributor of the crack propagation in the sample, as it follows the crack profile. The ε_{yy} strains around the crack show compressive and tensile strains. This figure shows the problem of using ε_{yy} because the actual strain direction is not aligned to the x and y axis. This is due to the fact that the strain is acting at an angle to the x and y axis. The strains are more easily resolved when

plotting the maximum normal 3D strain, which is the maximum principal strain which picks up the location of the maximum strain and is independent of the direction of the strain. The doubling effect seen in **Figure 121 (b)** confirms the presence of shear strain within the sample. **Figure 121 (a & c)** show that the normal strain in x and z axis, ε_{xx} and ε_{zz}, played an insignificant role in crack propagation.

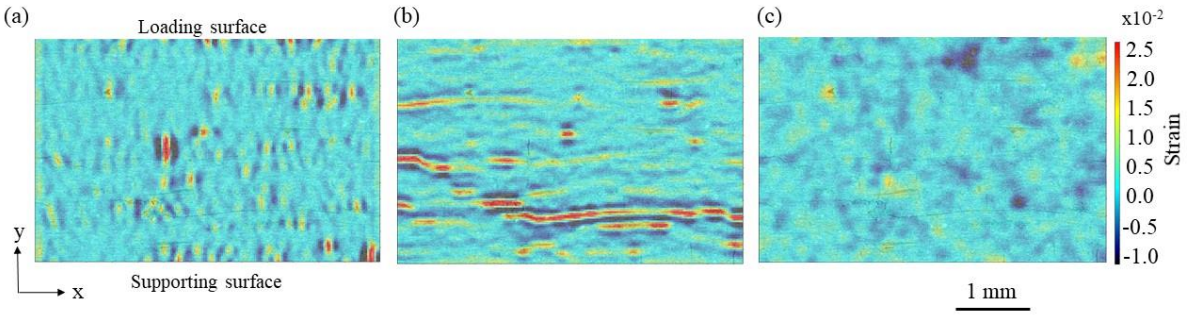

***Figure 121**: Strain distribution in sample EF 19-4, with normal components of strain along each axis (a) ε_{xx} (b) ε_{yy} and (c) ε_{zz}*

DVC analysis was also carried out on EF 20 samples, **Figure 122**. No measurable strains were observed in either EF 20-1 or EF 20-2, indicating that any permanent damage was below the resolution of the X-ray tomography. Sample 20-3 showed regions of high maximum 3D strains, which were coincident with the newly vertical and horizontal cracks observed in **Figure 119**. **Figure 119** (**c)** corresponds to the same orthoslice presented in **Figure 119**. Initial crack propagation was observed to initiate in both the vertical and horizontal directions, which was barely visible in the deformed tomographs in **Figure 119**, but was clearly visible in the corresponding maximum 3D strain fields, **Figure 122 c**.

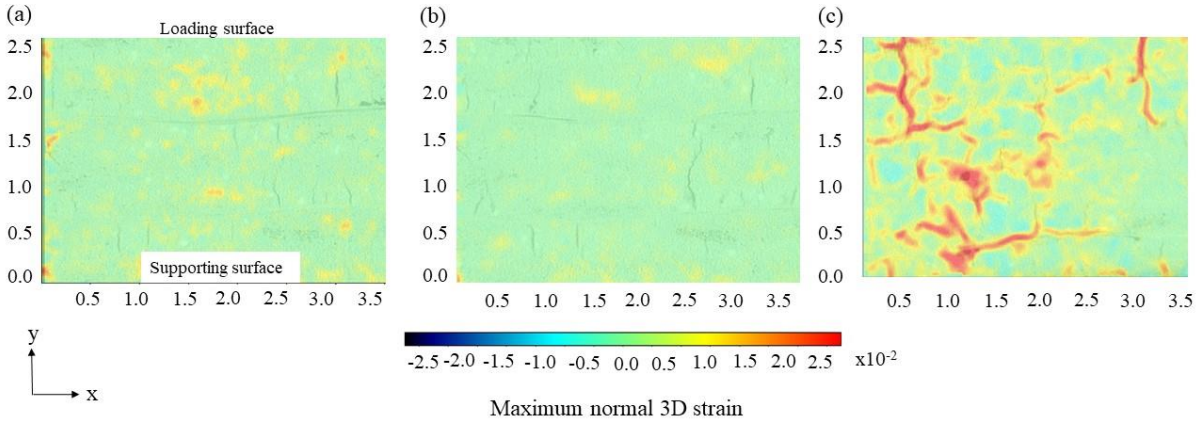

Figure 122: *Maximum normal strain profile in the samples (a) EF 20-1, (b) EF 20-2, (c) EF 20-3.*

In order to understand which component of strain played a role in crack propagation under loading, individual normal strains were looked at in **Figure 123**. It can be observed that the strain in EF 20-3, exhibits complicated strain characteristics and is a function of all three normal strains. This could be due to the involute fibre layup structure that results in a more intricate strain distribution. The compressive/tensile effect that was seen in EF 19-4 was also observed in EF 20-3 suggesting that the strain has a shear component attached to it.

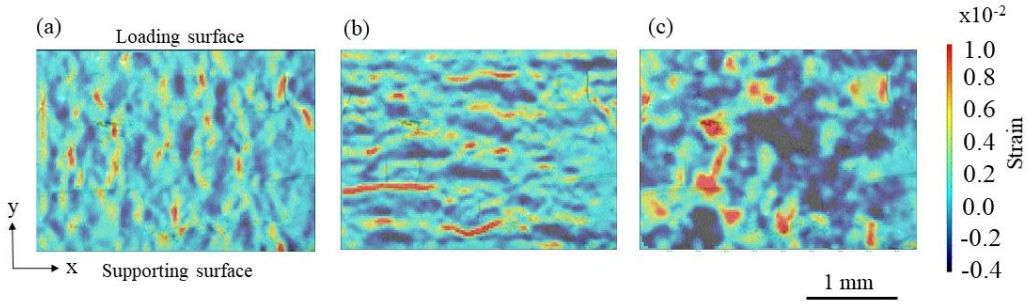

Figure 123: *Strain distribution in sample EF 20-3, with normal components of strain along each axis (a) ε_{xx} (b) ε_{yy} and (c) ε_{zz}*

6.6 Stress relaxation tests (Constant displacement)

As described in **SECTION 1.2**, a sealing ring functions as a piston ring, which is circular in its fitted state, but has an elliptical free state, which causes an out-springing force during service. **Figure**

124 (a) shows the difference between a free ring and a fitted ring. **Figure 124 (b)** shows a circular ring in its fitted condition which minimises leakage, on the other hand **Figure 124 (c),** shows a ring in its free shape, note it is not circular when free and only becomes circular when fitted. A sealing ring of 140 mm diameter was designed in order to evaluate the effectiveness of CMCs as sealing materials. The ring undergoes a constant deflection when in service, with the amount of stress relaxing with time as a function of strain relaxation taking place due to creep. This reduces the out-spring force of the ring over time.

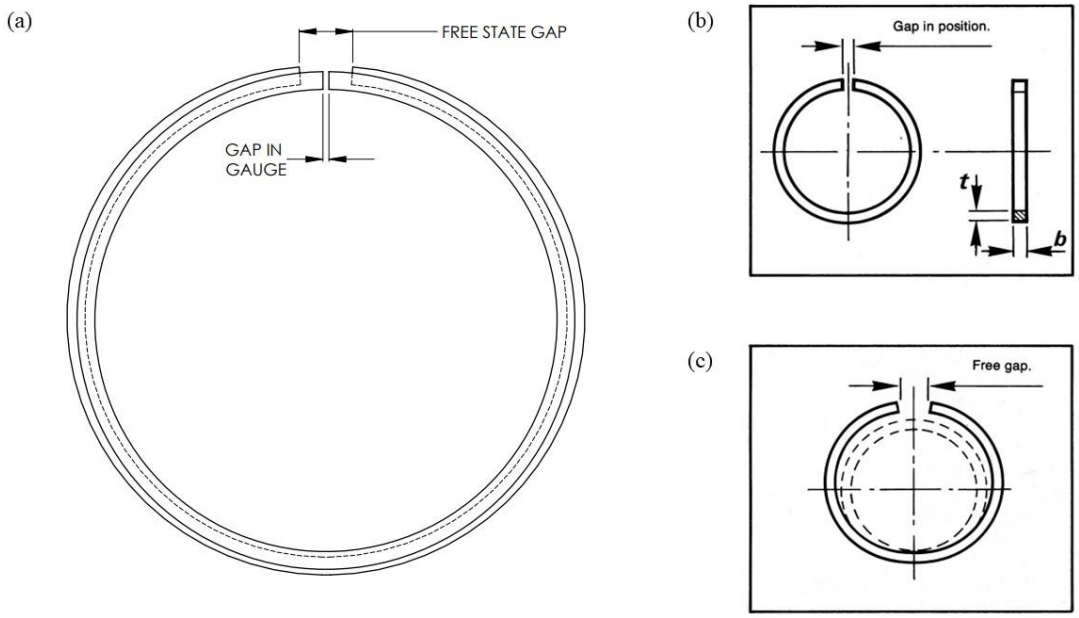

Figure 124: *The difference between a free ring and a fitted ring. (a) free ring over laid on a fitted ring (b) working position (c) free position.*

6.6.1 Ring design theory

A sealing ring can be analysed by treating it as a thin curved beam in the form of a semi-circle, fixed at its base and subjected to a point load at it free end, as seen in **Figure 125**. This curved beam theory is a good approximation for rings with a radius to axial thickness ratio of above 10 [158].

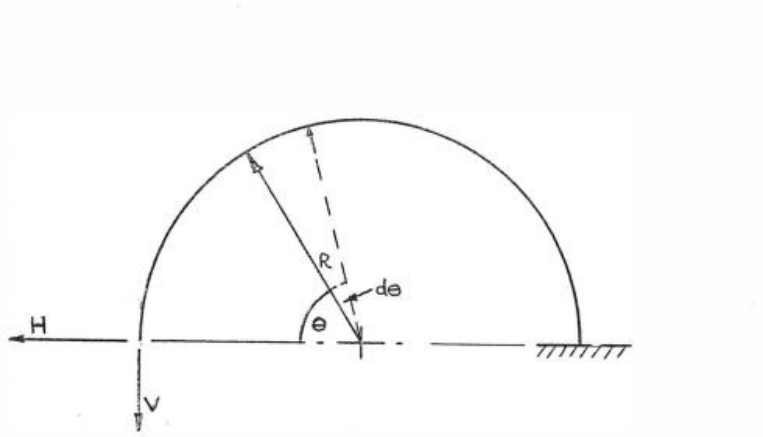

Figure 125*: Forces acting on the semi-circular ring. V is the tangential force and H is the force parallel to the cross-section* [159].

The free gap, Δ, due to the tangential force, V, on the ring is given by the following equation

$$\Delta = \frac{R^3}{EI}\left\{\frac{3\pi V}{2} - 2H\right\} \qquad 23$$

Where R is the radius to the neutral axis, E is the Young's Modulus, I is the second moment of area [158]. For a piston/sealing ring subjected to a tangential force, F, applied at the gap [158]:

$$V = F \qquad \& \qquad H = 0$$

For a complete ring the gap is given by the following equation

$$\Delta = \frac{3\pi F R^3}{EI} \qquad 24$$

Within a sealing ring there are two forces acting on the ring, namely bending moment due to tangential force, F, and Tension force. The maximum bending moment in a ring acts opposite to the ring gap.

$$Stress\ due\ to\ bending = \frac{MY}{I} \quad (25)$$

$$Stress\ due\ to\ tension\ = \frac{F}{A} \quad (26)$$

For a piston ring with a thin radial section the shift of the neutral axis from the centre of the ring is very small and can be ignored.

$$R = \frac{(D - t)}{2} \quad (27)$$

$$I = \frac{bt^3}{12} \quad (28)$$

Where D is the Diameter, t is the thickness, and b is the width, R is the radius and I is the second moment of area. Substituting 7 and 8 back into 4 and rearranging gives

$$E\ = \frac{14.137\ (D - t)^3}{bt^3} * \frac{F}{\Delta} \quad (29)$$

Hence by carrying out simple measurements of the tangential force along with the effective gap, as seen in **Figure 126**, change due to it the Youngs Modulus can be calculated [159].

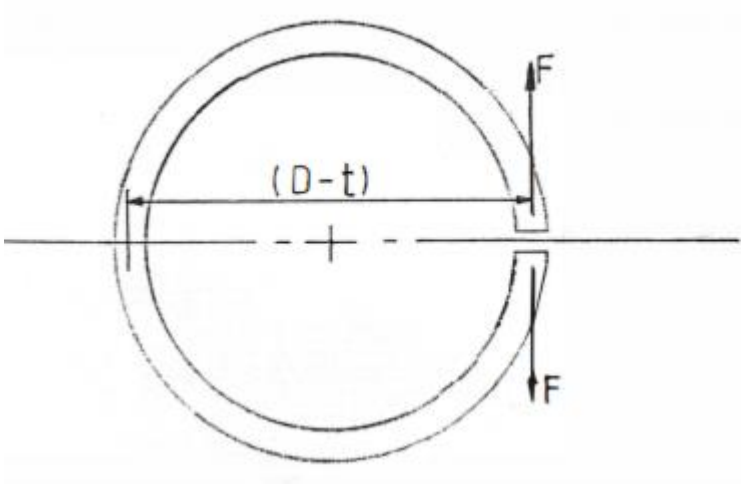

Figure 126: *The tangential force acting on a ring*

Taking moments:

$$M = F(D - t) \tag{30}$$

Maximum stress in the ring due to F = σ_I

σ_I = stress due to bending + stress due to tension force

$$\sigma_i = \frac{MY}{I} + \frac{F}{A} \tag{31}$$

Where y = t/2, I = $bt^3/12$, A = bt

Substituting it in equation 32,

$$\sigma_i = F\left\{\frac{1}{bt}\left[\frac{6(D - t)}{t} + 1\right]\right\} \tag{32}$$

By equating equation 12 and 9 and making F the subject of the formula

$$\frac{\sigma}{\left\{\frac{1}{bt}\left[\frac{6(D-t)}{t}+1\right]\right\}} = \frac{\Delta E b t^3}{14.137\,(D-t)^3} \quad 33$$

$$\sigma = \underbrace{\frac{\Delta E}{2.356t\left\{\frac{D}{t}-1\right\}^2}}_{\text{Stress due to bending}} + \underbrace{\frac{\Delta E}{14.1375t\left\{\frac{D}{t}-1\right\}^3}}_{\text{Stress due to tension}} \quad 34$$

In sealing ring design, the recommended D/t ratio is around 25 [159]. This makes the stress due to tension term in the equation very small in comparison to the bending moment term and hence it can be ignored (approximately 0.7% of the bending moment term). Hence the equation can be simplified to

$$\sigma = \frac{\Delta E}{2.356t\left\{\frac{D}{t}-1\right\}^2} \quad 35$$

6.6.2 Ring design

Figure 127 shows the design of the ring in its free and fitted conditions at a gauge diameter of 140mm. The cross section of the ring was designed to be a square of 5.08 mm..

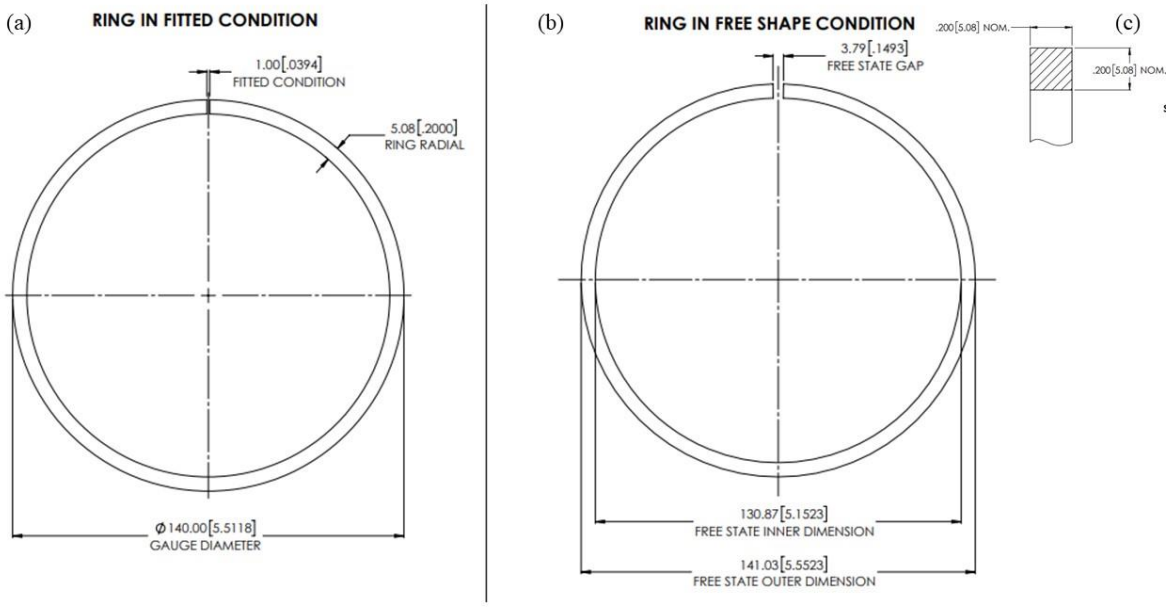

Figure 127: *The ring designed and manufactured from Ox.Ox CMCs where (a) is the ring in its fitted position, (b) ring in free shape condition and (c) is the cross section of the ring.*

In order to find out the free gap that would generate a maximum stress of around 25 MPa, equation 24 is used.

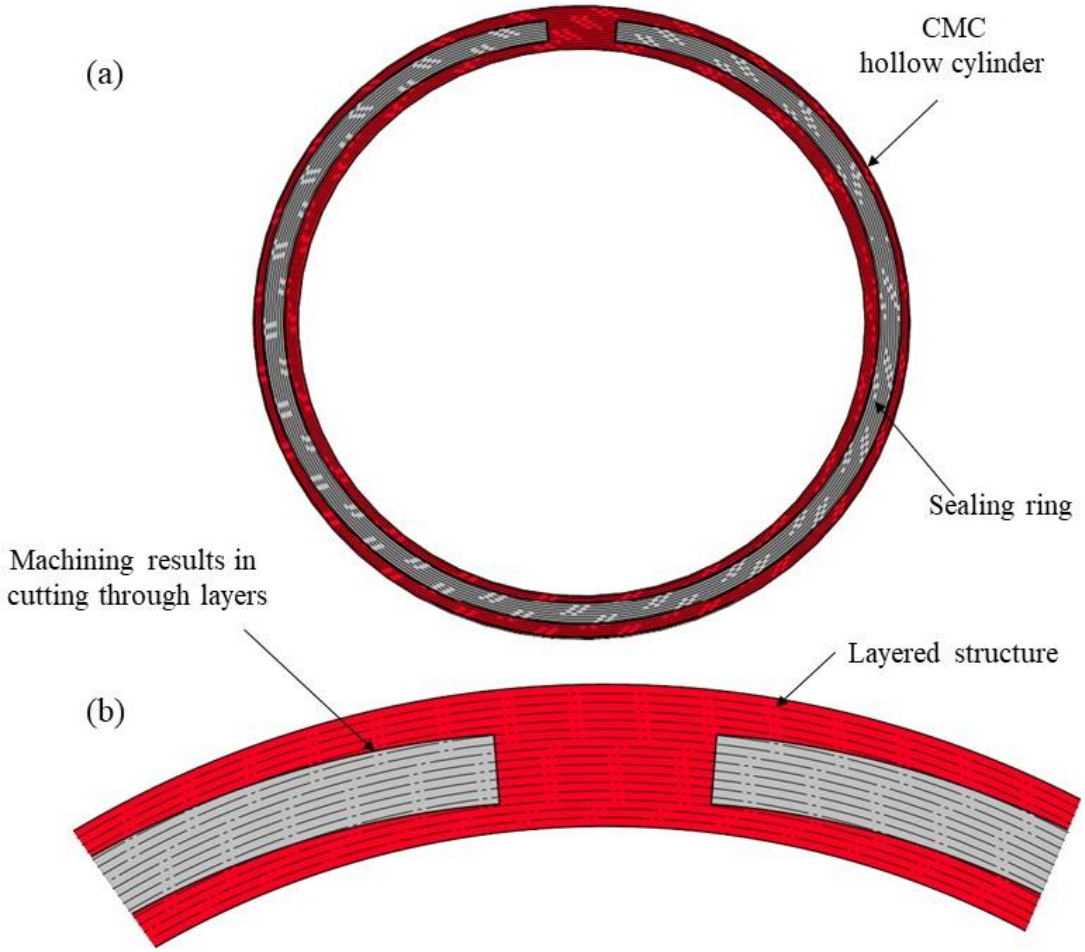

Figure 128: *The hollow cylinder used to machine the ring, the layered structure of the cylinder is visible. (a) The free shape ring overlaid on the cylinder blank. (b) Zoomed in version of the cylinder and the ring, it can be seen that the ring cuts through the different layers.*

Two cylinders, one with EF 19 and the other with EF 20 weave were manufactured, both with involute layup and processed at CHI sintering temperature. The cylinders had an internal diameter (I/D) of 129.8mm and an outer diameter (O/D) of 145.5mm, **Appendix 3**. **Figure 128 (a)** shows the ring in its free condition laid on top of the cylinder blank used to manufacture it. The ring was machined out of the cross-section of the cylinder using the steps detailed below.

1. Machine O/D, outer diameter, of the cylinder to 5.575"[141.61mm]

2. Part off

3. Gap to .150"[3.81] at 5.575"[141.61]

4. Compress into 5.535"[140.59] O/D machining jig (to provide 0.125"[3.175] outspring)

5. Machine O/D to 5.5118"[140.00] gauge

6. Side grind

7. Install into 5.5118"[140.00] jig & machine I/D, internal diameter to 5.112" ring I/D

8. Break all sharp corners

Due to limited CMCs machining skills, dimensional variations were observed during inspection of the manufactured parts. The machining process resulted in cutting through the layers, as seen in **Figure 128** which introduced surface defects, undermining the strength of the part. **Table 20** shows the actual measurements of the manufactured rings.

	Drawing Dimension	**EF 19**	**EF 20**
Free Diameter Ø (mm)	140	140.97	141.2
Internal Diameter as cast Ø (mm)	129.54	128.90	129.5
Gap at Gauge (mm)	0.62	1.17	0.76
Axial thickness (mm) b	5.08	5.05	5.05
Radial thickness (mm) t	5.23	5.20	5.77
Out-spring (mm)	3.17	3.45	3.84
Diametric Load (N) Q	-	5.5	17.8

Table 20: *The dimensions of the manufactured rings.*

6.6.3 Stress relaxation

Figure 129 shows the stress relaxation of both rings as a function of time. The difference between the free and fitted gaps is quantified as the spring of a piston ring. As stress relaxation takes place the spring starts to relax which reduces the effectiveness of the sealing ring. **Figure 129 (b)** shows the percentage spring retention for both rings.

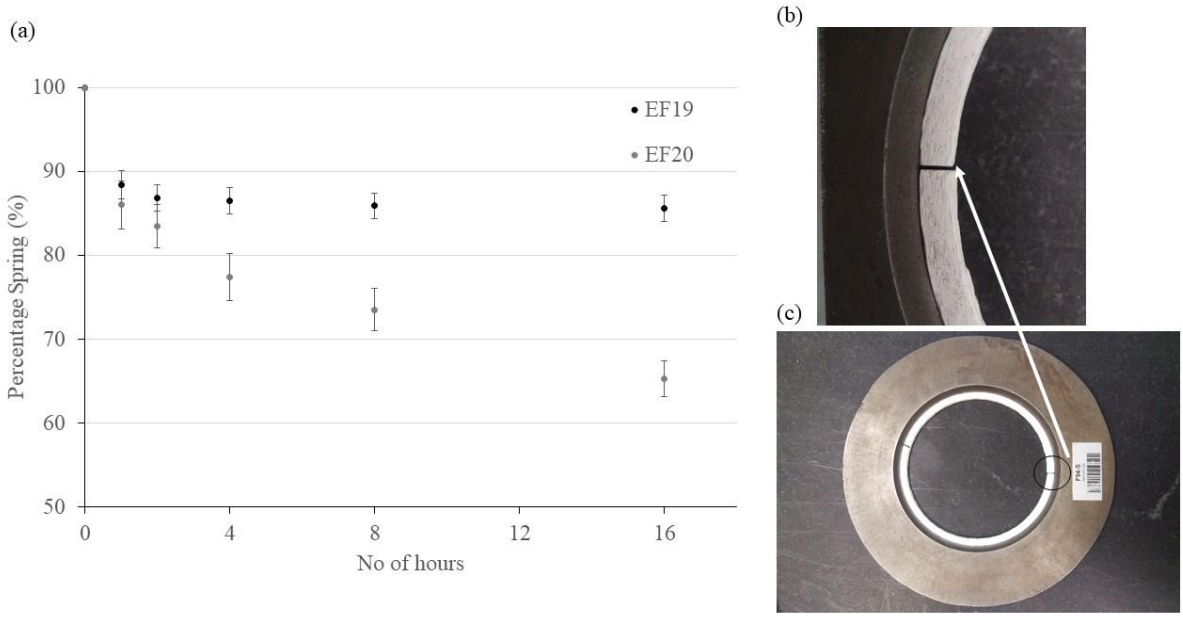

Figure 129: *(a) Percentage spring retention as a function of time at 1100°C, (b) fitted gap of the ceramic ring, (c) ring in a 140mm diameter gauge.*

Using the measured dimensions and the diametric load generated by the piston ring in its fitted condition, the actual stress in the ring was calculated using the following equation, which is a derivation of equation 25.

$$f = \frac{3Q(D-t)}{bt^2} \qquad 36$$

Where

f is the maximum stress in the ring, MPa

Q is the diametric force to close the ring, N

b is the ring axial thickness, m

D is the gauge diameter, m

t is ring radial thickness, m

This equation takes into consideration the actual dimensions and diametric force generated by the ring, as opposed to the modulus value initially used to design the ring, which assumed that the ring was isotropic. The actual stress came out to be different in both the rings due to the manufacturing process, fibre layup and effective modulus assumptions. The results were presented in **Table 21** along with the proportional limit stress, PLS.

	Modulus (GPa)	**Stress f (MPa)**	**PLS (MPa)**	**Stress % of PLS**
EF 19	39.3	16.15	19.4	83
EF 20	38.2	42.65	34.4	124

Table 21: *the modulus and proportional stress limit values calculated in the previous chapter against the stress generated in the service conditions.*

Table 21 indicates that the stress in ring EF 19 was 83% of the PLS, suggesting that permanent damage should not take place, whilst for EF 20, even though the PLS is 70% higher than that of EF 19, the stress generated is beyond the sample's PLS limit of 34.4MPa, which would result in permanent microstructural damage. Using the modulus values presented in **Table 21** the spring retention values were converted into maximum stress against time and maximum strain against time for both rings, as seen in **Figure 130**.

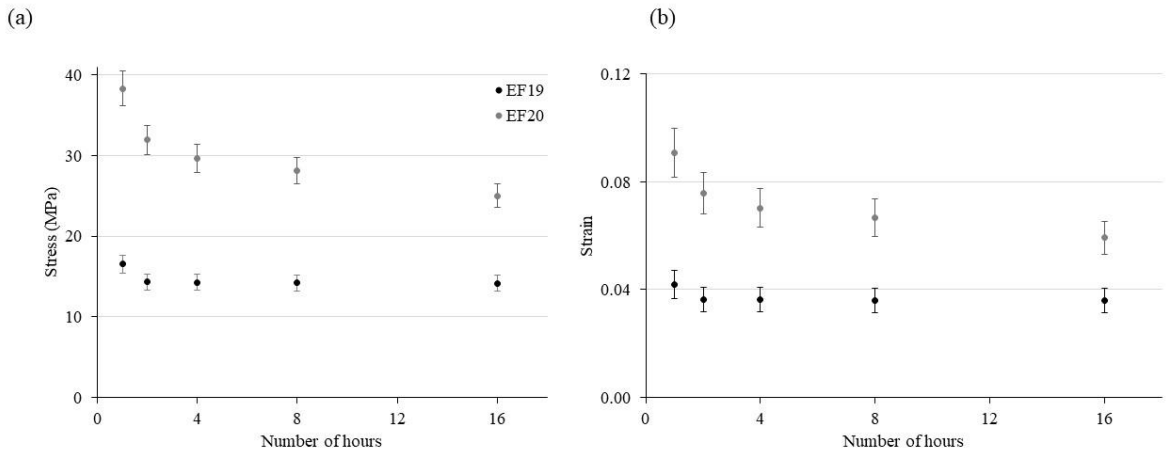

Figure 130: *Stress relaxation curves of the two rings (a) stress vs time (b) % strain vs time.*

6.6.4 Strain Analysis

X-ray tomographs for the rings were carried out at a voxel size of $6.9\mu m^3$ with an exposure time of 14 seconds per projection. The details of the experimental conditions have been presented in CHAPTER 3, section 3.2.1.5. The pre-creep test ring, tomographed at 0 hours, was taken as the reference scan and compared with the post-creep testing scan, tomographed after 16 hours of exposure, in its fitted state. Full details of the successive passes used for this analysis have been presented in CHAPTER 3, section 3.1.1.7. It was ensured that a correlation value of more than 0.8 was achieved throughout the region of interest, for any data used for analysis.

Figure 131 (a) shows the permanent maximum 3D strain in sample EF 19-1 after 16 hours of creep exposure. The maximum normal 3D strain was observed to be almost zero across the sample. DVC was also carried out on the EF 20-1 ring before and after 16 hours of exposure in its fitted state at 1100°C. **Figure 131 (b)** shows the permanent maximum normal 3D strain that was present in the sample after 16 hours of exposure. The strain profile mirrored the pre-existing matrix cracks present in the microstructure. DVC analysis shows regions of high maximum 3D strain at **Figure 131 (b)** that are

coincident with the matrix cracks such as those in regions (i) to (iii); these are presented in more detail in **Figure 131 (c)**. Measurable strains associated with the vertical matrix cracks, which are present in the as-fabricated microstructure, **Figure 131 (c)**, indicating that they were loaded significantly during the test. The maximum normal strain was visualised in 3D volume using Avizo 2020.2, as shown in **Figure 131 (d)**. It was observed that the 3D normal strains have similar dimensions and profiles as the vertical cracks observed in the matrix.

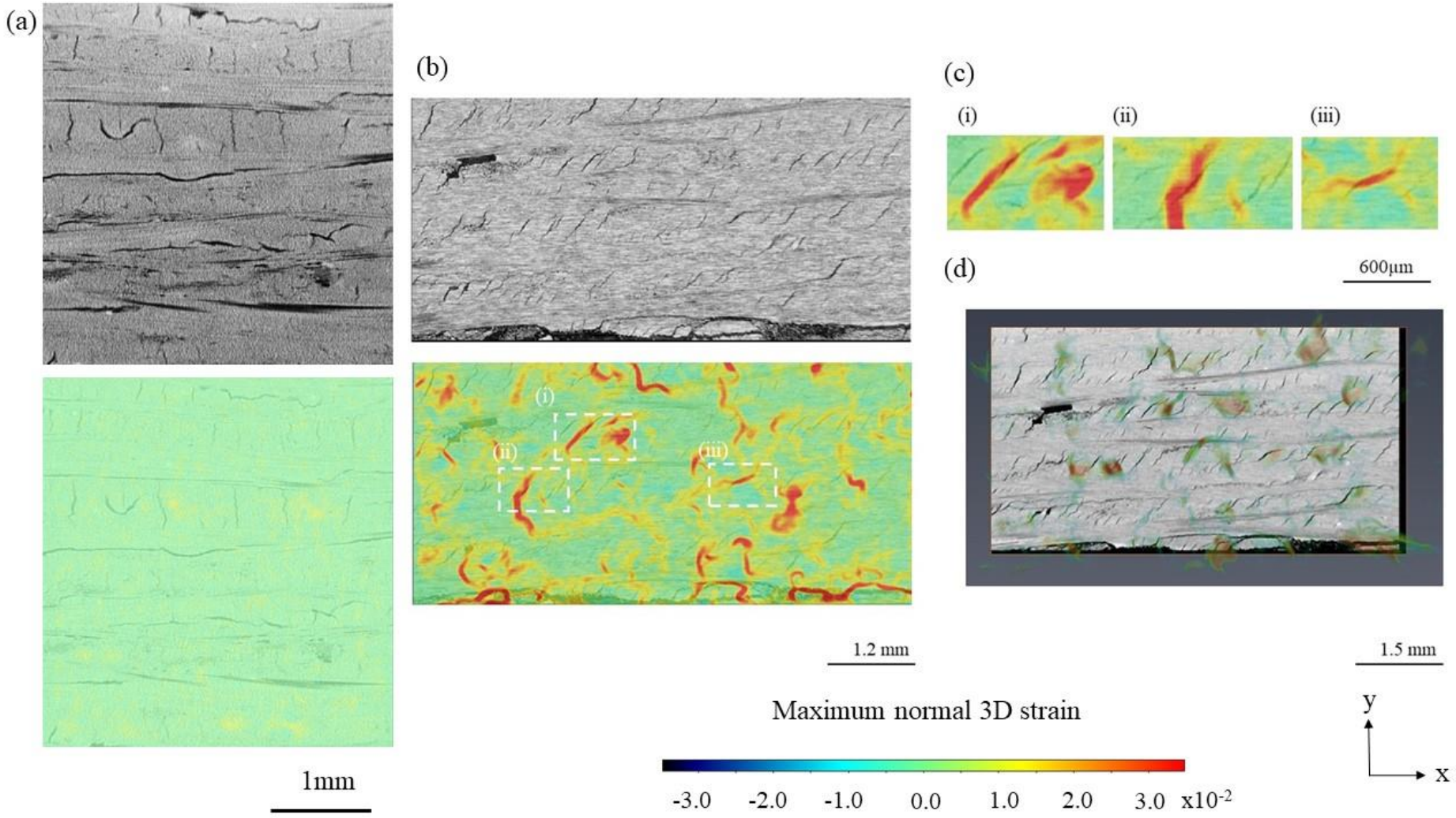

Figure 131: *Central slices of the maximum normal 3D strain field measured by DVC of the ring post-mortem creep test at 1100°C (referenced at 0 hours of exposure). The backgrounds are orthoslices of the crept tomograph at the same location, and all images have the same strain scale: a) the strain map after 16 hrs of exposure at 1100°C, compared with the same tomograph orthoslice for EF 19;b) the strain map after 16 hrs of exposure at 1100°C, compared with the same tomograph orthoslice for EF 20: c) higher magnification images of EF 20 at selected regions (i) to (iii) after 16 hours exposure: d) the maximum normal 3D strains plotted in 3D volume with a orthoslice of the tomograph underneath.*

6.7 Discussion

6.7.1 Three-point bend tests

Two different types of fibre weaves, namely EF 19 and EF 20, were selected in order to understand which one provided the most optimum mechanical properties. The layup of the weave plays an important role in the overall performance of the composite. Two different types of layup styles, 0/90° and involute, were looked at in order to optimise the PLS and modulus values. This study also looked at optimising the sintering temperature to maximise PLS along with the maximum elastic deflection. It must be noted that this method is mainly being used as a comparative analysis and values provided are effective flexural modulus values. Due to the size of the test chamber, samples of a particular dimension could only be tested.

In terms of the weave architecture the modulus values for EF 19 were within the error range of EF 20, **Figure 115**, but the PLS values were generally better for EF 20, EF 20-4 being an anomaly. The Proportional limit strength for EF 20 was higher in comparison to the EF 19 samples, due to the intrinsic fibre bias in the loading direction for the EF 20 weave. The flexural modulus value considers the strain measurements which were calculated by subtracting the machine compliance from the sample deflection. The error that would arise due to this estimation technique might be reflected in the flexural modulus values, which for most of the samples average around a value of 40±5GPa, with values for EF 19 being slightly higher than EF 20.

Sample EF 20-4 underperformed throughout, with modulus values half that of the other materials and PLS values 60% of the other samples. Hence EF 20-4 was not taken forward. This could be due to the bigger diener size and the plain weave style giving rise to delamination. It was observed, in **Figure**

115 that the involute layup outperformed the 0/90° by having a 23% higher modulus. PLS values for 0/90° were as low as 16.9±3.4 MPa in comparison to involute which were as high as 35.1±3.2 MPa. The increase in the PLS for the involute layup [153,154], could be due to due to an increase in shear strength between the layers. The involute layup gives rise to a much more complicated stress distribution within the microstructure. It also gives rise to a small step in the y direction which could provide a more of a 2.5 D. effect. The smaller sheets gives rise to an inherent discontinuity between the layers which could result in crack suppression.

In terms of temperature the samples that underwent CHI or 1250°C had a similar modulus value for both EF 19 and EF 20 weave patterns. The PLS was observed to be only marginally higher for 1250°C than for the CHI processed sample. The results show that EF 20 with involute layup and sintering at 1250°C outperformed all other samples by having both a high modulus and the highest PLS. It must be noted that due to the nature of the experiments, measurements were carried out on one specimen per sample type. In order to increase the accuracy of the measurements collected, a number of specimens per sample type should be tested.

6.7.2 Creep measurements in beams

The total strain in the system at 1100°C after 120 minutes under stress consists of four components, namely machine compliance, plastic strain due to classic creep, plastic strain due to damage and elastic strain. Permanent strain on the other hand is a function of two mechanisms, the first one being classic creep mechanisms and the second one due to microcracking damage. The damage results in a loss in stiffness which results in a higher strain for the same amount of stress. The strain data was first corrected by removing machine compliance at 25MPa. Andrade's law [51] was used to estimate the creep rates for the different samples tested under constant stress conditions at 1100°C. effective primary creep rate

is a function of $t^{1/3}$ whereas effective secondary creep rate is a function of t. **Figure 117** shows the two different creep rates plotted for each sample. It can be observed from **Figure 117** that the primary creep rate was 4 orders of magnitude greater than the secondary creep rate. This is in-line with the classic creep model presented in **Section 1.7.2**[46]. For both primary and secondary creep, the creep strains developed in EF 20, were approximately half that of EF 19. As the loading pin applies load vertically, parallel to the y axis, the fibre tows that are perpendicular to the load direction, 0° fibre tows, are the ones that resist creep deformation. The fibre layup in EF 20, 80% of the fibres being in the loading direction, outperforms EF 19 which only contain 50% of fibre tows perpendicular to the applied load. This is consistent with literature, which showed that at 1100°C, ply orientation had a significant effect on the mechanical properties of the material system [86]. A difference of three to four orders of magnitude in the creep rate at 1100°C, between samples with 0/90° and ±45° orientations was observed in literature [24].

In terms of the weave layup, the involute layup, EF 19-3, outperformed the 0/90°, EF 19-4, by having a lower strain rate both in primary and secondary creep. This is due to the densely packed involute layup providing greater shear strength between the layers in comparison to the 0/90° layup. The involute layup also gives rise to a 2.5D structure which produces a much more complicated stress distribution. In terms of the processing temperature, it was observed that the CHI and 1250°C produced similar primary and secondary creep strains, which were slightly lower in magnitude than the ones observed in the sample processed at 1200°C. This is because alumina matrix is resistant to densification up to 1300°C [36], hence a difference in 50°C would not have a major effect on the matrix morphology. Sample EF 19-4 had the highest creep rates out all the 7 samples tested. One of the reasons for this could be that the stress of 25MPa, applied on the sample, was beyond its proportional limit stress which

could have given rise to permanent damage, resulting in micro-cracking, which then manifests itself in the creep data. It must be noted that due to the time duration of the experiment only one specimen per sample type was tested. Repeat measurements should be carried out in order to increase the reliability and accuracy of the measurements.

6.7.3 Fracture behaviour of beams

Analysis of the *ex situ* X-ray tomographs in **Figure 118**, of sample EF 19-4 which developed the highest amount of creep strains, showed significant new cracks propagated in-between the fibre bundles. The crack path was observed to be in between the 0° fibre bundle, in which the fibres are oriented parallel to the x axis and loaded orthogonally in the *y*-direction, beyond the PLS of the material. This implies the fibre interfaces within the fibre bundle have low strength and were the main drivers of creep damage. Interfacial failure could be further encouraged by creep, which has been observed to occur at 1100°C in a Nextel 720/alumina composite at high stress [88]. A significant crack after creep loading, **Figure 118**, developed in the region below the neutral axis. This was observed to be the region of maximum normal 3D strain **Figure 120 (d)**, which indicates that matrix cracking had taken place and permanent creep strains have developed with the sample during the experiment. The nature of the crack loading was mainly shear, due to the difference in compliance between the different fibre bundles in the sample. **Figure 121 (b)** shows compressive and tensile ε_{yy} strain around the crack, which suggests that the sample was loaded in shear. It must be noted that due to the post mortem X-ray tomography being done without applying any load to the sample, this technique would restrict complete crack visualization. The unloading would result in some of the cracks, that developed during the creep test, to close and would not be picked using this technique. In order to overcome this, short term creep tests should be performed in tandem with an X-ray source.

Figure 120 (d) shows the maximum normal 3D strain developed in EF19-4. The strain perfectly mirrors the crack path observed in the tomography data in **Figure 118**. The individual components of normal strain in each axis were plotted, in **Figure 121**, for EF 19-4, to identify the dominant normal strain components. It was observed normal strain in y axis, ε_{yy}, was the main crack driver and resulted in shear loading of 0° fibre bundles resulting in delamination. The normal strain in x axis, ε_{xx}, corresponded with the regions of maximum normal 3D strain that was observed parallel to the y axis in **Figure 120 (d)**. Similar shear cracking of matrix and interlaminar deflection has been observed in compression testing of a Nextel 610/Alumina composite [145]. The pre-existing defects in the matrix, i.e. vertical cracks, did not propagate during loading. X-ray tomographs of EF 19-1, 2 and 3 were reviewed but showed no signs of damage, hence only maximum normal 3D strains, **Figure 120 (a-c)** have been presented for those samples. The possible formation of fine cracks below the resolution of μXCT cannot be discounted. A multi-scale analysis [99] should be carried out in a future study in order to observe the sample at a smaller voxel size to resolve macro cracks which were not visible at the current resolution.

Analysis of the *ex situ* X-ray tomographs in **Figure 119**, of sample EF 20-3, which developed the highest amount of creep strains out of the EF 20 samples, showed that significant new cracks propagated not only in-between the fibre bundles but also close to the vertical matrix cracks. The cracking observed in EF 20-3, **Figure 119**, was both parallel, (i) and (ii), and perpendicular, (iii), to the loading direction, y axis. The tomographs of sample EF 20-1 and 2 were also analysed but no signs of damage were observed. Maximum normal 3D strains were also plotted for the three EF 20 samples in **Figure 122**. It was observed that sample EF 20-1 and EF 20-2 developed negligible amounts of strains in the microstructure.

Sample EF 20-3, **Figure 122 (c)**, on the other hand showed maximum normal strain in the shape of vertical and horizontal cracks. The region of maximum normal 3D strain presented in **Figure 122 (c)**, directly coincided with the areas where the cracking was observed. This indicates that permanent damage has occurred in EF 20-3 which is a function of having a lower PLS than the applied stress. The normal components of strain plotted in **Figure 123** indicate that strains in all three axis, ε_{xx}, ε_{yy} and ε_{zz}, played a role in the overall crack propagation in the sample. This was due to the complex stress profile generated within the sample due to the involute layup. The tightly placed sheets give rise to displacement vectors of equal magnitude in both Ux and Uy, as seen in **Figure 123.** This implies a tensile load on the vertical cracks which tend to open up. Note that the strain map indicated areas of microcracks propagation with a lot more clarity than the tomography data itself. These cracks could be a function of shear loading between the layers as well as tensile loading of the vertical matrix crack. The involute structure gives rise to a complex loading regime within the sample. Due to the nature of the tomography analysis carried out, the possibility of cracks closing up after unloading cannot be ignored. Damage that might have appeared during loading would be closed after unloading. Due to the cracks being very thin, they offer very limited contrast and hence some of them might not be observable by tomography.

The strain maps in **Figure 121** and **Figure 123** show localised strain and are unable to reveal the classic beam bending behaviour, with a well-defined neutral axis, the top surface in compression and the bottom surface in tension, and are mainly used to show the effects of damage. This could be resolved by carrying out a radius of curvature change by comparing the in displacement across the volume in x, as a function of y similar to the analysis carried out in **CHAPTER 5, 5.3.3, Figure 109**. Due to limited resolution of the x-CT data the radius of curvature analysis didn't produce meaningful results.

From the beam bending creep experiments, it can be concluded that the EF 20 weave offered a greater resistance to creep in comparison to EF 19. In comparison to the 0/90° layup, the involute layup produced an intricate stress distribution within the sample resulting in lowering the overall creep strains that developed under a give load. In order to understand how the stress builds up in this material, the weave style along with the layup should be modelled. This would help provide a deeper understanding on how the strains developed in the material system under vertical loading. Creep experiments in tandem with X-ray tomography would also be able to help deepen the understanding of how strain builds up in these material systems, under load at temperature, with time.

6.7.4 Displacement and strain analysis in sealing rings

The design and manufacture of piston rings, using CMCs, is a new area of work and required prior CMC machining knowledge which did not exist as part of the project. Hence the method used to manufacture metallic sealing rings was mirrored to produce CMC sealing rings. This resulted in two rings being produced which were slightly different to the proposed engineering drawing. The spring produced in both rings was roughly the same as the design intent, but the fitted stress was substantially different. Although the design stress was expected to be less than 25 MPa for both rings, the manufactured EF 19 ring had a fitted stress of 16.2 MPa and EF 20 had a fitted stress of 42 MPa, as seen in **Table 21**. When compared to their PLS, the stress in the rings equated to around 83% of EF 19's PLS value, whilst 124% of EF 20's PLS value. This suggests that even though EF 20 had a much higher PLS, the stress it would experience in its fitted condition would be greater than its PLS resulting in permanent damage.

The percentage spring loss for EF 19, **Figure 129**, stabilised after undergoing initial stress relaxation, with a gradient of almost zero between 1-16 hours. The stress generated in the ring during

fitting, **Figure 130**, was lower than the PLS measured for EF 19 which suggests that no microstructural cracking should have taken place in the material during loading. Maximum normal 3D displacement was plotted in **Figure 131 (a)** for the ring. No visible damage was observed in the microstructure, which might suggest that the permanent strain that took place was either a function of classic creep mechanisms, interfacial sliding [47] or a function of microstructural cracking which either closed up after unloading, or was not visible at the μXCT voxel resolution, $5.5\mu m^3$. Studies carried out by Boitier et al. [160] to investigate creep mechanisms in a CMC suggest that interply microcracks between fibre bundles could give rise to plastic strain. Classic creep mechanisms, like microstructural dislocations or vacancies in the fibre could also play a role in the overall plastic strain, but should be small in comparison to the creep as a function of micro and macro structural defect in the microstructure. A multi-scale analysis should be done to observe the sample at smaller voxel size to resolve macro cracks which were not visible at the current resolution.

The percentage spring loss for sample EF 20, **Figure 129**, was observed to fall at a much steeper rate during the first hour, signifying primary creep, after which the gradient decreased at a much lower rate, suggesting secondary creep. The gradient did not completely stabilise, and a change in gradient over time was observed, decreasing from a value of 1.5% per hour to 0.5% per hour over a period of 15 hours. This change in gradient could be a function of permanent damage being generated in the sample. **Figure 130** shows that the fitted stress in the EF 20 ring was around 42MPa, which was much higher than the proportional stress limit of the ring. This would give rise to permanent damage in the sample, which could give rise to permanent strain with time. **Figure 130 (a)** indicates that the gradient of stress loss between consecutive points is decreasing, indicating that the ring is moving towards an equilibrium position. Tests conducted over a longer period of time would be able to predict the stabilisation stress

and strain condition. **Figure 131 (b)** indicates that permanent strain was present within the sample EF 20; the strain followed the same shape and profile as the matrix cracks, **Figure 119. Figure 131 (c)** shows the magnified version of the maximum normal 3D strain presented in **Figure 131 (b).** The maximum normal 3D strain was observed at the location of the matrix cracks which were present at 45° to the x axis. This suggests that even though the matrix cracks are completely dormant during loading in y, during three-point bend test loading configuration, they play a significant role in the development of creep strains produced in a ring sample at high stress levels. This is due to the nature of the cracks not being vertical but at an angle, resulting in loading in both x and y axis on the matrix cracks due to the hoop stress in the ring, which in turn act as stress concentrators. **Figure 131 (d)** shows the 3D nature of the strains present in the sample extrapolated over an orthoslice of the tomograph. This suggests that the strain mirrored the crack profile not only in x and y but also in z axis. This further confirms the nature of the strains and how they are linked to the matrix cracks present in the sample.

It can be concluded that due to the loading configuration in a sealing ring, the matrix cracks present are loaded in tension, acting as stress concentrators, generating high levels of strain, which result in permanent deformation in a piston ring. The production process must be reviewed to ensure the fibre layers are not cut across and the fitting stress is below the PLS limit of the material. By carrying out modelling on CMCs sealing ring profile with different weave and layup patterns, the generation strain on these micro cracks could be studied and their impact on the overall permanent strain within the material could be understood. Once a deeper understanding of the strain profile within the material is understood, the layup could be optimised such that these matrix cracks could be arranged parallel to the load direction.

6.8 Conclusion

This chapter looked at calculating the effective modulus and the proportional limit stress for eight different samples produced using different layups and processing parameters. The effective modulus value, calculated in the high temperature fracture analysis carried out at Advance Light Source, University of California, at Berkley, was used to calculate the compliance of the elevated temperature tensile testing machine at Imperial College London. The machine displacement was a linear function of the applied load, and was subtracted from total displacements measured during the three-point bend tests at 1100°C, to find out the actual vertical displacement of the sample. These corrected displacement values were used to generate the stress vs strain curves, presented in **Figure 114,** which were then used to calculate the effective flexural modulus along with the Proportional limit stress, PLS, for each of the 8 samples.

The results suggested that out of all 8 samples, EF 20 sintered at 1250°C, with an involute layup, gave the most optimum mechanical properties, whilst EF 20-4 underperformed in both categories. Both the modulus and the proportional limit stress values were used in to understand the creep behaviour of the samples.

It can be concluded that PLS played an important role in the permanent deformation of the samples. The hoop stress in a piston ring should be less than 80% of the measured PLS. This would reduce the chances of permanent damage development within the microstructure, minimising permanent strain. It can also be concluded that EF 20, due to its unidirectional weave configuration, developed lower primary and secondary creep strains in the three-point loading configuration, in comparison to EF 19 which had 50% fibre tows in the warp and the weft directions. The involute layup outperformed the 0/90° layup due to higher shear strain between the layers and a more complex load strain profile within

the sample. The CHI and 1250°C sintering temperature had similar creep performance to the samples sintered at 1200°C.

The EF 19 ring performed adequately, only losing 13% of their spring at 1100°C, in comparison to the best metallic ring losing 70% of its spring at 1000°C, at 20% of its proof stress. When the fitted stress was beyond the PLS limit permanent deformation was observed in the sample, EF 20, which resulted in higher stress relaxation than normal. Hence future ring design must be done keeping in mind the PLS. The manufacturing process should be reviewed, such that the machining of the piston ring does not result in cutting through the fibre layers, so that the component has lower number of defects and consequently a higher PLS.

The matrix cracks which were parallel to the stress applied in the three-point bend test configuration, were at an angle due to the layup and hence loaded in tensile direction in the sealing ring configuration. This resulted in the matrix cracks becoming stress concentrators, resulting in permanent damage. Detailed modelling should be carried out in order to further understand the relationship between stress and the matrix cracks, along with developing an optimised weave layup which could reduce stress concentrators in the loading direction.

CHAPTER 7. Conclusion and Future Work

7.1 Conclusion

The work presented in thesis has focused on evaluating two different oxide based ceramic matrix composites for their used in gas turbine sealing applications. The first material system investigated in this study was a Nextel 312 based fibre system with SiCO matrix and boron nitride (BN) interface. This was reviewed due to its cost advantage, being atleast half the price in comparison to other oxide fibres. After reviewing the literature, it was found that the temperature stability limit for this material could be improved by increasing the polymer infiltration and pyrolysis (PIP) temperature. After creating different variants and studying them mechanically and morphologically it was found that this system could only function for short periods at temperatures upto 900°C. This was well below the operating limit that was being looked at in this study, hence this system wasn't studied further.

Detailed review of another oxide-based system with Nextel 720 fibre and Alumina matrix was carried out. Literature review of the system suggested that this material had the capability of performing adequately at such temperatures. No previous work on the failure development of these material systems, at 1100°C, had been carried out. In order to understand the fracture behaviour *in situ* X-ray tomography was carried out on these materials at the ALS light source at Berkley. Using a three-point loading configuration it was found that the flexural strength was unaffected by temperature. 3D visualisation of the microstructure showed that fracture occurred by propagation of internal cracks at stresses close to the flexural strength. Shear fractures propagated across fibre bundles that were oriented perpendicular to the flexural stress at both room temperature and 1100°C. At the higher temperature,

an additional failure mode of delamination was observed, that may arise from relaxation of thermal residual stresses and creep.

Having confirmed that this Nextel720/Alumina system performed adequately at 1100°C, 8 different variants were produced, each with different weave patterns, fibre layups and sintering temperature, to optimise it for creep application. These were then tested at 1100°C to quantify the mechanical properties of the system. It was found that EF 20 weave, which was unidirectional in nature, with an involute layup and sintered at 1250°C had the highest proportional limit stress (PLS) and developed the lowest creep strains, with no cracking observed in the microstructure, under a 25MPa stress condition. The two systems that performed the best, namely EF 19-1 and EF20-1 were then used to make sealing rings. A 140 mm outer diameter, with a cross-section of 5x5 mm was designed to have a fitted stress of 25MPa. The two manufactured rings had different fitted stress, EF 19 having around 16 MPa and EF 20 having around 42 MPa. Limited creep was observed in the EF 19 ring with no visible microstructural damage observed in *ex situ* DVC analysis. EF 20, on the other hand, showed signs of microstructural cracking, which was mainly due to the fitted stress being higher than the PLS of the material. Overall both rings performed adequately for 16 hours under service conditions, maintaining 83% and 65% of their spring respectively.

It can be concluded that Ox.ox CMCs, Nextel 720/Alumina in particular, can be used to manufacture sealing rings for gas turbine sealing applications of 1100°C. These materials systems loose less than 13% of their spring over time at 1100°C, under a 25MPa stress condition, making them ideal candidates for sealing applications.

7.2 Future work

Creep tests need to be carried out for longer durations on optimised Nextel 720/Alumina matrix, at 1100°C, to the point where the material system enters tertiary creep cycle. This could be used to predict the long-term behaviour of the material system. Work should focus on iterating EF 20 weave further. Three-point bend tests, in tandem with *in situ* X-ray tomography, should be designed in a way which ensures that the sample enters tertiary creep. This could be used to measure the damage development during the creep process. A number of specimens per sample type should be tested in order to increase the reliability of the data.

The manufacturing of piston ring needs to be improved such that the machining process doesn't result in cutting across fibre layers, resulting in reduced mechanical properties. This could be achieved by making the cylinder in the free shape of a piston ring so that only slitting would be required after sintering. Work should be carried out on optimising the matrix composition which could result in further improving the creep performance of these systems.

The strain profile between a beam and a circular ring was observed to load the matrix cracks differently. The matrix cracks which were parallel to the stress applied in the three-point bend test configuration, were loaded in tensile direction in the sealing ring configuration. This resulted in the matrix cracks becoming stress concentrators, resulting in creep damage. Detailed computational stress analysis should be carried out in order to further understand the relationship between stress and the matrix cracks, along with developing an optimised weave layup which could reduce stress concentrators in the loading direction.

As of now this material system along with its prepreg, which is used by different UK and EU based Tier 1 aerospace manufacturers, is manufactured only in the US. This material falls under 1C007.c.1.a.1

(CAS 1344-28-1) of the US export control laws, which means that the de-minimis rule (EAR 734.4(d)) applies to this material which states that the US content of the final product should not be more than 25%. Due to the fragility of the prepreg, having to be kept at sub-zero temperatures during transport, along with the export control hurdles, alternative supply chains should be looked at if this material system is to be used extensively in the UK aerospace sector.

References

[1] H. Ohnabe, S. Masaki, M. Onozuka, K. Miyahara, T. Sasa, Potential application of ceramic matrix composites to aero-engine components, Compos. Part A Appl. Sci. Manuf. 30 (1999) 489–496. https://doi.org/10.1016/S1359-835X(98)00139-0.

[2] C. Kaya, F. Kaya, E.G. Butler, A.R. Boccaccini, K.K. Chawla, Development and characterisation of high-density oxide fibre-reinforced oxide ceramic matrix composites with improved mechanical properties, J. Eur. Ceram. Soc. 29 (2009) 1631–1639.

[3] J.J. Mecholsky Jr, Engineering research needs of advanced ceramics and ceramic-matrix composites, Am. Ceram. Soc. Bull. 68 (1989) 367–375.

[4] M.P. Boyce, Gas turbine engineering handbook: Chapter 13, in: Elsevier, 2012: pp. 557–604.

[5] J.R. Davis, others, ASM specialty handbook: heat-resistant materials, Asm International, 1997.

[6] A.O. Lebeck, Principles and design of mechanical face seals, John Wiley & Sons, 1991.

[7] M.P. Boyce, Gas turbine engineering handbook, 4th ed., Elsevier, 2012.

[8] N.P. Bansal, J. Lamon, Ceramic matrix composites: Materials, modeling and technology, in: John Wiley & Sons, 2014: pp. 236–240.

[9] E. Stoll, P. Mahr, H.G. Krüger, H. Kern, B.J.C. Thomas, A.R. Boccaccini, Fabrication technologies for oxide-oxide ceramic matrix composites based on electrophoretic deposition, J. Eur. Ceram. Soc. 26 (2006) 1567–1576.

[10] M.B. Ruggles-Wrenn, M. Ozer, Creep behavior of Nextel^{TM}720/alumina-mullite ceramic composite with ±45° fiber orientation at 1200°C, Mater. Sci. Eng. A. 527 (2010) 5326–5334.

[11] K.M. Prewo, Fiber-reinforced ceramics: new opportunities for composite materials, Ceram, Am. Ceram. Soc. Bull. 68 (1989) 395–400.

[12] J.R. Strife, J.J. Brennan, K.M. Prewo, Status of Continuous Fiber-Reinforced Ceramic Matrix Composite Processing Technology, John Wiley and Sons, Imc, Hoboken, NJ, USA, 1990.

[13] M.H. Lewis, A. Tye, E.G. Butler, P.A. Doleman, Oxide CMCs: interphase synthesis and novel fibre development, J. Eur. Ceram. Soc. 20 (2000) 639–644.

[14] R. Warren, S. Deng, Continous fibre reinforced ceramic composites for very high temperatures, Silic. Ind. 61 (1996) 99–107.

[15] D.B. Marshall, J.B. Davis, Ceramics for future power generation technology: Fiber reinforced oxide composites, Curr. Opin. Solid State Mater. Sci. 5 (2001) 283–289.

[16] F.W. Zok, Developments in oxide fiber composites, J. Am. Ceram. Soc. 89 (2006) 3309–3324.

[17] D. Asmi, I.M. Low, Advances in ceramic matrix composites, in: Adv. Ceram. Matrix Compos., 2nd ed., Woodhead Publishing, Cambridge, 2018: pp. 109–140.

[18] V. Mazars, O. Caty, G. Couégnat, A. Bouterf, S. Roux, S. Denneulin, J. Pailhès, G.L. Vignoles, Damage investigation and modeling of 3D woven ceramic matrix composites from X-ray tomography in-situ tensile tests, Acta Mater. 140 (2017) 130–139.

[19] B. Kanka, H. Schneider, Aluminosilicate fiber/mullite matrix composites with favorable high-temperature properties, J. Eur. Ceram. Soc. 20 (2000) 619–623.

[20] P. Myers, Narottam P. Bansal and Jacques Lamon (Eds): Ceramic Matrix Composites Materials, Modeling and Technology, in: John Wiley & Sons (Ed.), Am. Ceram. Soc., John Wiley & Sons, Hoboken, NJ, USA, 2015: pp. 295–330.

[21] C. Kaya, X. Gu, I. Al-Dawery, E.G. Butler, Microstructural development of woven mullite fibre-reinforced mullite ceramic matrix composites by infiltration processing, Sci. Technol. Adv. Mater. 3 (2002) 35.

[22] C. Kaya, J.Y. He, X. Gu, E.G. Butler, Nanostructured ceramic powders by hydrothermal synthesis and their applications, Microporous Mesoporous Mater. 54 (2002) 37–49.

[23] R.A. Jurf, S.C. Butner, Advances in Oxide-Oxide CMC, J. Eng. Gas Turbines Power. 122 (2000) 202–205.

[24] T.A. Parthasarathy, L.P. Zawada, R. John, M.K. Cinibulk, R.J. Kerans, J. Zelina, Evaluation of oxide-oxide composites in a novel combustor wall application, Int. J. Appl. Ceram. Technol. 2 (2005) 122–132.

[25] T. Tian, V.W. Wong, J.B. Heywood, Modeling the dynamics and lubrication of three piece oil control rings in internal combustion engines, SAE Tech. Pap. 122 (1998) 119–129.

[26] G.E. Totten, A.W. Batchelor, H. Liang, C.Y.H. Lim, S.C. Lim, T.W. Scharf, E. van der Heide, A. Nolan, S. Lampman, V. Burt, others, ASM Handbook W, (2017).

[27] W.J. Boettinger, M.E. Williams, S.R. Coriell, U.R. Kattner, B.A. Mueller, Alpha case thickness modeling in investment castings, Metall. Mater. Trans. B Process Metall. Mater. Process. Sci. 31 (2000) 1419–1427.

[28] J. Gayda, T.P. Gabb, P.T. Kantzos, Heat treatment devices and method of operation thereof to produce dual microstructure superalloy disks. патент №: US 6,660,110, 1 (2003) 10.

[29] R. Royce, The jet engine, John Wiley & Sons, 2015.

[30] A.K. Sehra, W. Whitlow, Propulsion and power for 21st century aviation, Prog. Aerosp. Sci. 40 (2004) 199–235.

[31] T.W. Ha, Rotordynamic analysis for stepped-labyrinth gas seals using Moody's friction-factor model, KSME Int. J. 15 (2001) 1217–1225.

[32] M.T. Ma, I. Sherrington, E.H. Smith, N. Grice, Development of a detailed model for piston-

ring lubrication in IC engines with circular and non-circular cylinder bores, Tribol. Int. 30 (1997) 779–788.

[33] F.E. Aslan-zada, V.A. Mammadov, F. Dohnal, Brush seals and labyrinth seals in gas turbine applications, Proc. Inst. Mech. Eng. Part A J. Power Energy. 227 (2013) 216–230.

[34] I.-M. Low, Advances in ceramic matrix composites, Woodhead Publishing, 2018.

[35] S. Maitra, J. Roy, Nanoceramic matrix composites: Types, processing, and applications, in: Adv. Ceram. Matrix Compos., Elsevier, 2018: pp. 27–48.

[36] P. Myers, Narottam P. Bansal and Jacques Lamon (Eds): Ceramic Matrix Composites Materials, Modeling and Technology, Chromatographia. 78 (2015) 843–844. https://doi.org/10.1007/s10337-015-2883-1.

[37] E.W. Neuman, G.E. Hilmas, W.G. Fahrenholtz, A high strength alumina-silicon carbide-boron carbide triplex ceramic, Ceram. Int. 43 (2017) 7958–7962.

[38] L.W. Yang, J.Y. Wang, H.T. Liu, R. Jiang, H.F. Cheng, Sol-gel temperature dependent ductile-to-brittle transition of aluminosilicate fiber reinforced silica matrix composite, Compos. Part B Eng. 119 (2017) 79–89.

[39] S. Gustafsson, L.K.L. Falk, J.E. Pitchford, W.J. Clegg, E. Lidén, E. Carlström, Development of microstructure during creep of polycrystalline mullite and a nanocomposite mullite/5 vol.% SiC, J. Eur. Ceram. Soc. 29 (2009) 539–550.

[40] H.T. Liu, L.W. Yang, X. Sun, H.F. Cheng, C.Y. Wang, W.G. Mao, J.M. Molina-Aldareguia, Enhancing the fracture resistance of carbon fiber reinforced SiC matrix composites by interface modification through a simple fiber heat-treatment process, Carbon N. Y. 109 (2016) 435–443.

[41] D. Asmi, I.M. Low, Manufacture of graded ceramic matrix composites using infiltration techniques, in: Elsevier (Ed.), Adv. Ceram. Matrix Compos., 1st ed., Woodhead Publishing, Cambridge, 2014: pp. 109–140.

[42] M.B. Ruggles-Wrenn, M.T. Pope, Creep behavior in interlaminar shear of a SiC/SiC ceramic composite with a self-healing matrix, Appl. Compos. Mater. 21 (2014) 213–225.

[43] L. Li, Synergistic Effects of Stress-Rupture and Cyclic Loading on Strain Response of Fiber-Reinforced Ceramic-Matrix Composites at Elevated Temperature in Oxidizing Atmosphere, Materials (Basel). 10 (2017) 182.

[44] E. Volkmann, L. Lima Evangelista, K. Tushtev, D. Koch, C. Wilhelmi, K. Rezwan, Oxidation-induced microstructural changes of a polymer-derived Nextel™ 610 ceramic composite and impact on the mechanical performance, J. Mater. Sci. 49 (2014) 710–719.

[45] S. Zhu, M. Mizuno, Y. Nagano, J. Cao, Y. Kagawa, H. Kaya, Creep and Fatigue Behavior in an Enhanced SiC / SiC Composite at, System. 77 (1998) 2269–2277.

[46] S. Rangarajan, Processing and characterization of ceramics and ceramic composites synthesized by pyrolysis of siloxane-based precursors, University of Texas, 1997.

[47] G. Boitier, J. Vicens, J.L. Chermant, Understanding the creep behavior of a 2.5 D Cf-SiC composite. III. From mesoscale to nanoscale microstructural and morphological investigation towards creep mechanism, Mater. Sci. Eng. A. 313 (2001) 53–63.

[48] R.W.E. B. Wilshire, Introduction to Creep, 1st ed., Maney Publishing, 1993.

[49] Roger C. Reed, Lectures on Creep, 2021.

[50] G. Itoh, Deformation of aluminum thin foils under uniaxial tensile stress, (2002) 915–916.

[51] A. H. Cottrell, The time laws of Creep, J. Mech. Phys. f Solids,. I (1952) 53–63.

[52] F. Louchet, P. Duval, Andrade creep revisited, Int. J. Mater. Res. 100 (2009) 1433–1439.

[53] A. H. Cottrell, The time laws of Creep, J. Mech. Phys. Solids. I (1952) 53–63.

[54] E. Fleischmann, M.K. Miller, E. Affeldt, U. Glatzel, Quantitative experimental determination of the solid solution hardening potential of rhenium, tungsten and molybdenum in single-crystal nickel-based superalloys, Acta Mater. 87 (2015) 350–356.

[55] G.Z. Nihon Naika, 3M Nextel Ceramic textiles technical handbook, 3M Data Sheet. 106 (2017) 8.

[56] J. Zhou, A.S. Almansour, G.G. Chase, G.N. Morscher, Enhanced oxidation resistance of SiC/SiC minicomposites via slurry infiltration of oxide layers, J. Eur. Ceram. Soc. 37 (2017) 3241–3253.

[57] M. Al-Hussien, S. Mall, J.R. Calcaterra, Fatigue behavior of Nextel™ 312/Blackglas™ ceramic matrix composite with tensile and zero mean load, Adv. Compos. Mater. 10 (2001) 1–15.

[58] P. Colombo, Polymer derived ceramics: from nano-structure to applications, DEStech Publications, Inc, 2010.

[59] P. Colombo, R. Raj, Advances in Polymer Derived Ceramics and Composites: Preface, Ceram. Trans. 213 (2010).

[60] R. Belardinelli, Processing and properties of Blackglas (TM) ceramic matrix composites reinforced with Nextel (TM) 312 (BN) fabric., The University of Texas at Arlington, 1996.

[61] R. Belardinelli, Processing and properties of Blackglas Ceramic Matrix Composites reinforced with Nextel 312BN Fabric, Universtiy of Illinois, 1996.

[62] M.D. Sacks, Fibre Coatings and the Mechanical Properties of Fibre-Reinforced Ceramic

Composites, in: Ceram. Trans. Vol. 19, Adv. Compos. Mater., The America Ceramic Society, 1991: pp. 619–630.

[63] T. Tiegs, Ceramic matrix composites: edited by R. Warren; Chapman and Hall;, Elsevier, NewYork, 1993.

[64] D.C. Joy, The theory and practice of high-resolution scanning electron microscopy, Ultramicroscopy. 37 (1991) 216–233.

[65] P. Makurunje, F. Monteverde, I. Sigalas, Self-generating oxidation protective high-temperature glass-ceramic coatings for Cf/C-SiC-TiC-TaC UHTC matrix composites, J. Eur. Ceram. Soc. 37 (2017) 3227–3239.

[66] K. Konopka, A. Boczkowska, K. Batorski, M. Szafran, K.J. Kurzydłowski, Microstructure and properties of novel ceramic-polymer composites, Mater. Lett. 58 (2004) 3857–3862.

[67] R.A. Lowden, R.D. James, K. More, Interfaces and Mechanical Properties of Continuous Fiber-Reinforced Ceramic Composites, Ceram. Trans. 19 (1990) 619–630.

[68] P. Colombo, G. Mera, R. Riedel, G.D. Sorarù, Polymer-Derived Ceramics: 40 Years of Research and Innovation in Advanced Ceramics, Am. Ceram. Soc. 93 (2010) 1805–1837.

[69] T. Tiegs, Ceramic matrix composites: edited by R. Warren; Chapman and Hall; New York; 1992; 272 pp.; ISBN 0-216-92682-3, (1993).

[70] M.N. Ghasemi Nejhad, J.K. Bayliss, A. Yousefpour, Processing and performance of continuous fiber ceramic composites by preceramic polymer pyrolysis: II - Resin transfer molding, J. Compos. Mater. 35 (2001) 2239–2255.

[71] D. Ding, Processing, properties and applications of ceramic matrix composites, SiCf/SiC: An overview, Adv. Ceram. Matrix Compos. (2014) 9–26.

[72] B. Jackson, A. Beaber, L. Visser, A. Barnes, J. Lincoln, 12244 Oxide Oxide Tech Paper Rebrand 9805248 Celum, (n.d.) 1–10.

[73] E. Volkmann, K. Tushtev, D. Koch, C. Wilhelmi, J. Göring, K. Rezwan, Assessment of three oxide/oxide ceramic matrix composites: Mechanical performance and effects of heat treatments, Compos. Part A Appl. Sci. Manuf. 68 (2015) 19–28.

[74] F.I. Hurwitz, L. Hyatt, J. Gorecki, L. D'Amore, Silsesquioxanes as precursors to ceramic composites, in: Ceram. Eng. Sci. Proc., 1987: pp. 732–743.

[75] F.I. Hurwitz, Approaches to polymer-derived CMC matrices, (1992).

[76] S.H. Yu, R.E. Riman, S.C. Danforth, R.Y. Leung, Pyrolysis of titanium-metal-filled poly (siloxane) preceramic polymers: effect of atmosphere on pyrolysis product chemistry, J. Am. Ceram. Soc. 78 (1995) 1818–1824.

[77] M.L. Antti, E. Lara-Curzio, R. Warren, Thermal degradation of an oxide fibre (Nextel 720)/aluminosilicate composite, J. Eur. Ceram. Soc. 24 (2004) 565–578.

[78] S. Mall, M.A. Sullivan, Creep rupture and fatigue behavior of a notched oxide/oxide ceramic matrix composite at an elevated temperature, Int. J. Appl. Ceram. Technol. 8 (2011) 251–260.

[79] M. Schmücker, B. Kanka, H. Schneider, Temperature-induced fibre/matrix interactions in porous alumino silicate ceramic matrix composites, J. Eur. Ceram. Soc. 20 (2000) 2491–2497.

[80] K.G. Dassios, M. Steen, C. Filiou, Mechanical properties of alumina Nextel^{TM} 720 fibres at room and elevated temperatures: Tensile bundle testing, Mater. Sci. Eng. A. 349 (2003) 63–72.

[81] M.K. Cinibulk, Effect of Yttria and Yttrium-Aluminum Garnet on Densification and Grain Growth of Alumina At 1200°--1300° C, J. Am. Ceram. Soc. 87 (2004) 692–695.

[82] S. Hackemann, F. Flucht, W. Braue, Creep investigations of alumina-based all-oxide ceramic

matrix composites, Compos. Part A Appl. Sci. Manuf. 41 (2010) 1768–1776.

[83] M. Schmücker, P. Mechnich, Microstructural coarsening of Nextel 610 fibers embedded in alumina-based matrices, J. Am. Ceram. Soc. 91 (2008) 1306–1308.

[84] Z.C. Chen, R. Kulkarni, K.K. Chawla, M. Koopman, K. Ikeda, Processing and microstructure of an all-oxide ceramic composite, Mater. Sci. Forum. 475–479 (2005) 1301–1304.

[85] M.B. Ruggles-Wrenn, P.D. Laffey, Creep behavior in interlaminar shear of Nextel™720/alumina ceramic composite at elevated temperature in air and in steam, Compos. Sci. Technol. 68 (2008) 2260–2266.

[86] M. Ruggles-Wrenn, S. Hilburn, Creep in interlaminar shear of a Nextel™720/aluminosilicate Composite at 1100°C in air and in steam, Int. J. Appl. Ceram. Technol. 12 (2015) 473–480.

[87] S. Hackemann, F. Flucht, W. Braue, Creep investigations of alumina-based all-oxide ceramic matrix composites, Compos. Part A Appl. Sci. Manuf. 41 (2010) 1768–1776.

[88] C.J. Armani, M.B. Ruggles-Wrenn, R.S. Hay, G.E. Fair, Creep and microstructure of Nextel™ 720 fiber at elevated temperature in air and in steam, Acta Mater. 61 (2013) 6114–6124.

[89] S. Zhao, 3D multi-scale characterization and modelling of damage in ceramic matrix composites, University of Oxford, 2018.

[90] C. Tomography, C.T. Imaging, Standard Guide for Computed Tomography (CT) Imaging, ASTM Int. (2005) 1–33.

[91] C.K. Egan, S.D.M. Jacques, M.D. Wilson, M.C. Veale, P. Seller, A.M. Beale, R.A.D. Pattrick, P.J. Withers, R.J. Cernik, 3D chemical imaging in the laboratory by hyperspectral X-ray computed tomography, Sci. Rep. 5 (2015) 1–9.

[92] R. Bertrand, O. Caty, V. Mazars, S. Denneulin, P. Weisbecker, J. Pailhes, G. Camus, F.

Rebillat, In-situ tensile tests under SEM and X-ray computed micro-tomography aimed at studying a self-healing matrix composite submitted to different thermomechanical cycles, J. Eur. Ceram. Soc. 37 (2017) 3471–3474.

[93] Z. Quiney, E. Weston, P. Ian Nicholson, S. Pattison, M.R. Bache, Volumetric assessment of fatigue damage in a SiCf/SiC ceramic matrix composite via in situ X-ray computed tomography, J. Eur. Ceram. Soc. 40 (2020) 3788–3794.

[94] L. Saucedo-Mora, T. Lowe, S. Zhao, P.D. Lee, P.M. Mummery, T.J. Marrow, In situ observation of mechanical damage within a SiC-SiC ceramic matrix composite, J. Nucl. Mater. 481 (2016) 13–23.

[95] X. Fang, J. Jia, X. Feng, Three-point bending test at extremely high temperature enhanced by real-time observation and measurement, Measurement. 59 (2015) 171–176.

[96] J.W. Kryinicki, R.E. Green, D.C. Nagle, Discrete failure mode detection in a woven SiC cloth reinforced glass composite, J. Mater. Sci. 26 (1991) 2184–2188.

[97] T. Robertson, X. Huang, R. Kearsey, High temperature performance of mullite whisker-reinforced ZTA, J. Compos. Mater. 50 (2016) 3719–3729.

[98] J. Tracy, A. Waas, S. Daly, A new experimental approach for in situ damage assessment in fibrous ceramic matrix composites at high temperature, J. Am. Ceram. Soc. 98 (2015) 1898–1906.

[99] J. Tracy, S. Daly, K. Sevener, Multiscale damage characterization in continuous fiber ceramic matrix composites using digital image correlation, J. Mater. Sci. 50 (2015) 5286–5299.

[100] A. Szweda, High-Frequency Fatigue Behavior of Woven-Fiber-Fabric-Reinforced Polymer-Derived Ceramic-Matrix Composites, 30 (1998) 1221–1230.

[101] F. Zhu, P. Bai, Y. Gong, D. Lei, X. He, Accurate measurement of elastic modulus of specimen with initial bending using two-dimensional DIC and dual-reflector imaging technique, Meas. J. Int. Meas. Confed. 119 (2018) 18–27.

[102] F. Wan, R. Liu, Y. Wang, Y. Cao, C. Zhang, T.J. Marrow, Damage development during flexural loading of a 5-directional braided C/C-SiC composite, characterized by X-ray tomography and digital volume correlation, Ceram. Int. (2018).

[103] A.Ž. Iveković, S. Novak, G. Dražić, D. Blagoeva, S.G. de Vicente, Current status and prospects of SiCf/SiC for fusion structural applications, J. Eur. Ceram. Soc. 33 (2013) 1577–1589.

[104] B.K. Bay, T.S. Smith, D.P. Fyhrie, M. Saad, Digital volume correlation: Three-dimensional strain mapping using X-ray tomography, Exp. Mech. 39 (1999) 217–226.

[105] T.S. Smith, B.K. Bay, M.M. Rashid, Digital volume correlation including rotational degrees of freedom during minimization, Exp. Mech. 42 (2002) 272–278.

[106] D.P. Finegan, E. Tudisco, M. Scheel, J.B. Robinson, O.O. Taiwo, D.S. Eastwood, P.D. Lee, M. Di Michiel, B. Bay, S.A. Hall, G. Hinds, D.J.L. Brett, P.R. Shearing, Quantifying bulk electrode strain and material displacement within lithium batteries via high-speed operando tomography and digital volume correlation, Adv. Sci. 3 (2015) 1–11.

[107] B. Pan, D. Wu, Z. Wang, Internal displacement and strain measurement using digital volume correlation: A least-squares framework, Meas. Sci. Technol. 23 (2012).

[108] G.N. Morscher, H.M. Yun, J.A. Dicarlo, In-plane cracking behavior and ultimate strength for 2D woven and braided melt-infiltrated SiC/SiC composites tensile loaded in off-axis fiber directions, J. Am. Ceram. Soc. 90 (2007) 3185–3193.

[109] G.N. Morscher, Stress-dependent matrix cracking in 2D woven SiC-fiber reinforced melt-infiltrated SiC matrix composites, Compos. Sci. Technol. 64 (2004) 1311–1319.

[110] S.K. Mital, B.A. Bednarcyk, S.M. Arnold, J. Lang, Modeling of Melt-In fi ltrated SiC / SiC Composite Properties October 2009, (2019).

[111] C. Li, G. Habler, L.C. Baldwin, R. Abart, An improved FIB sample preparation technique for site-specific plan-view specimens: A new cutting geometry, Ultramicroscopy. 184 (2018) 310–317.

[112] H.A. Bale, A. Haboub, A.A. MacDowell, J.R. Nasiatka, D.Y. Parkinson, B.N. Cox, D.B. Marshall, R.O. Ritchie, Real-time quantitative imaging of failure events in materials under load at temperatures above 1,600 °C., Nat. Mater. 12 (2013) 40–6.

[113] D. Liu, B. Gludovatz, H.S. Barnard, M. Kuball, R.O. Ritchie, Damage tolerance of nuclear graphite at elevated temperatures, Nat. Commun. 8 (2017).

[114] A. Haboub, H.A. Bale, J.R. Nasiatka, B.N. Cox, D.B. Marshall, R.O. Ritchie, A.A. Macdowell, Tensile testing of materials at high temperatures above 1700°C with in situ synchrotron X-ray micro-tomography, Rev. Sci. Instrum. 85 (2014).

[115] D. Gürsoy, F. De Carlo, X. Xiao, C. Jacobsen, TomoPy: a framework for the analysis of synchrotron tomographic data, J. Synchrotron Radiat. 21 (2014) 1188–1193.

[116] A. Hussey, R. De Meyere, C. Deck, D.E.J. Armstrong, Y. Zayachuk, Statistically sound application of fiber push-out method for the study of locally non-uniform interfacial properties of SiC-SiC fiber composites, J. Eur. Ceram. Soc. 40 (2020) 1052–1056.

[117] T. Datasheet, - MultiTest-i, (n.d.). https://www.mecmesin.com/sites/default/files/brochures/431-343-09_multitest-

i_technical_datasheet.pdf.

[118] T. Applications, I. Processing, 3M Nextel Ceramic Fabrics 312 and 440, (n.d.). https://multimedia.3m.com/mws/media/1242135O/3m-nextel-ceramic-fabrics-312-and-440.pdf.

[119] Bruker, Diffrac suite, (n.d.) 8–9. https://my.bruker.com/acton/attachment/2655/f-b016a843-48ea-4914-9507-a347f04d20d9/1/-/-/-/-/XRD DIFFRAC.SUITE Part11 Flyer DOC-H88-EXS060 V3 high.pdf.

[120] C.R. Hubbard, B.H. O'Connor, International centre for diffraction data (ICDD), (2002).

[121] M.K. Naskar, M. Chatterjee, A. Dey, K. Basu, Effects of processing parameters on the fabrication of near-net-shape fibre reinforced oxide ceramic matrix composites via sol–gel route, Ceram. Int. 30 (2004) 257–265.

[122] S. Rahimi, D.L. Engelberg, J.A. Duff, T.J. Marrow, In situ observation of intergranular crack nucleation in a grain boundary controlled austenitic stainless steel., J. Microsc. 233 (2009) 423–31. https://doi.org/10.1111/j.1365-2818.2009.03133.x.

[123] J.A. Duff, T.J. Marrow, In situ observation of short fatigue crack propagation in oxygenated water at elevated temperature and pressure, Corros. Sci. 68 (2012) 34–43.

[124] A. Cook, N. Stevens, J. Duff, A. Mshelia, T.-S. Leung, S. Lyon, J. Marrow, W. Ganther, I. Cole, Atmospheric-Induced Stress Corrosion Cracking of austenitic stainless steels under limited chloride supply, in: 18th Int. Corros. Congr. 2011, International Corrosion Congress, Perth, Australia, 2011: pp. 1438–1449.

[125] J. Kovac, C. Alaux, T.J. Marrow, E. Govekar, A. Legat, Correlations of electrochemical noise, acoustic emission and complementary monitoring techniques during intergranular stress-

corrosion cracking of austenitic stainless steel, Corros. Sci. 52 (2010) 2015–2025.

[126] S.R. Eugster, Geometric continuum mechanics and induced beam theories, in: Springer, New York, 2015: pp. 55–81.

[127] W.C. Oliver, G.M. Pharr, An improved technique for determining hardness and elastic modulus using load and dispalcement sensing indentation experiments, J. Mater. Res. 7 (1992) 1564–1583.

[128] C. Liang, J.W. Hutchinson, Mechanics of the Fiber Push-Out Test, Mech. Mater. 14 (1993) 207–221.

[129] B.D. Cullity, Elements of X-ray Diffraction, Addison-Wesley Publishing, 1956.

[130] P. Colombo, The SiCO System, in: Polym. Deriv. Ceram. from Nano-Structure to Appl., DEStech Publications, Inc, Lancaster, 2009: pp. 170–184.

[131] F.I. Hurwitz, M.A.B. Meador, Tailoring silicon oxycarbide glasses for oxidative stability, J. Sol-Gel Sci. Technol. 14 (1999) 75–86.

[132] H.-J. Kleebe, G. Gregori, F. Babonneau, Y.D. Blum, D.B. MacQueen, S. Masse, Evolution of C-rich SiOC ceramics: Part I. Characterization by integral spectroscopic techniques: Solid-state NMR and Raman spectroscopy, Zeitschrift Für Met. 97 (2006) 699–709.

[133] R.W. Goettler, K.T. Faber, Interfacial shear stresses in fiber-reinforced glasses, Compos. Sci. Technol. 37 (1990) 129–147.

[134] R.M.G. De Meyere, L. Gale, S. Harris, I.M. Edmonds, T.J. Marrow, D.E.J. Armstrong, Optimizing the fiber push-out method to evaluate interfacial failure in SiC/BN/SiC ceramic matrix composites, J. Am. Ceram. Soc. 104 (2021) 2741–2752.

[135] K.K. Phani, S.K. Niyogi, Young's modulus of porous brittle solids, J. Mater. Sci. 22 (1987)

257–263.

[136] T.J. Marrow, D. Liu, S.M. Barhli, L.S. Mora, Y. Vertyagina, D.M. Collins, C. Reinhard, S. Kabra, P.E.J. Flewitt, D.J. Smith, In situ measurement of the strains within a mechanically loaded polygranular graphite, Carbon N. Y. 96 (2016) 285–302.

[137] R. Bertrand, O. Caty, V. Mazars, S. Denneulin, P. Weisbecker, J. Pailhes, G. Camus, F. Rebillat, In-situ tensile tests under SEM and X-ray computed micro-tomography aimed at studying a self-healing matrix composite submitted to different thermomechanical cycles, J. Eur. Ceram. Soc. 37 (2017) 3471–3474.

[138] F. Wan, R. Liu, Y. Wang, Y. Cao, C. Zhang, T.J. Marrow, In situ observation of compression damage in a 3D needled-punched carbon fiber-silicon carbide ceramic matrix composite, Compos. Struct. 210 (2019) 189–201.

[139] D.R.G. Mitchell, DiffTools: Electron diffraction software tools for DigitalMicrograph™, Microsc. Res. Tech. 71 (2008) 588–593.

[140] J. Liu, A.H. Mir, G. He, M. Danaie, J. Hinks, S. Donnelly, H. Nordin, S. Lozano-Perez, C.R.M. Grovenor, In-situ TEM study of irradiation-induced damage mechanisms in monoclinic-ZrO2, Acta Mater. 199 (2020) 429–442.

[141] D. Liu, B. Gludovatz, H.S. Barnard, M. Kuball, R.O. Ritchie, Damage tolerance of nuclear graphite at elevated temperatures, Nat. Commun. 8 (2017) 1–9.

[142] G.P. Tandon, D.J. Buchanan, N.J. Pagano, R. John, Analytical and Experimental Characterization of Thermo-Mechanical Properties of a Damaged Woven Oxide-Oxide Composite, in: 25th Annu. Conf. Compos. Adv. Ceram. Mater. Struct. A Ceram. Eng. Sci. Proc., 2001: pp. 687–694.

[143] M. Ruggles-Wrenn, S. Hilburn, Creep in interlaminar shear of a Nextel™720/aluminosilicate Composite at 1100°C in air and in steam, Int. J. Appl. Ceram. Technol. 12 (2015) 473–480.

[144] E. Volkmann, K. Tushtev, D. Koch, C. Wilhelmi, J. Göring, K. Rezwan, Assessment of three oxide/oxide ceramic matrix composites: Mechanical performance and effects of heat treatments, Compos. Part A Appl. Sci. Manuf. 68 (2015) 19–28. https://doi.org/10.1016/j.compositesa.2014.09.013.

[145] C. Ben Ramdane, A. Julian-Jankowiak, R. Valle, Y. Renollet, M. Parlier, E. Martin, P. Diss, Microstructure and mechanical behaviour of a Nextel™610/alumina weak matrix composite subjected to tensile and compressive loadings, J. Eur. Ceram. Soc. 37 (2017) 2919–2932.

[146] J.M. Berthelot, J.F. Le Corre, A model for transverse cracking and delamination in cross-ply laminates, Compos. Sci. Technol. 60 (2000) 1055–1066.

[147] S. Cheng, X. Wei, T. Jiang, Stress distribution and deformation of adhesive-bonded laminated composite beams, J. Eng. Mech. 115 (1989) 1150–1162.

[148] D.M. Wilson, L.R. Visser, High performance oxide fibers for metal and ceramic composites, Compos. - Part A Appl. Sci. Manuf. 32 (2001) 1143–1153.

[149] J.B. Davis, R.S. Hay, D.B. Marshall, P.E.D. Morgan, A. Sayir, Influence of interfacial roughness on fiber sliding in oxide composites with La-monazite interphases, J. Am. Ceram. Soc. 86 (2003) 305–316.

[150] Y. Nawab, F. Jacquemin, P. Casari, N. Boyard, V. Sobotka, Y. Nawab, F. Jacquemin, P. Casari, N. Boyard, Y. Borjon-piron, Study of variation of thermal expansion coefficients in carbon / epoxy laminated composite plates, Compos. Part B Eng. 50 (2013) 144–149.

[151] T. Ishikawa, K. Koyama, S. Kobayashi, Thermal Expansion Coefficients of Unidirectional

Composites, J. Compos. Mater. 12 (1978) 153–168.

[152] W.J. Craft, R.M. Christensen, Coefficient of Thermal Expansion for Composites with Randomly Oriented Fibers, J. Compos. Mater. 15 (1981) 2–20.

[153] F. Fritz, G.F. Corliss, A. Johnson, D. Prohaska, J. Hart, Rocket Nozzle Design, 1998.

[154] W.H. Goodman, C.C. Lee, S.R. Lin, N.R. Patel, Star 37S solid rocket motor nozzle thermostructural analysis, Stud. Appl. Mech. 35 (1994) 405–422.

[155] Jay Morrison (Siemens Energy Inc.), UTSR 2017 Conference " Ceramic Matrix Composite Advanced Transition for 65 % Combined Cycle Efficiency " CMC Advanced Transition for Program Overview, in: 2017.

[156] ASTM Committee D-30 on Composite Materials, Standard test method for tensile properties of polymer matrix composite materials, ASTM international, 2008.

[157] J. Rosti, J. Koivisto, L. Laurson, M.J. Alava, Fluctuations and scaling in creep deformation, Phys. Rev. Lett. 105 (2010) 27–30.

[158] C. ROSS, Applied Stress Analysis, 1st ed., John Wiley & Sons, 1986.

[159] E.H. Cross, An investigation into some of the mechanical properties of nickel & cobalt alloy sealing rings, Polytechnic south west, 1990.

[160] X. Cao, X. Yin, X. Ma, X. Fan, Y. Cai, J. Li, L. Cheng, L. Zhang, The microstructure and properties of SiC/SiC-based composites fabricated by low-temperature melt infiltration of Al--Si alloy, Ceram. Int. 42 (2016) 10144–10150.

Appendix 1

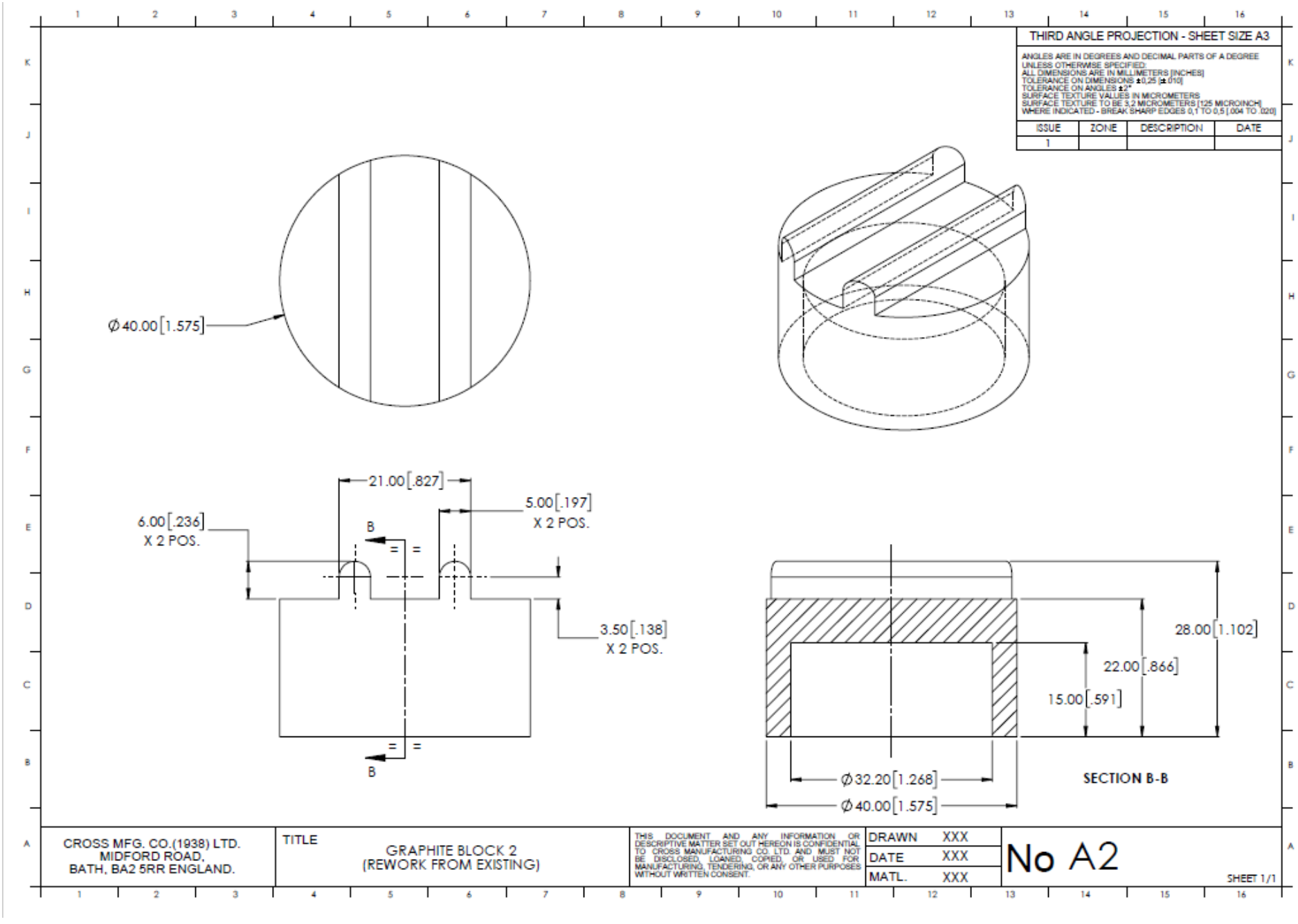
THIRD ANGLE PROJECTION - SHEET SIZE A3
ANGLES ARE IN DEGREES AND DECIMAL PARTS OF A DEGREE
UNLESS OTHERWISE SPECIFIED:
ALL DIMENSIONS ARE IN MILLIMETERS [INCHES]
TOLERANCE ON DIMENSIONS ±0,25 [±.010]
TOLERANCE ON ANGLES ±2°
SURFACE TEXTURE VALUES IN MICROMETERS
SURFACE TEXTURE TO BE 3,2 MICROMETERS [125 MICROINCH]
WHERE INDICATED - BREAK SHARP EDGES 0,1 TO 0,5 [.004 TO .020]
ISSUE
ZONE
DESCRIPTION
DATE
1
Ø 40.00 [1.575]
21.00 [.827]
5.00 [.197]
X 2 POS.
6.00 [.236]
X 2 POS.
B
B
3.50 [.138]
X 2 POS.
28.00 [1.102]
22.00 [.866]
15.00 [.591]
Ø 32.20 [1.268]
Ø 40.00 [1.575]
SECTION B-B
CROSS MFG. CO.(1938) LTD.
MIDFORD ROAD,
BATH, BA2 5RR ENGLAND.
TITLE
GRAPHITE BLOCK 2
(REWORK FROM EXISTING)
THIS DOCUMENT AND ANY INFORMATION OR DESCRIPTIVE MATTER SET OUT HEREON IS CONFIDENTIAL TO CROSS MANUFACTURING CO. LTD AND MUST NOT BE DISCLOSED, LOANED, COPIED, OR USED FOR MANUFACTURING, TENDERING, OR ANY OTHER PURPOSES WITHOUT WRITTEN CONSENT.
DRAWN XXX
DATE XXX
MATL. XXX
No A2
SHEET 1/1

Appendix 2

EF 20-1

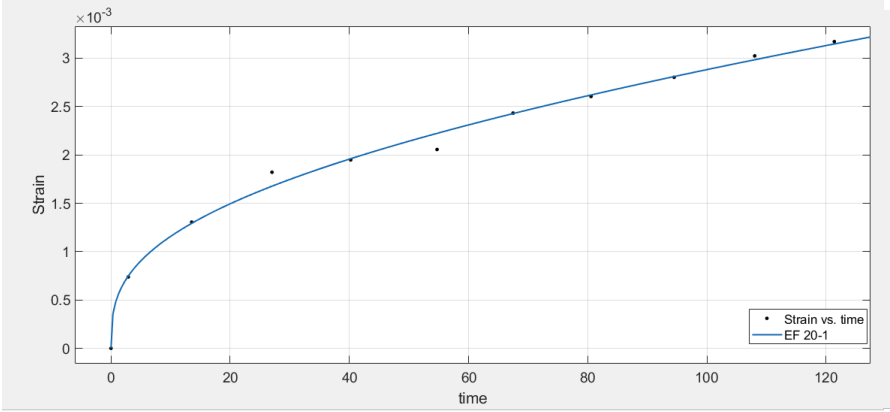

EF 20-2

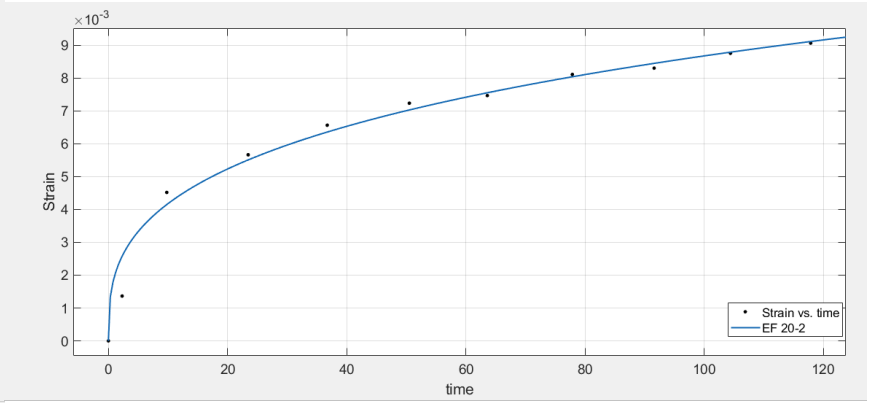

EF 20-3

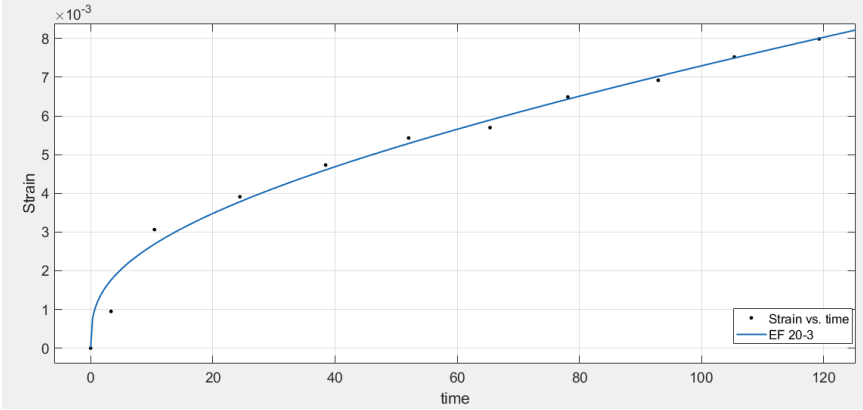

EF19-1

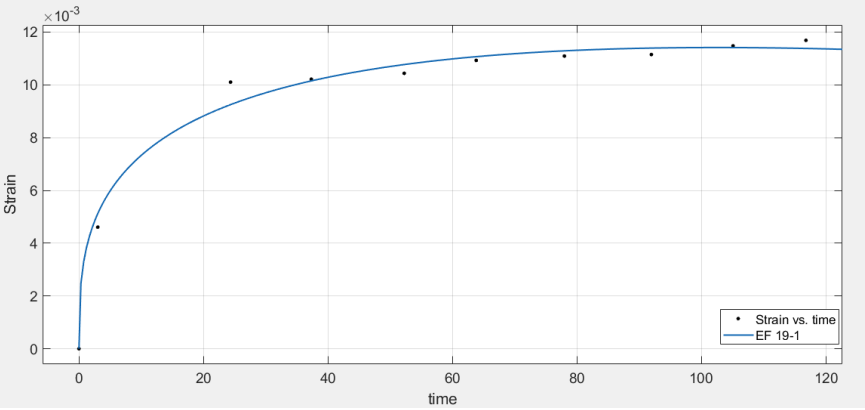

EF 19-2

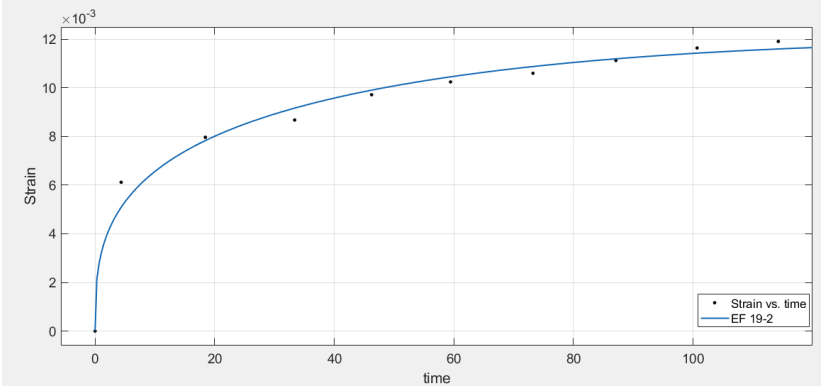

EF 19-3

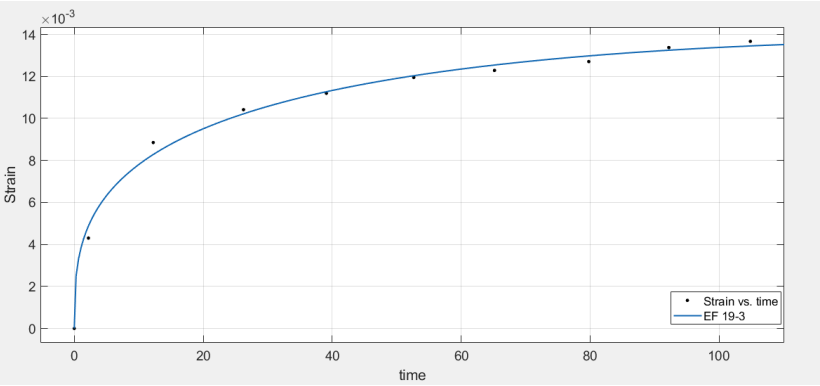

EF19-4

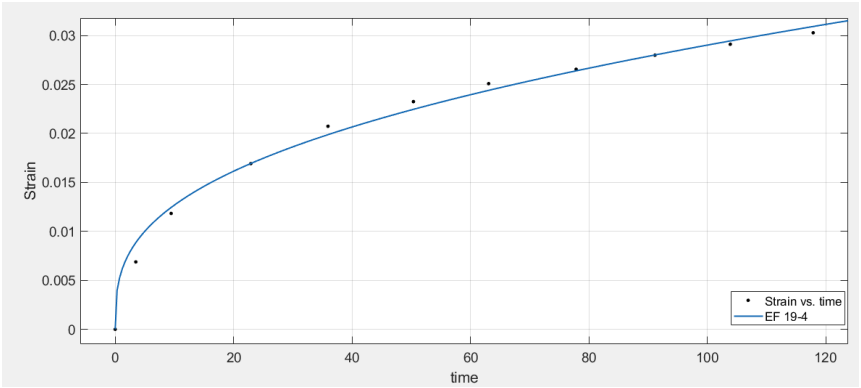

Appendix 3

PART NUMBER - A24218-3

SUPPLIER - COMPOSITE HORIZONS

MATERIAL- CMC N-720 FIBRE
INVOLUTE LAYERED

THIRD ANGLE PROJECTION - SHEET SIZE A3

ANGLES ARE IN DEGREES AND DECIMAL PARTS OF A DEGREE
UNLESS OTHERWISE SPECIFIED:
ALL DIMENSIONS ARE IN INCHES
TOLERANCE ON DIMENSIONS ± .010"
TOLERANCE ON ANGLES ± 2°
SURFACE TEXTURE VALUES IN MICROINCHES
SURFACE TEXTURE TO BE 125 MICROINCHES
BREAK SHARP EDGES .004" TO .020".

ISSUE	ZONE	DESCRIPTION	DATE
1	N/A	FINAL ISSUE	10-02-17
2	N/A	OD INCREASED SHEETS 2 & 3	08-08-19
3	N/A	OD INCREASED SHEETS 2 & 3	08-08-19

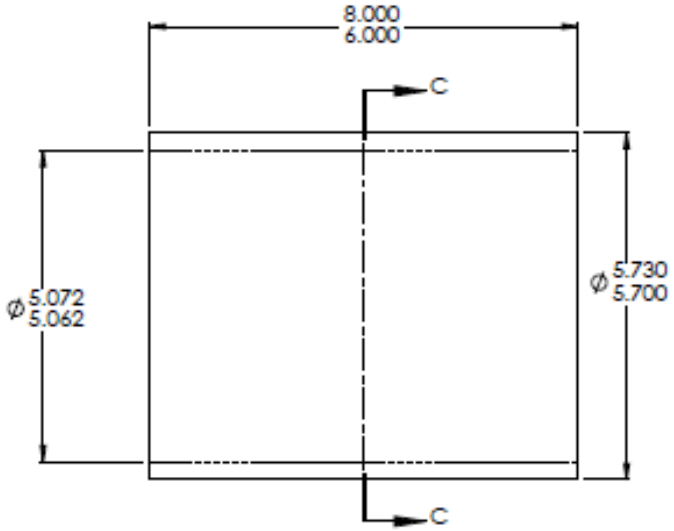

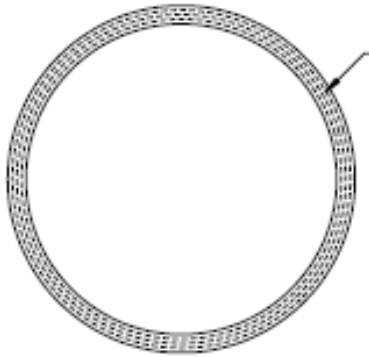

NOTE: LAMINATE DIRECTION SHOWN USING CONSTRUCTION LINES

SECTION C-C

CROSS MFG. CO.(1938) LTD.
MIDFORD ROAD,
BATH, BA2 5RR ENGLAND.

TITLE
CMC TUBING

DRAWN D WALKER
DATE 10-02-2017
MATL. SEE NOTE

No A24218

SHEET 3

THIRD ANGLE PROJECTION - SHEET SIZE A3			
ANGLES ARE IN DEGREES AND DECIMAL PARTS OF A DEGREE UNLESS OTHERWISE SPECIFIED: ALL DIMENSIONS ARE IN INCHES TOLERANCE ON DIMENSIONS ± .010" TOLERANCE ON ANGLES ± 2° SURFACE TEXTURE VALUES IN MICROINCHES SURFACE TEXTURE TO BE 125 MICROINCHES WHERE INDICATED - BREAK SHARP EDGES .004" TO .020".			
ISSUE	ZONE	DESCRIPTION	DATE
1	N/A	ISSUE 1	18/09/18
2	G13	ISSUE 2	19/03/19

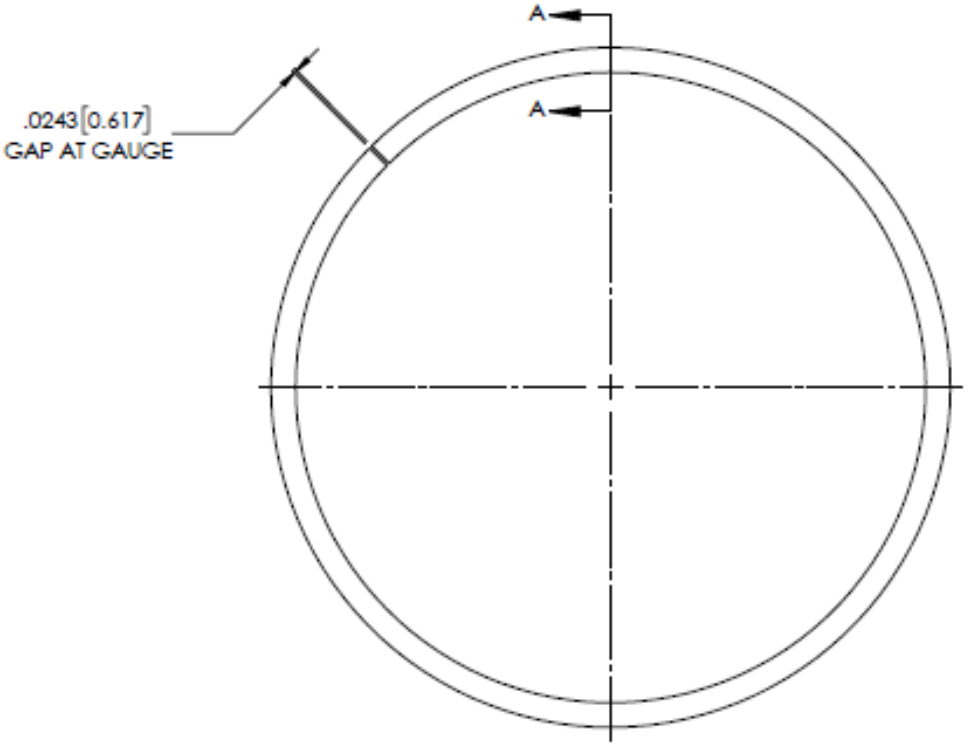

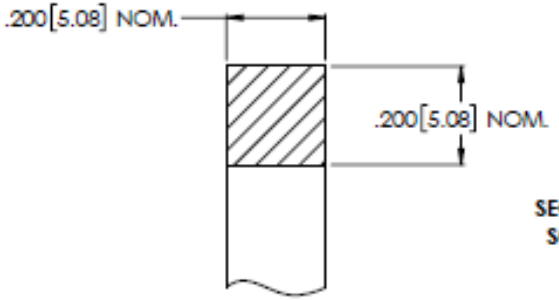

SECTION A-A
SCALE 4 : 1

MANUFACTURING PROCESS

1. MACHINE O/D TO 5.575"[141.61]
2. PART OFF
3. GAP TO .150"[3.81] AT Ø5.575"[141.61]
4. COMPRESS INTO Ø5.535"[140.59] O/D M/C JIG (TO PROVIDE 0.125"[3.175] OUTSPRING)
5. M/C O/D TO Ø5.5118"[140.00] GAUGE
6. SIDE GRIND
7. INSTALL INTO Ø5.5118"[140.00] JIG & MACHINE I/D TO Ø5.112" RING I/D
8. BREAK ALL SHARP CORNERS

PART NO. A24741

MATERIAL: OX-OX CERAMIC CMC

OUTSPRING TO BE 0.125"[3.175]

REMOVE ALL BURRS AND SHARP EDGES

CROSS MFG. CO.(1938) LTD. MIDFORD ROAD, BATH, BA2 5RR ENGLAND.	TITLE Ø5.5118" GAUGE CMC TEST RING		DRAWN AD8 DATE 18/09/18 MATL. OX-OX CMC	No A24741 SHEET 1/1

کئی بار اس کی خاطر ذرے ذرے کا جگر چیرا
مگر یہ چشم حیراں جس کی حیرانی نہیں جاتی

Many a times have I ripped open seashells to unravel their secrets,
But the curiosity of my wondering eye never ceases to extinguish

- Faiz

May this curiosity never cease to exist!

طلحہ جمال پیرزادا

Talha J. Pirzada

12th December 2021